

# Geodätisch-geophysikalische Arbeiten in der Schweiz

(Fortsetzung der Publikationsreihe  
«Astronomisch-geodätische Arbeiten in der Schweiz»)

herausgegeben von der

Schweizerischen Geodätischen Kommission  
(Organ der Akademie der Naturwissenschaften Schweiz)

**Achtundsechzigster Band  
Volume 68**

**Geodetic Mobile Solar Spectrometer**

Alexander Somieski

2005

Adresse der Schweizerischen Geodätischen Kommission:

Institut für Geodäsie und Photogrammetrie  
Eidg. Technische Hochschule Zürich  
ETH Hönggerberg  
CH-8093 Zürich, Switzerland

Internet: <http://www.sgc.ethz.ch>

ISBN 3-908440-11-4

Redaktion des 68. Bandes:  
Dr. A. Somieski, Dr. M. Troller

Druck: Print-Atelier E. Zingg, Zürich

## VORWORT

Mit den modernen satellitengestützten Positionierungsmethoden sind die Anforderungen gewachsen, hochpräzise geodätische Anwendungen im cm-Genauigkeitsbereich zu realisieren. Ein zentrales Problem ist weiterhin der Troposphäreneinfluss. Problematisch ist insbesondere die Korrektur des wasserdampfbedingten Feuchtanteils, da er sich örtlich und zeitlich schnell ändern kann. Im vorliegenden Band wird die Entwicklung des neuen mobilen Messsystems GEMOSS beschrieben, das auf Absorptionsmessungen mit einem hochauflösenden Sonnenspektrometer (SSM) beruht und für einen breiten Spektralbereich eingesetzt werden kann. Systematische Vergleiche mit anderen bodengestützten Verfahren, wie Wasserdampf radiometrie (WVR), GPS-Schätzung und Ballonsondierungen geben Aufschluss darüber, wie weit die Sonnenspektrometrie in der Lage ist, als zusätzliches Schätz- bzw. Kalibrationsverfahren eingesetzt werden zu können. Von besonderer Bedeutung ist die Validierung und Kalibration von Radiometern, die an Bord von Altimetrie-Satelliten zur Korrektur der Radar-Laufzeiten verwendet werden.

Ein wichtiger Teilaspekt ist die kritische Untersuchung des Fehlerbudgets. Umgerechnet auf die zenitale Laufzeitverzögerung von Mikrowellen ergibt sich eine Genauigkeit von 3 mm, welche die Anforderungen von hochpräzisen Anwendungen bestens erfüllt. Die durchgeführten Experimente gliedern sich auf in Langzeitbeobachtungen mit Parallelmessungen von Ballonsondierungen, GPS und Radiometrie, sowie in Vergleichsbeobachtungen mit dem Mikrowellenradiometer des Jason-Satelliten.

Der systematische Vergleich zwischen SSM, WVR, GPS und Ballonsondierungen auf der Meteo-Station von Meteoswiss in Payerne deutet darauf hin, dass die GPS-Schätzung unter feuchteren Bedingungen zu hohe Werte ergibt. Aus Langzeitbeobachtungen von über einem Jahr konnte eine lineare Abhängigkeit von zu hohen, GPS-geschätzten Wasserdampfmen gen in Funktion der Feuchte nachgewiesen werden. Die fundierte Analyse und der systematische, quantitative Vergleich zwischen den SSM-, WVR- und GPS-Methoden belegen eindrücklich die Leistungsfähigkeit des entwickelten Spektrometers GEMOSS.

Mit den erzielten Ergebnissen und potentiellen Anwendungsmöglichkeiten hat Herr Somieski einen gewichtigen wissenschaftlichen Beitrag der schweizerischen Geodäsie auf dem Gebiet der GPS-Meteorologie geleistet. Internationale Beteiligungen an EU-Projekten sowie im Rahmen von NASA's Ocean Surface Topography Mission Programm belegen das internationale Interesse an den Entwicklungsarbeiten. Die Schweizerische Geodätische Kommission SGK dankt Herrn Alexander Somieski für seinen überaus wertvollen Beitrag. Beat Bürki und Paul Sorber, IGP ETH Zürich, sowie das Institut für Analytische Wissenschaften, Berlin, haben massgeblich an dem Projekt mitgearbeitet, wofür wir unseren Dank aussprechen. Das Projekt wurde von dem EU Projekt „Gavdos“, der ETH Zürich und der SGK gefördert. Der Akademie der Naturwissenschaften Schweiz SCNAT danken wir für die Übernahme der Druckkosten.

**Prof. Dr. H.-G. Kahle**  
Institut für Geodäsie und Photogrammetrie,  
ETH Zürich

**Prof. Dr. A. Geiger**  
ETH Zürich  
Präsident der SGK

## PREFACE

Avec l'apparition des systèmes de positionnement par satellites les conditions pour la réalisation d'applications géodésiques de hautes précisions, dans la gamme du centimètre, ont considérablement augmentés. Un problème central reste cependant l'influence de la troposphère. Une difficulté particulière est l'évaluation de la correction de la part humide causée par la vapeur d'eau, ceci à cause de sa haute variabilité spatiale et temporelle. Le présent fascicule décrit le développement d'un nouveau système mobile (GEMOSS), basé sur des mesures d'absorption à l'aide d'un spectromètre solaire à large bande et à haute résolution (SSM). Des comparaisons systématiques avec d'autres techniques au sol comme la radiométrie de vapeur d'eau (WVR), l'estimation par GPS et des mesures par radiosondes ont été utilisées pour évaluer jusqu'à quel point la spectrométrie solaire pouvait être une méthode de calibration et d'estimation additionnelle. La validation et la calibration de radiomètres spatiaux à bord de satellites altimétriques sont d'un intérêt tout particulier.

Une partie importante de ce travail est dédiée à une étude critique du budget d'erreurs. L'erreur totale du retard sur le chemin humide zénithal est estimée à 3 millimètre. Ceci représente une excellente précision permettant une correction sûre des observations pour des applications de hautes précisions. Les expériences faites incluent des observations à long terme, en parallèle, de SSM, WVR et de ballons sondes ainsi que des campagnes conduites simultanément avec le radiomètre à micro-ondes monté à bord du satellite Jason.

Des observations à long terme à la station météorologique de Meteoswiss de Payerne montrent clairement que les estimations faites à l'aide du GPS sont systématiquement biaisées lors de conditions météorologiques humides. Une analyse profonde et une comparaison quantitative systématique entre les méthodes SSM, WVR et GPS prouvent le haut degré d'efficacité et de sûreté de la méthode de spectrométrie solaire développée et réalisée dans le nouvel instrument GEMOSS.

Avec les résultats obtenus et en considérant le potentiel élevé d'applications la contribution de Monsieur Alexander Somieski peut être considérée comme une contribution importante de la géodésie suisse à la météorologie par GPS. Les participations à des projets de l'Union Européenne aussi bien que dans le cadre des programmes de la NASA « Ocean Surface Topography Mission » révèlent l'intérêt international pour les recherches poursuivies. La commission suisse de géodésie remercie Monsieur Alexander Somieski pour cette contribution de haute valeur. Nous remercions également Messieurs Beat Burki et Paul Sorber de l'IGP de l'ETH Zürich ainsi que l'institut des sciences analytiques de Berlin pour leur collaboration. Cette étude a été supportée financièrement par le projet de l'Union Européenne « Gavdos », par l'ETH Zürich et par la Commission Suisse de Géodésie. Nous remercions l'Académie suisse des sciences naturelles pour avoir prit à sa charge les frais d'impression du présent fascicule.

**Prof. Dr. H.-G. Kahle**  
Institut de Géodésie et Photogrammetrie,  
ETH Zürich

**Prof. Dr. A. Geiger**  
ETH Zürich  
Président de la CGS

## FOREWORD

With the advent of modern satellite-based positioning techniques the requirements for the realization of high-precision geodetic applications in the cm range have increased considerably. A central problem is still imposed by the influence of the troposphere. Of particular difficulty is the mitigation of the wet part caused by the water vapor, because of its high spatial and temporal variability. This volume describes the development of a new mobile measuring system (GEMOSS), which is based on absorption measurements with a high-resolution broadband solar spectrometer (SSM). Systematic comparisons with other ground-based techniques, such as water vapor radiometry (WVR), GPS estimation and radiosonde soundings are used to evaluate to what extent solar spectrometry can be augmented as an additional estimation and calibration method. Validation and calibration of space borne radiometers aboard altimetry satellites are of particular interest.

An important part of this work is the extensive investigation on the error budget. The total error in the zenithal wet path delay is estimated at the 3 mm level. This represents an excellent accuracy which allows for a reliable correction of observations for high-precision applications. The experiments conducted include long-term observations of SSM, WVR and radiosonde measurements, as well as dedicated field campaigns carried out simultaneously with the microwave radiometer aboard the Jason satellite.

The long-term observations at the meteorology station of Meteoswiss at Payerne clearly show that the GPS estimates are systematically biased under relatively wet weather conditions: an important result in the field of GPS meteorology. The profound analysis and the systematic quantitative comparisons between SSM, WVR and GPS estimates prove to a high degree the effectiveness and reliability of the solar spectrometry method developed and realized in the new instrument GEMOSS.

With the results achieved and considering the high potential of applications Alexander Somieski has contributed a significant body of work of Swiss Geodesy in the field of GPS meteorology. Cooperation in an international EU project and in the frame of NASA's Ocean Surface Topography Mission Program reveal the international interest in the research work pursued and realized. The Swiss Geodetic Commission (SGC) expresses its gratitude to Alexander Somieski for his highly valued contribution. The collaboration with Beat Bürki and Paul Sorber, both at IGP of ETH Zürich, as well as with the Institute of Analytical Sciences, Berlin, is also gratefully acknowledged. The project was supported by the EU project "Gavdos", the ETH Zurich and the SGC. We are furthermore grateful to the Swiss Academy of Sciences for covering the printing costs of this volume.

**Prof. Dr. H-G. Kahle**  
Institute of Geodesy and Photogrammetry,  
ETH Zürich

**Prof. Dr. A. Geiger**  
ETH Zürich  
President of SGC



---

## Abstract

The goal of this work was to develop a portable prototype of a solar spectrometer for the determination of tropospheric water vapor with a high precision as needed for geodetic applications. It was realized in the construction of the “GEodetic MOBILE Solar Spectrometer” (GEMOSS), which allows the simultaneous measurement of numerous single vibrational-rotational absorption lines in the wide wavelength range between 728 nm and 915 nm.

In order to achieve the wide wavelength range and the envisaged high measurement accuracy, a new optical layout of a high-resolution echelle spectrograph was applied. Furthermore, its instrumental characteristics were determined and considered in the analysis and simulation of the spectrum. Therefore, investigations were carried out concerning hardware requirements, appropriate spectral intervals, stabilization of the wavelength scale, determination of the apparatus function and stray light. In addition to the theoretical aspects of molecular absorption and emission in Earth’s atmosphere, the meteorological model, ray tracing and the current state of molecular spectroscopic databases were examined. Furthermore, an algorithm for retrieving the integrated precipitable water vapor (PW) from GEMOSS spectra was developed. It is based on the “Differential Optical Absorption Spectroscopy” (DOAS) and includes the simulation of synthetic solar spectra. For the simulation the line strength parameters of  $H_2O$  absorption lines were taken from the molecular spectroscopic database by the European Space Agency (ESA). Although the line strength parameters, which have a large impact on the accuracy of the simulated spectra and the retrieved PW, were improved during the last years, they still reveal significant errors. The wide spectral range of GEMOSS enables the accurate correction of these parameters using solar spectra measured at atmospheric conditions controlled by radiosonde soundings and a water vapor radiometer (WVR). For this purpose, a dedicated campaign was carried out at the meteorological station at Payerne (Switzerland) in May and June 2004. GEMOSS and a co-located WVR were deployed next to a Global Positioning System (GPS) receiver of the Automated GPS Network of Switzerland (AGNES). The acquired dataset was utilized to improve line strength parameters of 69 individual transitions of the  $H_2O$  molecule between 732 nm and 906 nm.

In order to validate the performance of GEMOSS, a long-term series of PW was acquired at ETH Honggerberg where a permanent GPS station (AGNES) is operated. With the utilization of up to 40 selected  $H_2O$  absorption lines measured at the same time, an accuracy of the PW of  $0.5 \text{ kg/m}^2$  can be achieved. The comparison between GEMOSS and GPS revealed that GPS over-estimated the PW during the summer 2003 by about  $2\text{-}3 \text{ kg/m}^2$ . The same discrepancies were observed at Payerne in 2004 by comparing the GPS results with GEMOSS, WVR and radiosondes.

In the framework of the EU-project “GAVDOS”, GEMOSS was operated under the track of the altimeter satellite Jason at Rethimnon (Crete, Greece) and at Fiskardo

---

on the island of Kefalonia (Greece) in January and September in 2003. The highly precise PW measurements of GEMOSS were used to calibrate the on-board microwave radiometer of Jason (JMR). The integrated water vapor content which was simultaneously determined by GEMOSS and JMR agree at the 0.3-0.4  $kg/m^2$  level. On the basis of these promising results GEMOSS can be considered as a novel portable tool for space-borne radiometer calibration and it will be deployed for further calibration of Jason in the future.

---

## Zusammenfassung

Das Ziel dieser Arbeit war die Entwicklung eines transportablen Prototypen eines Sonnenspektrometers, welcher den troposphärischen Wasserdampfgehalt mit einer Präzision bestimmen kann, wie sie für geodätische Anwendungen benötigt wird. Dies wurde mit der Konstruktion des “GEodetic MOBILE Solar Spectrometer” (GEMOSS) realisiert, welches die simultane Messung vieler Absorptionslinien von Wassermolekülen im breiten Spektralbereich zwischen 728 nm und 915 nm ermöglicht.

Um diesen breiten Spektralbereich und die erwünschte hohe Messgenauigkeit erzielen zu können, wurde ein neuartiger optischer Aufbau eines hochauflösenden Echelle-Spektrographen verwendet, seine instrumentellen Eigenschaften bestimmt und bei der spektralen Analyse und Simulation berücksichtigt. Hierfür wurden Untersuchungen hinsichtlich der Anforderungen an Bauteile, geeignete Spektralintervalle, Stabilisierung der Wellenlängenskala, Bestimmung der Apparatefunktion und des Streulichtes durchgeführt. Neben theoretischen Aspekten der molekularen Absorption und Emission in der Erdatmosphäre wurden das meteorologische Modell, die Strahlenausbreitung und der aktuelle Stand der molekularen spektroskopischen Datenbanken behandelt. Weiterhin wurde ein Algorithmus zur Gewinnung des integralen ausfällbaren Wasserdampfes (PW) aus GEMOSS Spektren entwickelt. Er basiert auf der Methode der “Differentiellen Optischen Absorptionsspektroskopie” (DOAS) und enthält die Simulation synthetischer Sonnenspektren. Zur Simulation werden Linienparameter von Wassermolekülen verwendet, die der molekularen spektroskopischen Datenbank der Europäischen Raumfahrtbehörde (ESA) entnommen wurden. Obwohl die Linienparameter, die einen grossen Einfluss auf die Genauigkeit der simulierten Spektren und der daraus gewonnen Wasserdampfgehalte haben, in den letzten Jahren verbessert wurden, weisen sie noch immer signifikante Fehler auf. Das breite Spektrum von GEMOSS ermöglicht eine genaue Korrektur dieser Parameter für 69  $H_2O$ -Absorptionslinien. Dafür wurden Sonnenspektren analysiert, die bei, durch Radiosonden und Wasserdampfadiometer kontrollierten, meteorologischen Bedingungen gemessen wurden. Zu diesem Zweck wurde eine Messkampagne auf der meteorologischen Station in Payerne (Schweiz) im Mai und Juni 2004 durchgeführt. Neben einem Empfänger des “Globalen Positionierungssystems” (GPS), betrieben durch das Automatische GPS Netzwerk der Schweiz (AGNES), wurden GEMOSS und ein nebenstehendes Wasserdampfadiometer (WVR) eingesetzt. Zusätzlich wurden zwei Radiosonden pro Tag vom nationalen Wetterdienst der Schweiz (MeteoSchweiz) gestartet. Die erhaltenen Daten wurden zur Verbesserung der Linienparameter von 69  $H_2O$ -Absorptionslinien zwischen 732 nm und 906 nm verwendet.

Um die Leistungsfähigkeit von GEMOSS überprüfen zu können, wurde eine Messreihe über einen langen Zeitraum auf dem Gelände der ETH auf dem Höggerberg erstellt, wo auch ein GPS Empfänger von AGNES permanent betrieben wird. Unter Verwendung von bis zu 40 ausgewählten Absorptionslinien, die gleichzeitig in

---

einem Spektrum gemessen werden, konnte eine Genauigkeit des PW von  $0.5 \text{ kg/m}^2$  erreicht werden. Der Vergleich zwischen GEMOSS and GPS zeigte, dass GPS den Wasserdampfgehalt während der Sommermonate um etwa  $2\text{-}3 \text{ kg/m}^2$  überschätzt. Die gleichen Abweichungen konnten auch 2004 in Payerne beim Vergleich der GPS Resultate mit denen von GEMOSS, WVR und Radiosonden beobachtet werden.

Im Rahmen des EU-Projektes "GAVDOS" wurde GEMOSS unter der Bahn des Altimetersatelliten Jason in Rethimnon (Kreta, Griechenland) und in Fiskardo auf der Insel Kefalonia (Griechenland) im Januar und September 2003 eingesetzt. Die hochpräzisen Wasserdampfmessungen von GEMOSS wurden zur Kalibrierung des Wasserdampfradiometers (JMR) an Bord von Jason benutzt. Der von GEMOSS und JMR simultan gemessene PW stimmt auf einem Niveau von  $0.3\text{-}0.4 \text{ kg/m}^2$  überein. Anhand dieser vielversprechenden Ergebnisse kann GEMOSS als ein neues, transportables Instrument zur Kalibrierung von weltraumgestützten Radiometern angesehen werden. Weitere diesbezügliche Einsätze von GEMOSS im Rahmen des "GAVDOS"-Projektes sind bereits geplant.

# Contents

<b>1</b>	<b>Introduction</b>	<b>1</b>
1.1	The significance of atmospheric water vapor . . . . .	1
1.1.1	Climatology and meteorology . . . . .	1
1.1.2	Space geodesy . . . . .	2
1.2	Goals of this work . . . . .	3
<b>2</b>	<b>Propagation of microwave signals in Earth's atmosphere</b>	<b>6</b>
2.1	Introduction . . . . .	6
2.2	Refraction of microwave signals . . . . .	6
2.3	Wet and dry path delay . . . . .	7
2.4	Precipitable water vapor . . . . .	10
<b>3</b>	<b>GPS meteorology</b>	<b>12</b>
3.1	Introduction . . . . .	12
3.2	Observation equation . . . . .	13
3.3	Estimation of tropospheric parameters . . . . .	15
<b>4</b>	<b>Water Vapor Radiometry</b>	<b>17</b>
4.1	Introduction . . . . .	17
4.2	Brightness temperatures . . . . .	17
4.3	Linearized and effective brightness temperatures . . . . .	19
4.4	Retrieval algorithm . . . . .	21
4.5	Inversion coefficients . . . . .	22
4.6	The new Water Vapor Radiometer WVR2000 . . . . .	36
4.7	Conclusions . . . . .	39
<b>5</b>	<b>Solar Spectrometry</b>	<b>40</b>
5.1	Introduction . . . . .	40
5.2	Differential Optical Absorption Spectroscopy . . . . .	40
<b>6</b>	<b>Solar Spectrometry - Atmospheric Absorption Model</b>	<b>43</b>
6.1	Introduction . . . . .	43
6.2	Absorption of radiation . . . . .	43
6.3	The line strength . . . . .	44
6.4	Line broadening . . . . .	47

6.4.1	Introduction . . . . .	47
6.4.2	Collision broadening . . . . .	47
6.4.3	Doppler broadening . . . . .	49
6.4.4	Voigt profile . . . . .	51
6.5	HITRAN molecular spectroscopic database . . . . .	51
6.6	ESA-WVR molecular spectroscopic database . . . . .	52
6.7	Ray tracing . . . . .	53
6.8	Meteorological profiles . . . . .	56
<b>7</b>	<b>GEodetic MObile Solar Spectrometer I (GEMOSS I)</b>	<b>59</b>
7.1	System requirements . . . . .	59
7.2	Hardware configuration . . . . .	60
7.3	Wavelength stabilization . . . . .	67
7.4	Apparatus function . . . . .	71
7.5	Determination of stray light . . . . .	76
<b>8</b>	<b>GEMOSS I - Tropospheric Water Vapor Retrieval</b>	<b>80</b>
8.1	Selection criteria of absorption lines . . . . .	80
8.1.1	Saturation . . . . .	80
8.1.2	Fraunhofer lines . . . . .	80
8.1.3	Base intervals . . . . .	83
8.2	Pre-processing of measured solar spectra . . . . .	85
8.2.1	Normalization . . . . .	85
8.2.2	Correction for stray light . . . . .	90
8.3	Simulation of absorption spectra . . . . .	91
8.3.1	Introduction . . . . .	91
8.3.2	High-resolution spectrum . . . . .	91
8.3.3	Convolution . . . . .	92
8.3.4	Digitalization . . . . .	93
8.4	Least-squares fit algorithm . . . . .	95
8.5	Accuracy analysis . . . . .	98
8.5.1	Introduction . . . . .	98
8.5.2	Noise of CCD . . . . .	98
8.5.3	Stray light . . . . .	101
8.5.4	Apparatus function . . . . .	101
8.5.5	Line strength parameter . . . . .	102
8.5.6	Meteorological model . . . . .	106
8.5.7	Conclusions . . . . .	108
<b>9</b>	<b>Improvement of absorption line strength parameter</b>	<b>109</b>
9.1	Motivation . . . . .	109
9.2	Strategy . . . . .	110
9.3	Fit algorithm . . . . .	110
9.4	Results . . . . .	112

---

<b>10 Campaigns and results</b>	<b>125</b>
10.1 Jason Microwave Radiometer calibration campaigns . . . . .	125
10.1.1 Jason . . . . .	125
10.1.2 Campaigns . . . . .	127
10.1.3 Results . . . . .	128
10.2 Long-term measurements at Höggerberg . . . . .	136
10.2.1 Introduction . . . . .	136
10.2.2 Results . . . . .	138
10.2.3 Comparison . . . . .	143
10.3 COMPA - Comparison campaign at Payerne . . . . .	145
10.3.1 Introduction . . . . .	145
10.3.2 Results . . . . .	147
10.3.3 Comparison . . . . .	161
10.3.4 Discussion . . . . .	163
<b>11 Conclusions and Outlook</b>	<b>167</b>
<b>Bibliography</b>	<b>173</b>
<b>A Statistic</b>	<b>181</b>
<b>B GEMOSS - Solar Spectrum</b>	<b>182</b>



## Abbreviations

AGNES	Automated GPS Network of Switzerland
CCD	Charge-Coupled Device
Doris	Doppler Orbitography and Radiopositioning Integrated by Satellite System
ERS	European Remote-Sensing Satellite
ESA	European Space Agency
ESA-WVR	Molecular Spectroscopic Database of ESA for the Water Vapor Red Region
GEMOSS	Geodetic Mobile Solar Spectrometer
GPS	Global Positioning System
HITRAN	High Resolution Transmission Molecular Absorption Database
Jason	Oceanographic Altimeter Satellite
JMR	Jason Microwave Radiometer
LRA	Laser Retroreflector Array
PW	Integrated Precipitable Water Vapor
RMS	Root Mean Square
SEM	Standard Error of the Mean
TRSR	Turbo Rogue Space Receiver
WVR	Water Vapor Radiometer
ZPW	Zenithal Integrated Precipitable Water Vapor
ZWD	Zenith Wet Path Delay



# 1 Introduction

## 1.1 The significance of atmospheric water vapor

### 1.1.1 Climatology and meteorology

Global warming and greenhouse effect are the keywords within the public discussion about recent Earth's climate changes. Both are subject to intensive scientific investigations and are related to the hydrological cycle. The greenhouse effect is caused by many atmospheric gases, from which water in the gaseous phase (natural and anthropogenic) is the most important one. The varying atmospheric water vapor is involved in numerous chemical reactions, such as the decomposition of the ozone layer and the creation of acid rain. The permanent movement of the hydrological cycle leads to an ever-changing distribution of water vapor, occurrence of clouds, rain and pollution.

Furthermore, water vapor transports large amounts of energy over long distances through the atmosphere by evaporating and re-condensing. On the one hand, the increasing amount of water vapor due to global warming absorbs more energy and amplifies again the warming trend. On the other hand, more water vapor causes more clouds, which reverses the trend by reflecting incident solar radiation. The complicated processes affecting the Earth's energy balance are issues of recent scientific studies, in which the variable water vapor plays an important role. A precise long-range and long-term observation of the spatial and temporal distribution of moisture can improve the theory and thus forecast of global climate change.

Water vapor is also a fundamental quantity in meteorology, because it influences directly the formation of clouds, the amount of precipitation and the process of energy transport. Therefore, the accuracy of numerical models for weather forecasting can be improved by considering the temporal and spatial distribution of atmospheric moisture. Several ground-based remote sensing techniques are deployed to measure the abundance and distribution of water vapor. The introduction of their observations into numerical models can contribute to a better weather modeling. Although dedicated for special geodetic applications, the "GEodetic MOBILE Solar Spectrometer" (GEMOSS) can be deployed for meteorological purposes as well.

### 1.1.2 Space geodesy

In space-borne geodetic techniques the radio signal has to traverse the Earth's atmosphere. Especially for those using microwaves, the transatmospheric signal is significantly delayed due to refraction. This is causing an excess path length to which the distance between satellite and receiver is over-estimated.

In the ionosphere the propagation delay depends on the electron content along the signal path and on the frequency of the signal. This enables the determination of the *ionospheric* delay by combining two different frequencies. In the case of the Global Positioning System (GPS) the so-called ionospheric free linear combination is built from observations on the frequencies  $L_1$  and  $L_2$  which eliminates the ionospheric delay. The *tropospheric* delay can be divided into a dry and a wet part. The first one can be quantified with sufficient accuracy by measuring the ground pressure of air, whereas the latter depends on the variable integrated water vapor content (PW) along the signal propagation path. Changes in the water vapor content during a space geodetic measurement cause path delay fluctuations which result in significant errors of the coordinate solution. Due to the observation geometry the tropospheric delay reduces the accuracy of the vertical component three times more than that of the horizontals. For high-precision positioning with GPS, the knowledge of the properties of the refracting medium is required in order to correct the wet path delay. Because of the limited use of meteorological models and the increasing significance of GPS in Geodynamics and other disciplines, several remote sensing techniques have been developed for the determination of PW, such as water vapor radiometers [Jarlemark (1997), Kruse (2001), Somieski et al. (2002), Deuber et al. (2004)], solar spectrometers [Sierk (2000), Somieski et al. (2003)], Sun photometers [Ingold et al. (2000)], radiosondes and Lidars [Bock et al. (2001)]. Especially in Geodynamics, where tectonic movements of several millimeters are determined by GPS measurements, a precise tropospheric correction is necessary [Hollenstein et al. (2002), Hollenstein et al. (2003)]. Furthermore, altimeter satellite observations have to be corrected due to tropospheric refraction. For this purpose the altimeter satellite Jason carries an on-board microwave radiometer (JMR) which measures the amount of water vapor along the propagation path of the signal. In order to calibrate those radiometers, the PW is measured by ground-based remote sensing techniques simultaneously [Somieski et al. (2004)]. The calibration of the on-board microwave radiometer of Jason by means of GEMOSS measurements is described in section 10.1. The new water vapor radiometer of ETH developed at the Geodesy and Geodynamics Laboratory (GGL) in collaboration with CAPTEC is presented in chapter 4.

Nowadays, the networks of continuously operating GPS receivers, whose position is already accurately determined, enable the estimation of the water vapor content by reverting the problem of signal refraction in the troposphere. The estimated tropospheric path delay can directly be related to the integrated precipitable water vapor content. This method, called GPS meteorology, is outlined in chapter 3. A second

method based on GPS observations (GPS tomography) applies the tomographic approach to the signal delays in order to estimate the spatial and temporal distribution of water vapor [Kruse (2001), Troller (2004)].

## 1.2 Goals of this work

Motivated by the promising results of the first prototype “Solar Atmospheric Monitoring Spectrometer” (SAMOS) [Sierk (2000)] the development of an improved portable prototype of solar spectrometer was planned at the Geodesy and Geodynamics Laboratory (GGL). The “GEodetic MOBILE Solar Spectrometer” (GEMOSS) should be able to determine the tropospheric water vapor content with an accuracy as needed for high-precision geodetic applications. The retrieval of PW from solar spectra measured by GEMOSS is based on the “Differential Optical Absorption Spectroscopy” (DOAS) [Platt (1994)], which was already successfully applied to the high-resolution spectra of SAMOS. The research project “Geodetic Mobile Solar Spectrometer” is a collaboration of GGL and the Institute for Analytical Sciences (ISAS, Berlin). The new optical construction of the first GEMOSS allows extensive investigations of numerous  $H_2O$  absorption lines in the wide wavelength range between 728 nm and 915 nm. Based on the results of the study, a further improved solar spectrometer (GEMOSS II) is to be developed.

The following investigations and improvements concerning the construction of the GEMOSS measurement system were carried out:

- Quantification of instrumental error sources by introducing errors into the simulation of synthetic solar spectra
- Determination of the spectral resolution required for PW retrieval from single  $H_2O$  absorption lines with the envisaged accuracy of  $0.3 \text{ kg/m}^2$
- Selection of suitable wavelength intervals for DOAS
  - Localization of Fraunhofer lines
  - Localization of suitable base intervals with negligible absorption
  - Unsaturated  $H_2O$  absorption lines
  - Absence of absorption lines of other molecules
- Selection of the optical components and design of the echelle spectrograph
- Construction of the spectrometer
- Construction of the Sun tracking telescope
- Determination of the instrumental characteristics

- Spectrum extraction from CCD image
  - Apparatus function
  - Stray light
  - Real-time wavelength stabilization using absorption lines of the solar spectrum
- Implementation of remote control via Internet and mobile phone

The wide wavelength range (723 - 915 nm) was chosen in order to include all absorption lines potentially suitable for DOAS. Another reason was the idea of improving the PW accuracy by averaging the results of numerous absorption lines. Furthermore, the correction of the line strength parameters should be made for as many  $H_2O$ -transitions as possible.

After the construction and calibration phase, the software packages for controlling and data processing were developed. This includes:

- Development of the control software with *Labview*<sup>®</sup>
- Development of the processing software with  $C^{++}$ 
  - Modeling of the atmospheric absorption process
  - Meteorological model
  - Ray tracing
  - Simulation of a synthetic solar spectrum (normalization, convolution, digitization)
  - Least-squares fit of the simulated to the measured spectrum

First tests of the completed GEMOSS measurement system were successfully carried out at ETH Honggerberg. Afterwards GEMOSS was deployed at several campaigns, which are described in chapter 10. Based on the acquired datasets the following issues were investigated:

- Retrieval of high-precision precipitable water vapor content
- Validation and comparison with WVR, GPS and radiosondes soundings
- Improvement of line strength parameters
- Calibration of the on-board microwave radiometer of the altimeter satellite Jason

In the first part of this work, the theory of signal propagation in the Earth's atmosphere is outlined followed by the description of the remote sensing techniques GPS meteorology and Water Vapor Radiometry. The second part is addressed to the Solar Spectrometry which is used for the determination of tropospheric water vapor. The method of DOAS as well as the atmospheric absorption model is examined in chapters 5 and 6. The development of GEMOSS and the determination of its instrumental characteristics are discussed in chapter 7. The selection of suitable absorption lines and the algorithm used to retrieve the water vapor content from solar spectra with a concluding accuracy analysis is written in chapter 8. Chapters 9 and 10 describe the correction of the line strength parameters by fitting simulated with measured GEMOSS spectra. The results of the campaigns, in which GEMOSS was involved are compiled and summarized. The work ends with conclusions and an outlook.

## 2 Propagation of microwave signals in Earth's atmosphere

### 2.1 Introduction

The transatmospheric signals of the GPS satellites are effected by the ionosphere, troposphere as well as multipath propagation at the satellite and in the vicinity of the receiver antenna. Since the precise determination of the tropospheric delay is the main subject of this work the theory of the signal propagation is focused on the troposphere. In the following sections the partition of the tropospheric delay into dry and wet delay and the relation of the latter one to the precipitable water vapor is examined.

### 2.2 Refraction of microwave signals

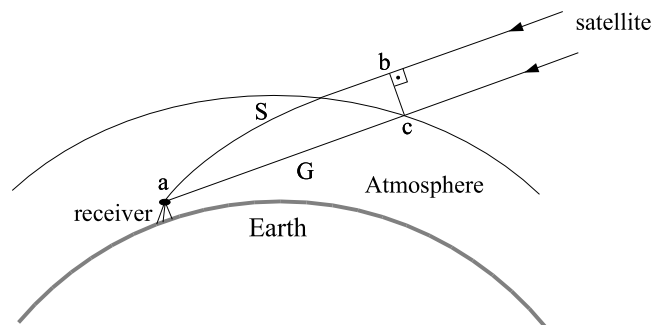


Figure 2.1: Propagation of the satellite signal through the Earth's atmosphere. The signal minimizes its travel time according to the Fermat's principle and propagates along the path  $S$  due to the refraction index which is increasing towards the Earth's surface.

In a refractive medium the geometry of a propagation path of radiation between two points is determined by the *Fermat's principle* by minimizing the travel time of the propagating signal. The travel time  $\tau$  of a microwave signal from a satellite to a receiver at the ground is calculated by integrating the infinitesimal path elements  $ds$  along the propagation path  $S$  [Elgered (1993)]:

$$\tau = \int_{\tau} dt = \int_S \frac{1}{v_p} ds \quad (2.1)$$

where  $v_p$  denotes the phase velocity of an electromagnetic wave. Introducing the refraction index

$$n = \frac{c_{vac}}{v_p} \quad (2.2)$$

with the speed of light in vacuum  $c_{vac}$  into Eq. 2.1, the electrical path length  $L$  along the ray path  $S$  becomes:

$$L = c_{vac} \int_{\tau} dt = \int_S n ds \quad (2.3)$$

Fig. 2.1 shows the ray path  $S$  bended due to increasing air density towards the Earth's surface as well as the geometrical straight-line distance  $G$ , which is always shorter than path  $S$ . The *electrical* path length along  $G$  is *longer* than that along  $S$ , because the propagating microwave signal would travel a longer distance with lower velocity close to the surface of the Earth, where the index of refraction is largest. The difference between the electrical path length and the geometrical straight-line distance is called *total path delay* and is defined by

$$\Delta L = (L - G) = \int_S n ds - G = \int_S (n - 1) ds + S - G \quad (2.4)$$

The integral in Eq. 2.4 accounts for the delay due to the lower phase velocity and  $(S - G)$  represents the geometrical deviation of the ray bending, which is usually neglected.

## 2.3 Wet and dry path delay

The index of refraction is conveniently replaced by the refractivity  $N$ :

$$N = 10^6(n - 1) \quad (2.5)$$

A common formula by Essen and Froome (1951) approximating the refractivity of the neutral atmosphere is:

$$N = k_1 \frac{P_d}{T} + k_2 \frac{e}{T} + k_3 \frac{e}{T^2} \quad (2.6)$$

where  $P_d$  and  $e$  denote the partial pressure of dry air and water vapor, respectively. The first two terms of Eq. 2.6 account for the influence of the induced dipole effect, while the last addend represents the permanent dipole moment of the water vapor molecule. The coefficients  $k_1$ ,  $k_2$  and  $k_3$  have empirically been determined in numerous laboratory studies. The values retrieved by Thayer (1974) are widely used:

$$\begin{aligned} k_1 &= 77.61 \pm 0.01 \text{ K/hPa} \\ k_2 &= 64.79 \pm 0.08 \text{ K/hPa} \\ k_3 &= (3.776 \pm 0.004) \cdot 10^5 \text{ K}^2/\text{hPa} \end{aligned}$$

With the assumption that the air is an ideal gas, the partial pressures in the two terms of Eq. 2.6 can be replaced with the gas law

$$P_i = \rho_i \frac{R}{M_i} T \quad (2.7)$$

where  $R = 8314.34 \pm 0.35 \text{ J/kmol K}$  is the universal gas constant,  $\rho_i$  the mass density and  $M_i$  the molar mass of gas  $i$ . Eq. 2.6 becomes [Elgered (1993)]:

$$\begin{aligned} N &= k_1 \frac{R}{M_d} \rho_d + k_2 \frac{R}{M_w} \rho_w + k_3 \frac{e}{T^2} \\ &= \underbrace{k_1 \frac{R}{M_d} \rho}_{N_h} + \underbrace{\left( k_2 - k_1 \frac{M_w}{M_d} \right) \frac{e}{T} + k_3 \frac{e}{T^2}}_{N_w} \end{aligned} \quad (2.8)$$

With the refractivity of the *hydrostatic* and *non-hydrostatic* or “*wet*” part as defined above the *wet* and *hydrostatic delay* can be written as:

$$\Delta L_h = 10^{-6} \int_s N_h ds \quad (2.9)$$

$$\Delta L_w = 10^{-6} \int_s N_w ds \quad (2.10)$$

As shown by Saastamoinen (1973) the zenithal hydrostatic delay can be related to the ground pressure  $P_0$  with high accuracy:

$$\Delta L_h^z = [0.0022768 \pm 2.4 \cdot 10^{-6} \text{ (m/hPa)}] \frac{P_0}{f(\Phi, H)} \quad (2.11)$$

with

$$f(\Phi, H) = 1 - 0.00266 \cdot \cos(2\Phi) - 0.00028 \cdot H \quad (2.12)$$

Eq. 2.12 is used to model the variation of the acceleration due to gravity and  $\Phi$  is the latitude and  $H$  is the height in  $km$  of the station above the ellipsoid. The non-hydrostatic (“wet”) delay in zenith direction can be calculated from the surface pressure, temperature and partial pressure of water vapor [Saastamoinen (1972), Troller (2004)]:

$$\Delta L_{w,Saast}^z = 0.002277 \left( \frac{1255}{T} - 0.044529 \right) e \quad (2.13)$$

Another definition of the wet refractivity separates Eq. 2.6 into different terms:

$$N = \underbrace{k_1 \frac{P - e}{T}}_{N_d} + \underbrace{k_2 \frac{e}{T} + k_3 \frac{e}{T^2}}_{N'_w} \quad (2.14)$$

According to Dalton's law, the partial pressure of dry air  $P_d$  is replaced by the difference of the air pressure  $P$  and the partial pressure of water vapor  $e$ .

The *dry* and *wet delay* are found by:

$$\Delta L_d = 10^{-6} \int_s N_d ds \quad (2.15)$$

$$\Delta L'_w = 10^{-6} \int_s N'_w ds \quad (2.16)$$

The differences of the delays defined in Eq. 2.9, 2.10 and 2.15, 2.16 are visualized in Fig. 2.2. Subtracting Eq. 2.10 from 2.16 yields the difference between the non-hydrostatic and wet delay as well as hydrostatic and dry delay [e.g. Mendes and Langley (2002)]:

$$\Delta L'_w - \Delta L_w = \Delta L_h - \Delta L_d = 10^{-6} \int_s k_1 \frac{M_w}{M_d} \frac{e}{T} ds \quad (2.17)$$

Since the notation “wet delay” is commonly associated with the definition of Eq. 2.10, in this study the wet delay will always denote the non-hydrostatic delay. The retrieval algorithm (Eq. 4.24) used to relate the microwave radiometer observations to the wet delay is also based on this definition. For correct comparison of wet delays retrieved by different techniques, a prior “equalization” of the wet delay definitions is required to avoid systematic deviations.

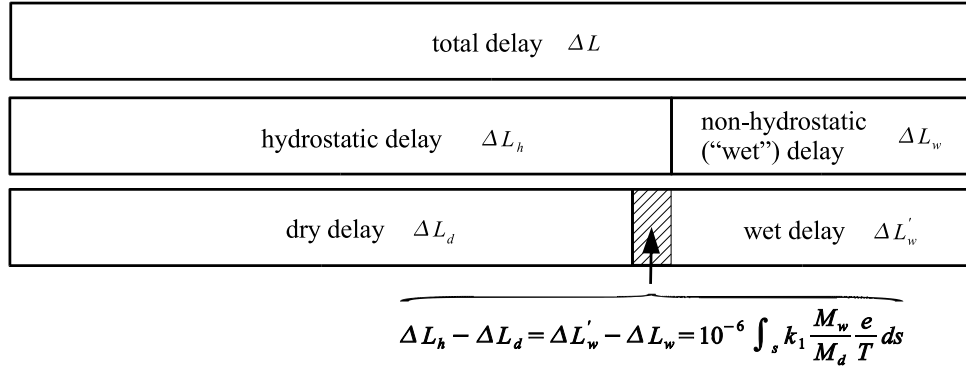


Figure 2.2: Deviations between different definitions of wet delay. The amount of the wet delay depends on the definition of the remainder (total delay - wet delay) as hydrostatic or dry delay.

## 2.4 Precipitable water vapor

The precipitable water vapor or integrated water vapor content  $PW$  [ $kg/m^2$ ] is found by integrating the mass density of water vapor  $\rho_w$  [ $kg/m^3$ ] along the path:

$$PW = \int_s \rho_w ds \quad (2.18)$$

The  $PW$  can also be expressed in terms of the column height [ $mm$ ] of precipitable water vapor by dividing Eq. 2.18 with the liquid water density  $\rho_l = 1000$   $kg/m^3$ . The  $PW$  into zenith direction is given by:

$$ZPW = \int_{h_0}^{h_t} \rho_w dh \quad (2.19)$$

In order to relate the wet delay with the  $PW$  the mean weighted temperature  $T_m$

$$T_m = \frac{\int_s \frac{e}{T} ds}{\int_s \frac{e}{T^2} ds} \quad (2.20)$$

is introduced into Eq. 2.10:

$$\Delta L_w = 10^{-6} \left( k'_2 + \frac{k_3}{T_m} \right) \int_s \frac{e}{T} ds \quad (2.21)$$

with

$$k'_2 = k_2 - k_1 \frac{M_w}{M_d} = 16.52 \frac{K}{hPa} \quad (2.22)$$

Replacing the partial pressure of water vapor  $e$  in Eq. 2.21 with the gas law (Eq. 2.7) the resulting integral of the water vapor density corresponds to the  $PW$  (Eq. 2.18) and Eq. 2.21 has changed to:

$$\Delta L_w = 10^{-6} \cdot \underbrace{\left( k_2' + \frac{k_3}{T_m} \right)}_{\kappa} \frac{R}{M_w} PW \quad (2.23)$$

The proportionality factor  $\kappa$  between  $\Delta L_w$  and  $PW$  is not constant, because the mean weighted temperature depends on the vertical profile of the partial pressure of water vapor and temperature. The analysis of 8718 radio soundings at 13 stations in the United States revealed that  $T_m$  can be estimated from the surface temperature  $T_s$  with an accuracy better than 2% [Bevis et al. (1992)]:

$$T_m = 70.2 + 0.72 \cdot T_s \quad (2.24)$$

Eq. 2.23 associates the satellite geodesy with the meteorology by relating the geodesic wet path delay with the precipitable water vapor. Vice versa, the  $PW$  measured by GEMOSS is converted into wet path delay with high accuracy by Eq. 2.23.

## 3 GPS meteorology

### 3.1 Introduction

The Global Positioning System (GPS) is a satellite-based radio navigation system providing precise three-dimensional position, navigation and time information. It is operated by the US Department of Defense (DoD) for military navigation purposes and is used by the geodetic community since about 1989, when the constellation allowed for kinematic positioning. The GPS consists of 24 active satellites distributed on six orbital planes, inclined by  $55^\circ$  and separated by  $60^\circ$  with respect to the Earth's equator. The orbital planes are almost circular ( $\varepsilon = 0.0232$ ) with an orbital height of about 20'200 km above the Earth's surface which is equivalent to a semi-major axis of about 26'600 km. The orbital revolution of a GPS satellite is 11 hours and 58 minutes. Each satellite carries a rubidium and a cesium oscillator used to generate the two frequencies  $f_1 = 1575.42 \text{ MHz}$  and  $f_2 = 1227.60 \text{ MHz}$  by multiplying the fundamental frequency  $f_0 = 10.23 \text{ MHz}$  by 154 and 120, respectively. In satellite geodesy the GPS is applied to determine tectonic motions and crustal deformation with positioning accuracies of several millimeters [e.g. Hollenstein et al. (2002), Hollenstein et al. (2003)]. A detailed description of GPS is given by e.g. Seeber (2003) and Teunissen and Kleusberg (1998). Concerning GPS processing strategies and observation equations, the reader is referred to e.g. Rothacher (1992), Mervart (1995), Schaer (1999) and Beutler et al. (2001).

As examined in the previous chapter the microwave signals of the GPS satellites are refracted while propagating through the Earth's atmosphere. This causes errors in the determined position, especially in the height component. The approach of the GPS meteorology, established in the past decade, is to revert the problem of refraction in order to retrieve the precipitable water vapor from the refraction path delay. This method requires a network of geodetic GPS receivers providing continuous phase measurements of the GPS satellite signals. Next to the integrated water vapor content the double difference residuals from the Bernese GPS Processing Software [Beutler et al. (2001)] are used to resolve the spatial and temporal distribution of the tropospheric water vapor by a tomographic approach which became generally known as GPS Tomography [Flores et al. (2000), Seko et al. (2000), Kruse (2001), Troller (2004)]. This chapter will outline the fundamentals of estimating tropospheric parameters with GPS.

## 3.2 Observation equation

The GPS receiver measures the difference between the phase of the received carrier wave generated by the satellite  $i$  and the phase generated by an oscillator within the receiver  $k$ . This phase difference can be written as:

$$\Psi_{Fk}^i(t) = \Phi_{Fk}(t) - \Phi_F^i(t - \tau) + n_{Fk}^i \quad (3.1)$$

where

$t$  is the signal reception time (GPS time)

$\tau$  is the signal traveling time

$\Psi_{Fk}^i(t)$  is the phase measurement at frequency  $f_F$  (in cycles) at epoch  $t$

$\Phi_{Fk}(t)$  is the phase generated by the receiver oscillator at signal reception time  $t$

$\Phi_F^i(t - \tau)$  is the phase of the carrier at emission time  $t - \tau$

$n_{Fk}^i$  is the unknown integer number of cycles (initial phase ambiguity)

Applying a Taylor series development, the phase difference becomes:

$$\Psi_{Fk}^i(t) = \Phi_{Fk}(t) - \Phi_F^i(t) + \tau \cdot f_F + n_{Fk}^i \quad (3.2)$$

where  $f_F$  denotes the frequency of the carrier. Considering the receiver clock error  $\delta_k$  and the satellite clock error  $\delta^i$  the difference  $\Phi_{Fk}(t) - \Phi_F^i(t)$  can be replaced with  $(\delta_k - \delta^i) \cdot f_F$  and Eq. 3.2 is modified to:

$$\Psi_{Fk}^i(t) = (\delta_k - \delta^i) \cdot f_F + \tau \cdot f_F + n_{Fk}^i \quad (3.3)$$

Multiplying Eq. 3.3 by the wavelength  $\lambda_F$  gives the carrier phase observation  $L_{Fk}^i$  in units of length:

$$L_{Fk}^i = c \cdot \delta_k - c \cdot \delta^i + \underbrace{c \cdot \tau}_{\rho_k^i} + \lambda_F \cdot n_{Fk}^i \quad (3.4)$$

where  $\rho_k^i$  is the geometric distance between satellite and receiver at signal emission time  $t - \tau$ . The phase measurement is affected by both systematic and random errors. The main GPS error contribution to the single range observation are assigned to three groups [Seeber (2003)]:

- Satellite
  - Orbit
  - Clock
  - Relativistic effects
- Signal propagation

- Ionosphere
- Troposphere
- Multipath effects
- Receiver
  - Observation noise
  - Hardware delays
  - Antenna phase center

Here the systematic errors of tropospheric and ionospheric refraction are reviewed. The geometric distance  $\rho_k^i$  in Eq. 3.4 contains the tropospheric and ionospheric delays. Keeping the notation  $\rho_k^i$  for the geometric distance (although the tropospheric and ionospheric delays are excluded) Eq. 3.4 can be rewritten:

$$L_{Fk}^i = \rho_k^i - \Delta\rho_{Fk,ion}^i + \Delta\rho_{k,trop}^i + c \cdot \delta_k - c \cdot \delta^i + \lambda_F \cdot n_{Fk}^i \quad (3.5)$$

where  $\Delta\rho_{k,trop}^i$  is the tropospheric refraction due to the neutral Earth's atmosphere and  $\Delta\rho_{Fk,ion}^i$  is the frequency-dependent ionospheric refraction. Since the ionosphere is a dispersive medium for microwaves the latter can be eliminated by the so-called *ionosphere-free linear combination*:

$$L_3 = \frac{1}{f_1^2 - f_2^2} (f_1^2 L_1 - f_2^2 L_2) \quad (3.6)$$

Furthermore, some biases can be eliminated or at least reduced by subtracting the original observations of the two receivers  $k$  and  $l$  to a satellite  $i$  (*single-difference*):

$$L_{Fkl}^i = L_{Fk}^i - L_{Fl}^i \quad (3.7)$$

Subtracting the observations to a second satellite  $j$  the *double-difference* eliminates the clock errors of the receivers and satellites:

$$L_{Fkl}^{ij} = L_{Fkl}^i - L_{Fkl}^j = \rho_{kl}^{ij} - \Delta\rho_{Fkl,ion}^{ij} + \Delta\rho_{kl,trop}^{ij} + \lambda_F \cdot n_{Fkl}^{ij} \quad (3.8)$$

The *triple-difference* of the double-difference observations from two different epochs  $t_1$  and  $t_2$

$$L_{Fkl}^{ij}(t_2) - L_{Fkl}^{ij}(t_1) = \rho_{kl}^{ij}(t_2) - \rho_{kl}^{ij}(t_1) - \Delta\rho_{Fkl}^{ij}(t_2) + \Delta\rho_{Fkl}^{ij}(t_1) \quad (3.9)$$

eliminates the phase ambiguities, which are assumed to remain the same within the time interval  $t_1 \leq t \leq t_2$ . Since the tropospheric refraction does not usually change rapidly in a short time period the triple-difference reduces it considerably.

To achieve the highest degree of accuracy the estimation of tropospheric parameters, as described in the following section, is necessary.

### 3.3 Estimation of tropospheric parameters

Assuming a homogeneous distribution of satellite observations over the hemisphere a systematic range error (for instance due to the tropospheric delay) is amplified by a factor of 3 in the height component, whereas the horizontal components remain unaffected [Geiger (1987)]. Disregarding the total tropospheric delay at all the height is biased by about 6 to 8 m. In other words, the absolute precision of the vertical component is the crucial factor for the estimation of the precipitable water vapor (PW) from GPS observations because the total tropospheric zenith delay, from which the wet delay and the PW is retrieved, will have an error of about one-third of the error in the height. The high correlation between the vertical component and the total tropospheric zenith delay can be defused by introducing observations at low elevation angles into the analysis and averaging the station coordinate parameters over a long period of time.

Instead of using only a simple a priori model of the tropospheric delay the tropospheric parameters are commonly estimated for individual stations. The corrections  $\Delta\rho_k(t)$  with respect to the a priori model  $\Delta\rho_{apr,k}$  are given by:

$$\Delta\rho_k^i = MF_{apr}(z_k^i)\Delta\rho_{apr,k} + MF(z_k^i)\Delta\rho_k(t) \quad (3.10)$$

where  $z_k^i$  is the zenith distance of the satellite,  $MF_{apr}(z_k^i)$  and  $MF(z_k^i)$  are the mapping functions of the a priori model and the estimated parameters, respectively. The corrections  $\Delta\rho_k(t)$  are time-dependent and a set of parameters  $\Delta\rho_k(t_i, t_{i+1})$  per station  $k$  and time interval  $t_i \leq t \leq t_{i+1}$  is estimated. The shorter the time interval is chosen, the greater the noise will be on the estimated results. This can be reduced by constrains in the least-squares adjustment, but it will also lead to a reduction of sensitivity to rapid changes of the atmospheric refraction. The wet part (Eq. 2.10) of the estimated total tropospheric delay into zenith direction is found by subtracting the zenithal hydrostatic delay calculated from the surface pressure (Eq. 2.11):

$$\Delta L_w^z = \Delta\rho_{apr,k} + \Delta\rho_k(t_i, t_{i+1}) - \Delta L_h^z(P_0) \quad (3.11)$$

The slant precipitable water vapor corresponding to the zenith distance  $z_k^i$  can be retrieved according to Eq. 2.23 from the zenithal wet path delay:

$$PW = MF(z_k^i) \cdot \frac{\Delta L_w^z}{\kappa} \quad (3.12)$$

where  $\kappa$  is the proportionality factor of Eq. 2.23 and  $MF(z_k^i)$  denotes the so-called mapping function. The simplest mapping function

$$MF(z) = \frac{1}{\cos(z)} \quad (3.13)$$

assumes an atmosphere with horizontal layers. During the last decades numerous more accurate mapping functions depending on the meteorological parameters, the season and the geographic location were developed [e.g. Marini (1972), Davis et al. (1985), Ifadis (1986), Herring (1992), Niell (1996)]. A commonly used mapping function approximates the dependence of the delay on the elevation angle by a continuous fraction geometrically [Marini (1972)]:

$$MF(z) = \frac{1}{\cos(z) + \frac{a}{\cos(z) + \frac{b}{\cos(z) + \frac{c}{\cos(z) + \dots}}}} \quad (3.14)$$

The constants  $a$ ,  $b$  and  $c$  were determined and improved by several scientist. Furthermore, the mapping function can be divided into a wet and a dry part to map the wet and dry delay separately [e.g. Davis et al. (1985), Rothacher (1992)]. For more detailed descriptions the reader is referred to the literature as cited above.

# 4 Water Vapor Radiometry

## 4.1 Introduction

Water vapor radiometer (WVR) measure the intensity of the radiation emitted by water molecules due to thermal excitation. The amount of water vapor is related to the thermal radiation emitted at  $22.235\text{ GHz}$ . In order to correct the influence of liquid water the thermal radiation is also measured at a second frequency. The WVR2000 of GGL uses the frequencies  $23.8\text{ GHz}$  (water vapor) and  $31.5\text{ GHz}$  (liquid water) (section 4.6). The accuracy of the PW highly depends on the so-called inversion coefficients of the retrieval algorithm. These coefficients have to be determined for every observation site from external measurements, usually from radiosonde soundings. In addition, the strong seasonal variation of the inversion coefficients increases the effort to guarantee reliable WVR observations. The results of investigating the seasonal and spatial variation of the inversion coefficients in Central Europe are discussed in section 4.5. The theoretical background of the retrieval algorithm is outlined in the next sections.

## 4.2 Brightness temperatures

Since the radiation received by the Water Vapor Radiometer (WVR) is in the microwave region, the Planck's law can be replaced by the Rayleigh-Jeans approximation:

$$B(f, T) = \frac{2f^2 k_B T}{c^2} \quad (4.1)$$

where  $f$  denotes the frequency,  $T$  the temperature,  $k_B$  the Boltzmann constant and  $c$  the light velocity. Furthermore, the brightness temperature  $T_B(f, s)$  can be expressed by the radiative flux density per frequency interval  $I(f, s)$ :

$$T_B(f, s) = \frac{c^2}{2k_B f^2} I(f, s) \quad (4.2)$$

The intensity  $I(f, s)$  is emitted by a black body radiator with the temperature  $T_B(f, s)$ . The absorption and emission in a non-scattering atmosphere can be described by the radiative transfer equation of Chandrasekhar (1960):

$$I(f, s_b) = I(f, s_a)e^{-\tau_f(s_a, s_b)} + \int_{s_a}^{s_b} k(f, s)B(f, T)e^{-\tau(s, s_b)} ds \quad (4.3)$$

with the absorption coefficient  $k(f, s)$  of the ambient medium and the optical depth or opacity  $\tau_f(s_a, s_b)$ , which is quantified by

$$\tau_f(s_a, s_b) = \int_{s_a}^{s_b} k(f, s) ds \quad (4.4)$$

The first term of Eq. 4.3 represents the absorption of the incident radiation while traversing the atmosphere from  $s_a$  to  $s_b$  along the propagation path. The second addend quantifies the emission of the medium along the propagation path by the Planck's function  $B(f, T)$  attenuated by the absorption factor  $e^{-\tau_f(s, s_b)}$ . For an azimuthal symmetric atmosphere with spherical layers the brightness temperature can be described by the radiation transfer Eq. 4.3:

$$T_B(f, s) = T_C e^{-\tau_\infty} + \int_0^\infty T(s)k(s)e^{-\tau(s)} ds \quad (4.5)$$

The brightness temperature of the cosmic background radiation is  $T_C = 2.8K$  and assumed to be independent from frequency. The total absorption coefficient  $k(f, s)$  consists of the absorption coefficients for water vapor, oxygen and liquid water:

$$k(f, s) = k_v + k_o + k_l \quad (4.6)$$

The contribution of other molecules to the total absorption coefficient is negligibly small. In order to eliminate the liquid water the brightness temperature has to be measured at two different frequencies:

$$T_{B,1}(f, s) = T_{C,1} + \int_0^\infty T(s)k_1(s)e^{-\tau_1(s)} ds \quad (4.7)$$

$$T_{B,2}(f, s) = T_{C,2} + \int_0^\infty T(s)k_2(s)e^{-\tau_2(s)} ds \quad (4.8)$$

Since  $T_C \ll T_B$  and usually  $\tau_\infty \ll 1$  for  $f < 40 GHz$  the attenuated cosmic background radiation terms can be replaced with two constants  $T_{C,1}$  and  $T_{C,2}$ . In this frequency range, the liquid water absorption coefficient due to clouds  $k_l$  is proportional to the square of frequency. Therefore, Eq. 4.7 and 4.8 can be combined to

$$\frac{T_{B,1} - T_{C,1}}{f_1^2} - \frac{T_{B,2} - T_{C,2}}{f_2^2} = \int_0^\infty W(s) \frac{\rho_v}{T} ds + T_0 \quad (4.9)$$

with the weighting function

$$W(s) = \frac{T^2}{\rho_v} \left( \frac{k_{v,1}}{f_1^2} e^{-\tau_1} - \frac{k_{v,2}}{f_2^2} e^{-\tau_2} \right) \quad (4.10)$$

and

$$T_0 = \int_0^\infty T \left( \frac{k_{o,1}}{f_1^2} e^{-\tau_1} - \frac{k_{o,2}}{f_2^2} e^{-\tau_2} \right) ds + \int_0^\infty T \frac{k_{l,2}}{f_2^2} [e^{-\tau_1} - e^{-\tau_2}] ds \quad (4.11)$$

As shown by Bean and Dutton (1966) the path length error due to water vapor  $\Delta L_w$  can be calculated from the density  $\rho_v$  and temperature  $T_v$  of water vapor:

$$\Delta L_w = \int_0^\infty \frac{\rho_v}{T_v} ds \quad k = 1.723 \cdot 10^{-3} \frac{K}{g/m^3} \quad (4.12)$$

A comparison of Eqs. 4.9 and 4.12 reveals, that if  $T_0$  is constant the weighting function  $W(s)$  is non-constant and implies non-uniqueness of the path length correction  $\Delta L_w$ . According to Wu (1979), the weighting function  $W(s)$  can be assumed to be constant for small opacities  $\tau_1$  and  $\tau_2$  at low air masses<sup>1</sup>. The opacities increase rapidly for high air masses and the brightness temperature becomes insensitive to changes in water vapor content.

### 4.3 Linearized and effective brightness temperatures

In order to remove the saturation effect as described in section 4.2 the weighting function  $W(s)$  is made to be constant by “linearizing” the brightness temperatures  $T_{B,1}$  and  $T_{B,2}$  according to Wu (1979):

$$T'_B \equiv T_C \left( 1 - \int_0^\infty k(s) ds \right) + \int_0^\infty T k(s) ds \quad (4.13)$$

$$= T_C + \int_0^\infty (T - T_C) k(s) ds \quad (4.14)$$

Similar to the procedure in the previous section the combination of the linearized brightness temperatures  $T'_{B,1}$  and  $T'_{B,2}$  yields the new weighting function  $W'(s)$ :

$$W'(s) = \frac{T(T - T_C)}{\rho_v} \left( \frac{k_{v,1}}{f_1^2} - \frac{k_{v,2}}{f_2^2} \right) \quad (4.15)$$

<sup>1</sup>The air mass  $m$  is defined as the ratio of the tropospheric ray path length corresponding to the elevation angle  $\theta$  to the path length into zenith direction and is approximated by  $m = \frac{1}{\sin(\theta)}$ .

Since the exponential terms of Eq. 4.10 are eliminated,  $W'(s)$  is constant for all air masses and a homogeneous atmosphere. In order to calculate  $T'_B$  from  $T_B$  we insert the “effective” temperatures

$$T_{eff} = \frac{\int_0^\infty T k(s) e^{-\tau} ds}{\int_0^\infty k(s) e^{-\tau} ds} \quad (4.16)$$

and

$$T'_{eff} = \frac{\int_0^\infty T k(s) ds}{\int_0^\infty k(s) ds} \quad (4.17)$$

into Eq. 4.5 and 4.13

$$T_B = T_C e^{-\tau_\infty} + T_{eff} (1 - e^{-\tau_\infty}) \quad (4.18)$$

$$T'_B = T_C (1 - \tau_\infty) + T'_{eff} \tau_\infty \quad (4.19)$$

and finally eliminate  $\tau_\infty$  in Eqs. 4.18 and 4.19

$$T'_B = T_C - (T'_{eff} - T_C) \ln \left( 1 - \frac{T_B - T_C}{T_{eff} - T_C} \right) \quad (4.20)$$

As shown by Jarlemark (1997), the effective temperatures  $T_{eff}$  and  $T'_{eff}$  are highly correlated frequency-dependent average temperatures of the attenuation medium and can be calculated with high accuracy from the daily maximum of the surface temperature  $T_{0,max}$  by

$$T_{eff} = (b_0 + m \cdot b_1) T'_{eff} \quad (4.21)$$

$$T'_{eff} = b'_0 + b'_1 T_{0,max} \quad (4.22)$$

The coefficients  $b_0$ ,  $b_1$ ,  $b'_0$  and  $b'_1$  were empirically obtained by Jarlemark (1997) with the method of least-squares from radiosonde data. The values for the measurement frequencies of the WVR at the Onsala space observatory in Sweden are listed in Tab. 4.1. For the ETH WVR's measuring at slightly different frequencies the coefficients can also be used with negligible decrease of accuracy.

	$b_0$	$b_1$	$b'_0$	$b'_1$
22.73 GHz	1.0004	$1.37 \cdot 10^{-3}$	62.16	0.7283
31.40 GHz	1.0002	$9.80 \cdot 10^{-4}$	58	0.738

Table 4.1: Empirical coefficients estimated by Jarlemark (1997) used to calculate the effective temperatures  $T_{eff}$  and  $T'_{eff}$  from the daily maximum temperature  $T_{0,max}$ .

## 4.4 Retrieval algorithm

A simple statistic method is the approximation of the path length error due to water vapor  $\Delta L_w$  using a linear function of measured quantities [Elgered (1993)]:

$$\Delta L_w = c_0 + \sum_{i=1}^n c_i X_i \quad (4.23)$$

where  $c_0$  and  $c_i$  denote the *inversion coefficients* and  $X_i$  the observation quantity. The observation quantity  $X_i$  consists of the linearized brightness temperatures and ground meteorological parameters such as air temperature, pressure and humidity. The appropriate inversion coefficients can be determined by a linear regression of  $\Delta L_w$  values and their corresponding observation quantities. The required dataset can be achieved by two different methods:

- Observation quantity  $X_i$  from WVR measurements and calculation of  $\Delta L_w$  from simultaneous radiosonde launches or other independent measurements
- Calculation of both  $X_i$  and  $\Delta L_w$  from representative radiosonde profiles (simulation method)

As defined in Eq. 4.6, the total absorption coefficient  $k(s, f)$  has a contribution  $k_l(f, s)$  from the cloud liquid water. Since the liquid and the gaseous phase of water molecules feature a different frequency dependence, the influence of  $k_l(f, s)$  can be reduced to a minimum by a linear combination of the linearized brightness temperatures measured at frequencies in the vicinity of the  $H_2O$  emission line. As described by Johansson et al. (1993), the implementation of the linearized brightness temperatures into Eq. 4.23 yields

$$\Delta L_w = c \cdot X \quad (4.24)$$

with the linear combination of  $T'_{B,1}$  and  $T'_{B,2}$

$$X = \left( \frac{f_2}{f_1} \right)^2 T'_{B,1} - T'_{B,2} - T_{C,Ox} \quad (4.25)$$

and

$$c = \frac{(1 + 6 \cdot 10^{-5} T_m) \cdot 0.3754 \cdot \int_0^\infty \frac{e}{T^2} Z_w^{-1} ds}{\int_0^\infty (T - T_{C,1}) \left[ \left( \frac{f_2}{f_1} \right)^2 k_{w,1} - k_{w,2} \right] ds} \quad (4.26)$$

where  $T_m$  is the average temperature of the atmosphere,  $e$  the partial pressure of water vapor and  $Z_w^{-1}$  the inverse compressibility factor for water vapor. The coefficient

$c$  exhibits significant annual variations, which can be approximated by expressing it as a function of ground meteo values:

$$c = c_{eff} [1 + c_1(P_0 - \bar{P}_0) + c_2(T_{0,max} - \bar{T}_{0,max}) + c_3(X - \bar{X})] (1 + 6 \cdot 10^{-5} \cdot T_{0,max}) \quad (4.27)$$

with

- the inversion coefficients  $c_{eff}$ ,  $c_1$ ,  $c_2$  and  $c_3$
- ground pressure  $P_0$  and its one year average  $\bar{P}_0$
- daily maximum of ground temperature  $T_{0,max}$  and its one year average  $\bar{T}_{0,max}$
- observation quantity  $X$  and its one year average  $\bar{X}$

Eq. 4.24 combined with Eq. 4.27 by Elgered (1993) is called **PTX-algorithm** and is used for further investigations. The inversion coefficients have to be determined by least-squares analysis for every WVR measurement site from radiosonde data separately as mentioned above. If no balloon soundings are available, the inversion coefficients of an other site with comparable climatic conditions can be used. The computation of inversion coefficients for an arbitrary WVR operation site in Central Europe without local radiosonde launches is described in the next section.

## 4.5 Inversion coefficients

The estimation of the inversion coefficients  $c_{eff}$ ,  $c_1$ ,  $c_2$  and  $c_3$  of Eq. 4.27 with sufficient accuracy is essential for precise  $\Delta L_w$  retrievals. The effective coefficient  $c_{eff}$  has the strongest effect on the results of Eq. 4.24, whereas  $c_1$ ,  $c_2$  and  $c_3$  can be regarded as non-critical. The amount of  $\Delta L_w$  errors caused by a certain inaccuracy of the inversion coefficients is tabulated in Tab. 4.2.

coefficient	absolute (relative) error of coefficient	$\Delta L_w$ error [%]
$c_{eff}$	0.01 cm/K ( $\sim 3\%$ )	3.3
$c_1$	$1 \cdot 10^{-5}$ 1/hPa ( $\sim 14\%$ )	0.04
$c_2$	$1 \cdot 10^{-4}$ 1/K ( $\sim 11\%$ )	0.07
$c_3$	$5 \cdot 10^{-5}$ 1/K ( $\sim 17\%$ )	0.07

Table 4.2: Error of the tropospheric path length correction  $\Delta L_w$  resulting from uncertainties of the inversion coefficients in Eq. 4.27.

In order to study the seasonal and spatial variation of the inversion coefficients for Central Europe a large set of radiosonde data was analyzed. The dataset was

provided by the *British Atmospheric Data Center* (BADC) and includes 19 sites during the time period from 1990 to 1999. The network of the launch sites is visualized in Fig. 4.1. The selection criteria for the sites are

- large dataset without interruptions
- uniform network centered in Germany
- significant variation in longitude and latitude
- various climatic conditions
- comparison with existing inversion coefficients

For the retrieval of the inversion coefficients from balloon soundings the simulation method was applied. The analysis software used for the data processing was written by Gunnar Elgered, Per O. Jarlemark and modified by L. P. Kruse. In a first step, the brightness temperatures, representing the missing WVR observations, are simulated from radiosonde data and the tropospheric path length error  $\Delta L_w$  is calculated. These quantities combined with ground meteorological parameters enable the least-squares fit of the inversion coefficients defined in Eq. 4.27. Generally, four radiosondes were launched at each site per day. They provide a adequate time resolution for the estimation of monthly and annual inversion coefficients. The average values of the annual coefficients for the chosen time period are listed in Tab. 4.3.

The annual coefficients  $c_{eff}$ ,  $c_1$ ,  $c_2$  and  $c_3$  of the *PTX-algorithm* are shown for selected sites in Fig. 4.2-4.5.

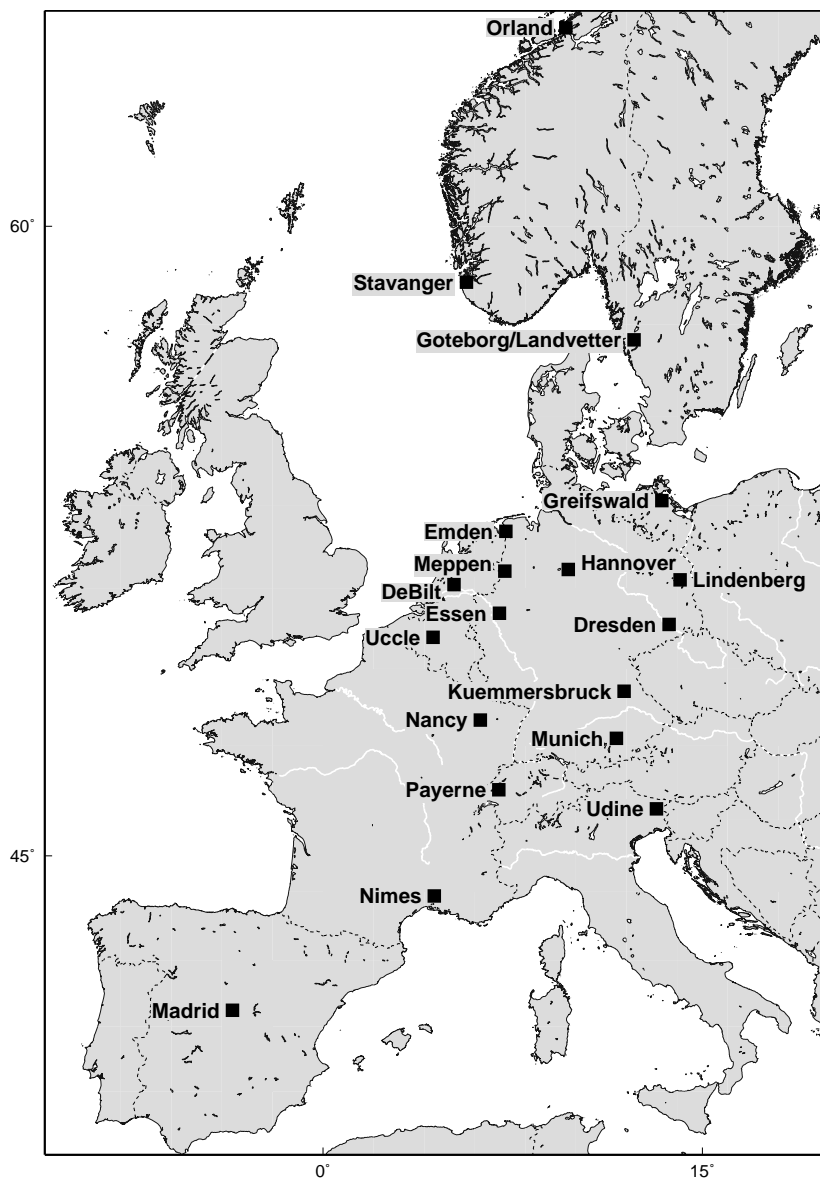


Figure 4.1: The radiosonde launch sites used to analyze the seasonal and spatial variation of the inversion coefficients  $c_{eff}$ ,  $c_1$ ,  $c_2$  and  $c_3$  in Central Europe: Orland, Stavanger, Goteborg-Landvetter, Greifswald, Emden, Meppen, de Bilt, Essen, Hannover, Lindenberg, Dresden, Kümmerbruck, Uccle, Nancy, Munich, Payerne, Udine, Nimes and Madrid.

station	time period	$c_{eff}$ [ $\frac{cm}{K}$ ]	$\sigma_{ceff}$ [ $\frac{cm \cdot 10^{-4}}{K}$ ]	$c_1$ [ $\frac{10^{-5}}{hPa}$ ]	$\sigma_{c1}$ [ $\frac{10^{-6}}{hPa}$ ]	$c_2$ [ $\frac{10^{-3}}{hPa}$ ]	$\sigma_{c2}$ [ $\frac{10^{-5}}{hPa}$ ]	$c_3$ [ $\frac{10^{-4}}{hPa}$ ]	$\sigma_{c3}$ [ $\frac{10^{-6}}{hPa}$ ]
Orland	1990-99	0.3122	1.2	5.19	8.4	-1.24	2.1	-2.47	7.6
Stavanger	1994-96	0.3108	1.8	-3.63	15	-1.14	3.2	-2.47	12
Goteborg	1990-99	0.3084	0.74	-4.42	5.8	-1.01	0.99	-2.80	4.5
Greifswald	1992-99	0.3066	0.74	-5.52	6.5	-1.01	1.0	-2.68	4.4
Emden	1990-99	0.3054	0.71	-7.23	6.2	-0.90	1.1	-2.94	4.4
Meppen	1990-98	0.3049	1.4	-10.82	12	-0.43	2.2	-4.54	7.5
Hannover	1990-97	0.3051	0.90	-2.83	8.4	-1.05	1.3	-2.44	5.5
Lindenberg	1991-99	0.3044	0.62	2.56	5.4	-1.08	0.76	-2.20	3.5
de Bilt	1990-99	0.3054	0.58	-3.71	5.3	-1.12	0.89	-2.29	3.5
Essen	1990-99	0.3029	0.70	-2.79	6.8	-1.13	1.0	-2.23	4.3
Dresden	1992-99	0.3020	0.90	4.36	9.1	-1.08	1.1	-2.06	5.3
Uccle	1990-99	0.3050	0.95	-2.94	9.6	-1.24	1.5	-1.68	5.4
Kümmersbruck	1990-99	0.2997	0.79	-1.94	8.7	-0.86	0.10	-2.66	4.7
Nancy/Essey	1990-99	0.3021	0.91	-0.61	11	-1.18	1.3	-1.31	5.3
Munich	1990-99	0.2978	0.81	11.4	9.3	-1.17	1.1	-1.35	5.0
Payerne	1990-99	0.2968	0.73	-3.33	9.1	-1.09	1.1	-1.77	5.1
Udine	1994-96	0.2975	0.92	-4.19	12	-1.26	1.4	-0.99	5.7
Nimes	1994-96	0.2967	1.2	-4.69	16	-1.30	1.6	-1.12	6.9
Madrid	1990-99	0.2868	0.69	-16.0	10	-1.35	0.8	-0.72	4.8

Table 4.3: Inversion coefficients of the *PTX-algorithm* for selected sites in Central Europe averaged over the time period of up to 10 years. The estimation is based on radiosonde data used to simulate the WVR observations and to calculate the tropospheric path length correction (simulation method) [Somieski (2000)].

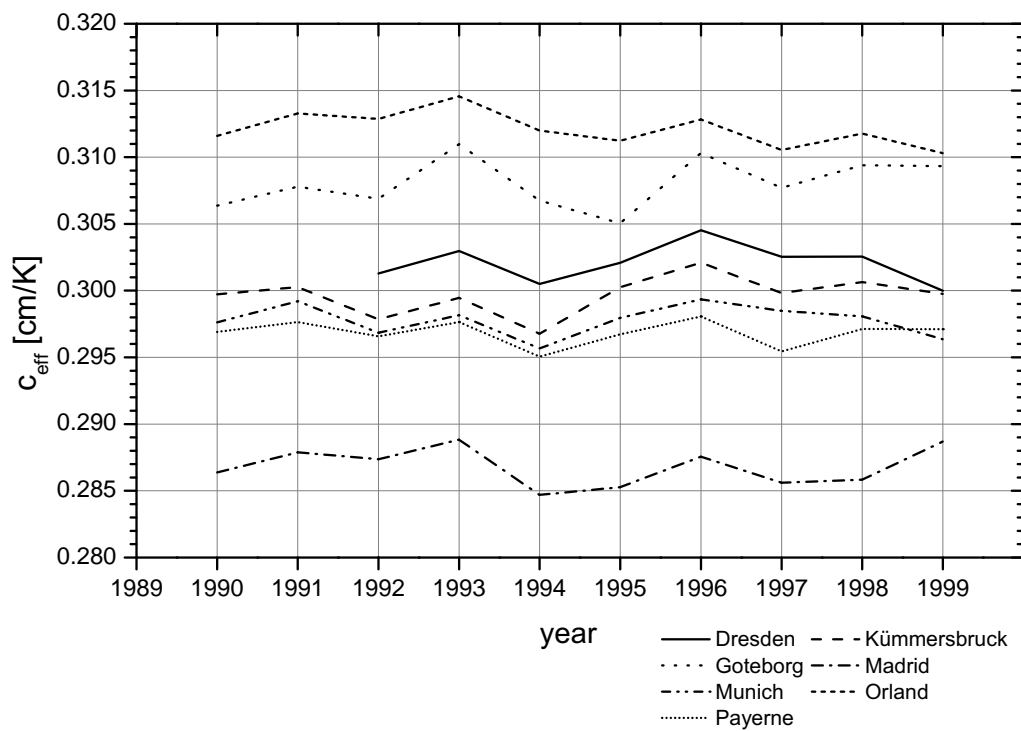


Figure 4.2: Annual effective coefficients  $c_{eff}$  for seven selected radiosonde launch sites from 1990 to 1999. The data of approximately 1460 radiosondes per year were used for the estimation of an annual  $c_{eff}$  [Somieski (2000)].

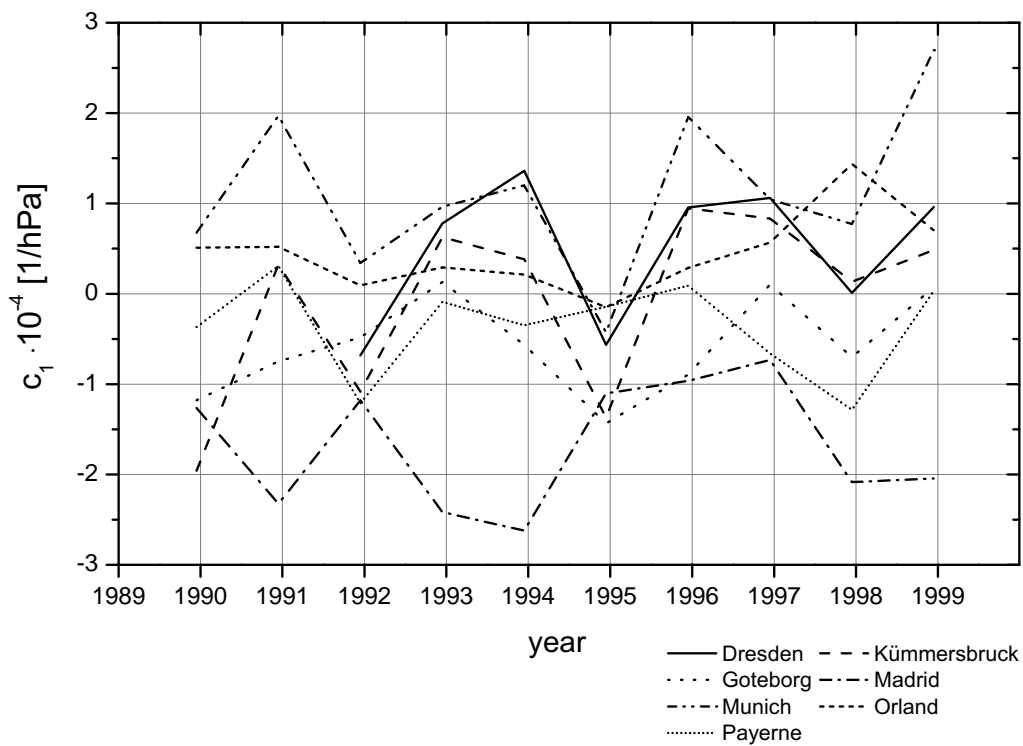


Figure 4.3: Annual inversion coefficients  $c_1$  for seven selected radiosonde launch sites from 1990 to 1999. The variation of  $c_1$  depends on the local conditions of the site [Somieski (2000)].

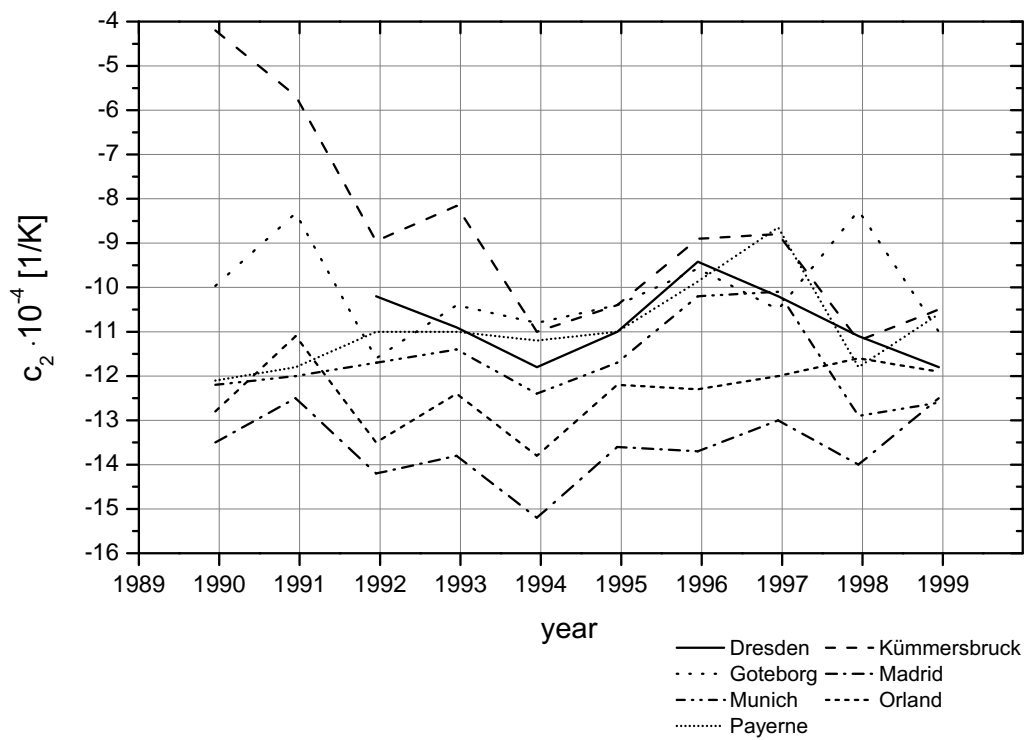


Figure 4.4: Annual inversion coefficients  $c_2$  for seven selected radiosonde launch sites from 1990 to 1999. Compared to  $c_1$  the annual  $c_2$  exhibit a more common behavior [Somieski (2000)].

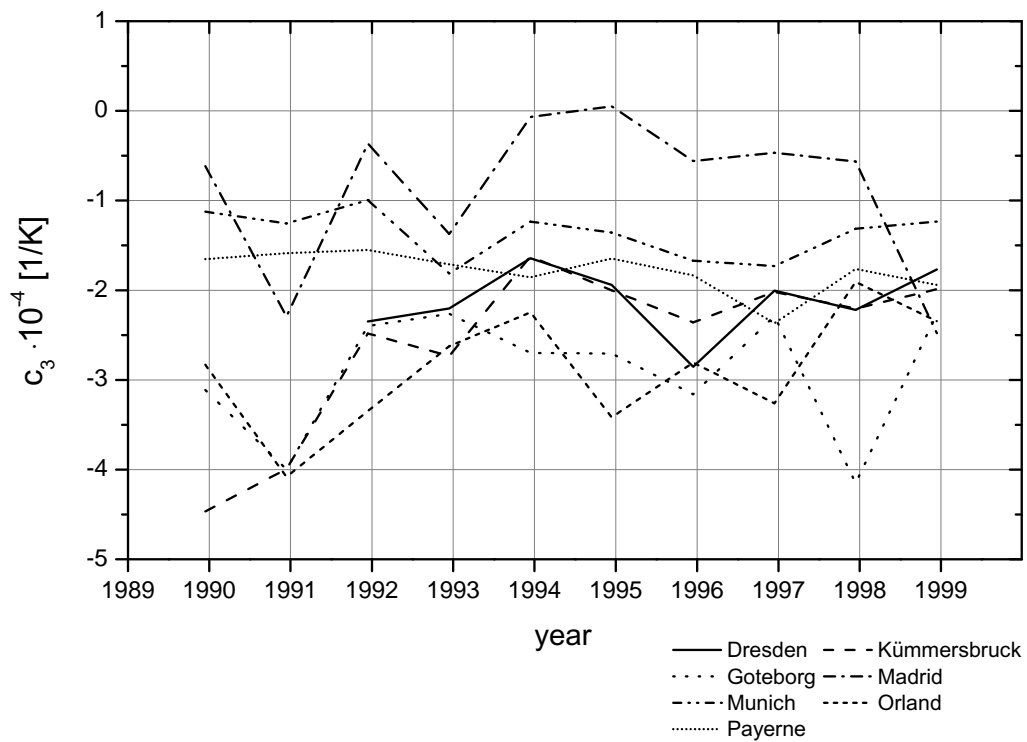


Figure 4.5: Annual inversion coefficients  $c_3$  for seven selected radiosonde launch sites from 1990 to 1999 [Somieski (2000)].

The variation of all  $c_{eff}$  exhibits an almost similar trend. For example, the  $c_{eff}$  of the year 1993 is for each site larger than in 1994. Furthermore, the curves in Fig. 4.2 have an almost constant offset among themselves. The reason stands out clear, if  $c_{eff}$  of Tab. 4.3 is plotted against the corresponding geographic latitude  $\Phi$  of the station. Fig. 4.6 reveals the dependence of the effective inversion coefficient on the latitude  $\Phi$  of the observation site. The correlation is tested for significance by calculating the empirical correlation coefficient  $r$  by Stingl (1992):

$$r = \frac{\sum_{i=1}^n x_i \cdot y_i - n \cdot \bar{x} \cdot \bar{y}}{(n-1) \cdot s_x \cdot s_y} \quad (4.28)$$

where  $x$  and  $y$  denote the random variables,  $s_x$  and  $s_y$  their empirical standard deviations and  $n$  the number of  $x, y$  couples. If the absolute value of the test variable

$$t = r \cdot \sqrt{\frac{n-2}{1-r^2}} \quad (4.29)$$

is larger than the bound of the t-distribution  $t_{\alpha, n-2}^*$ , the variables  $x$  and  $y$  are *not* statistically independent on the level of significance  $\alpha$ . A high correlation of  $c_{eff}$  with  $\Phi$  is obtained with  $r = 0.95$  and  $\alpha = 0.1$ . Whereas the coefficients  $c_1$  and  $c_2$  are not correlated with the geographical latitude on the level of significance  $\alpha = 0.1$  as demonstrated by the empirical correlation coefficients  $r = 7 \cdot 10^{-16}$  and  $0.27$ , respectively. For  $c_3$  a slight negative correlation with  $\Phi$  is found ( $r = -0.62$ ). A correlation of any coefficient with the geographical longitude  $\Lambda$  does not exist on the level of significance  $\alpha = 0.1$ . The high correlation of the effective inversion coefficient  $c_{eff}$  with  $\Phi$  enables the determination of  $c_{eff}(\Phi)$  for an arbitrary WVR operation site within the station network. The least-squares fit of a second-grade polynome is shown in Fig. 4.6 and yields [Somieski (2000)]:

$$c_{eff}(\Phi) = a_0 + a_1\Phi + a_2\Phi^2 \quad (4.30)$$

with

$$\begin{aligned} a_0 &= 0.1638 \pm 0.0013 \left[ \frac{cm}{K} \right] \\ a_1 &= 4.35 \cdot 10^{-3} \pm 5 \cdot 10^{-5} \left[ \frac{cm}{K} \right] \\ a_2 &= -3.17 \cdot 10^{-5} \pm 5 \cdot 10^{-7} \left[ \frac{cm}{K} \right] \end{aligned}$$

The mean error of  $c_{eff}(\Phi)$  in Eq. 4.30 is approximately  $\pm 1.3 \cdot 10^{-3} \text{ cm/K}$ , which corresponds to 0.3% of  $\Delta L_w$  (Eq. 4.24). In addition, monthly coefficients are estimated to investigate their annual variation. The monthly inversion coefficients for Goteborg-Landvetter, Payerne and Madrid are shown in Fig. 4.7-4.10. The effective coefficients of each site vary similar with time and exhibit a recurring maximum and minimum in the winter and summer, respectively, caused by annual temperature changes. The difference between the extremal values is approximately  $\Delta c_{eff} = c_{eff,max} - c_{eff,min} \approx 0.03 \text{ cm/K}$ . For this reason, the use of at least monthly estimated  $c_{eff}$  is recommended to avoid errors in  $\Delta L_w$  of up to 5%. The coefficients  $c_1$ ,  $c_2$  and  $c_3$  show also annual fluctuations, but less systematic. In contrast to  $c_{eff}$ , a considerable improvement of the algorithm accuracy of Eq. 4.27 by using monthly  $c_1$ ,  $c_2$  and  $c_3$  is in the majority of cases negligible.

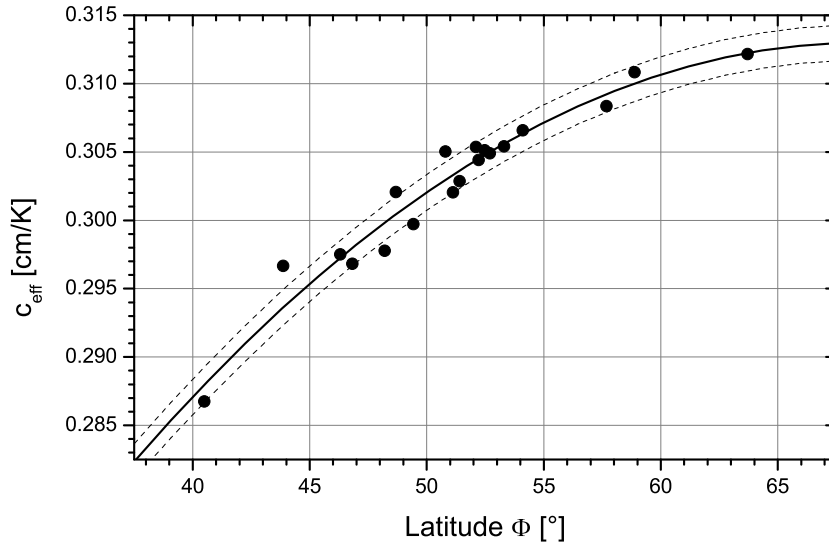


Figure 4.6: The effective coefficient  $c_{eff}$  is significantly correlated with the latitude  $\Phi$  of the WVR observation site. The mean error of  $c_{eff}(\Phi)$ , which was calculated with Eq. 4.30 (solid curve), is approximately  $\pm 1.3 \cdot 10^{-3} \text{ cm/K}$  [Somieski (2000)].

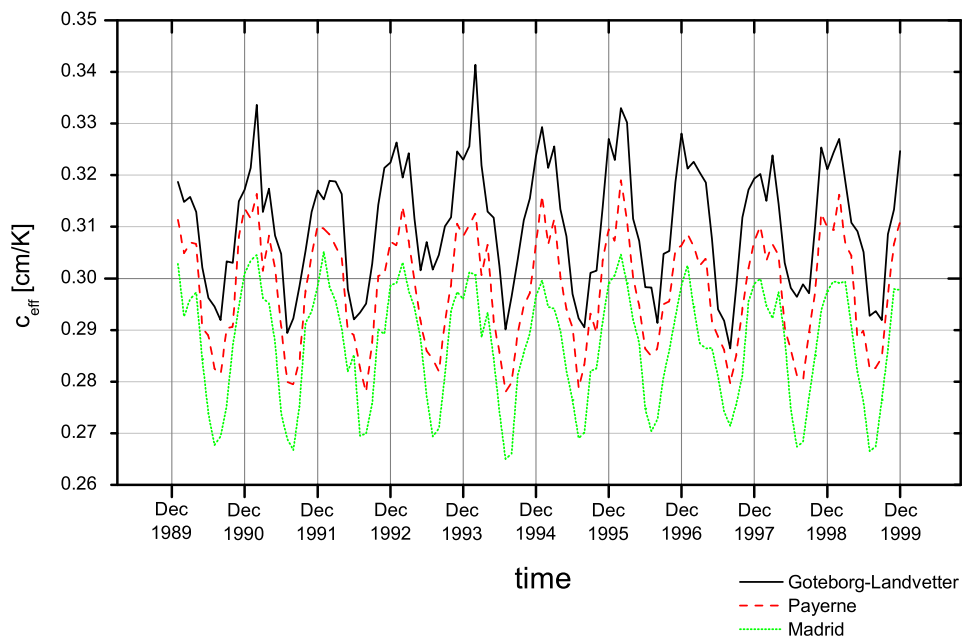


Figure 4.7: The effective coefficients  $c_{eff}$  of Goteborg-Landvetter, Payerne and Madrid determined monthly by applying the simulation method using data of about 120 balloon soundings. The annual variation with the maximum in the winter (January, February) and the minimum in the summer (July, August) is quantified with  $\Delta c_{eff} = c_{eff,max} - c_{eff,min} \approx 0.03 \text{ cm/K}$  for each site [Somieski (2000)].

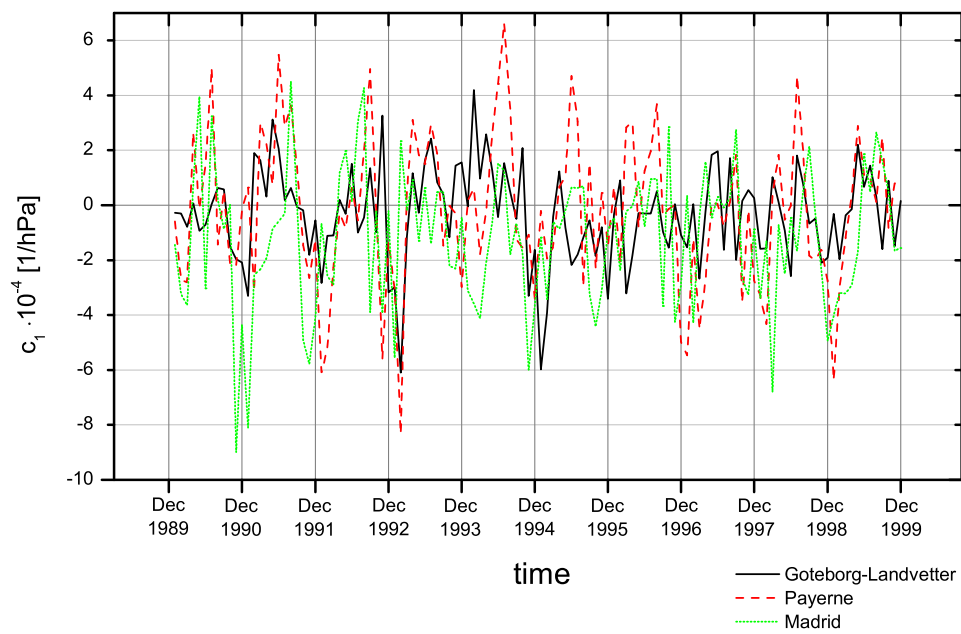


Figure 4.8: Monthly determined inversion coefficients  $c_1$  for Goteborg-Landvetter, Payerne and Madrid from 1990 to 1999 [Somieski (2000)].

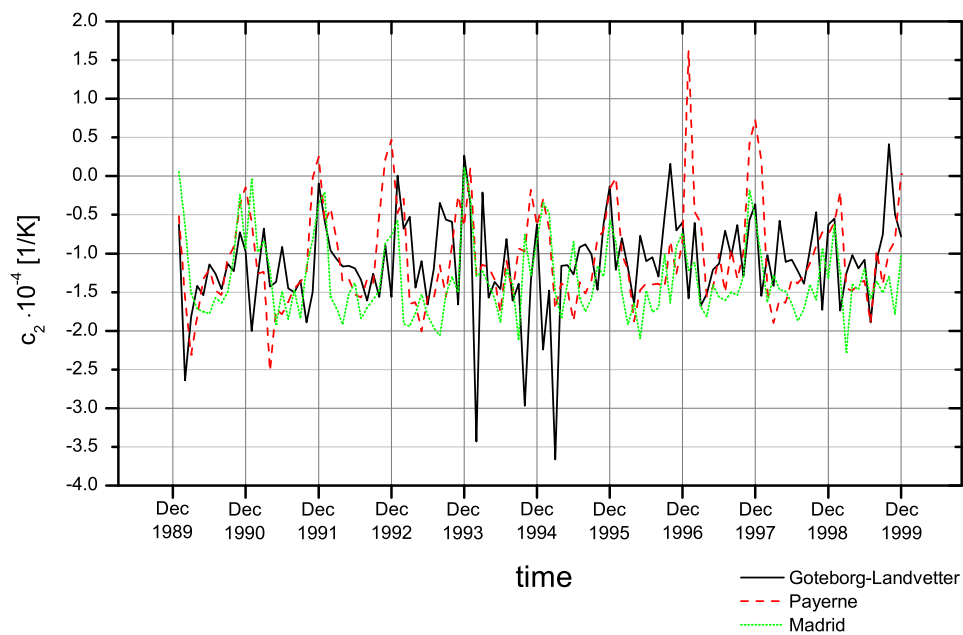


Figure 4.9: Monthly determined inversion coefficients  $c_2$  for Goteborg-Landvetter, Payerne and Madrid from 1990 to 1999 [Somieski (2000)].

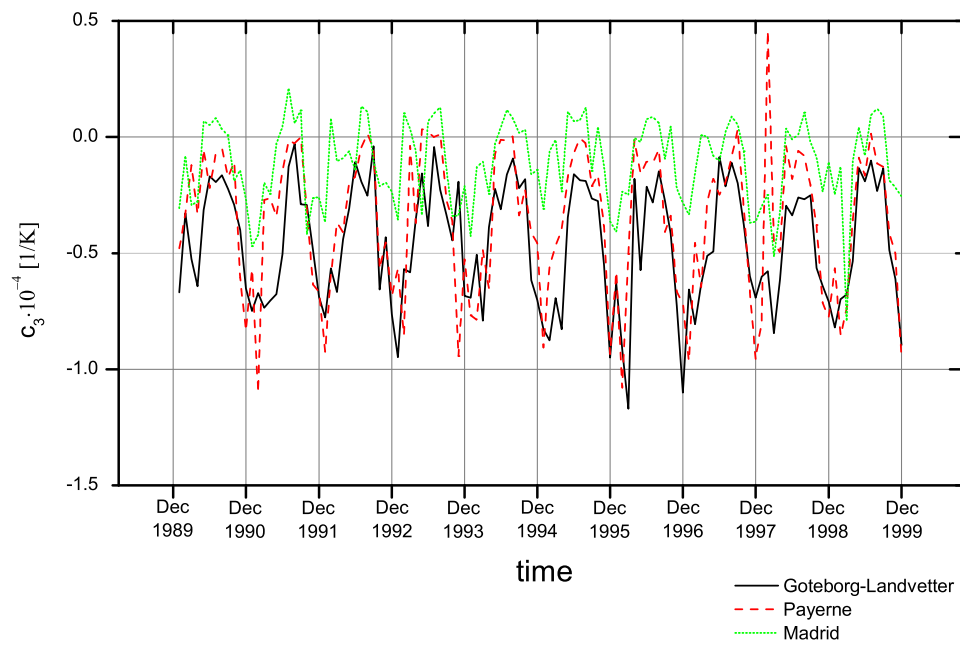


Figure 4.10: Monthly determined inversion coefficients  $c_3$  for Goteborg-Landvetter, Payerne and Madrid from 1990 to 1999 [Somieski (2000)].

## 4.6 The new Water Vapor Radiometer WVR2000

Fig. 4.11 shows the third generation of radiometers developed by the Geodesy and Geodynamics Laboratory (GGL) of ETH Zurich in cooperation with CAPTEC. The new design and construction offer advantages in stability and comfortable handling.



Figure 4.11: The new water vapor radiometer *WVR 2000* installed on the roof of the HPV building at ETH Honggerberg. Two mirrors reflect the radiation from the sky into two horn antennas.

The functional scheme of the ETH-radiometer is illustrated in Fig. 4.12. The radiation emitted by the sky is collected by two horn antennas (23.8 and 31.5 GHz). A noise diode generates calibration reference signals. A pin switch behind the horn antennas selects the radiation source (antennas or noise diode) to be conducted to a detector. Through microwave waveguides the signal is transmitted to a frequency mixer, an amplifier and finally to a detector which is read out by an A/D converter. The detector delivers an analog voltage signal which is linear proportional to the sensed radiation power. But this proportionality varies with the non-constant system amplification  $\gamma$  over time and has to be calibrated continuously. The calibration is realized by measuring the reference loads generated by switching *on* or *off* the noise diode, respectively. The signal  $V_H$  of the activated noise diode is equal to the radiation of a black body with the so-called “hot load temperature”  $T_H$  whereas the deactivated diode represents the ambient or the so-called “cold load temperature”  $T_A$  proportional to the corresponding voltage  $V_A$ .

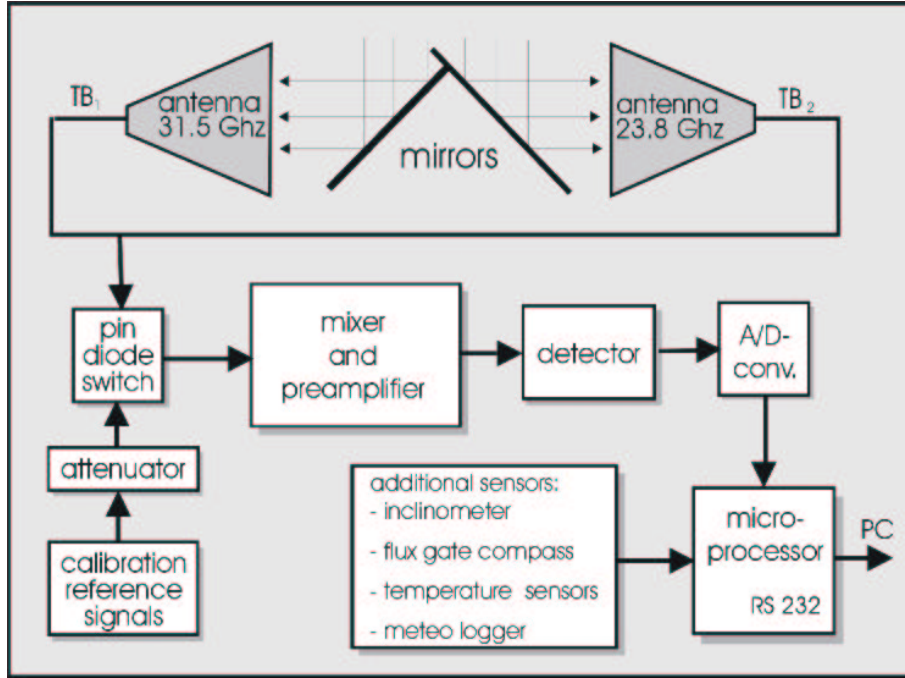


Figure 4.12: Scheme of the Water Vapor Radiometer WVR2000.

The brightness temperature defined in Eq. 4.5 can be expressed by the measured voltages  $V_B$ ,  $V_H$  and  $V_A$ :

$$T_B = T_A + (T_H - T_A) \cdot \gamma \quad (4.31)$$

with

$$\gamma = \frac{V_B - V_A}{V_H - V_A} \quad (4.32)$$

Eq. 4.32 assumes the non-existence of signal attenuation and reflection in the horn antennas, waveguides and circuits. Since those effects appear in practice, the hot load temperature has to be corrected by  $\Delta T_H$  and Eq. 4.31 becomes:

$$T_B = T_A + (T_H + \Delta T_H - T_A) \cdot \gamma \quad (4.33)$$

The hot load correction  $\Delta T_H$  can iteratively be adjusted by the method of *tipping curves*. This method utilizes the linear proportionality of the linearized brightness temperature  $T'_B$  (Eq. 4.20) to the air mass  $m$  introduced in section 4.3. In Fig. 4.13 the linearized brightness temperatures calculated from radiometer measurements are plotted against the air mass. Considering the fact that a radiometer would measure only the cosmic background radiation if the Earth's atmosphere is removed (air mass  $m = 0$ ) the linear regression through the  $T'_B$  measurements should intersect the abscissa at  $T_C = 2.8 K$ , exactly. Since the intersection point  $T(0)' \neq 2.8 K$  a

“hot load correction”  $\Delta T_H$  is adjusted by an iteration and added to each  $T'_B$ . A valid approximation of  $\Delta T_H$  to start the iteration is

$$\Delta T_H = \frac{[T_C - T'_B(0)] \cdot [T_H - T_A]}{T'_B(0) - T_A} \quad (4.34)$$

and the correction of the brightness temperature  $T_B$  is

$$\Delta T_B = \Delta T_H \cdot \frac{T_B - T_A}{T_H - T_A} \quad (4.35)$$

Finally, the *linearized* brightness temperature  $T'_B$  is corrected by inserting the corrected  $T_B$  into Eq. 4.20.

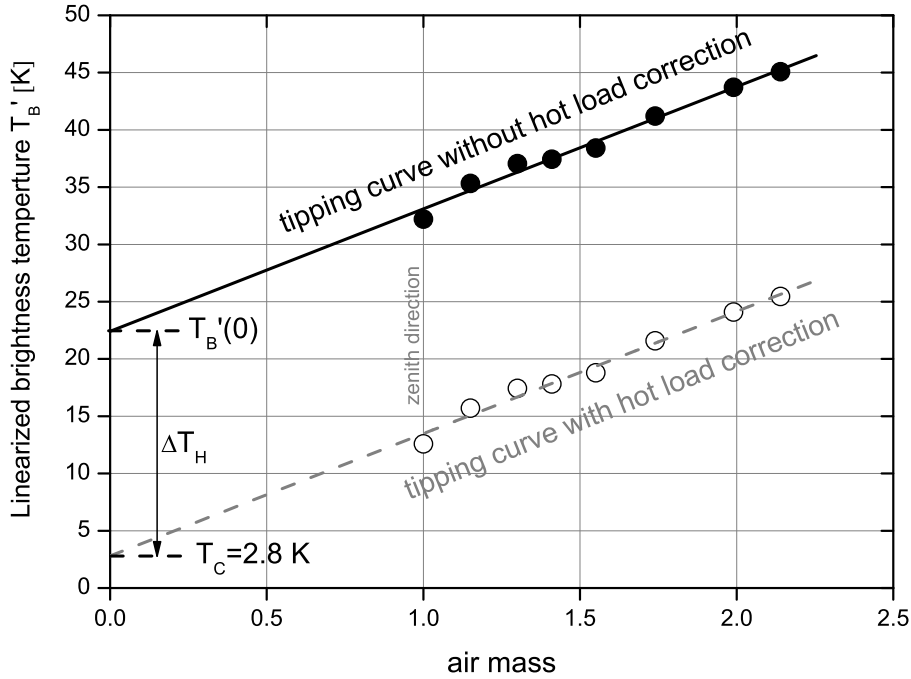


Figure 4.13: The linearized brightness temperatures  $T'_B$  are plotted against the air mass  $m = \frac{1}{\sin(\theta)}$  with  $\theta = \text{elevation angle}$ . After adding the iteratively determined hot load correction  $\Delta T_H$  the linear regression intersects the abscissa at  $T_C = 2.8 \text{ K}$ .

## 4.7 Conclusions

Among instrumental effects, the accuracy of the inversion coefficients (Eq. 4.27) is essential for precise retrieval of PW and  $\Delta L_w$  from radiometer measurements. An error of 3 % in  $c_{eff}$  causes a relative error of about 3.3 % in  $\Delta L_w$ . The strong spatial and seasonal variation of  $c_{eff}$  requires a precise determination of the coefficient at least every month from radiosonde soundings. Since  $c_{eff}$  is significantly correlated with the latitude  $\Phi$  of the WVR observation site, the effective coefficient can be calculated by an empirical formula (Eq. 4.30) with an accuracy of approximately  $\pm 1.3 \cdot 10^{-3} \text{ cm/K}$ .

In the future, the inversion coefficients can be determined more precisely and continuously from solar absorption spectra measured by GEMOSS. The huge number of GEMOSS measurements (up to six spectra per minute at daylight) allow a more accurate and continuous calibration of radiometers than four radiosonde soundings per day.

# 5 Solar Spectrometry

## 5.1 Introduction

The method of solar spectrometry used to retrieve the atmospheric water vapor content differs completely from the remote sensing techniques discussed in the previous chapters. Instead of measuring the intensity of the emitted radiation of  $H_2O$  molecules (water vapor radiometry) or exploiting the transatmospheric refraction of microwaves (GPS meteorology) the absorption of solar radiation due to  $H_2O$  molecules is utilized. In contrast to the Sun photometry which measures the integrated solar irradiance in broad spectral intervals, single  $H_2O$  vibrational-rotational absorption lines are analyzed. This results in a completely different error budget compared to all other methods mentioned above and indicates the solar spectrometry as an important tool for validation purposes. The algorithms used to retrieve the atmospheric water vapor content from solar absorption spectra is based on the *Differential Optical Absorption Spectroscopy (DOAS)* [Platt (1994)] which is introduced in the following section.

## 5.2 Differential Optical Absorption Spectroscopy

In the Earth's atmosphere the incident sunlight is attenuated by scattering at molecules (Rayleigh-scattering) and aerosol particles (Mie-scattering) as well as by molecular absorption at discrete characteristic wavelengths depending on the energy of the transition between different vibration-rotation states of the molecules of atmospheric constituents. Due to its asymmetry the  $H_2O$  molecule generates a complicated spectrum structure with absorption bands containing thousands of individual absorption lines. The intensity of the attenuated sunlight arriving the Earth's surface is quantified according to the Bouguer-Lambert-Beer law:

$$I(\lambda) = I_0(\lambda) \cdot \exp\left(-s \cdot \sum_i k_i(\lambda) \cdot \rho_i\right) \quad (5.1)$$

where

- $I_0(\lambda)$  is the intensity of the solar radiation before entering the atmosphere (initial or incident intensity)

- $k_i(\lambda)$  is the absorption cross section or absorption coefficient of the species  $i$
- $\rho_i$  is the density of the species  $i$
- and  $s$  is the length of the propagation path.

The problem of atmospheric measurements is the determination of the incident intensity  $I_0(\lambda)$  which would be received from the radiation source in absence of the Earth's atmosphere. The solution by DOAS is the splitting of the molecular absorption into two parts with respect to their variation with the wavelength: a “rapidly” and a “slowly” varying part. Accordingly, the absorption coefficient of a given molecule  $i$  is given by:

$$k_i(\lambda) = k_{i0}(\lambda) + k'_i(\lambda) \quad (5.2)$$

Substituting the absorption coefficient in Eq. 5.1 with Eq. 5.2 yields:

$$I(\lambda) = I'_0(\lambda) \cdot \underbrace{\exp\left(-s \sum_i k'_i(\lambda) \cdot \rho_i\right)}_{\text{“rapid”}} \quad (5.3)$$

with

$$I'_0(\lambda) = I_0 \cdot \underbrace{\exp\left(-s \sum_i k_{i0}(\lambda) \cdot \rho_i\right)}_{\text{“slow”}} \cdot A(\lambda) \quad (5.4)$$

where the attenuation factor  $A(\lambda)$  describes the wavelength-dependent transmission of the optical system. The “slowly” varying part includes the influence of Mie and Rayleigh scattering as well. The “rapidly” varying differential absorption  $I'_0(\lambda) - I(\lambda)$  depends only on the amount and distribution of the molecular species in the atmosphere. Broad-band effects including scattering are eliminated. Fig. 5.1 shows the principle of interpolating the intensity level  $I'_0(\lambda)$  from the intensities of so-called “baselining intervals” at either side of a sufficient narrow wavelength interval:

$$I'_0(\lambda) = \frac{I(\lambda_r) - I(\lambda_l)}{\lambda_r - \lambda_l} \cdot (\lambda_r - \lambda) + I(\lambda_l) \quad (5.5)$$

where  $\lambda_l$ ,  $\lambda_r$ ,  $I(\lambda_l)$  and  $I(\lambda_r)$  denote the center wavelength and averaged intensity of the left and right baselining interval, respectively.

The implementation of DOAS into the algorithms used to retrieve the tropospheric water vapor content from solar spectra measured by GEMOSS is described in chapter 8. The atmospheric absorption model used to simulate absorption line intensities for different meteorological conditions is examined in the next chapter.

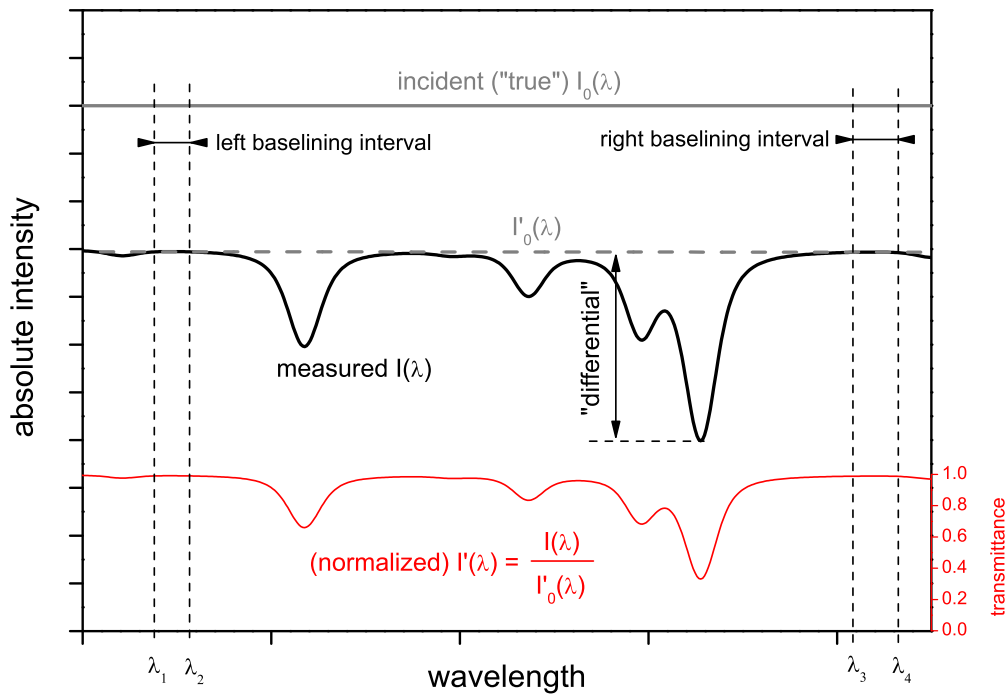


Figure 5.1: Differential Optical Absorption Spectroscopy (DOAS). The intensity level  $I'_0(\lambda)$  can be interpolated from the intensities of the left and right baselining interval if the wavelength interval lying in between is sufficient narrow. The “differential” absorption depends only on the number of absorbers and their distribution. Broad-band effects including Rayleigh- and Mie-scattering are eliminated.

# 6 Solar Spectrometry - Atmospheric Absorption Model

## 6.1 Introduction

In solar spectrometry a radiation transfer model is utilized to retrieve information about the Earth's atmosphere. The absorption process is simulated to compute synthetic spectra needed for the iterative fit of PW. The simulation of high-resolution DOAS spectra is based on the molecular line absorption. Broad band effects including scattering can be neglected. In this chapter, the theory of the radiative transfer model, the ray tracing as well as the meteorological model used to compute vibrational-rotational absorption spectra are outlined.

## 6.2 Absorption of radiation

In a homogeneous medium the intensity of the received radiation  $I$  after propagating a path of length  $s$  is characterized by the exponential Bouguer-Lambert-Beer law:

$$I(\nu) = I_0(\nu) \cdot e^{-k(\nu) \cdot s} \quad (6.1)$$

where  $I_0(\nu)$  denotes the initial intensity and  $k(\nu)$  the absorption coefficient of the propagation medium. The wave number  $\nu$  is the reciprocal value of the wavelength  $\lambda$ :

$$\nu = \frac{1}{\lambda} \quad (6.2)$$

The relation of the received to the initial intensity is defined as the spectral transmittance  $I'(\nu)$ :

$$I'(\nu) = \frac{I(\nu)}{I_0(\nu)} \quad (6.3)$$

Applying Eq. 6.1 to the inhomogeneous Earth's atmosphere, the varying absorption coefficients are integrated along the ray path from the station at the ground  $s_0$  to the

end of troposphere  $s_{tropo}$ . Furthermore, the individual contributions of all relevant absorption lines  $l$  superposing each other are summarized:

$$I(\nu) = I_0(\nu) \cdot \exp \left( \sum_l - \int_{s_0}^{s_{tropo}} \tau_l(\nu, s) ds \right) \quad (6.4)$$

The absorption coefficient of Eq. 6.1 is replaced by the quantity  $\tau_l(\nu, s)$  which is the optical density depending on the wave number  $\nu$  and the absorption path  $s$ . In an inhomogeneous atmosphere, the optical density is calculated from the monochromatic absorption coefficient  $k_l(\nu, s)$  and the molecular density  $\rho(s)$ :

$$\tau_l(\nu, s) = \rho(s) \cdot k_l(\nu, s) \quad (6.5)$$

The absorption coefficient  $k_l(\nu, s)$  can be described by the intensity of the energy transition or line strength  $S_l$  and the spectral shape  $f_l(\nu)$  of the absorption line  $l$  on the wave number scale:

$$k_l(\nu) = S_l \cdot f_l(\nu) \quad (6.6)$$

The line strength depends on the transition probability of the molecule whereas the spectral shape is affected by the collision and Doppler broadening. The line broadening is described in detail in section 6.4.

Introducing the normalized function of the spectral shape

$$\int_{-\infty}^{+\infty} f_l(\nu) d\nu = 1 \quad (6.7)$$

into Eq. 6.6, the line strength  $S_l$  can be expressed as the integral absorption

$$S_l = \int_{-\infty}^{+\infty} k_l(\nu) d\nu \quad (6.8)$$

The determination of the line strength based on laboratory measurements is addressed in the following section.

### 6.3 The line strength

The strength of a spectral line at the wave number  $\nu$  depends on the population of the initial energy state and the probabilities of three types of transitions:

- Spontaneous emission
- Induced or stimulated emission

- Induced absorption

Their probabilities are characterized by the Einstein coefficients  $A_{nm}$ ,  $B_{nm}$  and  $B_{mn}$ :

- $A_{nm}$ : coefficient for the spontaneous emission which gives the probability of a transition from an upper state  $n$  to a lower state  $m$
- $B_{nm}$ : coefficient for the induced emission which gives the probability of a transition from state  $n$  to state  $m$
- $B_{mn}$ : coefficient for the induced absorption which gives the probability of a transition from state  $m$  to state  $n$

Multiplying the Einstein coefficients  $B_{nm}$  and  $B_{mn}$  with the quotient of the radiant density per wave number  $w(\nu)$  and the light velocity  $c$  yields the probabilities of the induced emission and absorption:

$$P_{nm} = B_{nm} \cdot \frac{w(\nu)}{c} \quad (6.9)$$

$$P_{mn} = B_{mn} \cdot \frac{w(\nu)}{c} \quad (6.10)$$

Since the spontaneous emission is independent from the radiant density, its probability is the Einstein coefficient  $A_{nm}$  itself. The Einstein coefficients are related to the weighted transition-moment squared  $\mathfrak{R}_{mn}$  by:

$$B_{nm} = \frac{8\pi^3}{3h^2} \frac{g_m}{g_n} \mathfrak{R}_{mn} \quad (6.11)$$

$$B_{mn} = \frac{8\pi^3}{3h^2} \mathfrak{R}_{mn} \quad (6.12)$$

$$A_{nm} = \frac{64\pi^4}{3h} \nu_{nm}^3 \frac{g_m}{g_n} \mathfrak{R}_{mn} \quad (6.13)$$

where  $h$  denotes the Planck's constant,  $g_n$  and  $g_m$  the degeneracies of the upper and lower states, respectively. Furthermore, the spectral line intensity is defined for a single molecule according to the radiative transfer theory for two states of a vibrational-rotational system by:

$$S = \frac{h\nu_{mn}n_m}{cN} \left(1 - \frac{g_m n_n}{g_n n_m}\right) B_{mn} \quad (6.14)$$

where  $N$  is the molecular number density,  $n_n$  and  $n_m$  the populations of the upper and lower states. Assuming local thermodynamic equilibrium, the population partition between states is governed by Boltzmann statistics at the ambient temperature  $T$  and allows to write:

$$\frac{g_m n_n}{g_n n_m} = \exp\left[\frac{-c_2 \nu_{mn}}{T}\right] \quad (6.15)$$

The relation of the number of molecules  $n_m$  in state  $m$  with the molecular number density  $N$  becomes:

$$\frac{n_m}{N} = \frac{g_m}{Q(T)} \exp\left[\frac{-c_2 E_m}{T}\right] \quad (6.16)$$

$E_m$  is the lower state energy and  $c_2$  the second radiation constant ( $= hc/k_B = 1.439 \text{ cm/K}$ ). The *total internal partition sum*  $Q(T)$  in Eq. 6.16 is given by:

$$Q(T) = \sum_m g_m \exp\left[\frac{-c_2 E_m}{T}\right] \quad (6.17)$$

After inserting Eqs. 6.12 and 6.15 at  $T_{ref}$  and introducing the natural terrestrial isotopic abundance  $I_a$ , Eq. 6.14 becomes:

$$S(T_{ref}) = \frac{8\pi^3 \nu_{nm}}{3hc} \cdot \frac{I_a g_m \mathfrak{R}_{mn}}{Q(T_{ref})} \cdot \exp\left[\frac{-c_2 \nu_{mn}}{T_{ref}}\right] \cdot \left(1 - \exp\left[\frac{-c_2 \nu_{mn}}{T_{ref}}\right]\right) \quad (6.18)$$

The determination of the spectral line strength at a fixed reference temperature  $T_{ref}$  is realized by laboratory measurements. The ratio of Eq. 6.18 yields the line intensity  $S(T)$  for an arbitrary temperature  $T$ :

$$S(T) = S(T_{ref}) \cdot \frac{Q(T_{ref})}{Q(T)} \cdot \frac{\exp[-c_2 E_m/T]}{\exp[-c_2 E_m/T_{ref}]} \cdot \frac{1 - \exp[-c_2 \nu_{mn}/T]}{1 - \exp[-c_2 \nu_{mn}/T_{ref}]} \quad (6.19)$$

The total internal partition sum can be approximated by a polynomial expression in the temperature  $T$  with high accuracy [Gamache (2000)]:

$$Q(T) = a + b \cdot T + c \cdot T^2 + d \cdot T^3 \quad (6.20)$$

In Eq. 6.20 the centrifugal distortion corrections are considered for the water vapor molecule as an asymmetric rotor. The four coefficients are quantified for water vapor isotopes and the lower temperature range ( $70 \text{ K} \leq T \leq 500 \text{ K}$ ) in Tab. 6.1.

molecule	a	b	c	d
$H_2^{16}O$	-4.4405	0.27678	$0.12536 \cdot 10^{-2}$	$0.48938 \cdot 10^{-6}$
$H_2^{18}O$	-4.3624	0.27647	$0.12802 \cdot 10^{-2}$	$0.52046 \cdot 10^{-6}$
$H_2^{17}O$	$-0.25767 \cdot 10^2$	1.6458	$0.76905 \cdot 10^{-2}$	$0.31668 \cdot 10^{-5}$

Table 6.1: Values of the coefficients of Eq. 6.20 for the isotopologues  $H_2^{16}O$ ,  $H_2^{18}O$  and  $H_2^{17}O$ .

## 6.4 Line broadening

### 6.4.1 Introduction

Next to the line strength as treated in section 6.3 the strength of an absorption line is also determined by line shape and line width. Since the natural line broadening is too small to have practical significance in this study, it won't be discussed in the following. Instead, the collision and Doppler broadening significantly effect the line shape and width and are examined together with their combination, the Voigt function, in the next sections.

### 6.4.2 Collision broadening

The disturbance of the radiative transitions by molecular collisions causes a broadening of the spectral lines. Since the number of collisions depends on the molecule density and consequently on the pressure, the collision broadening is also often called *pressure broadening*. The collision broadening attains a maximum in the ground layer and decreases with altitude in proportion to the pressure reduction. Due to the collision of the water vapor molecules among each other as well as with molecules of other atmospheric gases, the molecular energy levels are both lifted and lowered and the absorbed energy has a greater bandwidth.

In 1906 Lorentz described the shape of a collision broadened absorption line by means of a damped oscillator assuming a homogeneous distribution of the velocity and acceleration vectors after the collision:

$$f_L(\nu) = \frac{\gamma_L}{\pi(\nu - \nu_0)^2 + \gamma_L^2} \quad (6.21)$$

where  $\gamma_L$  is the *Lorentz half width* (half width of the collision broadening) and  $\nu_0$  is the center wave number of the absorption line. For a more precise approximation of the absorption line shape in the far line wings an expression is found by the assumption that the distribution of the molecules over the quantum states as well

as the velocity and acceleration after the collision corresponds to the Boltzmann distribution law. An average over all directions yields [Vleck and Huber (1974)]:

$$f_L(\nu) = \frac{\nu}{\pi\nu_0} \left( \frac{\gamma_L}{(\nu + \nu_0)^2 + \gamma_L^2} + \frac{\gamma_L}{(\nu - \nu_0)^2 + \gamma_L^2} \right) \quad (6.22)$$

By evaluating the half width  $\gamma_L(T)$  at a series of temperatures (pressure = constant) the variation with temperature can be determined in terms of a particular model [Gamache and Rothman (1988)]:

$$\gamma_L(T) = \rho(T) \cdot v(T) \cdot \sigma(T) \quad (6.23)$$

where  $\rho$  denotes the number density,  $v$  the velocity of the molecule and  $\sigma$  the optical cross section. The number density for a temperature  $T$  is given by:

$$\rho(T) = \frac{\rho_0 \cdot T_0}{T} \quad \text{with} \quad T_0 = 273.15K \quad (6.24)$$

The velocity is related to

$$v(T) = \sqrt{\frac{8k_B T}{\pi\mu}} \quad (6.25)$$

with

$$\mu = \frac{m_{H_2O} \cdot m_d}{m_{H_2O} + m_d} \quad (6.26)$$

where  $m_{H_2O}$  is the mass of the  $H_2O$  molecule and  $m_d$  the mean mass of dry air molecules. The optical cross section  $\sigma(T)$  is usually assumed to be dependent on the temperature to a power  $m$ :

$$\sigma(T) = T^m \cdot \sigma_0 \quad (6.27)$$

where  $\sigma_0$  is independent from the temperature. The ratio of Eq. 6.23 for two different temperatures  $T_1$  and  $T_2$  gives:

$$\frac{\gamma_L(T_1)}{\gamma_L(T_2)} = \left( \frac{T_1}{T_2} \right)^{-1/2} \cdot \left( \frac{T_1}{T_2} \right)^m \quad (6.28)$$

Simplifying Eq. 6.28 by setting  $n = \frac{1}{2} - m$  produces:

$$\gamma_L(T_1) = \gamma_L(T_2) \cdot \left( \frac{T_2}{T_1} \right)^n \quad (6.29)$$

Eq. 6.29 requires a constant pressure. Due to linearity between  $\gamma_L$  and the pressure,  $\gamma_L$  can be expressed for a constant temperature by means of pressure:

$$\gamma_L(p_1) = \gamma_L(p_2) \cdot \left(\frac{p_1}{p_2}\right) \quad (6.30)$$

Finally, the relation between  $\gamma_L(T_0, p_0)$  for norm conditions and  $\gamma_L(T, p)$  for an arbitrary pressure and temperature is found by:

$$\gamma_L(p, T) = \gamma_L(p_0, T_0) \frac{p}{p_0} \left(\frac{T_0}{T}\right)^n \quad (6.31)$$

Referring to “*The HITRAN Molecular Spectroscopic Database and HAWKS*” documentation, the collision broadened line half width for a gas at pressure  $p$  [atm], temperature  $T$  [K] and partial pressure  $p_S$  [atm] is also calculated as [Rothman et al. (1998)]:

$$\gamma_L(p, T) = \left(\frac{T_{ref}}{T}\right)^n \cdot [\gamma_{air}(p_{ref}, T_{ref})(p - p_S) + \gamma_{self}(p_{ref}, T_{ref})p_S] \quad (6.32)$$

where  $\gamma_{air}$  denotes the air-broadened half width and  $\gamma_{self}$  the self-broadened half width at  $T_{ref} = 296$  K and  $p_{ref} = 1$  atm. In the HITRAN database the parameters  $\gamma_{air}$ ,  $\gamma_{self}$  and the exponent  $n$  are given for different molecules. Formula 6.32 is used to calculate the Voigt profile in the solar spectrum simulation as described in section 8.3.

### 6.4.3 Doppler broadening

The Doppler effect is caused by the thermal motion of an absorbing molecule whose molecular velocity components along any direction of observation produce Doppler broadening of spectral lines. Hence the molecular velocity depends on the temperature, the term *temperature broadening* is often used. The Doppler-shifted frequency due to velocity  $v$  of either a source or a receiver is:

$$\nu_D = \nu_0 \cdot \left(1 + \frac{v}{c}\right) \quad (6.33)$$

where  $\nu_D$  and  $\nu_0$  are the shifted and unshifted frequencies. Rearranging Eq. 6.33 gives:

$$v = \frac{c(\nu_D - \nu_0)}{\nu_0} \quad (6.34)$$

The relationship between the velocity  $v$  and the corresponding shifted frequency  $\nu_D$  is written as:

$$dv = \frac{c}{\nu_0} d\nu_D \quad (6.35)$$

Considering an unit volume of gas in thermal equilibrium consisting of  $N$  identical molecules moving at random speeds in random directions, the number  $dN$  of molecules having velocity into a reference direction is defined by the Maxwell distribution:

$$dN = N \sqrt{\frac{m}{2\pi k_B T}} \cdot \exp\left[-\frac{m}{2k_B T} \cdot v^2\right] dv \quad (6.36)$$

Reviewing Eq. 6.8, the absorption coefficient  $k(\nu)$  at the shifted frequency  $\nu_D$  must be proportional to the partial population  $dN$  in the interval  $dv$  just as the line strength  $S$  is proportional to the total population  $N$ :

$$\frac{k(\nu_D)}{dN} = \frac{S}{N} \quad (6.37)$$

Introducing Eqs. 6.34, 6.35 and 6.36 into Eq. 6.37 and solving for  $k(\nu_D)$  yields an expression for  $k(\nu_D)$ :

$$k(\nu_D) = S \cdot \frac{c}{\nu_0} \sqrt{\frac{m}{2\pi k_B T}} \cdot \exp\left[-\frac{mc^2}{2k_B T \nu_0^2} (\nu_D - \nu_0)^2\right] d\nu_D \quad (6.38)$$

with the maximum value

$$k(\nu)_{max} = S \cdot \frac{c}{\nu_0} \sqrt{\frac{m}{2\pi k_B T}} \quad (6.39)$$

The Doppler half width  $\gamma_D = \nu_{half} - \nu_0$  is found by equating Eq. 6.38 to  $k(\nu)_{max}/2$ :

$$\gamma_D = \frac{\nu_0}{c} \sqrt{\frac{2k_B T}{m} \ln 2} \quad (6.40)$$

The corresponding line shape is obtained by:

$$f_D(\nu) = \frac{1}{\gamma_D \sqrt{\pi}} \cdot \exp\left[-\left(\frac{\nu - \nu_0}{\gamma_D}\right)^2\right] \quad (6.41)$$

Hence the effect of Doppler broadening decreases with temperature less than that of collision broadening, the fraction of the Doppler broadening to the Voigt profile increases with height. The combination of both collision and Doppler broadening, the Voigt profile, is examined in the next section.

### 6.4.4 Voigt profile

The two different effects of line broadening due to collision and thermal motion of molecules can be combined by the Voigt function which is achieved by convoluting the Lorentz line shape (Eq. 6.21) and the Doppler line shape (Eq. 6.41) [Zuev (1974)]:

$$f_V(\nu) = y \cdot \frac{f_0}{\pi} \cdot \int_{-\infty}^{+\infty} \frac{e^{-t^2}}{y^2 + (x - t)^2} dt \quad (6.42)$$

where

$$f_0 = \frac{1}{\gamma_D} \cdot \sqrt{\frac{\ln 2}{\pi}} \quad x = \frac{\nu - \nu_0}{\gamma_D} \sqrt{\ln 2} \quad y = \frac{\gamma_L}{\gamma_D} \cdot \sqrt{\ln 2} \quad (6.43)$$

Since Eq. 6.42 cannot be evaluated analytically, the numerical algorithm as proposed by Humlicek (1982) is utilized for computing the Voigt profile used to simulate the absorption spectra [Kuntz (1997)].

## 6.5 HITRAN molecular spectroscopic database

The *High resolution Transmission molecular absorption database* (HITRAN) compilation consists of several components useful for radiative transfer calculations: high-resolution spectroscopic parameters of molecules in the gas phase, absorption cross-sections for molecules with very dense spectral features, aerosol refractive indices, ultraviolet line-by-line parameters and absorption cross-sections. The line-by-line portion of HITRAN contains fundamental spectroscopic parameters of a number of molecules and their isotopologues and isotopomers suitable for calculating atmospheric transmission and radiance properties [Rothman et al. (2003)]. The parameters of a spectral line necessary for the calculation of synthetic solar absorption spectra are listed in Tab. 6.2.

Parameter	Definition	Unit
$\nu_0$	Vacuum wavenumber of line center	$cm^{-1}$
$S_0$	Line strength at $T_0 = 296 K$	$cm/molecule$
$\gamma_{air}$	air-broadened half width at standard conditions	$cm^{-1}/atm$
$\gamma_{self}$	self-broadened half width at standard conditions	$cm^{-1}/atm$
$E_m$	Lower-state energy	$cm^{-1}$
$n$	temperature-dependent exponent of half width $\gamma_L$	

Table 6.2: Spectral line parameters provided by the HITRAN molecular spectroscopic database.

Most of the line parameters for the  $H_2O$  molecule are determined by long-path laboratory observations in absorption cells. In these cells the incident light beam is repeatedly reflected by a mirror system before it is diffracted by a spectrometer.

Compared to the 1996 edition of HITRAN [Rothman et al. (1998)] several improvements and corrections of line parameters were applied. The intensities of all lines in HITRAN beyond  $8000\text{ cm}^{-1}$  have been adjusted due to the correction of a problem with intensity unit conversion of lines in the near-IR and visible found by Giver et al. (2000). A major update has occurred with the addition of the  $3\nu$  polyad of bands from  $9600$  to  $11400\text{ cm}^{-1}$  [Brown et al. (2002) and Chevillard et al. (1989)]. For the isotopologue  $H_2^{18}O$  the calculated positions predicted by Partridge and Schwenke (1997) have occasionally been superseded using upper levels observed by Chevillard et al. (1987). The few lines of the  $H_2^{17}O$  molecule in this region have line positions and intensities taken from Camy-Peyret et al. (1999).

However, new results of water vapor spectroscopic measurements in the visible and near-infrared band reveal a significant under-estimation of the line intensities of the HITRAN (version 1996) list [Callies et al. (2000) and Belmiloud et al. (2000)]. The details of the experiment giving rise to this assertion, and the associated parameters were subsequently published by Schermaul et al. (2001) and made available electronically as the *ESA-WVR molecular spectroscopic database*. The data published by Brown et al. (2002) also leads to an increase in the overall absorption by water but only by about half that given by ESA-WVR. An independent validation by Tolchenov et al. (2003) suggests that a re-analysis of the spectra measured by Schermaul et al. (2001) with a better determination of the baseline (reference intensity level) by an iterative fit would lead to intensities closer to those observed by Brown et al. (2002). This re-analysis including simultaneous fits to all the spectra recorded by Schermaul et al. (2001) and iterative determination of the baseline is currently underway. Recently, the new edition HITRAN2004 was made accessible.

A self-consistency check of the resulting line intensities is made by comparing the modeled spectra with the measured one. But any systematic errors are often self-canceling and thus remain hidden. Therefore, independent water vapor measurements by means of ground-based atmospheric spectra are necessary to systematically validate the water line parameters in controlled situations, in which the atmospheric water vapor column is sufficiently well-determined [Tolchenov et al. (2003)]. Following this approach the line strength parameters are fitted using solar spectra measured by GEMOSS at a time periode when the water vapor column was simultaneously determined by a water vapor radiometer and radiosondes. This estimation of line strength parameters is described in chapter 9. The ESA-WVR database, which was widely used in this study, will be presented in the next section .

## 6.6 ESA-WVR molecular spectroscopic database

The *European Space Agency* (ESA) initiated a study about line-broadening in the near-infrared and visible ( $8592 - 15000\text{ cm}^{-1}$ ) in order to interpret its spectra acquired by nadir-looking visible and near-infrared spectrometers (GOME, SCIAMACHY) [Callies et al. (2000)]. In this study it soon became apparent that the mea-

measurements were in considerable disagreement with the water data in the HITRAN molecular spectroscopic database (version 1996). For this reason the primary aim became the re-measurement of the line intensities in order to replace the water data of HITRAN and create the *ESA-WVR (Water Vapor Red region) molecular spectroscopic database*. For the experimental work a high-resolution Fourier transform spectrometer and two absorption cells at the *Rutherford Appleton Laboratory* (RAL) were used. The absorption measurements with optical path lengths of 5, 32, 128 and 512 m were made with pure water vapor and with mixtures of water vapor and synthetic air. For the longer path length spectra were measured at the two temperatures 252 and 296 K. Duplicated observations of the same line at different path lengths were then merged to give error-weighted best values of line strength and profile parameters for each line. Tab. 6.3 shows the ratio between the sum of the observed intensities and the sum of the corresponding HITRAN values for different bands of the water molecule [Callies et al. (2000)].

Temperature	$2\nu + \delta$	$3\nu$	$3\nu + \delta$	$4\nu$
296 K	1.26	1.21	1.25	1.06
252 K	1.20	1.27	1.33	1.12

Table 6.3: Ratio between the sum of the observed intensities (ESA-WVR) and the sum of the corresponding HITRAN-96 values for different bands of the water molecule at two temperatures [Callies et al. (2000)].

## 6.7 Ray tracing

The modeling of the atmospheric absorption of the incident solar radiation requires an accurate ray tracing. The calculation of the path geometry is based on a homogeneous atmosphere divided into spherical layers (Fig. 6.1). At lower solar elevation angles the refraction of the light path has to be considered.

The path length  $s_n$  of the *geometrical ray path* from the intersection with the upper border of layer  $n$  at height  $h_n$  to the observation site is calculated by:

$$s_n = \sum_{i=0}^n ds_i = \sqrt{R^2 + (h_n + R)^2 - 2R(h_n + R) \cdot \cos(\gamma_n)} \quad (6.44)$$

where  $R$  is the Earth's radius and  $\gamma$  is related to the solar elevation angle  $\theta$  by:

$$\gamma_n = \frac{\pi}{2} - \theta - \beta_n \quad (6.45)$$

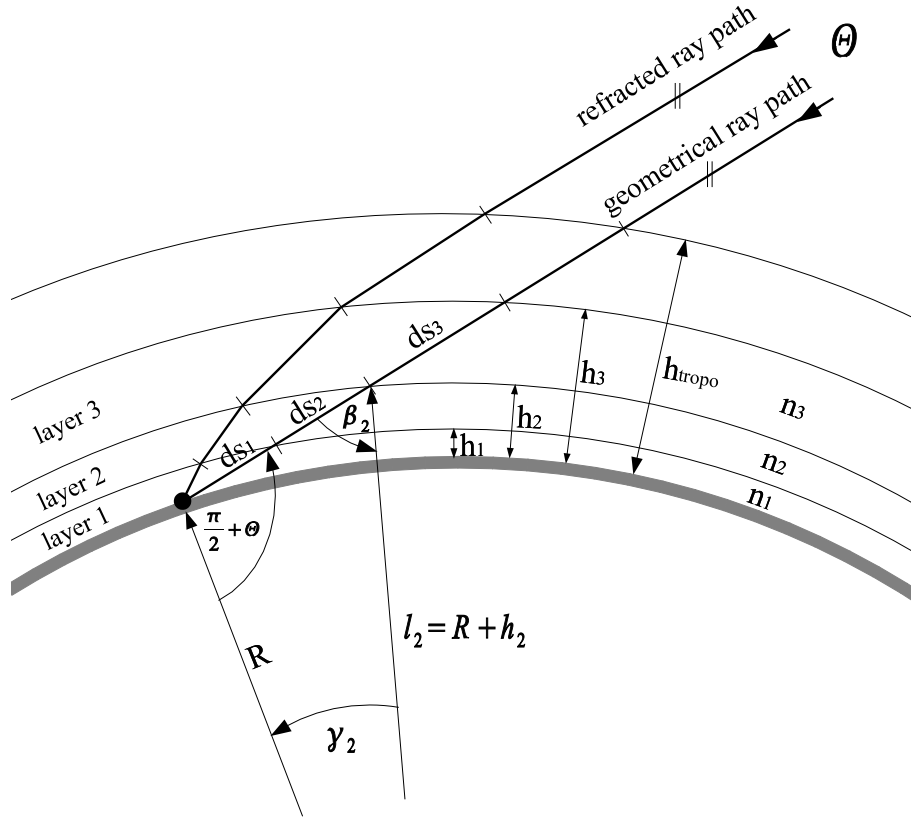


Figure 6.1: Model of homogeneous Earth's atmosphere with spherical layers used to calculate the absorption path. The refraction is considered by applying the Snellius' law of light refraction to the atmospheric layers with different refraction indices.

with

$$\beta_n = \arcsin \left( \frac{R}{R + h_n} \cdot \sin \left( \theta + \frac{\pi}{2} \right) \right) \quad (6.46)$$

The calculation of the geometry of the *refracted ray path* is sketched in Fig. 6.2.

The zenith angle  $z'_{i+1}$  of the refracted light is given by the Snellius' law:

$$z'_{i+1} = \arcsin \left( \frac{n_i}{n_{i+1}} \cdot \sin(\beta'_{i+1}) \right) \quad (6.47)$$

with

$$\beta'_{i+1} = z'_i - \gamma'_{i+1} = \arcsin \left( \frac{l_i}{l_{i+1}} \cdot \sin(\pi - z'_i) \right) \quad (6.48)$$

and

$$l_i = R + h_i \quad (6.49)$$

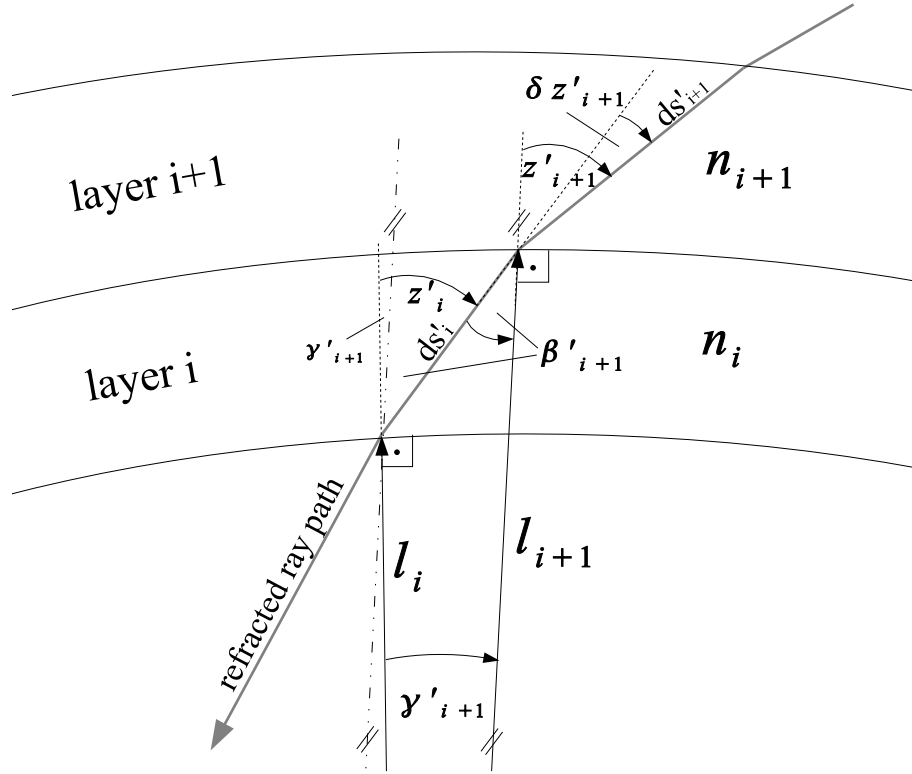


Figure 6.2: Sketch of the refraction of the incident sunlight between two layers  $i$  and  $i + 1$  with the different refraction indices  $n_i$  and  $n_{i+1}$ .

The refraction index for visible and near-infrared waves in the atmosphere is calculated from meteorological parameters by [Ciddor and Hill (1996) and Ciddor (1999)]:

$$n_i = \left[ \frac{273.15 \cdot N_g \cdot P_i}{P_{ref}} \cdot \frac{100}{T_i} - 11.27 \cdot \frac{e_i}{T_i} \right] \cdot 10^{-6} + 1 \quad (6.50)$$

with the group refractivity  $N_g$  of standard air

$$N_g = 287.6155 + \frac{4.88660}{\lambda_{mean}^2} + \frac{0.06800}{\lambda_{mean}^4} \quad (6.51)$$

where  $\lambda_{mean}$  [ $\mu m$ ] denotes the mean wavelength of the corresponding spectral region. The zenith angles  $z'_i$  are calculated one after another starting with the zenith angle at the observation site  $z'_0$  which is approximated for the visible and near-infrared by [Schödlbauer (1999)]:

$$z_0 = \frac{\pi}{2} - \theta = z'_0 + 1.6583 \cdot 10^{-7} \cdot \frac{P_0}{1 + \alpha \cdot (T_0 - 273.15)} \cdot \tan(z'_0) \quad (6.52)$$

where  $\alpha = 0.003675 \text{ K}^{-1}$  denotes the cubic expansion coefficient of the air. The zenith angle  $z'_0$  is iteratively modified until the direction of the incident solar radiation retrieved by Eqs. 6.47 and 6.52 corresponds to the geometrical solar position so that the *refracted* and the *geometrical* ray path run parallel (Fig. 6.1):

$$\left( z'_0 + \sum_{i=0}^{tropo} \delta z'_i \right) - \left( \frac{\pi}{2} - \theta \right) \approx 0 \quad (6.53)$$

Finally, the path length through layer  $i$  is given by:

$$ds'_i = \frac{\sin(\gamma'_{i+1})}{\sin(\pi - z_i)} \cdot l_{i+1} \quad (6.54)$$

The meteorological parameters  $P$ ,  $T$  and  $e$  of each single atmospheric layer used to determine the broadening of an absorption line as well as the refraction of the ray path are defined by meteorological profiles examined in the following section.

## 6.8 Meteorological profiles

The meteorological profiles of temperature, pressure and partial pressure of water vapor are essential for the radiative transfer model. In Eqs. 6.5, 6.19, 6.20, 6.32 and 6.40 the line shape depends on the temperature and(or) pressure distribution in the atmosphere. Furthermore, the calculation of the geometry of the ray path requires the knowledge of the refraction index at various heights which is also determined in Eq. 6.50 by temperature, pressure and partial pressure. Based on the definition of the standard atmosphere combined with surface measurements the following approach is applied to achieve the meteorological parameters at an arbitrary height.

The temperature in the atmosphere is computed with individual gradients for different height intervals [Boiffier (1998)]. The gradients are given in Tab. 6.4.

Definition	Altitude $h$	Gradient of temperature $dT/dh$ [ $K/m$ ]
$Th_H$	$h_{Station} \leq h \leq H$	(Eq. 6.55)
$Th_{11}$	$H < h \leq 11km$	$-6.5 \cdot 10^{-3}$
$Th_{20}$	$11km < h \leq 20km$	0
$Th_{32}$	$20km < h \leq 32km$	$1.0 \cdot 10^{-3}$
$Th_{47}$	$32km < h \leq 47km$	$2.8 \cdot 10^{-3}$

Table 6.4: Temperature gradients according to the definition of the standard atmosphere in combination with surface measurements [Boiffier (1998)].

Hence the warm ground influences the lower layers of the atmosphere, the measured ground temperature  $T_s$  is introduced into the standard model by calculating the

temperature gradient  $Th_H$  from the station at height  $h_{station}$  up to  $H = 3 \text{ km}$  above ground:

$$Th_H = \frac{T_0 + Th_{11} \cdot (h_{station} + H) - T_s}{H} \quad (6.55)$$

The partition of the atmosphere into the height intervals as defined in Tab. 6.4 is also applied to the calculation of the air pressure. The corresponding equations are:

$h_{station} \leq h \leq H$ :

$$T(h) = T_s + Th_H \cdot (h - h_{station}) \quad (6.56)$$

$$P(h) = P'_0 \left( 1 + \frac{Th_{11}}{T_0} h \right)^{-g/(R \cdot Th_{11})} \quad (6.57)$$

with

$$P'_0 = P_s \cdot \left( 1 + \frac{h_{station} \cdot Th_{11}}{T_0} \right)^{g/(R \cdot Th_{11})} \quad (6.58)$$

and

$$T_0 = 288.16 \text{ K} \quad g = 9.806 \text{ m} \cdot \text{s}^{-2} \quad R = 287 \text{ J/K/kg}$$

where  $T_0$  is the temperature at sea level,  $P_s$  the measured air pressure at the surface,  $g$  the gravity for a medium latitude and  $R$  is the gas constant for air.

$H < h \leq 11 \text{ km}$ :

$$T(h) = T_0 + Th_{11} \cdot h \quad (6.59)$$

$$P(h) = P'_0 \left( 1 + \frac{Th_{11}}{T_0} h \right)^{-g/(R \cdot Th_{11})} \quad (6.60)$$

$11 \text{ km} < h \leq 20 \text{ km}$ :

$$T(h) = 216.66 \text{ K} \quad (6.61)$$

$$P(h) = P(11 \text{ km}) \cdot e^{-g[R \cdot T(11 \text{ km})][h - 11000]} \quad (6.62)$$

$20 \text{ km} < h \leq 32 \text{ km}$ :

$$T(h) = T(20 \text{ km}) + Th_{32} \cdot (h - 20000 \text{ m}) \quad (6.63)$$

$$P(h) = P(20 \text{ km}) \left( 1 + \frac{Th_{32}}{T(20 \text{ km})} (h - 20000 \text{ m}) \right)^{-g/(R \cdot Th_{32})} \quad (6.64)$$

$32 \text{ km} < h \leq 47 \text{ km}$ :

$$T(h) = T(32 \text{ km}) + Th_{47} \cdot (h - 32000 \text{ m}) \quad (6.65)$$

$$P(h) = P(32 \text{ km}) \left( 1 + \frac{Th_{47}}{T(32 \text{ km})} (h - 32000 \text{ m}) \right)^{-g/(R \cdot Th_{47})} \quad (6.66)$$

The profile of the partial pressure of water vapor is approximated by a simple function:

$$e(h) = e_s \cdot e^{-(h-h_s)/H_v} \quad (6.67)$$

where  $H_v = 1.5 \text{ km}$  denotes the scale height for the partial pressure. Although Eq. 6.67 can deviate substantially from the true vertical distribution of the partial pressure for water vapor and thus of the true number of  $H_2O$  molecules, the mean error of the PW retrievals is  $< 0.3 \text{ kg/m}^2$  [Sierk (2000)]. This low sensitivity of the PW to Eq. 6.67 is the reason for the difficulties of determining a vertical humidity distribution from absorption spectra.

# 7 GEodetic MOBILE Solar Spectrometer I (GEMOSS I)

## 7.1 System requirements

The general feasibility of measuring tropospheric water vapor by high-resolution solar spectrometers has been verified in former studies by Sierk (2000). For further investigations the first prototype of a “GEodetic MOBILE Solar Spectrometer” (GEMOSS I) was developed by the Geodesy and Geodynamics Laboratory (GGL) at ETH Zurich in cooperation with the Institute for Analytical Sciences (ISAS) in Berlin (Germany). GEMOSS I represents a new generation of spectrometers with an innovative self-adjusting optical system covering a broad spectral range. GEMOSS I enables extensive investigations in order to define the specifications of the next improved generation of *GEodetic MOBILE Solar Spectrometers* (GEMOSS II). The aimed specifications of GEMOSS II are:

- High accuracy of the measured tropospheric precipitable water vapor
- High light sensitivity for bad weather conditions or moon light
- Field deployment
  - Low weight and small size
  - Robust construction
  - Sustained continuous operation
  - Insensitivity to undesirable external effects
  - Low energy consumption
- Low purchasing and operating cost

In order to achieve the improvements as mentioned above various issues have to be investigated. These are:

- Sufficient spectral resolution for determination of absolute water vapor content

- Selection of water vapor absorption lines with
  - Base intervals on both sides
  - Absence of Fraunhofer lines
  - No saturation effects
  - Well determined line parameters
- Test of the self-calibrating optical system
- Improvement of line strength parameters
- High time resolution and redundancy

These issues are discussed in the following section.

## 7.2 Hardware configuration

The first spectrometer GEMOSS I was constructed at the Institute for Analytical Sciences (ISAS) in Berlin (Germany) in November 2002. The telescope, several electronic components and the data accumulation software *gemoss control* written in Labview<sup>®</sup> of National Instruments were developed at the Geodesy and Geodynamics Laboratory (GGL) at ETH Zurich. The principle approach of GEMOSS I is illustrated in Fig. 7.1.

The solar radiation is collected by means of an external tracking telescope (T) and transmitted via an optical fiber (OF) onto the entrance slit (ES) of the spectrograph. The radiation passing through the slit and the shutter (S) is dispersed by means of a cross dispersion prism (SF3, Schott, Mainz, Germany; apex angle 35°) in double pass mode (P) and an echelle diffraction grating (EG) (RGL, Rochester, USA; 23.2 grooves/mm; 64.5° blaze angle). Using spherical collimator (SM1) and camera (SM2) mirrors, both with  $R = 1000$  mm, a two-dimensional spectral pattern of 22 echelle orders is focused on the CCD-array (CCD). This permits the simultaneous observation of the wavelength range from 728 nm to 915 nm comprising a sufficient number of prominent water vapor and oxygen absorption lines. The Peltier-cooled CCD sensor C7041/S7031-1006 from HAMAMATSU has 1044x256 pixels of 23.54  $\mu\text{m}$  width. It transforms the radiation into an electrical signal which is digitized and transmitted to a mobile computer. The optical design of the high-resolution echelle spectrograph [Becker-Ross and Florek (1997)] with a light path illustration is depicted in Fig. 7.2. A novel hard- and software-supported wavelength stabilization routine guarantees high wavelength accuracy under field conditions and will be described in section 7.3 [Becker-Ross et al. (2002)].

In addition, a portable GPS receiver (Antaris<sup>™</sup>GPS Positioning Engine,  $\mu\text{blox}$ ) is connected to the computer and provides the position of the measurement site

and a time synchronization for a precise calculation of the position of the Sun. Optional, the computer can be remote controlled via mobile phone or Internet. For the accumulation of meteorological data the software *gemoss control* communicates with a mobile meteo unit constructed by CAPTEC (Biel, Switzerland).

The corresponding telescope was taken from the SAMOS measurement system and was modified to operate with GEMOSS I. The filter wheel was removed and the former halogen lamp mounting was replaced by a slide. Fig. 7.3 is an image of the modified sun tracking telescope. Two motors adjust the telescope to the calculated solar position and a third motor moves the slide with the halogen lamp covered by a small black cylinder.

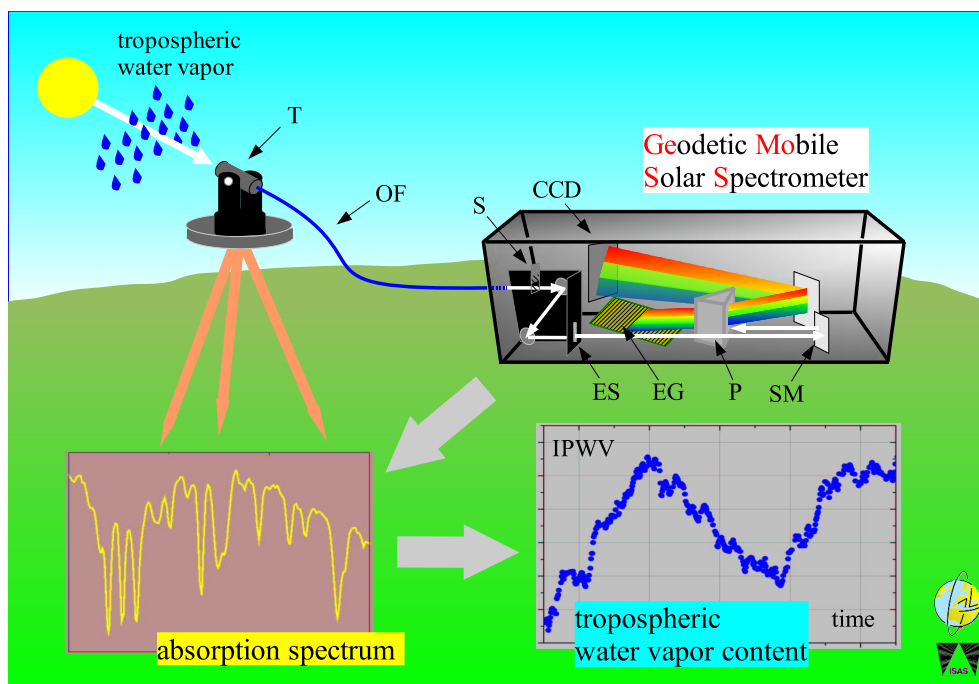


Figure 7.1: Illustration of the principle approach of the GEodetic Mobile Solar Spectrometer I (GEMOSS I) measurement system. The sun light is automatically collected by a telescope (T) and transmitted via an optical fiber cable (OP) into the spectrometer. After passing the shutter (S) and entering the entrance slit (ES) the light is reflected by the first spherical mirror (SM) through the prism (P) onto the echelle grating (EG). The echelle grating diffracts the light and reflects it back through the prism. The second spherical mirror focuses the diffracted light on the cooled charge-coupled device (CCD). The tropospheric water vapor content (PW) can be retrieved by analyzing the solar absorption spectrum.

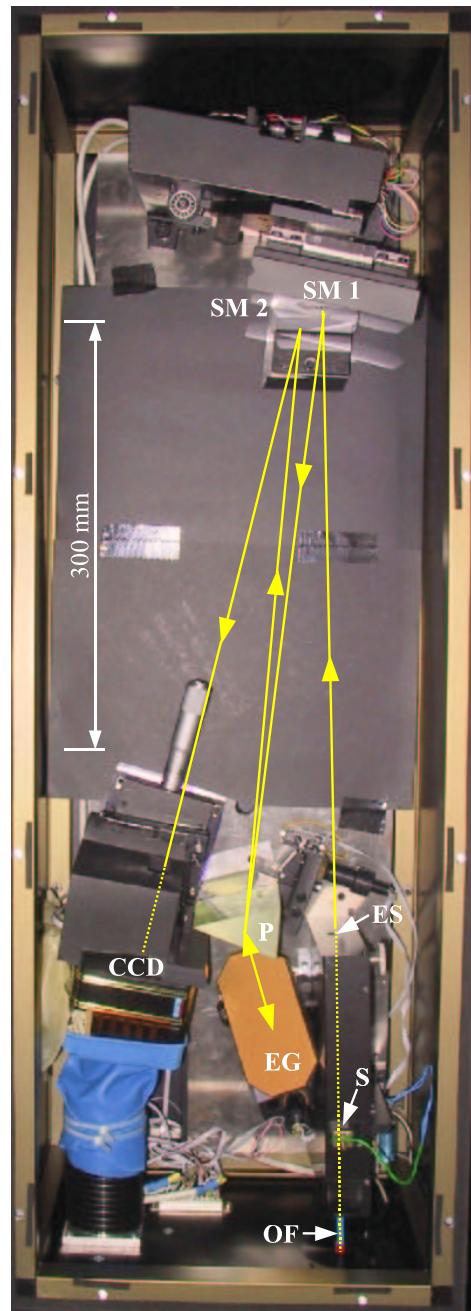


Figure 7.2: Optical and electrical components in the opened spectrometer GEMOSS I with light path illustration. The spectrometer box has the dimension of 90x30x30 cm. The components are labeled as followed: optical fiber (OP), shutter (S), entrance slit (ES), spherical collimator (SM1) and camera (SM2), prism (P), echelle grating (EG) and cooled CCD sensor (CCD).



Figure 7.3: The telescope of GEMOSS I measurement system tracks the Sun using pre-calculated coordinates. A halogen lamp for calibration measurements covered by a black cylinder is mounted on a vertical slide.

As mentioned above the new concept of light diffraction allows to acquire a solar spectrum from 728 to 915 nm with a resolution of about 11 pm by “one shot”. The innovation is the two-dimensional arrangement of the different diffraction orders on the CCD-matrix. This is realized by an optical prism in front of the echelle grating which is fixed in that way that the diffraction directions of both optical elements are perpendicular to each other. This “2-direction dispersion” results in a pattern with parallel diffraction orders and an effective utilization of the CCD area. In Fig. 7.4 the optical configuration with the corresponding light dispersion is shown. After collimating by a spherical mirror the optical prism refracts the incident light on the echelle grating which diffracts it back through the prism. A (spherical camera-) mirror focuses the spectrum onto the CCD sensor. A CCD-image of a solar spectrum is shown in Fig. 7.5.

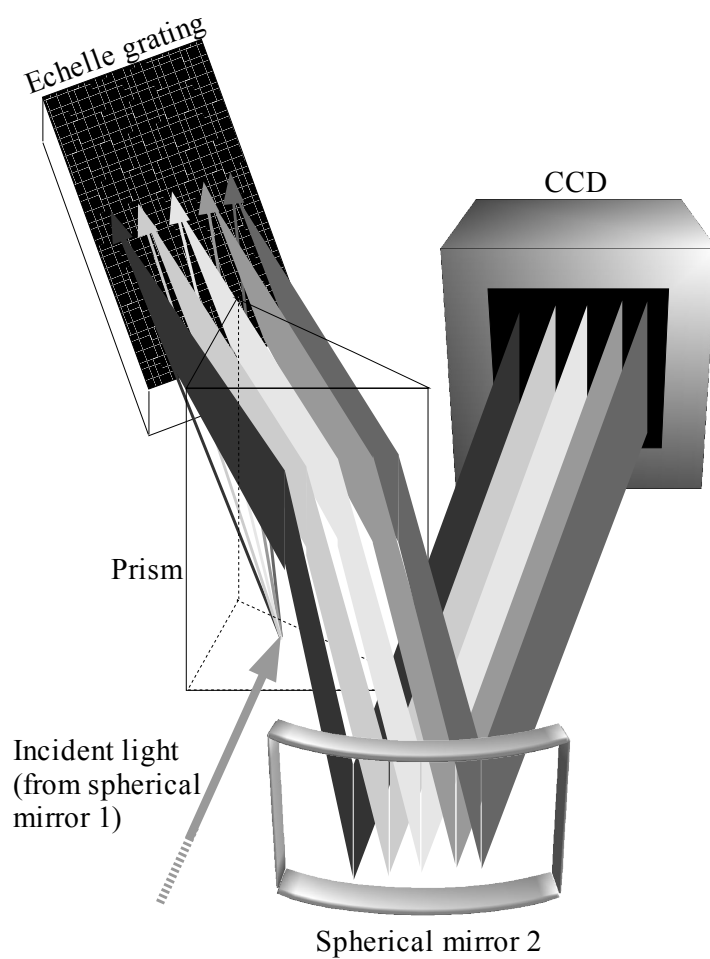


Figure 7.4: Depiction of the “2-direction dispersion” of GEMOSS I realized by combination of an optical prism and an echelle grating. The prism causes a horizontal and the echelle grating a vertical diffraction, respectively. This results in a “stripe pattern” of diffraction orders without overlapping on the CCD.

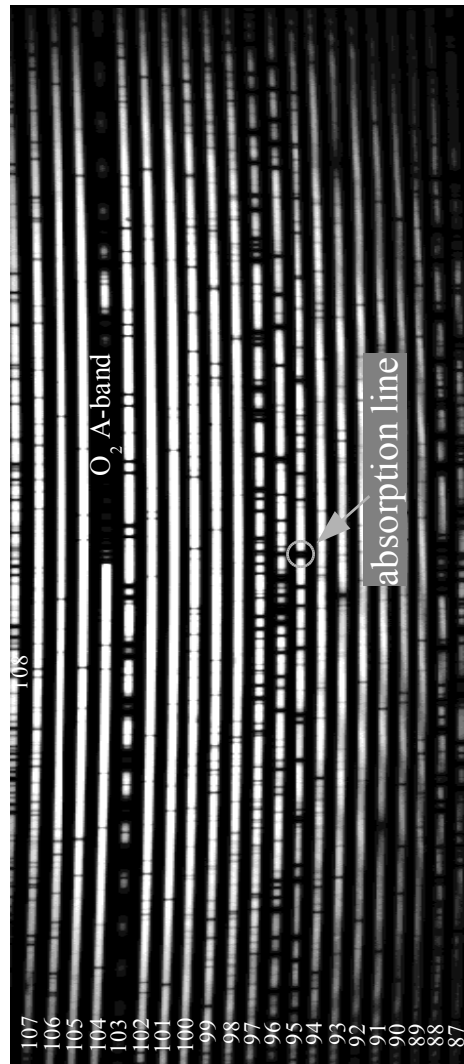


Figure 7.5: Image of a solar spectrum ranging from 728 nm in order 108 (upper left side) to 915 nm in order 87 (lower right side) generated by GEMOSS I. The white stripes are the diffraction orders 87-108 with Fraunhofer lines and absorption lines of oxygen, water vapor and other atmospheric molecules (small black vertical lines).

### 7.3 Wavelength stabilization

The stripe pattern of diffraction orders on the CCD is transferred into a solar spectrum by binning the pixel counts which correspond to the same wavelength range defined by the pixel width of the CCD. The binning procedure is shown in Fig. 7.6.

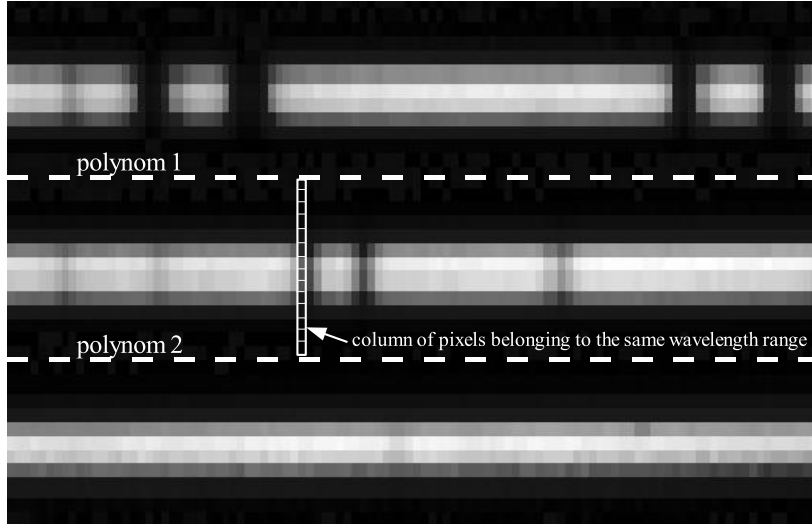


Figure 7.6: Pixel binning in order to achieve the spectrum from the CCD image. All pixels, which belong to a column between two neighboring minima represented by polynom 1 and 2, correspond to the same wavelength range. The sum of the counts of these pixels yields all detected counts corresponding to a wavelength range of 11 pm. The whole spectrum is retrieved by shifting the “column template” along all diffraction orders and summarizing all pixel counts of a column.

The resulting count sum is achieved by adding the counts of all pixels of a column between two neighboring minima (black stripes). These minima are mathematically described by a group of polynoms:

$$F(X, Y) = a \cdot X + b \cdot X^2 + c \cdot Y + d \cdot Y^2 \quad (7.1)$$

where  $X$  and  $Y$  represent the pixel coordinates of the CCD and  $a, b, c$  and  $d$  are the polynom coefficients achieved by the so-called “rolling ball” method developed by M. Okruss (GOS, Berlin). This method determines the  $X, Y$  coordinates of each minimum by rolling a virtual ball through the “minimum valley” and fits the polynom coefficients by least-squares adjustment. Finally, all diffraction orders are “scanned” by shifting the column template of Fig. 7.6 along each diffraction order. The resulting count sum array for a solar spectrum is shown in Fig. 7.7.

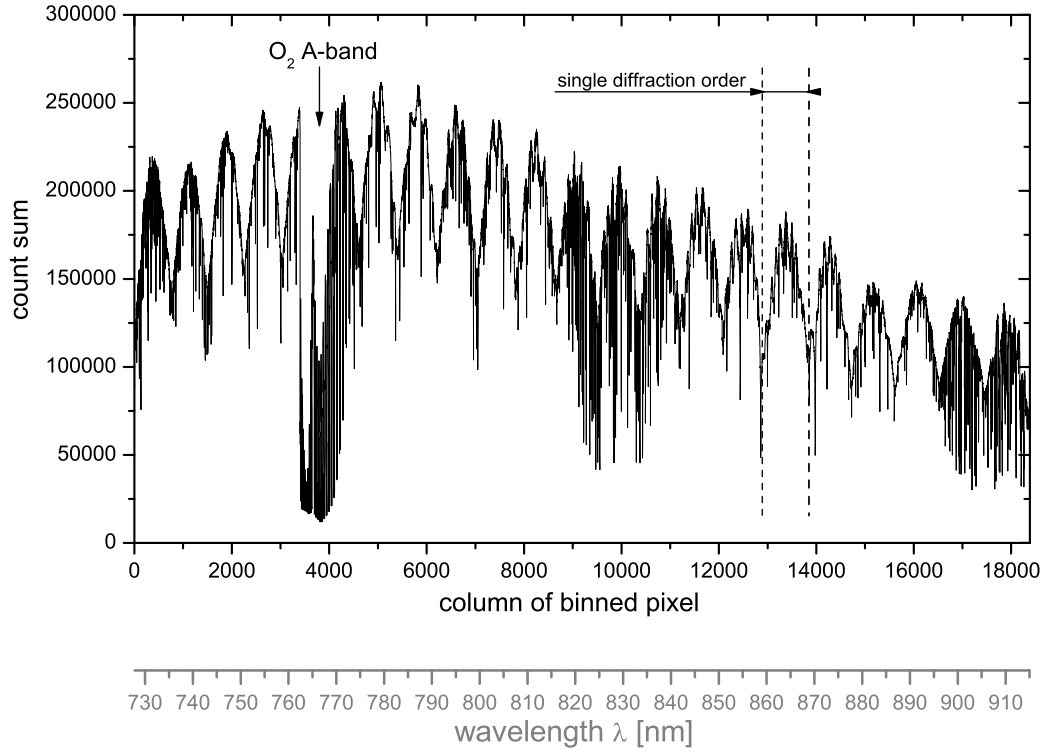


Figure 7.7: Count sums resulting from pixel binning of a solar spectrum measured by GEMOSS I. Since the radiation intensity decreases from the middle of each diffraction order towards its ends, the solar spectrum exhibits an “intensity curve” for each order. The corresponding wavelength scale is given in gray below the abscissa “column of binned pixels”. The relation between CCD pixel and wavelength is known from a wavelength calibration with emission lines for a pre-defined spectrum reference position on the CCD.

In order to be able to associate the retrieved count sum array to the correct wavelength scale the spectrum image has to be always fixed on the CCD in a *reference position*. The reference position of the spectrum image is realized by four step motors which rotate the camera mirror about two axis, the echelle grating and the CCD. This stabilization system is able to shift, rotate and scale the spectrum in relation to the  $X$ ,  $Y$  coordinate system of the CCD. The current spectrum position is determined by calculating the coordinates  $(X_{c,1}, Y_{c,1})$  and  $(X_{c,2}, Y_{c,2})$  of the center of gravity of two absorption lines. From the differences  $X_{c,1} - X_{r,1}$ ,  $Y_{c,1} - Y_{r,1}$  and  $X_{c,2} - X_{r,2}$ ,  $Y_{c,2} - Y_{r,2}$  (c: current, r: reference) as well as the difference of the

distance of the two absorption lines the number of motor steps is calculated needed to compensate the deviation of the current spectrum position from the reference position. The motors 1 and 2 rotate the spherical mirror and shift the spectrum in  $X$  and  $Y$  direction. Motor 3 tilts the echelle grating and changes the spread of the echelle orders whereas motor 4 turns the CCD and causes a relative rotation of the spectrum. The motor stabilization system keeps the spectrum in the reference position with an accuracy of 0.02 pixel or 0.1 pm wavelength, respectively. The wavelength scale was related to the CCD grid by a calibration procedure which had to be carried out only once. It consists of three steps:

- Adjusting the spectrum reference position using two sun absorption lines
- Measuring flat field spectrum (halogen) to define the position of diffraction orders on the CCD
- Measuring emission lines of neon, argon, krypton and xenon for  $\lambda - X, Y$ -correlation

Due to the relative constant radiation intensities over a large wavelength range a halogen spectrum is suitable to retrieve the polynom coefficients by the “rolling ball” method described above. Since the wavelengths of the emission lines are well known, the wavelength scale can be related to the  $X, Y$  coordinates of the CCD for the reference position (Fig 7.7). Figs. 7.8 and 7.9 show an image of a halogen and a neon spectrum measured by GEMOSS I. Replacing  $Y$  with the diffraction order  $m$  in which the pixels of the CCD row  $Y$  are located, the wavelength  $\lambda$  can be calculated from  $X$  and  $m$  by:

$$\lambda(X, m) = a'_0(m) + a'_1(m) \cdot X + a'_2(m) \cdot X^2 \quad (7.2)$$

with

$$a'_0(m) = a_0 \frac{m_0}{m} + a_1(m - m_0) + a_2(m - m_0)^2 + a_3(m - m_0)^3 \quad (7.3)$$

$$a'_1(m) = a_4 \frac{m_0}{m} + a_5(m - m_0) \quad (7.4)$$

$$a'_2(m) = a_8 \frac{m_0}{m} \quad (7.5)$$

where  $m_0$  is the reference diffraction order with the number 95. The coefficients  $a_0, a_1, a_2, a_3, a_4, a_5$  and  $a_8$  were determined by the calibration procedure as described above. Their values are listed in Tab. 7.1.

$a_0$	$8.180815 \cdot 10^2 \text{ nm}$
$a_1$	$2.070210 \cdot 10^{-3} \text{ nm}$
$a_2$	$-5.796832 \cdot 10^{-5} \text{ nm}$
$a_3$	$1.222364 \cdot 10^{-6} \text{ nm}$
$a_4$	$1.072262 \cdot 10^{-2} \text{ nm}$
$a_5$	$-2.538436 \cdot 10^{-7} \text{ nm}$
$a_8$	$-4.518981 \cdot 10^{-7} \text{ nm}$

Table 7.1: Coefficients used to relate the wavelength  $\lambda$  to the CCD coordinate  $X$  and the corresponding diffraction order  $m$  in which the pixel is located.



Figure 7.8: Image of a halogen spectrum measured by GEMOSS I. The approximate constant emission of radiation enables the determination of the polynoms describing the shape of the minima (black interstices between the white orders).



Figure 7.9: Image of a neon spectrum measured by GEMOSS I. The emission lines (white vertical lines) are used to correlate the pixels with the wavelength scale.

## 7.4 Apparatus function

The special arrangement of the diffraction orders and the large wavelength range cause a variation of the apparatus function depending on the position on the CCD and the wavelength scale, respectively. Therefore, the apparatus function was determined by applying a new approach as follows. Each emission line of neon gas (Figure 7.9) was measured at two symmetrical positions:

- One pixel with maximum intensity in the center of the emission line and two flanking pixels with the same intensity
- Two pixels with equal intensity with the center of the emission line in between

Fig. 7.10 shows both cases in which the center of the emission line is known: in the middle of one or between two pixels. Since the emission line width of the used neon lamp is negligibly narrow compared to the apparatus function width, the shape of the lines is assumed to be the apparatus function itself.

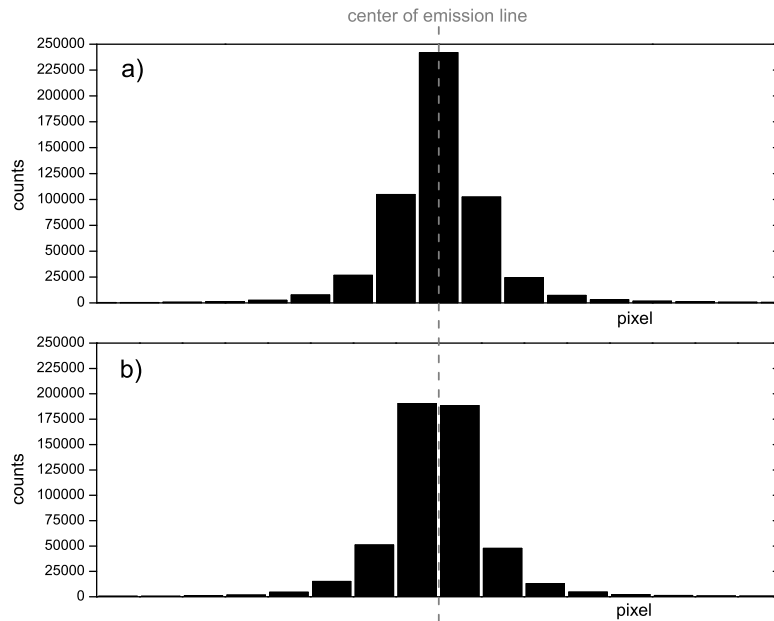


Figure 7.10: Neon emission line measured at two symmetrical positions: center of line a) in the middle of one pixel and b) between two pixels.

The apparatus function is mathematically approximated by a normalized Voigt function  $V(x)$  which is calculated by convoluting a Lorentz function  $L(x)$  with a Gauss function  $G(x)$ :

$$V(x) = L(x) * G(x) \quad (7.6)$$

$$L(x) = \frac{1}{4 \cdot x^2 + W_L^2} \cdot \frac{2 \cdot W_L}{\pi} \quad (7.7)$$

$$G(x) = e^{-2[x \cdot \sqrt{\ln(4)} \cdot W_G]^2} \cdot \frac{\sqrt{\ln(4)}}{W_G \sqrt{\frac{\pi}{2}}} \quad (7.8)$$

where  $W_L$  and  $W_G$  are the *Full Width at Half Maximum* (FWHM) of the normalized Lorentz and Gauss function, respectively. In order to retrieve the  $V(x)$  approximating both symmetrical cases of the neon emission line as best as possible,  $W_L$  and  $W_G$  are estimated by least-squares adjustment:

$$\underline{\mathbf{v}} = \underline{\mathbf{A}} \cdot \underline{\mathbf{x}} - \underline{\mathbf{l}} \quad (7.9)$$

with

$$\underline{\mathbf{A}} = \begin{bmatrix} \frac{\delta V_{digit,1}}{\delta W_L} & \frac{\delta V_{digit,1}}{\delta W_G} \\ \frac{\delta V_{digit,2}}{\delta W_L} & \frac{\delta V_{digit,2}}{\delta W_G} \\ \vdots & \vdots \end{bmatrix} \quad \underline{\mathbf{x}} = \begin{bmatrix} \delta W_L \\ \delta W_G \end{bmatrix}$$

$$\underline{\mathbf{l}} = \begin{bmatrix} C_{meas,1} - V_{digit,1} \\ C_{meas,2} - V_{digit,2} \\ \vdots \end{bmatrix} \quad \underline{\mathbf{v}} = \begin{bmatrix} v_1 \\ v_2 \\ \vdots \end{bmatrix}$$

The subscript *digit* indicates the digitization of the Voigt function which corresponds to the digitization of the measured neon emission line by the CCD. In matrix  $\underline{\mathbf{l}}$ , the value  $C_{meas,i}$  is the number of the detected counts and  $V_{digit,i}$  is the digitized Voigt function value of pixel  $i$ . Matrix  $\underline{\mathbf{x}}$  contains the corrections of  $W_L$  and  $W_G$  and matrix  $\underline{\mathbf{v}}$  the improvements fulfilling the condition of the least-squares adjustment:

$$\sum pvv = \min \quad \text{with} \quad \underline{\mathbf{P}} = \text{diag} \left[ \frac{1}{\sigma_{apriori,1}^2}, \frac{1}{\sigma_{apriori,2}^2}, \dots \right] \quad (7.10)$$

$\underline{\mathbf{P}}$  is the weighting matrix containing the weights of the observations calculated from the apriori errors  $\sigma_{apriori}$ . The elements of matrix  $\underline{\mathbf{A}}$  can be expressed as follows:

$$\frac{\delta V_{digit,i}}{\delta W_L} = \frac{1}{n} \cdot \sum_0^n G(x) * \frac{\delta L(x)}{\delta W_L} \quad \frac{\delta V_{digit,i}}{\delta W_G} = \frac{1}{n} \cdot \sum_0^n \frac{\delta G(x)}{\delta W_G} * L(x) \quad (7.11)$$

with  $x \in \text{pixel } i$  and  $n = \text{number of } x$

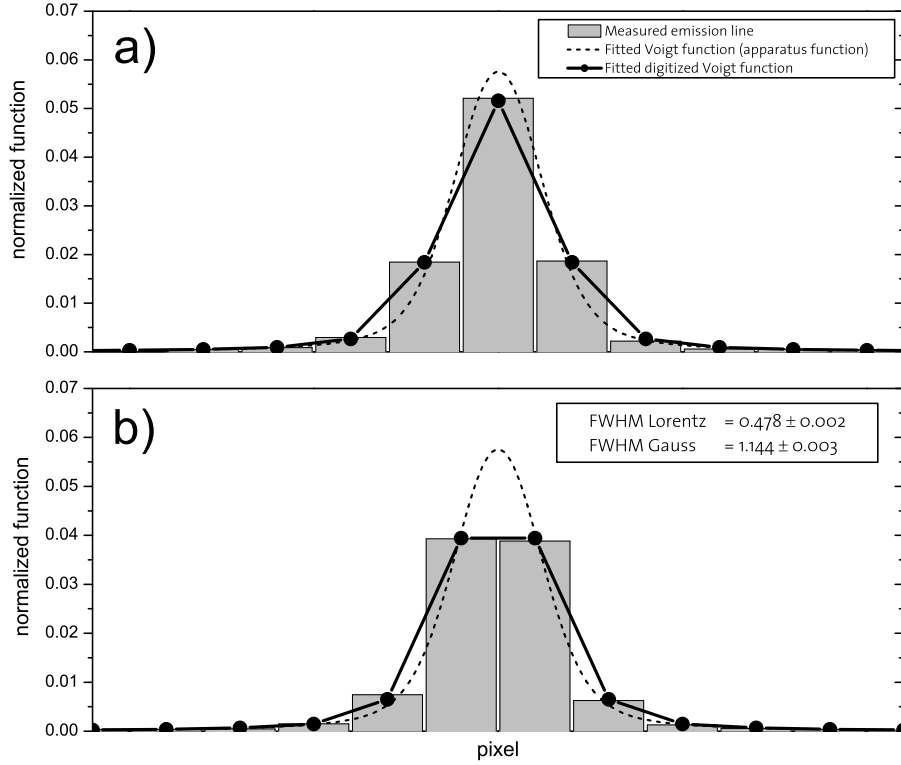


Figure 7.11: A neon emission line representing the digitized apparatus function is measured at two symmetrical positions a) and b). It is approximated by a fitted digitized Voigt function. By least-squares adjustment the *Full Width at Half Maximum* (FWHM) of the normalized Lorentz and Gauss function are determined. The convolution of both functions yields the Voigt function which is assumed to be the apparatus function.

An example of fitting the Voigt function to a measured emission line is given in Fig. 7.11. In this way, the FWHM of Lorentz and Gauss function are determined for each appropriate neon emission line within the wavelength range of GEMOSS. Fig. 7.12 shows the results depending on the position of the neon line on the CCD. The averaged accuracy of the achieved  $W_L$  and  $W_G$  is  $\pm 0.004$  pixel width. In order to calculate the Voigt function for an arbitrary pixel with the coordinates  $(X, Y)$ ,  $W_L$  and  $W_G$  are described by slant layers:

$$W_L(X, Y) = a_0 + a_1 \cdot X + a_2 \cdot Y \quad (7.12)$$

$$W_G(X, Y) = b_0 + b_1 \cdot X + b_2 \cdot Y \quad (0 \leq X \leq 1043, 0 \leq Y \leq 255) \quad (7.13)$$

The coefficients are estimated by least-squares adjustment using all 26 neon emission lines (Figure 7.12). Their values and estimation errors are listed in Tab. 7.2.

	coefficient	error		coefficient	error
$a_0$	0.38	0.05	$b_0$	1.07	0.08
$a_1$	$-8.4 \cdot 10^{-5}$	$5.2 \cdot 10^{-5}$	$b_1$	$-5.68 \cdot 10^{-4}$	$0.9 \cdot 10^{-4}$
$a_2$	$9.4 \cdot 10^{-4}$	$2.2 \cdot 10^{-4}$	$b_2$	$-1.3 \cdot 10^{-3}$	$0.4 \cdot 10^{-3}$

Table 7.2: Coefficients of the layers of Eqs. 7.12 and 7.13 determined by least-squares adjustment using 26 values of FWHM of the Lorentz and Gauss function distributed over the CCD area (Fig. 7.12).

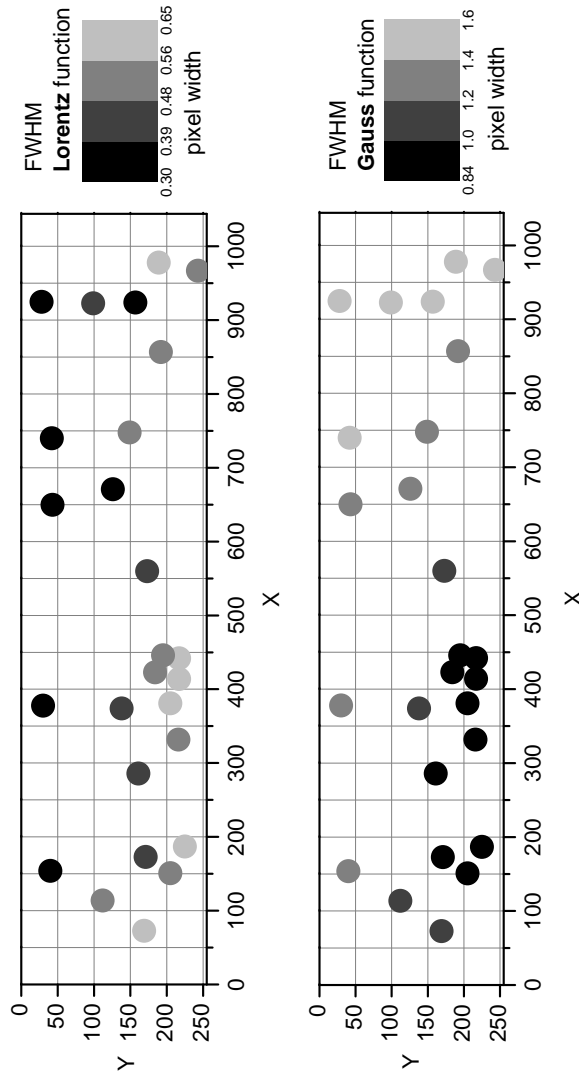


Figure 7.12: FWHM of normalized Lorentz and Gauss function determined by fitting of the corresponding Voigt function to a measured neon emission line at position  $(X, Y)$ . The variation of the FWHM depending on the position on the CCD indicates a change of the apparatus function. The width of a pixel of the deployed Peltier-cooled CCD sensor C7041/S7031-1006 from HAMAMATSU is  $23.54 \mu m$ .

## 7.5 Determination of stray light

In optical spectrometers imperfect optical elements cause undesirable stray light. This effect results in an additional amount of counts detected by the CCD which has to be determined and subtracted from the measured spectrum. For conventional types of spectrometers with a CCD line and a narrow wavelength range the stray light is approximately invariable with the wavelength. This simple assumption can not be applied to GEMOSS with a two-dimensional spectrum pattern. A more detailed investigation had to be carried out to determine the stray light depending on the wavelength and the pixel of the CCD array, respectively. In a first step, the strong oxygen A-band as well as saturated water vapor absorption lines are utilized where the atmospheric absorption of the solar radiation reaches 100% at low solar elevation angles [Sierk (2000)]. The remaining radiation is assumed to be stray light. Fig. 7.13 shows a part of a solar spectrum acquired at a low elevation angle ( $4^\circ$ ) which belongs to the oxygen A-band. The *stray light level* is marked by the pattern. A time series of 130 solar spectra measured on seven days at elevation angles from  $9^\circ$  down to  $3^\circ$  yields an averaged stray light correction of  $4.6 \pm 0.4$  % for the oxygen absorption line at 760.654 nm. The achieved amount of stray light for selected saturated absorption lines of  $H_2O$  are given in Tab. 7.3.

wavelength [nm]	molecule	absorption	stray light [%]		
			$\sigma$	count ratio	diff
730.180	$H_2O$	6.8	0.3	6.1	0.7
760.654	$O_2$	4.6	0.4	5.0	-0.4
817.224	$H_2O$	8.3	0.5	8.2	0.1
823.365	$H_2O$	7.4	0.5	7.6	-0.2
832.386	$H_2O$	8.4	0.4	8.2	0.2
897.408	$H_2O$	13.9	0.5	14.3	-0.4
899.329	$H_2O$	14.6	0.5	14.9	-0.3
			<b>0.4</b>		<b> 0.3 </b>

Table 7.3: Stray light determined by analyzing the remaining count level at saturated absorption lines of oxygen and water vapor molecules (*absorption*) and by calculating the ratio of counts of the diffraction order ( $C_{max}$ ) and of the “valleys” in direction to the neighboring orders ( $C_{min}$ ). Both methods agree within 0.3 % stray light.

Since saturated absorption lines suitable for the determination of stray light are rarely within the wavelength range of GEMOSS and not well distributed over the CCD array, a second method was found for further detailed investigation. It is based on the assumption that the detected counts within the minima between the diffraction orders are caused by stray light. The ratio of the counts of a diffraction order  $C_{max}$  and of a neighboring minimum  $C_{min}$  yields the percentage of stray light

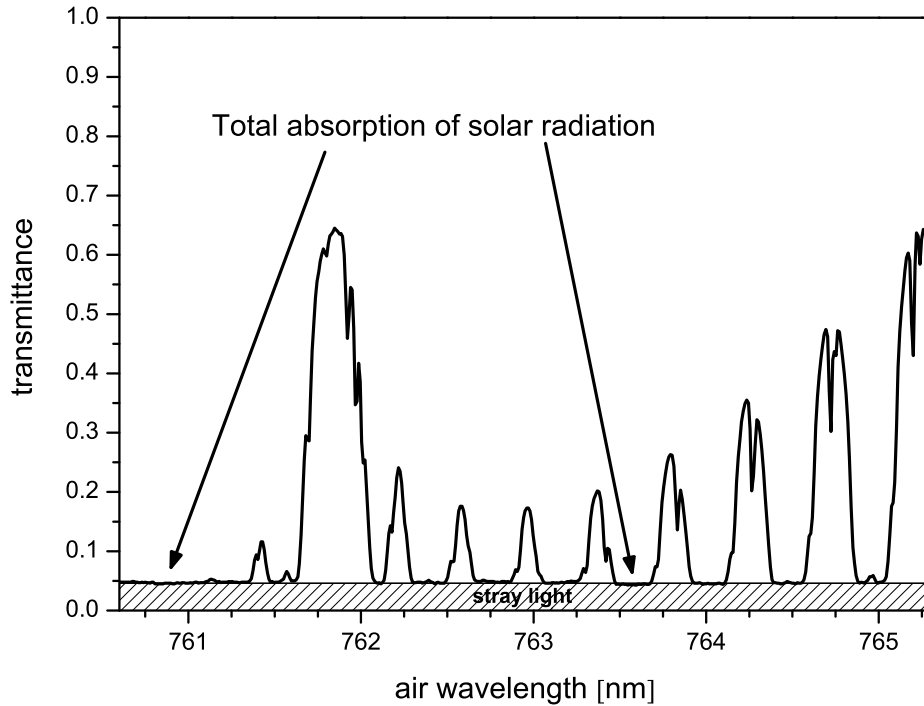


Figure 7.13: Part of a solar spectrum measured at a solar elevation angle of  $4^\circ$  containing absorption lines of the strong oxygen A-band. At such low elevation angles the solar radiation is completely absorbed by Earth's atmosphere and the remaining radiation intensity is caused by stray light in the spectrometer (pattern).

*SL*:

$$SL = \frac{C_{min}}{C_{max}} \cdot 100 \quad [\%] \quad (7.14)$$

Eq. 7.14 was validated by determining the counts ratio  $SL$  near the saturated absorption lines of Tab. 7.3. The mean deviation between the results of both methods is quantified to  $\pm 0.3\%$  stray light. Fig. 7.15 shows the amount of stray light retrieved by applying Eq. 7.14 to the measured counts  $C_{max}$  and  $C_{min}$ . The counts of  $C_{max}$  and  $C_{min}$  were measured at positions where they are not influenced by absorption lines. The stray light increases with the row number of the CCD significantly. After relating each CCD position (Fig. 7.15) to the corresponding vacuum wavelength, the stray light variation can be compared to the values obtained by analyzing the saturated absorption lines (Fig. 7.14). The strong rise of the stray light with increasing wavelength as well as with increasing distance from the intensity maximum of a single diffraction order is clearly visible. This indicates the necessity of a continuous stray light determination over the full wavelength range to ensure a precise stray light correction of the detected counts at every CCD position.

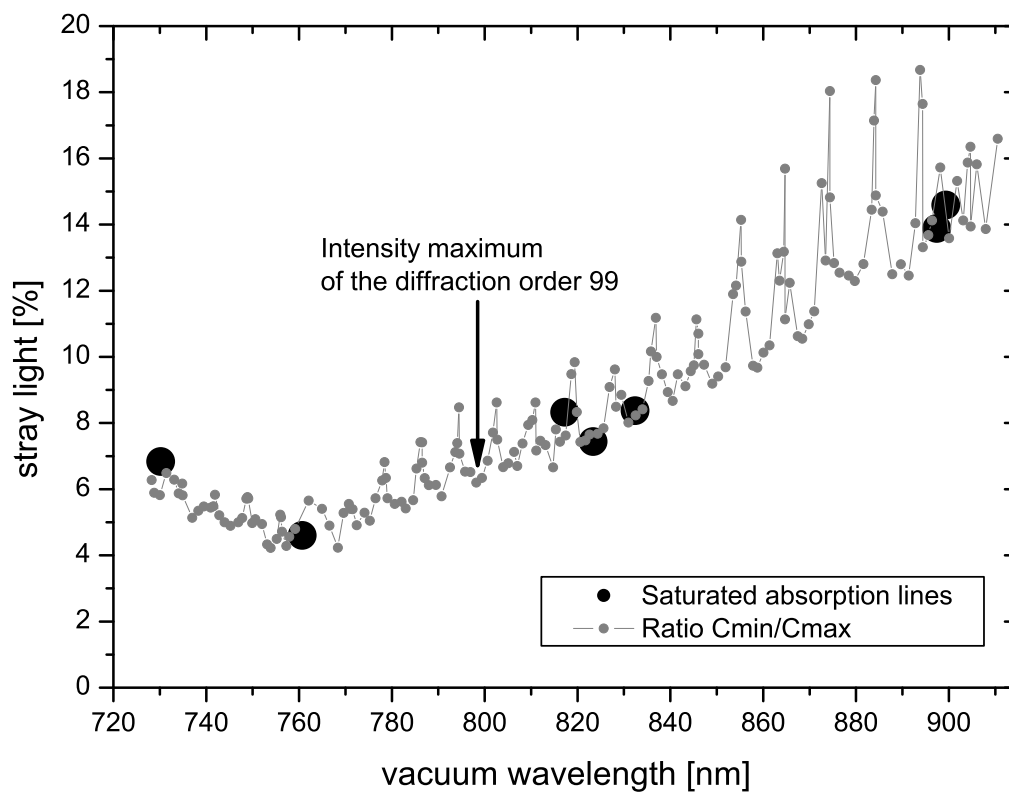


Figure 7.14: Variation of stray light depending on the wavelength. An increase with the distance from the intensity maximum of a single diffraction order to its ends can be seen clearly. The values determined by analyzing saturated absorption lines of oxygen and water vapor agree with those achieved by calculating the counts ratio  $C_{min} / C_{max}$ .

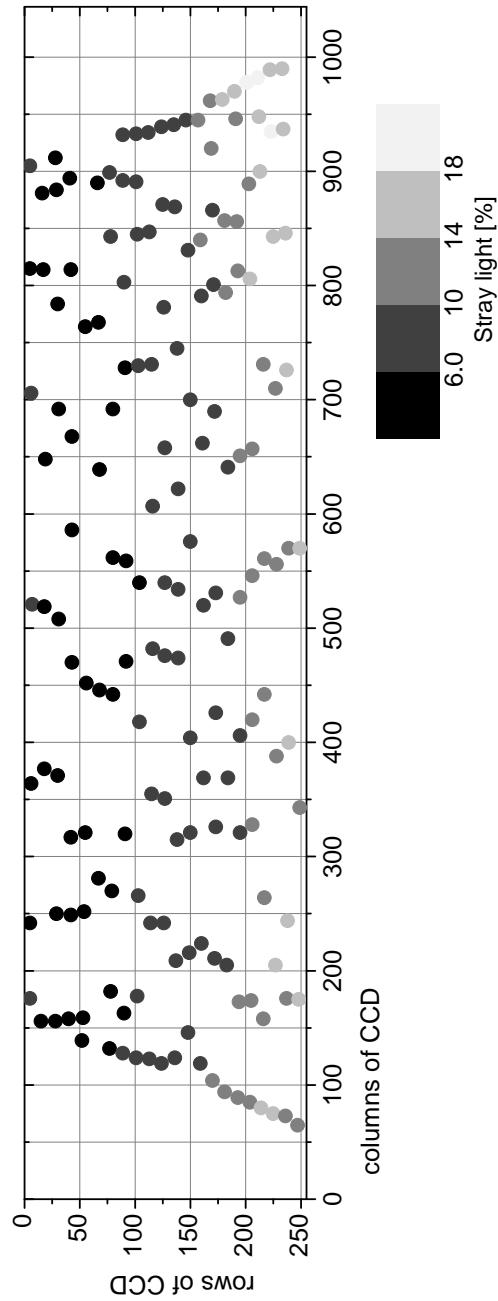


Figure 7.15: Systematic stray light determination by measuring the counts of a diffraction order  $C_{max}$  and its neighboring minima  $C_{min}$  and calculating the ratio  $C_{min} / C_{max}$ .

# 8 GEMOSS I - Tropospheric Water Vapor Retrieval

## 8.1 Selection criteria of absorption lines

### 8.1.1 Saturation

An absorption line is regarded as saturated when the amount of absorbed radiation becomes 100%. It is obvious that a saturated absorption line does not contain reliable information about the water vapor content since the saturation causes an insensitivity of the absorption line and a loss of proportionality between radiation intensity and water vapor content. In addition, the signal-to-noise ratio decreases for low line intensities. In order to avoid those saturation effects, lines with a transmittance lower than 0.5 were not used for water vapor retrieval. For this reason various appropriate absorption lines have to be selected to have assess the PW at any condition.

### 8.1.2 Fraunhofer lines

Before traversing the Earth's atmosphere the constituents of the solar atmosphere absorb a part of the radiation emitted by the Sun and cause numerous absorption lines, the so-called Fraunhofer lines. If one of these absorption lines overlap with one of water vapor, the amount of radiation absorbed due to tropospheric water vapor can not be determined by DOAS without previous subtraction of the Fraunhofer line. Otherwise, the retrieved PW will be over-estimated systematically. For precise determination of all Fraunhofer lines a solar spectrum measured in the absence of the Earth's atmosphere is required. Unfortunately, such a solar spectrum is currently not accessible for the wavelength range of GEMOSS. Therefore, a spectrum was computed using the stellar spectral synthesis program *SPECTRUM* of Richard O. Gray (Department of Physics and Astronomy, Appalachian State University, Boone, USA). The *SPECTRUM*-software simulates the emission and absorption processes in the solar atmosphere. As input the wavelength-sorted atomic lines provided by Robert L. Kurucz (Harvard-Smithsonian Center for Astrophysics, Cambridge) were used. The comparison of the resulting

- synthetic solar spectrum (*excluding* the Earth's atmosphere)

with a

- solar spectrum measured by GEMOSS (from Earth's surface)

and a

- H<sub>2</sub>O spectrum fitted to the measured using ESA line parameter

enables the identification and sorting-out of water vapor absorption lines which are overlapped by Fraunhofer lines. Fig. 8.1 shows the three spectra between 732.5 nm and 734.8 nm:

It can be seen in Fig. 8.1, that several *H<sub>2</sub>O* absorption lines are overlapped by Fraunhofer lines which results in measuring lower transmittance than simulated with ESA line parameters. Without the knowledge about the existence of the Fraunhofer lines the discrepancies in transmittance could be interpreted as inaccuracies of ESA line parameters. Furthermore, deviations between the measured and computed transmittance of a Fraunhofer line can be observed near 732.82 nm. The Fraunhofer line is much more stronger than the model of the SPECTRUM-software predicts. On the other hand, the line near 734.18 nm is more weak than estimated by the model. According to the procedure as described above, all water vapor absorption lines usable for PW retrieval were checked for overlapping Fraunhofer lines in the wavelength range of GEMOSS.

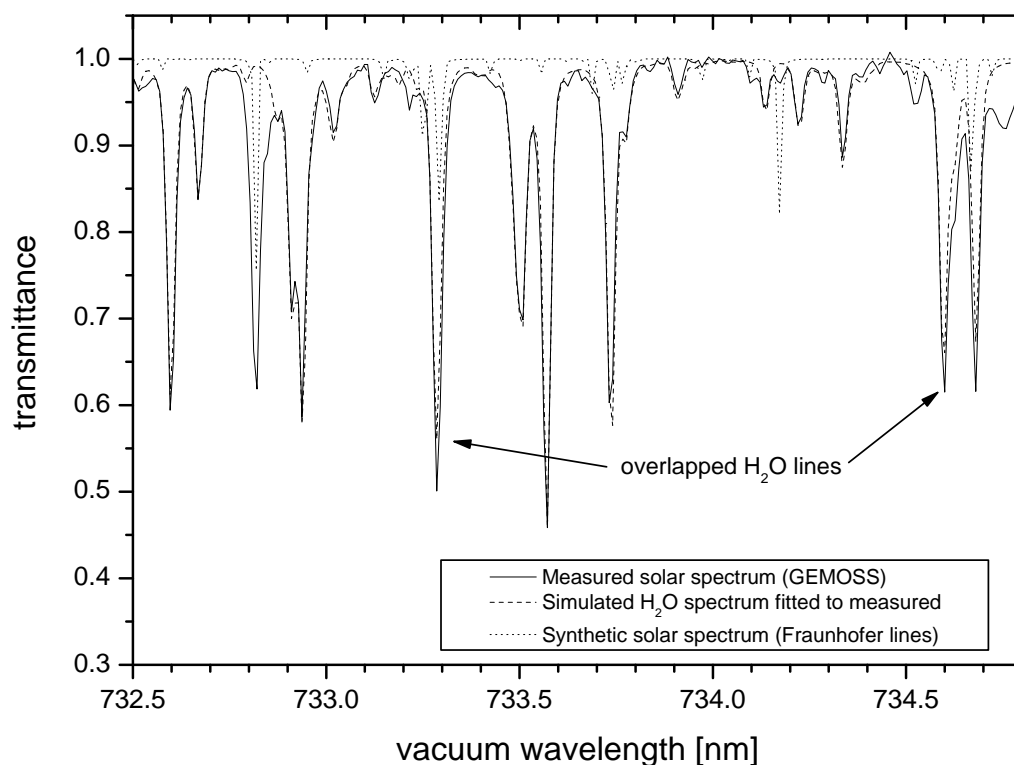


Figure 8.1: Identification of “hidden” Fraunhofer lines by comparing a solar spectrum measured by the ground-based GEMOSS with a synthetic solar spectrum excluding the Earth’s atmosphere and a simulated solar spectrum fitted to the measured using ESA  $H_2O$  line parameters. It is clearly visible that several  $H_2O$  lines are overlapped by Fraunhofer lines where the measured line intensity is usually significant lower than simulated with ESA parameters. These  $H_2O$  lines can not be used for the retrieval of tropospheric water vapor.

### 8.1.3 Base intervals

The method of DOAS requires intervals of the solar spectrum with negligible absorption, so-called *baseline intervals* or just *base intervals*. For high accuracy of the transmittance of a vibrational-rotational absorption line (section 8.2.1) neighboring base intervals of both sides are necessary. It has to be considered that the base intervals become more narrow or disappear with decreasing transmittance of the flanking absorption line due to line broadening. A selection of wavelength intervals was carried out which contains non-saturated  $H_2O$  absorption lines bordered by base intervals for a dedicated amount of PW. Suitable intervals were detected by comparing a measured solar spectrum with a simulated  $H_2O$  spectrum (Fig. 8.2). This method has the advantage that wavelength intervals with evident discrepancies between model and reality due to bad line parameters or Fraunhofer lines can be identified reliable. The selected wavelength ranges between 728 nm and 915 nm, where both spectra agree sufficiently and the DOAS method can be performed, are listed in Tab. 8.1.

interval	from [nm]	to [nm]
1	730.0	735.0
2	788.0	794.0
3	794.8	802.0
4	810.0	813.3
5	819.5	822.0
6	824.0	827.0
7	834.8	839.5
8	845.5	852.2
9	885.3	894.6
10	902.7	906.7

Table 8.1: Selection of wavelength intervals which contains non-saturated  $H_2O$  vibrational-rotational absorption lines bordered by base intervals for a dedicated amount of tropospheric water vapor.

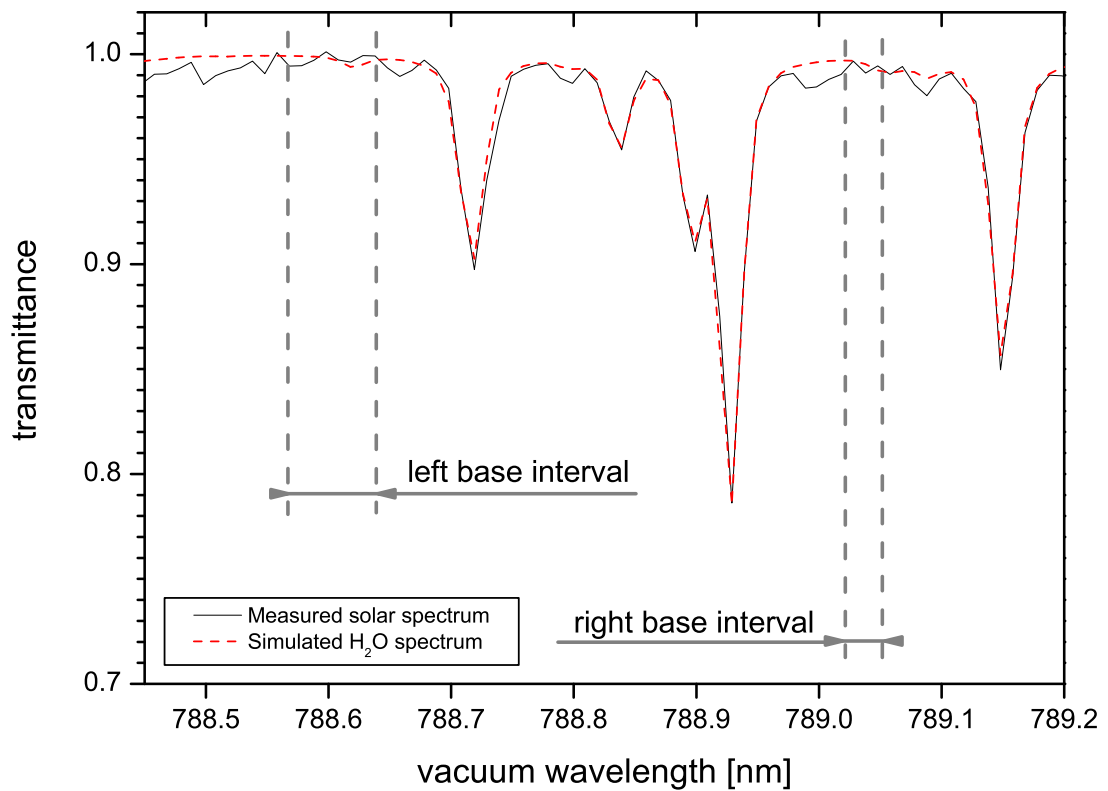


Figure 8.2:  $H_2O$  absorption lines bordered by base intervals. The existence of the left and right base interval allows the calculation of the transmittance according to the method of DOAS with high accuracy.

## 8.2 Pre-processing of measured solar spectra

### 8.2.1 Normalization

As described in section 5.2 the DOAS method is based on the normalization of a spectrum with respect to a reference intensity level using base line intervals with negligible absorption of radiation. This normalization procedure eliminates or minimizes the following effects:

- Instrumental effects due to imperfection of the spectrometer
- Individual sensitivity of each pixel of the CCD detector
- Broadband effects, like scattering at aerosols

The instrumental effects cause a periodic structure superposing the spectrum intensities. Fig. 8.3 shows as examples the diffraction orders 107 (a), 97 (b), 92 (c) and 88 (d) of a solar and a calibration spectrum of a halogen lamp which represents the reference intensity level. The periodic features stand out clearly in (b) and (c) whereas they are much weaker in (a) and (d).

The spectrum of the halogen lamp contains the individual sensitivity of each pixel of the CCD, too. Fig. 8.4 shows six spectra measured one after another with a time interval of half an hour. The spectra exhibit a structure of high frequency which is constant and due to the individual pixel sensitivity.

Although the exposure time needed for a single spectrum of a halogen lamp is very short (10 - 20 ms), a large time interval of the spectra would enable a higher frequency of measurements to the Sun. This requires the constancy of the halogen lamp spectrum within two measurements. Fig. 8.5 shows again eight spectra measured one after another with a time interval of one hour. The intensities of the raw spectra in Fig. 8.5a differ due to slightly different exposure times. If this effect is eliminated by factorizing, all eight spectra agree within 0.25 % over the wavelength range from 728 nm to 915 nm and reveal a high system stability and precision (Fig. 8.5b). Therefore, a calibration spectrum of the halogen lamp is measured only every half an hour.

Following the principle of DOAS the measured solar spectrum will be converted into differential absorption with respect to a reference intensity level [Platt (1994)]. This method was successfully applied by Sierk to retrieve the PW from measured intensities of single absorption lines [Sigrist (1994) and Sierk et al. (1997)]. Fig. 8.6 shows a measured solar spectrum (a) and a calibration spectrum of a halogen lamp (b). In a first step, the halogen lamp spectrum is modified to coincide with intervals of the solar spectrum with negligible absorption (Fig. 8.6c). The spectrum is shifted

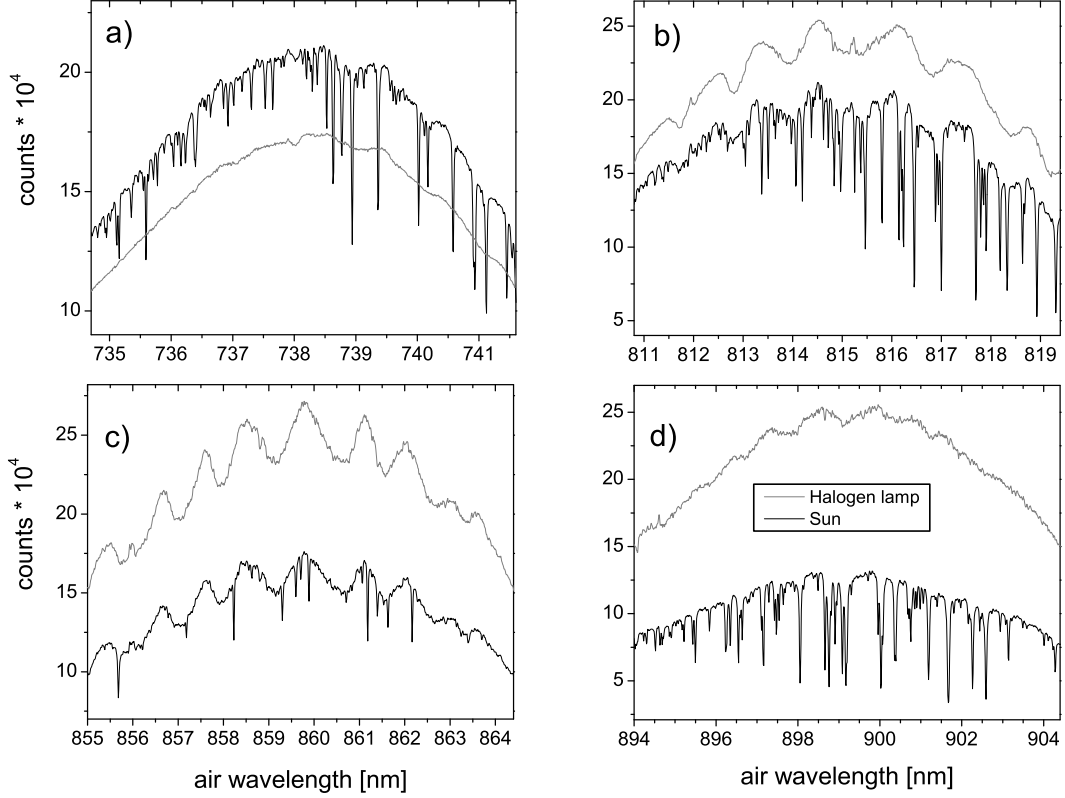


Figure 8.3: A spectrum of a halogen lamp is used to define the reference intensity level for the normalization of the solar spectrum. Instrumental effects are eliminated in the normalized solar spectrum. The four figures show the diffraction orders 107 (a), 97 (b), 92 (c) and 88 (d). The orders (b) and (c) exhibit a significant periodic structure caused by instrumental effects. These periodic features change their structure with the wavelength. They are weak in the orders (a) and (d).

onto the level of the solar spectrum using the factor  $R$  of a base interval with the mean wavelength  $\lambda_m$ :

$$R(\lambda_m) = \frac{\sum_{i=0}^e C_S(\lambda_i)}{\sum_{i=0}^e C_H(\lambda_i)} \quad (8.1)$$

The  $C_S(\lambda_i)$  and  $C_H(\lambda_i)$  are the counts of the solar and the halogen lamp spectrum at wavelength  $\lambda_i$ , respectively, which belong to the base interval involving the pixels  $i = 0..e$ . In the majority of cases, more than one base interval exist within the

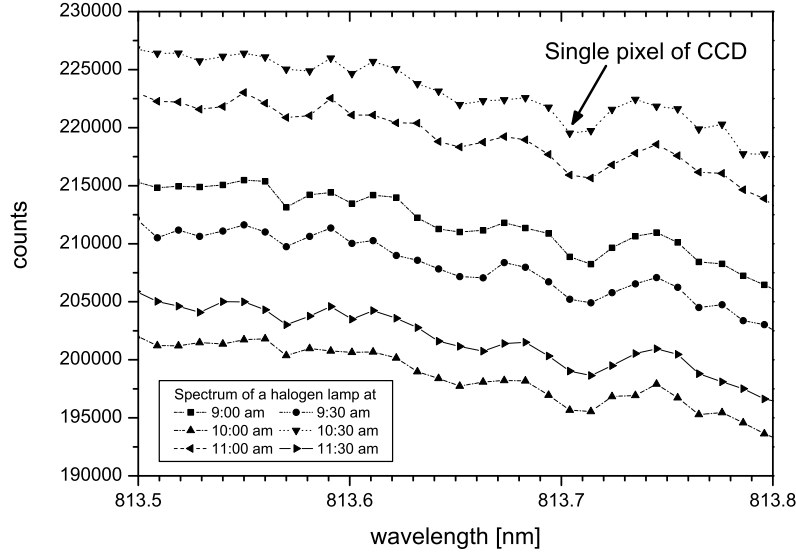


Figure 8.4: Six halogen lamp spectra measured one after another with a time interval of half an hour. The constant structure within the chosen narrow wavelength range represents the individual sensitivity of the pixel of the CCD.

wavelength intervals selected for PW retrieval from GEMOSS spectra. Therefore, the factor  $R_i$  of  $\lambda_i$  is interpolated between  $R_l$  and  $R_r$  (Eq. 8.1) corresponding to the mean wavelengths  $\lambda_l$  and  $\lambda_r$  of the left and right base interval:

$$R(\lambda_i) = \frac{R_r - R_l}{\lambda_r - \lambda_l} \cdot (\lambda_i - \lambda_l) + R_l \quad (8.2)$$

The counts  $C_{mH}(\lambda_i)$  of the shifted spectrum of the halogen lamp are computed as follows:

$$C_{mH}(\lambda_i) = R(\lambda_i) \cdot C_H(\lambda_i) \quad (8.3)$$

The modified halogen spectrum defines the reference intensity level and the solar spectrum can be normalized by calculating the transmittance (Fig. 8.6d):

$$I'_S(\lambda_i) = \frac{C_S(\lambda_i)}{C_{mH}(\lambda_i)} \quad (8.4)$$

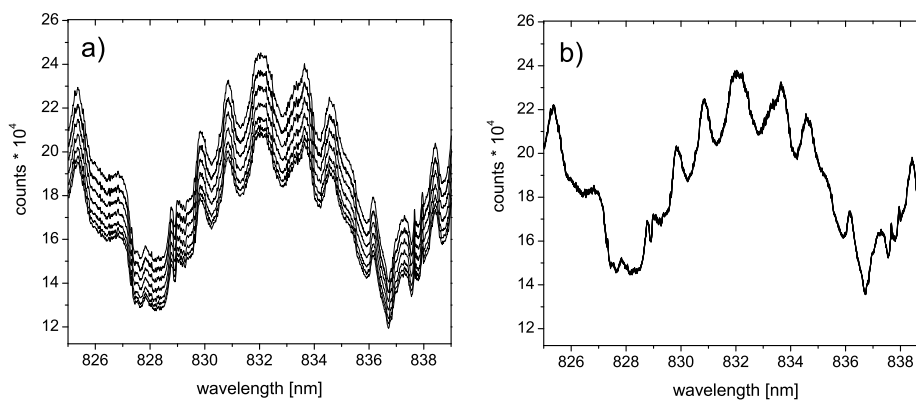


Figure 8.5: Eight halogen lamp spectra measured one after another with a time interval of one hour (a). Their counts vary due to different exposure times. If these differences are eliminated by factorizing, all spectra agree within 0.25 % over the wavelength range from 728 nm to 915 nm (b).

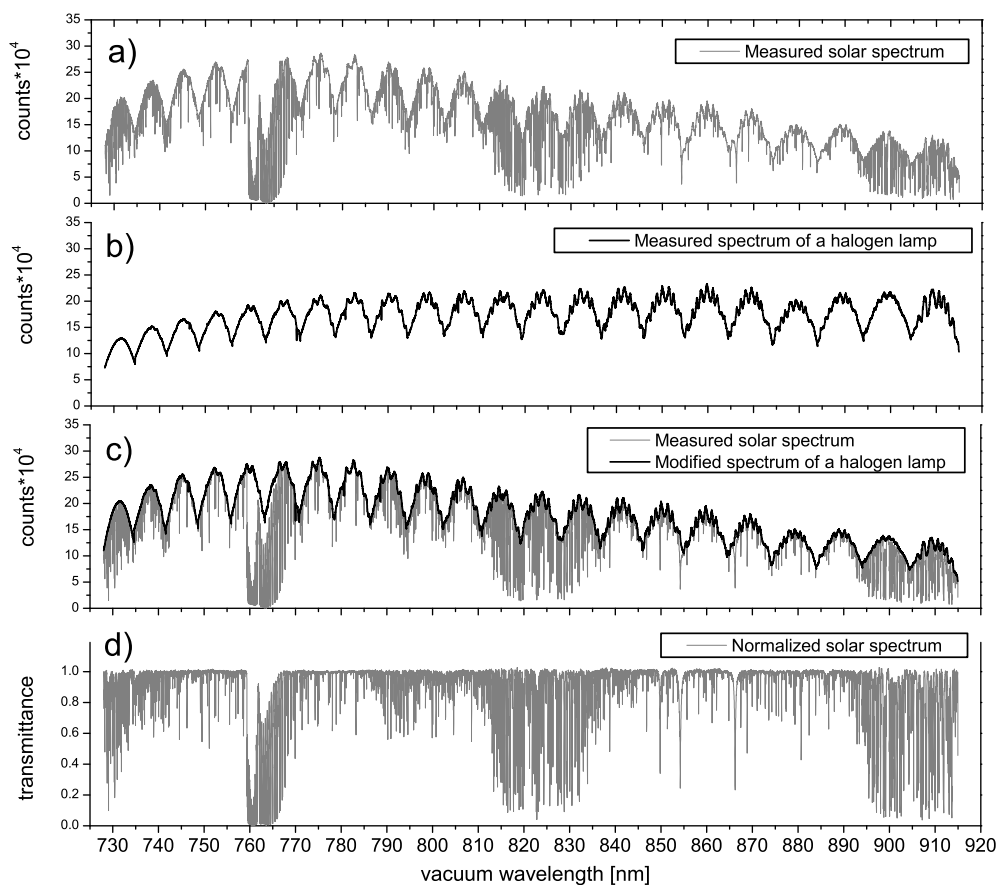


Figure 8.6: The raw solar spectrum (a) is normalized by a calibration spectrum of a halogen lamp (b) which is modified for definition of the reference intensity  $I_0 = 1$  (c). After the normalization the solar spectrum is expressed in terms of transmittance (d).

## 8.2.2 Correction for stray light

The normalization in section 8.2.1 was made without any correction of the detected counts due to stray light. Previously, the amount of stray light  $SL$  was precisely determined as described in section 7.5. The stray light correction is applied by introducing  $SL(\lambda_i)$  into Eq. 8.4:

$$I'_{S,corr}(\lambda_i) = \frac{C_S(\lambda_i) - SL(\lambda_i)/100 \cdot C_{mH}(\lambda_i)}{(1 - SL(\lambda_i)/100) \cdot C_{mH}(\lambda_i)} \quad (8.5)$$

where  $I'_{S,corr}(\lambda_i)$  denotes the transmittance of the stray light corrected normalized solar spectrum and  $SL(\lambda_i)$  the percentage of the stray light. Since the amount of stray light depends on the wavelength  $\lambda_i$ , the  $SL(\lambda_i)$  has to be interpolated between the values which were empirically determined by measuring the counts ratio  $C_{min}/C_{max}$  (Eq. 7.14). Fig. 8.7 shows the impact of the stray light correction on the normalized solar spectrum. The transmittance minima of the absorption lines decrease significantly whereas the transmittance maxima stay almost unchanged.

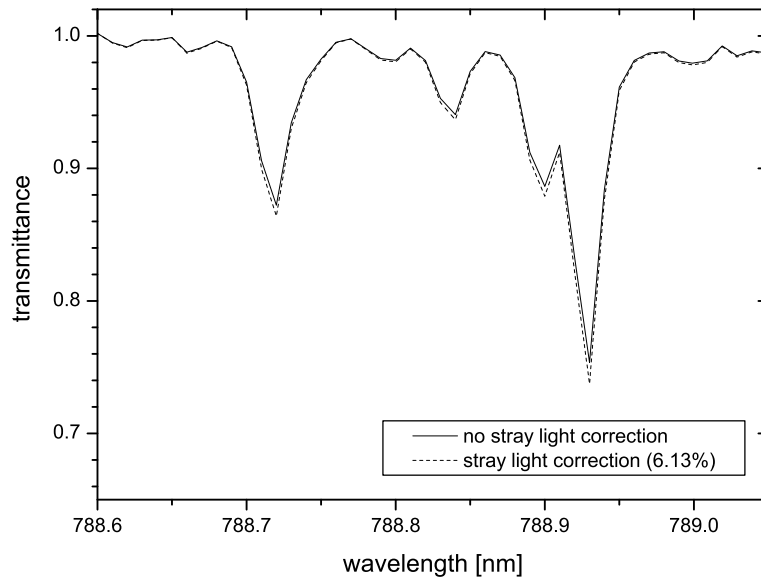


Figure 8.7: Solar spectra normalized with/without stray light correction. The transmittance minima of the absorption lines decrease significantly after applying the stray light correction.

## 8.3 Simulation of absorption spectra

### 8.3.1 Introduction

The retrieval of the precipitable water vapor (PW) utilizes the fit of a (normalized and stray light corrected) solar spectrum to a simulated spectrum by applying the method of least-squares fit. In order to simulate a solar spectrum, the physical process of molecular absorption and emission is computed with the radiative transfer equation of Chandrasekhar (1960) using a spherical model of the standard atmosphere including ground meteorological data. A detailed description of the theoretical fundamentals concerning the atmospheric absorption model, ray tracing and meteorological parameters can be found in the previous chapter 6. In order to calculate a solar spectrum approximating the real solar spectrum as best as possible, the simulation procedure consists of three main steps:

- Computation of a high-resolution spectrum with the radiative transfer model
- Convolution of the spectrum (apparatus function)
- Digitalization of the convoluted spectrum (CCD)

The convolution of the spectrum includes the apparatus function of GEMOSS and the digitalization the pixel grid of the CCD.

### 8.3.2 High-resolution spectrum

For the computation of a spectrum with high resolution of wavelength the atmosphere is divided into the same spherical layers as used for the ray tracing model (section 6.7). For each layer the temperature, air and partial pressure of water vapor and water vapor density is calculated according to the meteorological models defined in sections 6.8. In the following, the absorption coefficient  $k_{l,i,j}$  of the absorption line  $l$  is calculated for the wavelength  $\lambda_i$  with  $\lambda_i - \lambda_{i+1} = 1pm$  and the layer  $j$  (section 6.6). The absorption coefficients of all absorption lines are added pixel-wise for each layer:

$$k_{i,j} = \sum_{l=0}^n k_{l,i,j} \quad (8.6)$$

where  $n$  is the number of water vapor absorption lines within the simulated wavelength range. Finally, the differential intensity or transmittance  $I'_i$  of  $\lambda_i$  is calculated by:

$$I'_i = e^{-\int_{j=0}^m \tau_{i,j} ds_j} \quad (8.7)$$

with

$$\tau_{i,j} = \rho_j \cdot k_{i,j} s_j \quad (8.8)$$

where  $m$  denotes the number of atmospheric layers,  $s_j$  the absorption path length through the layer  $j$ ,  $\rho_j$  the water vapor density and  $\tau_{i,j}$  the optical density for  $\lambda_i$ . This layer-wise calculation of absorption and emission in the atmosphere is illustrated in Fig. 8.8. The sum of the contributions of the water vapor molecules along the ray trace through a single layer yields the absorption spectrum at the ground.

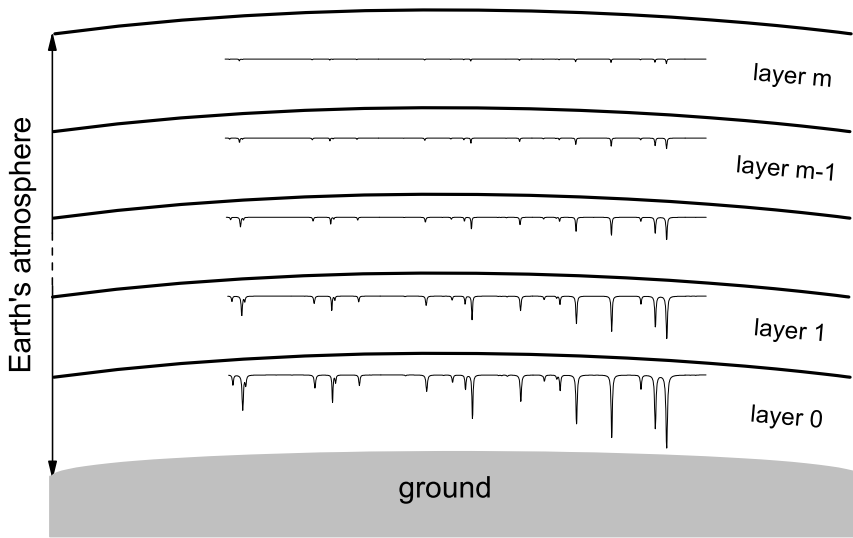


Figure 8.8: Illustration of the layer-wise calculation of the absorption and emission of radiation by water vapor molecules along the ray trace through a layer.

### 8.3.3 Convolution

The measured solar spectrum is convoluted with the apparatus function of GEMOSS. This device-specific apparatus function can be approximated by a Voigt function which is determined by a least-squares fit to single neon emission lines (section 7.4). The Voigt function  $V_{digit}$ , digitized according to the resolution of the spectrum, is used to convolute the high-resolution spectrum  $SPC$ :

$$SPC_{conv} = SPC * V_{digit} \quad (8.9)$$

Fig. 8.9 shows the effect of the convolution with the Voigt function on the high-resolution spectrum. The simulated convoluted solar spectrum corresponds to the

measured spectrum after diffraction on the echelle grating and before digitalization by the CCD.

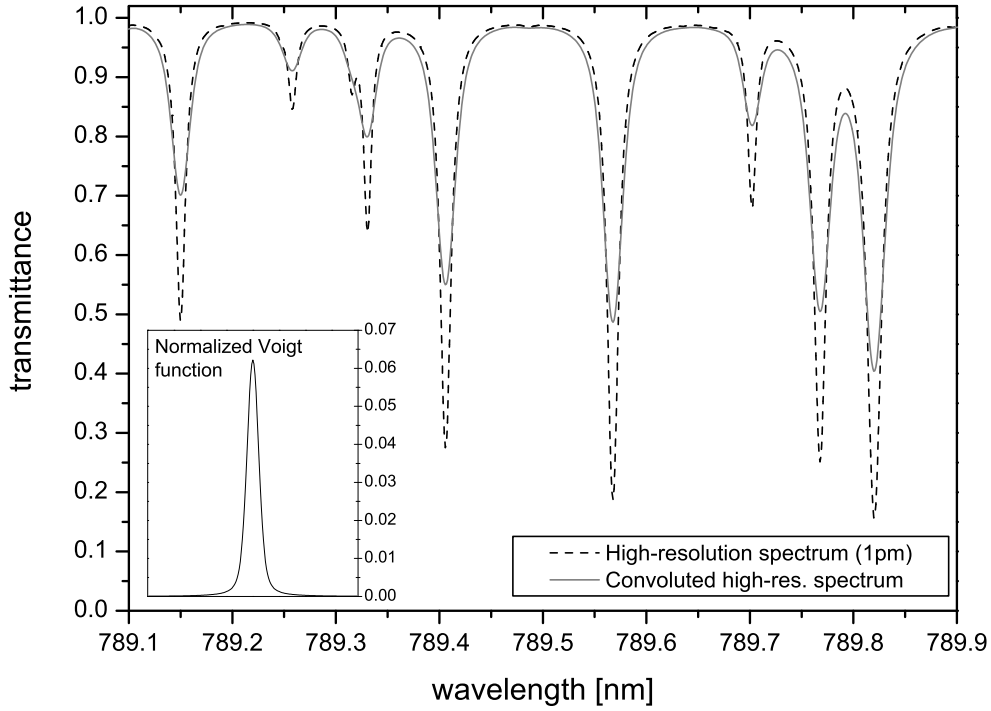


Figure 8.9: Convolution of a simulated high-resolution spectrum with a Voigt function representing the apparatus function of GEMOSS.

### 8.3.4 Digitalization

As a last step the digitalization of the spectrum by the CCD has to be applied to the simulated spectrum. According to the width of the CCD-pixel, the intensities  $I'_i$  corresponding to a single pixel  $j$  with  $\lambda_j$  are summarized to the mean intensity:

$$I'_{digit,j} = \sum_i I'_i \quad (8.10)$$

A digitized spectrum is shown in Fig. 8.10.

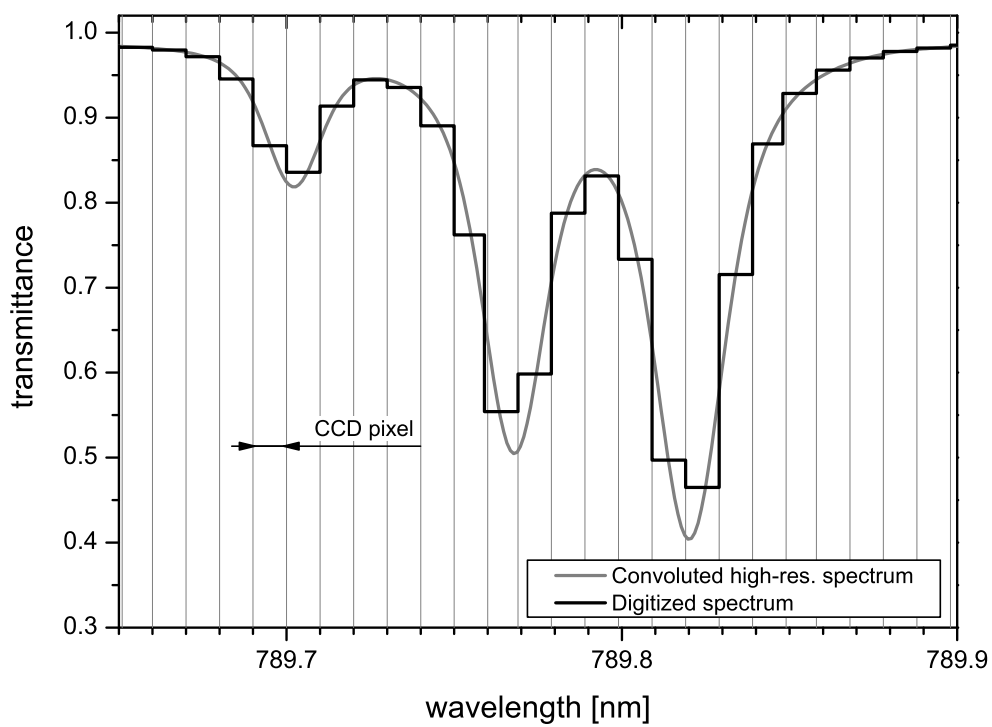


Figure 8.10: Digitalization of a simulated high-resolution spectrum by averaging the intensities which belong to the same CCD pixel.

## 8.4 Least-squares fit algorithm

The fit of the simulated spectrum to the measured is carried out by an iteration procedure. The integrated amount of the mass density of water vapor or absolute humidity  $\rho_v$  is adjusted until both spectra agree within a sufficient accuracy. For the least-squares adjustment the following approach was chosen:

$$\mathbf{v} = \mathbf{A} \cdot \mathbf{x} - \mathbf{l} \quad (8.11)$$

with

$$\mathbf{v} = \begin{pmatrix} \delta I'_{digit}(\lambda_0) \\ \delta I'_{digit}(\lambda_1) \\ \delta I'_{digit}(\lambda_2) \\ \vdots \\ \delta I'_{digit}(\lambda_n) \end{pmatrix} \quad \mathbf{A} = \begin{pmatrix} \partial I'_{digit}(\lambda_0)/\partial PW \\ \partial I'_{digit}(\lambda_1)/\partial PW \\ \partial I'_{digit}(\lambda_2)/\partial PW \\ \vdots \\ \partial I'_{digit}(\lambda_n)/\partial PW \end{pmatrix}$$

$$\mathbf{x} = ( \delta PW ) \quad \mathbf{l} = \begin{pmatrix} I'_S(\lambda_0) - I'_{digit}(\lambda_0) \\ I'_S(\lambda_1) - I'_{digit}(\lambda_1) \\ I'_S(\lambda_2) - I'_{digit}(\lambda_2) \\ \vdots \\ I'_S(\lambda_n) - I'_{digit}(\lambda_n) \end{pmatrix}$$

where  $\mathbf{v}$  denotes the improvements of the intensities,  $\mathbf{A}$  the partial derivations,  $\mathbf{x}$  the improvement of  $PW$  and  $\mathbf{l}$  the differences of the measured and the simulated intensities. The vector  $\mathbf{x}$  with the unknown improvement of  $PW$  is determined by:

$$\mathbf{x} = \mathbf{N}^{-1} \mathbf{A}^T \mathbf{P} \mathbf{l} \quad (8.12)$$

and

$$\mathbf{N} = \mathbf{A}^T \mathbf{P} \mathbf{A} \quad (8.13)$$

where  $\mathbf{P}$  contains the weightings of the observations  $I'_S(\lambda_i)$  and  $\mathbf{N}$  is the matrix of the normal equations. The partial derivations of the intensities of the simulated digitized spectrum are calculated by:

$$\frac{\partial I'_{digit}(\lambda_i)}{\partial PW} = \frac{1}{n} \left( \frac{\partial I'_{conv}(\lambda_j)}{\partial PW} + \frac{\partial I'_{conv}(\lambda_{j+1})}{\partial PW} + \dots + \frac{\partial I'_{conv}(\lambda_n)}{\partial PW} \right) \quad (8.14)$$

where  $I'_{conv}(\lambda_i)$  represents the intensities of the simulated convoluted spectrum without digitalization. The variable  $n$  is the number of  $I'_{conv}(\lambda_i)$  used to compute  $I'_{digit}(\lambda_i)$  by averaging (section 8.3.4). The partial derivations  $\partial I'_{conv}(\lambda_i)/\partial PW$  can be written according to Eq. 8.9 as:

$$\frac{\partial I'_{conv}(\lambda_i)}{\partial PW} = a_{j-m} \frac{\partial I'(\lambda_{j-m})}{\partial PW} + a_{j-m+1} \frac{\partial I'(\lambda_{j-m+1})}{\partial PW} + \dots + a_{j+m} \frac{\partial I'(\lambda_{j+m})}{\partial PW} \quad (8.15)$$

The coefficients  $a_i$  are the  $2m + 1$  elements of the Voigt function representing the apparatus function of GEMOSS which is utilized to convolute the simulated spectrum. Furthermore, the partial derivations  $\partial I'(\lambda_i)/\partial PW$  are retrieved by:

$$\frac{\partial I'(\lambda_i)}{\partial PW} = \frac{b}{c} \cdot e^{\frac{b}{c}PW} \quad (8.16)$$

with

$$b = - \int_{j=s_0}^{\infty} e^{-\frac{h_j-h_0}{H_s}} \cdot k(\lambda_i) ds \quad c = \int_{j=s_0}^{Strato} e^{-\frac{h_j-h_0}{H_s}} ds \quad (8.17)$$

The  $h_j$  and  $h_0$  are the heights of the atmospheric layer  $j$  and the ground, respectively.  $H_s$  denotes the scale height for the water vapor density and  $k(\lambda_i)$  the absorption coefficient.

The least-squares adjustment as described above is repeated until the improvement  $\delta PW$  is smaller than an accuracy limit of  $0.01 kg/m^2$ . Fig. 8.11 shows a measured solar spectrum which is iteratively approximated in three steps by a simulated spectrum.

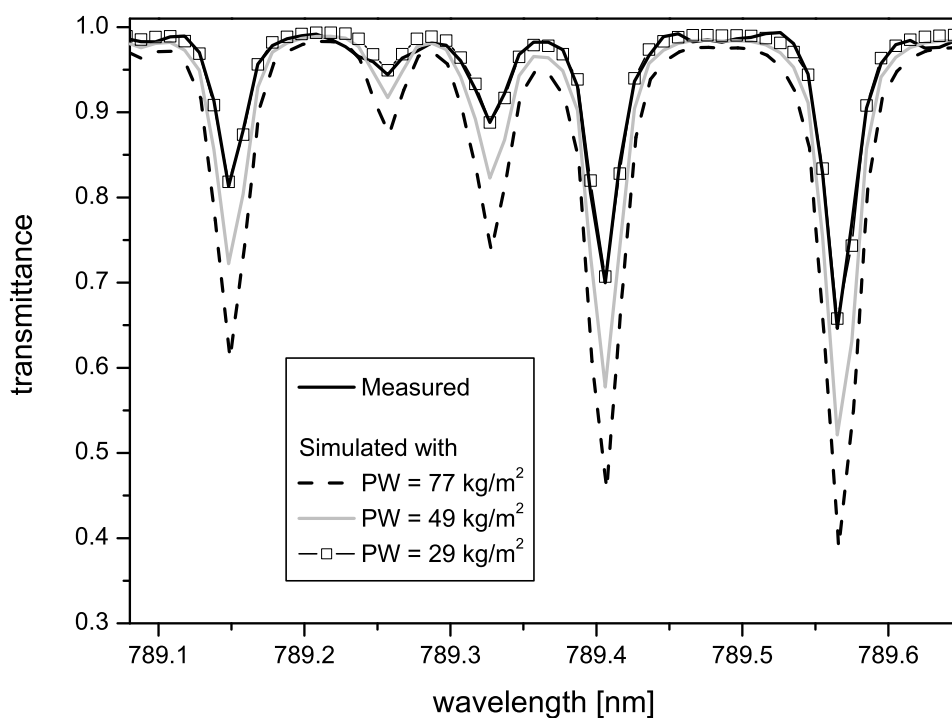


Figure 8.11: Fit of a simulated spectrum to a measured by adjusting the precipitable water vapor (PW) into measurement direction.

## 8.5 Accuracy analysis

### 8.5.1 Introduction

In order to quantify the accuracy of the PW retrieved from GEMOSS measurements, different error sources have to be investigated. In this section the following error sources are analyzed which are suspected to contribute to the total error budget:

- Instrumental errors:
  - Noise of CCD (shot-noise, readout-noise)
  - Stray light
  - Apparatus function
- Model errors:
  - Line strength parameters
  - Meteorological parameters

If an analytical error propagation can not be carried out, an adequate error estimation is performed. In the case of the meteorological profiles, radio soundings are used to assess the real atmospheric conditions for comparison. The influence of the uncertainties in the line strength parameters are expected to be the largest error source. The standard deviations of the line strengths, which were estimated from GEMOSS spectra using radiosonde and WVR observations (chapter 9), are utilized to estimate the error of retrieved PW.

### 8.5.2 Noise of CCD

The property of the photodiodes can be characterized by the shot-noise:

$$\sigma_{shot} = \sqrt{\text{number of } e^-} = \sqrt{C \cdot E} \quad (8.18)$$

where  $C$  is the number of detected counts and  $E$  the number of electrons per count. The CCD area image sensor C7041 (HAMAMATSU) of GEMOSS converts 10 electrons to one count which yields a shot-noise of  $\pm 71$  counts for  $C = 50000$ . The readout-noise  $\sigma_{read}$  is given by HAMAMATSU with  $\pm 2$  counts. The resulting error of the number of detected counts for one pixel is found by:

$$\sigma_{shot,read} = \sigma_{shot} + \sigma_{read} = \pm 73 \text{ counts} \quad (8.19)$$

Since each CCD image is corrected due to dark current by subtracting a *dark current image*, the error introduced by the dark current correction has to be analyzed. The

dark current is caused by a device-dependent offset of counts and by thermal effects. Therefore, the error of the dark current is given by:

$$\sigma_{dark} = \sqrt{\sigma_{offset}^2 + \sigma_{therm}^2} \quad (8.20)$$

where  $\sigma_{offset}$  denotes the error of the counts-offset and  $\sigma_{therm}$  the error due to thermal effects. Since the counts-offset is constant, the error  $\sigma_{offset}$  is zero. The error due to thermal effects is proportional to the exposure time and temperature of the sensor. For the very short exposure times of solar spectra and the low temperature of the cooled CCD  $\sigma_{therm}$  is negligible as well and  $\sigma_{dark}$  becomes zero.

After subtracting the dark current, the CCD image is binned as described in section 7.3 in order to obtain the spectrum. The error of the counts sum of  $i$  pixels belonging to the same wavelength is quantified by:

$$\sigma_{binned} = \sqrt{\sum_{n=0}^i \sigma_{shot,read,i}^2} \quad (8.21)$$

The detected counts of nine pixels of a cross-section of a diffraction order as well as their corresponding  $\sigma_{shot,read}$  are shown in Fig. 8.12. For this example  $\sigma_{binned}$  of the resulting sum of counts ( $C_S = 225000$ ) representing the intensity of radiation at a certain wavelength is  $\pm 150$  counts.

In order to transform the counts into transmittance the solar spectrum has to be normalized according to section 8.2.1 by dividing with a shifted spectrum of the halogen lamp. The mean error of the transmittance  $I'$  calculated from the counts of the solar and halogen spectrum  $C_S(\lambda_i)$  and  $C_{mH}(\lambda_i)$  (Eq. 8.4) is found by the error propagation law:

$$\sigma_{I'} = \sqrt{\left[\frac{1}{C_{mH}(\lambda_i)}\right]^2 \cdot \sigma_{S,binned}^2 + \left[-\frac{C_S(\lambda_i)}{C_{mH}^2(\lambda_i)}\right]^2 \cdot \sigma_{mH,binned}^2} \quad (8.22)$$

For solar spectra of GEMOSS the mean error of the transmittance  $\sigma_{I'}$  varies between  $\pm 0.001$  and  $\pm 0.002$ . Finally, the mean error of PW retrieved from a *single* water vapor absorption line by applying a least-squares fit as described in section 8.4 is determined by:

$$\sigma_{PW} = \sqrt{\sigma_0^2 \mathbf{N}^{-1}} \quad (8.23)$$

where the matrix of normal equations  $\mathbf{N}$  is calculated using Eq. 8.13. The weights in matrix  $\mathbf{P}$  in Eq. 8.13 are calculated with  $\sigma_{I'}$ :

$$P = \text{diag} \left[ \frac{1}{\sigma_{I'}^2(\lambda_0)}, \frac{1}{\sigma_{I'}^2(\lambda_1)}, \dots, \frac{1}{\sigma_{I'}^2(\lambda_n)} \right] \quad (8.24)$$

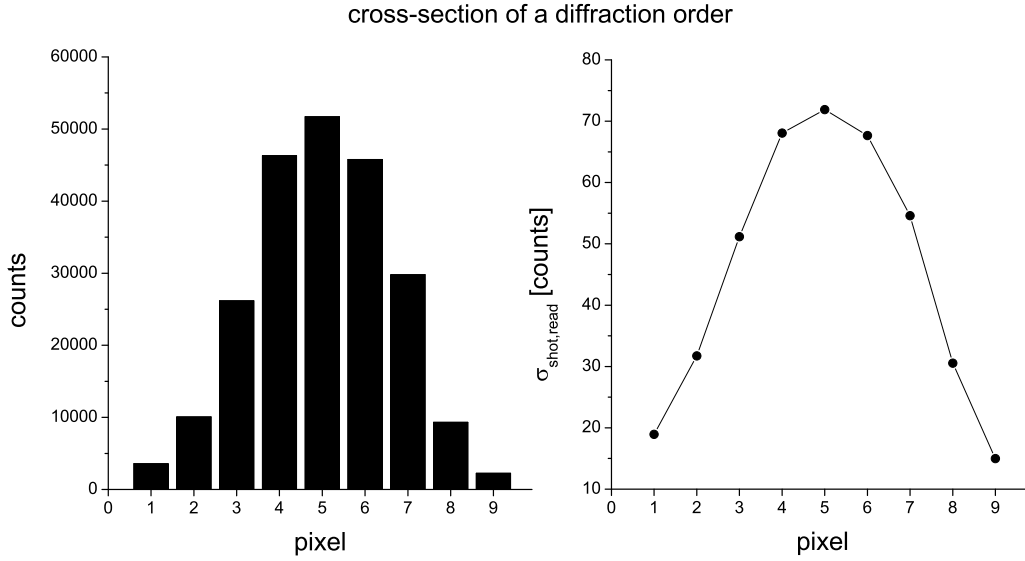


Figure 8.12: The counts and their corresponding mean errors (shot-noise, readout-noise) of pixels of a cross-section through a diffraction order. Since these pixels detect the radiation at the same wavelength, their counts are summarized.

The mean unit error  $\sigma_0$  in Eq. 8.23 is defined by:

$$\sigma_0 = \sqrt{\frac{\sum_{i=1}^n \mathbf{P}_{i,i} \mathbf{V}_{1,i} \mathbf{V}_{1,i}}{n-1}} \quad (8.25)$$

where  $\mathbf{p}$  and  $\mathbf{v}$  are the elements of the matrices  $\mathbf{P}$  and  $\mathbf{v}$  and  $n$  is the number of observations (measured transmittance of an absorption line). Depending on the sensitivity of the water vapor absorption line and the wavelength range used for least-squares fit  $\sigma_{PW}$  varies between  $\pm 0.2 \text{ kg/m}^2$  and  $\pm 0.3 \text{ kg/m}^2$ . These values are valid for a least-squares fit with a single absorption line. In order to increase the accuracy of PW the retrievals of numerous absorption lines are averaged and  $\sigma_{PW}$  becomes for  $m$  absorption lines:

$$\sigma_{PW} = \sqrt{\frac{\sum_{i=1}^m \sigma_{PW,i}^2}{m^2}} \quad (8.26)$$

In the case of 40 absorption lines  $\sigma_{PW}$  does not exceed  $\pm 0.05 \text{ kg/m}^2$ . This low error of PW only represents the influence of the measurement error due to imperfection of the CCD and does not include further error sources which are examined in the next sections. It can be pointed out that errors of PW caused by the CCD are negligible.

### 8.5.3 Stray light

The detected counts  $C_S$  and  $C_{mH}$  have to be corrected due to stray light (section 8.2.2). The stray light was determined in section 7.5 with an accuracy of  $\sigma_{SL} = \pm 0.3\%$ . The error of transmittance due to the uncertainty of stray light is derived by applying the error propagation law to Eq. 8.5:

$$\sigma_{I'} = \sqrt{\left[ \frac{C_S - C_{mH}}{C_{mH} \left( \frac{1-SL}{100} \right)^2} \right]^2} \sigma_{SL}^2 \quad (8.27)$$

Assuming a common transmittance  $I' = 0.7$ ,  $\sigma_{I'}$  is determined to  $\pm 0.001$ . According to the error propagation as examined in the previous section (Eq. 8.23-8.26)  $\sigma_{I'}$  causes an error of PW  $\sigma_{PW} = \pm 0.03 \text{ kg/m}^2$ . The extremely low  $\sigma_{PW}$  indicates that the amount of stray light was determined with sufficient accuracy and the effect of  $\sigma_{SL}$  on the accuracy of the PW retrievals can be regarded as negligible.

### 8.5.4 Apparatus function

As described in section 7.4 the apparatus function is approximated by a Voigt function which is calculated by convoluting a Lorentz with a Gauss function (Eq. 7.6-7.8). The *Full Width at Half Maximum* (FWHM) of the Lorentz and Gauss function is determined with high accuracy ( $\sigma_{FWHM} = \pm 0.004$  pixel width) by measuring neon emission lines. Since the effect of  $\sigma_{FWHM}$  on the accuracy of retrieved PW can not be derived analytically, the impact of the apparatus function is investigated experimentally. Therefore, the FWHM of the Lorentz and Gauss function are changed about  $\pm 0.1$  pixel width. The modified FWHM's were used to calculate the Voigt function utilized as apparatus function to convolute the simulated solar spectrum (section 8.3.3). The least-squares fits of these simulated spectra to measured solar spectra yield PW's which do not deviate more than  $0.05 \text{ kg/m}^2$  from those calculated with correct FWHM's. Considering the fact that the accuracy of the determined FWHM's ( $\sigma_{FWHM} = \pm 0.004$  pixel width) is much more better than the applied deviations ( $\pm 0.1$  pixel width), uncertainties of the apparatus function do not cause significant errors in the PW retrievals.

### 8.5.5 Line strength parameter

While the errors of the retrieved PW due to the CCD noise, stray light and uncertainty of the apparatus function are relative small, the influence of errors of the line strength parameters on the PW are expected to be larger [Sierk (2000)]. Furthermore, an inaccurate line strength causes systematic errors of the integrated water vapor content. Other line parameters as line position and half width do not affect the estimated amount of water molecules. The line position is adjusted while fitting the simulated spectrum to the measured, and the half width determines the shape of the absorption line but not the integral absorption and thus the PW retrieval. The statistic error in the retrieval  $\sigma_{PW}$  due to the error of the line strength parameter  $\sigma_{S_l(T_{ref})}$  of line  $l$  can be evaluated by [Rodgers (2000)]:

$$\sigma_{PW} = \sqrt{\mathbf{H}^T \mathbf{H}} \cdot \sigma_{S(T_{ref})} \quad (8.28)$$

with

$$\mathbf{H} = (\mathbf{A}^T \mathbf{P} \mathbf{A})^{-1} \mathbf{A}^T \mathbf{P} \mathbf{A}_S \quad (8.29)$$

where

$$\mathbf{A} = \begin{pmatrix} \partial I'(\lambda_0)/\partial PW \\ \partial I'(\lambda_1)/\partial PW \\ \partial I'(\lambda_2)/\partial PW \\ \vdots \\ \partial I'(\lambda_n)/\partial PW \end{pmatrix}^T$$

$$\mathbf{A}_S = \begin{pmatrix} \partial I'(\lambda_0)/\partial S_l(T_{ref}) \\ \partial I'(\lambda_1)/\partial S_l(T_{ref}) \\ \partial I'(\lambda_2)/\partial S_l(T_{ref}) \\ \vdots \\ \partial I'(\lambda_n)/\partial S_l(T_{ref}) \end{pmatrix}$$

$$\mathbf{P} = \text{diag} \left( 1/\sigma_{I'_0}^2 \quad 1/\sigma_{I'_1}^2 \quad 1/\sigma_{I'_2}^2 \quad \dots \quad 1/\sigma_{I'_n}^2 \right)$$

Matrix  $\mathbf{P}$  contains the weights of the intensities  $I'$  which are the reciprocal values of the squared measurement accuracy  $\sigma_{I'} \approx \pm 0.005$ . The matrices  $\mathbf{A}$  and  $\mathbf{A}_S$  consist of the partial derivations  $\partial I'/\partial PW$  and  $\partial I'(\lambda_0)/\partial S_l(T_{ref})$ , respectively, which belong to the processing interval of the corresponding absorption line. The standard deviation of the line strength  $\sigma_{S(T_{ref})}$  was taken from the fitted line strength as determined in chapter 9.

Eq. 8.28 was applied to the 69 selected  $H_2O$  transitions whose line strengths were estimated by means of measured solar spectra and co-located radiosonde and WVR observations (chapter 9). The calculated errors of the PW retrievals caused by  $\sigma_{S(T_{ref})}$  are listed in Tab. 8.2 and Tab. 8.3. The mean values of  $\sigma_{S(T_{ref})}$  and  $\sigma_{PW}$  are determined to  $\pm 0.79 \text{ cm/molecule}$  and  $\pm 0.58 \text{ kg/m}^2$ . It is noted that

four lines (788.2991 nm, 812.5057 nm, 834.9617 nm, 846.2665 nm), whose weak line strengths are not well determined, might cause PW errors larger than  $1 \text{ kg/m}^2$ . If these four lines are sorted out, the mean standard deviation  $\bar{\sigma}_{PW}$  decreases and becomes  $\pm 0.38 \text{ kg/m}^2$ . It can be pointed out that the error due to the uncertainty of the individual line strength parameter varies between  $0.2 \text{ kg/m}^2$  and  $0.6 \text{ kg/m}^2$ . Lines with a weak and inaccurate determined line strength increase the error of the retrieval and should not be used. As already mentioned in previous sections the accuracy of the retrieved water vapor abundance can significantly be increased by the use of numerous absorption lines.

$\lambda_0$ [nm]	$\sigma_{S(T_{ref})}$ [ $\frac{10^{-25}cm^{-1}}{molecule \cdot cm^{-2}}$ ]	$\sigma_{PW}$ [kg/m <sup>2</sup> ]
732.599284	1.15	0.38
732.670108	0.22	0.27
732.938448	1.18	0.27
733.508311	0.74	0.38
733.570803	3.02	0.26
734.337114	0.26	0.51
735.123753	1.31	1.25
735.211677	0.56	0.35
735.912863	0.40	0.22
736.088010	0.17	0.20
736.237682	0.67	0.25
787.496198	0.63	1.01
787.872431	0.39	0.34
788.299119	0.67	3.78
788.927746	0.42	0.33
789.150008	0.35	0.44
789.406032	0.49	0.31
789.567632	0.61	0.29
789.767800	0.47	0.28
789.820153	0.74	0.27
790.393201	1.17	0.35
791.092945	2.16	0.58
791.286020	0.41	0.43
792.283920	0.75	0.20
793.079720	1.07	0.30
793.153408	0.22	0.31
794.992185	0.27	0.35
796.067478	0.69	0.21
796.245676	0.28	0.34
796.292234	0.80	0.36
796.380419	0.54	0.54
796.653742	0.49	0.41
797.030469	0.42	0.31
800.249319	1.35	0.46
800.717520	0.12	0.43
800.969384	1.64	0.56

Table 8.2: Error of the retrieved PW due to uncertainties in the individual line strength parameters.

$\lambda_0$ [nm]	$\sigma_{S(T_{ref})}$ [ $\frac{10^{-25}cm^{-1}}{molecule \cdot cm^{-2}}$ ]	$\sigma_{PW}$ [kg/m <sup>2</sup> ]
801.310450	0.19	0.39
812.289155	0.39	0.25
812.505698	1.41	2.04
813.268746	1.41	0.16
813.462591	0.19	0.44
820.224505	1.49	0.18
820.294513	1.55	0.05
824.218493	1.21	0.19
824.888013	0.22	0.37
825.499147	2.04	0.16
826.012877	0.52	0.61
826.195438	1.31	0.04
826.501711	0.25	1.07
826.571291	2.55	0.13
826.722242	0.23	0.83
834.625998	0.39	1.18
834.961717	1.20	2.74
835.226723	0.17	0.87
835.701433	0.43	0.38
835.932243	1.88	0.18
835.972953	0.58	0.30
836.182905	0.21	0.28
836.459804	1.28	0.27
836.884303	0.43	1.12
837.684490	0.37	0.57
837.866730	1.13	0.37
837.945504	0.36	0.37
838.647317	0.34	0.40
846.266472	0.67	7.60
850.818483	0.13	0.31
851.463619	0.21	0.37
890.307128	0.40	0.61
903.186704	1.50	0.17
903.738591	0.60	0.26
904.255968	1.24	0.14
904.360225	0.78	0.45
904.529498	1.25	0.02
904.988956	0.83	0.13
905.101927	0.51	0.31
906.653141	1.34	0.05
mean	<b>0.79</b>	<b>0.58</b>

Table 8.3: Continuation of Tab. 8.2

### 8.5.6 Meteorological model

The formulas in section 6.8 represent the characteristics of the standard atmosphere which is in general close to the real atmosphere [Boiffier (1998)]. The following four hypothesis concerning the properties of the standard atmosphere were made:

- The state of the atmosphere is “frozen” (Taylor hypothesis which can be extended to the velocity of the air)
- Air is an ideal gas
- The atmosphere can be weighed and is subject of the Laplace’s law
- The temperature depends on the altitude according to the Toussaint law

The vertical gradient of the temperature is certainly the hypothesis which causes the largest deviations with respect to the real atmosphere. In addition, the simple exponential height function (Eq. 6.67) used to calculate the vertical humidity distribution will almost ever differ from the truth. Whereas the air pressure can be described by the barometric formulas with sufficient accuracy.

Due to the disagreement of the meteorological model with the real atmospheric conditions, the retrieved water vapor content deviates from the true value. Since a separate error analysis for each of the meteorological profiles is very difficult, their influence on the retrieved water vapor abundance was investigated in all statistically. 59 radio soundings carried out at Payerne in May and June 2004 around noon were used to simulate solar absorption spectra. These 59 spectra were processed with the assumptions of the meteorological model in order to retrieve the PW from 31  $H_2O$  absorption lines. The differences of the obtained PW’s from the “true” values (radiosondes) are a measure of the errors resulting from deviations of the model from the real atmosphere. Fig. 8.13 presents the differences of the zenithal PW for the selected dataset. In most cases the differences of the ZPW do not exceed  $0.5 \text{ kg/m}^2$ . The mean difference is  $0.3 \text{ kg/m}^2$ . If the ZPW is averaged from all 31 absorption lines, the mean difference decreases considerably from  $0.3 \text{ kg/m}^2$  to  $0.1 \text{ kg/m}^2$ .

It can be pointed out that an uncertainty of the meteorological model does not cause large errors in the PW retrievals, especially if numerous absorption lines are used. Variations of the vertical distribution of water vapor molecules in the atmosphere do not cause significant errors in the integrated water vapor content. This is also the reason for the difficulties in estimating vertical profiles of atmospheric water vapor from the amount of absorption of solar radiation due to  $H_2O$  molecules.

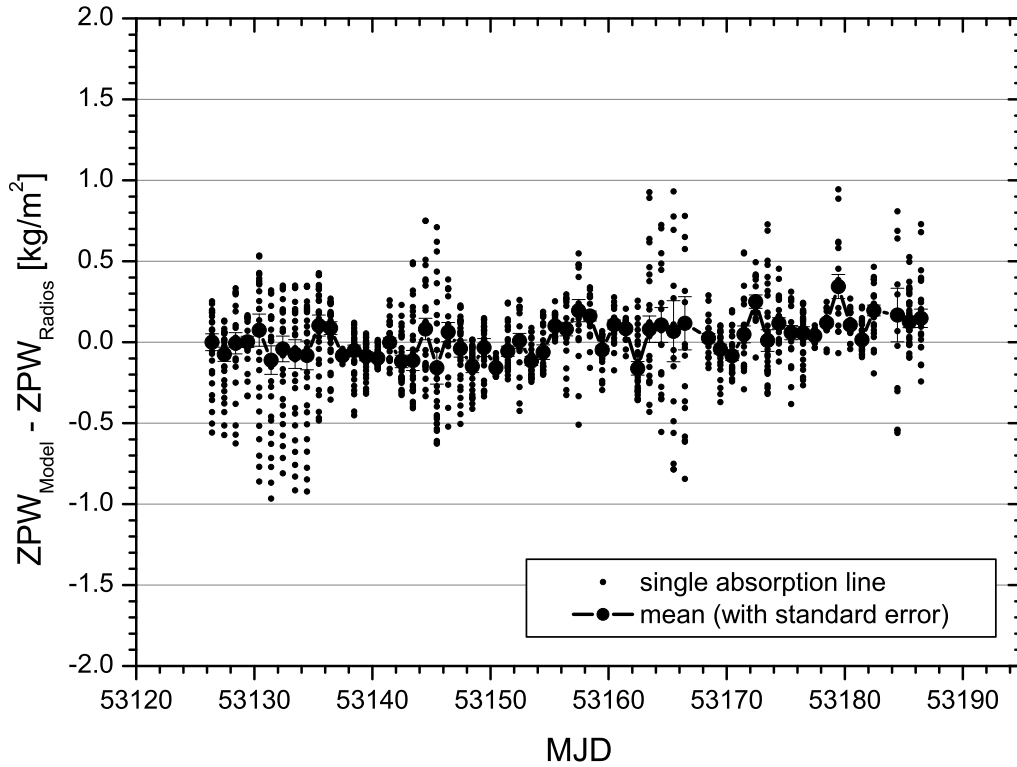


Figure 8.13: Difference of the zenithal PW caused by the uncertainty of the meteorological model used to retrieve the PW from 31 single  $H_2O$  absorption lines. The “true” ZPW was determined with the vertical profiles of temperature, air pressure and humidity measured by 59 radio soundings in May and June 2004 at Payerne. The influence of deviations between the model and the real atmospheric conditions on the ZPW retrievals is small and does not exceed  $0.3 \text{ kg/m}^2$  if the retrievals of all 31 absorption lines are averaged (large circles with standard errors). The standard deviation of the mean ZPW difference is  $\pm 0.3 \text{ kg/m}^2$ .

### 8.5.7 Conclusions

In general, the use of numerous absorption lines increases the accuracy of the water vapor abundance retrieved from GEMOSS spectra significantly. The error of the PW due to the noise of the CCD, stray light and apparatus function is determined to  $0.2 \text{ kg/m}^2$  and can be regarded as small. The deviations of the meteorological model from the real atmospheric conditions cause an error of about  $0.1 \text{ kg/m}^2$  which shows a relative high insensibility of the estimated total amount of  $H_2O$  molecules concerning their vertical distribution in Earth's atmosphere. The influence of an inaccurate line strength parameter on the PW retrieval varies between  $0.2 \text{ kg/m}^2$  and  $0.6 \text{ kg/m}^2$  if a single absorption line is used. In the case of averaging the retrievals of numerous absorption lines the mean error decreases down to  $0.1 \text{ kg/m}^2$ . A systematic under- or over-estimation of the line strength parameters as published by ESA, which would not be eliminated by the averaging procedure, was not detected in the comparison campaign at Payerne (section 10.3). Considering further error sources like reflections of the solar radiation in clouds or low signal to noise ratio at the edges of a diffraction order, the accuracy of PW retrieved from GEMOSS spectra can be quantified to approximately  $0.5 \text{ kg/m}^2$ . This high accuracy can only be achieved by taking as many appropriate  $H_2O$  absorption lines into account as possible whose line strength parameters are well determined.

# 9 Improvement of absorption line strength parameter

## 9.1 Motivation

As discussed in section 6.3 the strength of an absorption line relates the measured radiation intensity to the absorber abundance. In general, no other instrumentation is necessary for calibration purposes. Since the accuracy of the line strength has a large impact on the accuracy of the determined amount of tropospheric  $H_2O$  molecules, a precise line strength is required.

As mentioned in sections 6.5 and 6.6 the spectral line parameters are usually determined in laboratories by measuring a light beam which was multiply reflected in long-path absorption cells. Within the absorption cells the temperature, pressure and density of the absorbing species are controlled by sensors. Since the length of the absorption path through the cells is limited to several hundred meters, the amount of absorption due to weak transitions is not strong enough to determine the line parameters reliably. The absorption signal can be amplified by increasing the density of the absorbing gas but this will result in a stronger collision broadening and difficulties in separating the individual lines.

As a consequence of these problems, ground-based solar spectra measured by GEMOSS are utilized to determine and validate the water line strength parameters in controlled situations when the PW is well known. The absorption cell is replaced by the atmosphere which provides an extreme long absorption path compared to those of the cells. In-situ measurements by water vapor radiometers (WVR) and radio soundings are used to observe PW as well as the vertical distribution of the temperature, pressure and water vapor at a certain point of time. Although this procedure can be regarded as an external calibration by radiosondes, the method of solar spectrometry remains to be inherently independent. The atmospheric solar spectrometry is only utilized to determine physical parameters which are widely used in atmospheric science. In the future, Laser Absorption Spectroscopy (LAS) with improved resolution, sensitivity and signal-to-noise ratio will potentially be able to detect and measure low concentrations of  $H_2O$  molecules and to assess absorption parameters of weak transitions with high accuracy. Nowadays, the improvement and validation of the absorption line parameters can be realized by means of ground-

based spectrometers and radio soundings. As described in the next sections, this approach was applied to the GEMOSS measurements when the atmospheric conditions were simultaneously acquired by radiosondes and WVR during the **comparison** campaign at **Payerne** (COMPA).

## 9.2 Strategy

In a first step, the measurements of GEMOSS, microwave radiometer (WVR), GPS and radiosondes acquired during COMPA were processed. The results are presented in section 10.3.2. In the second step, 90 spectra of GEMOSS were selected corresponding the following selection criteria:

- Validation of GEMOSS measurements by radio soundings and WVR
- Large range of zenithal precipitable water vapor
- Suitable weather conditions for accurate comparison
- Temporal independent observations

For 15 different points of time 90 spectra (six for each) are selected for the analysis of the line strength parameters of 69 selected  $H_2O$  absorption lines. The corresponding 15 ZPW's were calculated from the solar spectra by averaging the retrievals from the 69 absorption lines. The obtained mean ZPW's were independently validated by WVR and radiosondes. The six spectra measured at the same point of time (within a few minutes) allow six fits of the line strength parameter of a single absorption line. Applying this procedure to all 15 points of time, 90 fitted line strength parameters are retrieved for each absorption line which are finally averaged to one mean parameter per absorption line. The least-squares algorithm is described in detail in the following section.

## 9.3 Fit algorithm

The least-squares algorithm used to fit the absorption line strength parameter  $S(T_{ref})$  is similar to the algorithm used to retrieve the integrated water vapor content (section 8.4). A synthetic absorption spectrum is simulated which has to fit the spectrum measured by GEMOSS. In order to realize the least-squares adjustment, the line strength parameter used to simulate the synthetic spectrum is modified until both spectra match each other and the improvement  $\delta S(T_{ref})$  falls below  $1 \cdot 10^{-32} \text{ cm}^{-1}$ . The water vapor content, introduced as a constant into the algorithm, was determined from the solar spectrum by averaging the retrievals of numerous water vapor absorption lines. It was validated independently by comparing with the

measurements of the microwave radiometer and radiosondes. The mean offset between the ZPW measured by GEMOSS and WVR/radiosondes was determined with  $0.04 \pm 0.03 \text{ kg/m}^2$ . This very small difference is maybe caused by the stratospheric water vapor content which was measured by GEMOSS but not by the radiosondes. The sondes as used in Payerne provided reliable data only until 12 km height. Since the ZPW's of GEMOSS and WVR/radiosondes agree very well, the ZPW averaged from the retrievals of 69 absorption lines is regarded as verified and is introduced into the fit algorithm as described above. The matrices of the least-squares algorithm

$$\mathbf{v} = \mathbf{A} \cdot \mathbf{x} - \mathbf{l} \quad (9.1)$$

are composed as follows:

$$\mathbf{v} = \begin{pmatrix} \delta I'_{digit}(\lambda_0) \\ \delta I'_{digit}(\lambda_1) \\ \delta I'_{digit}(\lambda_2) \\ \vdots \\ \delta I'_{digit}(\lambda_n) \end{pmatrix} \quad \mathbf{A} = \begin{pmatrix} \partial I'_{digit}(\lambda_0)/\partial S(T_{ref}) \\ \partial I'_{digit}(\lambda_1)/\partial S(T_{ref}) \\ \partial I'_{digit}(\lambda_2)/\partial S(T_{ref}) \\ \vdots \\ \partial I'_{digit}(\lambda_n)/\partial S(T_{ref}) \end{pmatrix}$$

$$\mathbf{x} = ( \delta S(T_{ref}) ) \quad \mathbf{l} = \begin{pmatrix} I'_S(\lambda_0) - I'_{digit}(\lambda_0) \\ I'_S(\lambda_1) - I'_{digit}(\lambda_1) \\ I'_S(\lambda_2) - I'_{digit}(\lambda_2) \\ \vdots \\ I'_S(\lambda_n) - I'_{digit}(\lambda_n) \end{pmatrix}$$

where  $\mathbf{v}$  denotes the improvements of the intensities,  $\mathbf{A}$  the partial derivations,  $\mathbf{x}$  the improvement of  $S(T_{ref})$  and  $\mathbf{l}$  the differences of the simulated and measured intensities  $I'_S(\lambda)$  and  $I'_{digit}(\lambda)$ . According to Eqs. 8.14 and 8.15 the derivations  $\partial I'_{digit}(\lambda_i)/\partial S(T_{ref})$  are calculated with:

$$\frac{\partial I'(\lambda_i)}{\partial S(T_{ref})} = I'(\lambda_i) \cdot \left[ - \int_{h=0}^{stropo} \frac{\tau_l(\nu, s)}{S(T_{ref})} ds \right] \quad (9.2)$$

If  $n$  measured spectra are analyzed by applying Eq. 9.1, the fitted line strength parameters  $S_i(T_{ref})$  of spectra  $i$  are averaged:

$$\overline{S(T_{ref})} = \frac{\sum_{i=1}^n S_i(T_{ref})}{n} \quad (9.3)$$

The results of fitting the line strength of 69 absorption lines using the data set of COMPA are presented in the following section.

## 9.4 Results

The line strength parameters of ESA (section 6.6) are introduced into the fit as start values. Fig. 9.1 shows a solar spectrum between 732.5 nm and 733.7 nm measured by GEMOSS. The absorption lines, whose line strength parameters were fitted, are indicated. The improvements of the absorption line intensities are revealed by comparing with the corresponding spectrum simulated with the parameters of ESA. In order to validate the quality of the ESA parameters, the slant precipitable water vapor (PW) was retrieved from the 90 selected spectra using each of the 69 absorption lines separately. Fig. 9.2 shows the PW determined by WVR, radiosonde soundings and GEMOSS if the parameters of ESA are used to simulate the absorption line intensities.

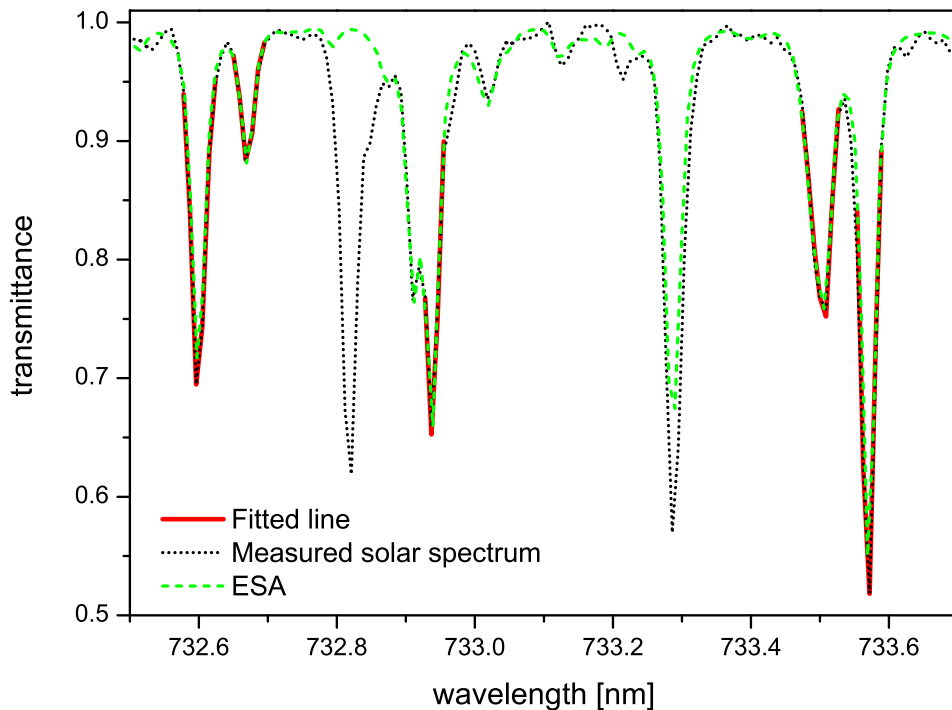


Figure 9.1: Fit of line strength parameters for selected  $H_2O$  absorption lines between 732.5 nm and 733.7 nm. The line strength parameter of the line near 733.29 nm can not be fitted because this line is superposed by a Fraunhofer line. The third spectrum (ESA) was simulated with the line strength parameters as published by ESA. The strong line measured near 732.8 nm, which does not exist in the ESA-spectrum, is a Fraunhofer line.

The PW retrievals of the 69 absorption lines exhibit a large scattering between 8 and 15  $kg/m^2$  around the mean when ESA line strength parameters are used. The standard deviation of the different mean PW's (average of all lines) varies between  $\pm 1.2$  and  $\pm 2.7 kg/m^2$ . The corresponding standard error of the mean PW's is  $\pm 0.1 kg/m^2$ . The PW offset of each single absorption line with respect to the mean PW is shown in Fig. 9.3. The use of ESA parameters cause large deviations from the mean PW of up to 4  $kg/m^2$ . A fit of the line strength parameters as examined in the previous section should reduce those deviations. In order to exclude instrumental effects or systematic errors in the analysis, the dependence of the PW offset of each single absorption line on its transmittance and position on the CCD sensor is reviewed. Figs. 9.4 and 9.5 show that the PW offsets as determined with ESA line strength parameters are correlated neither to the individual line transmittance nor the position of the absorption line on the CCD. The PW offsets with respect to transmittance and CCD position are randomly distributed and do not exhibit any significant systematic dependence.

The results of the line strength fitting are presented for the 69 selected  $H_2O$  absorption lines in Tabs. 9.1 and 9.2.

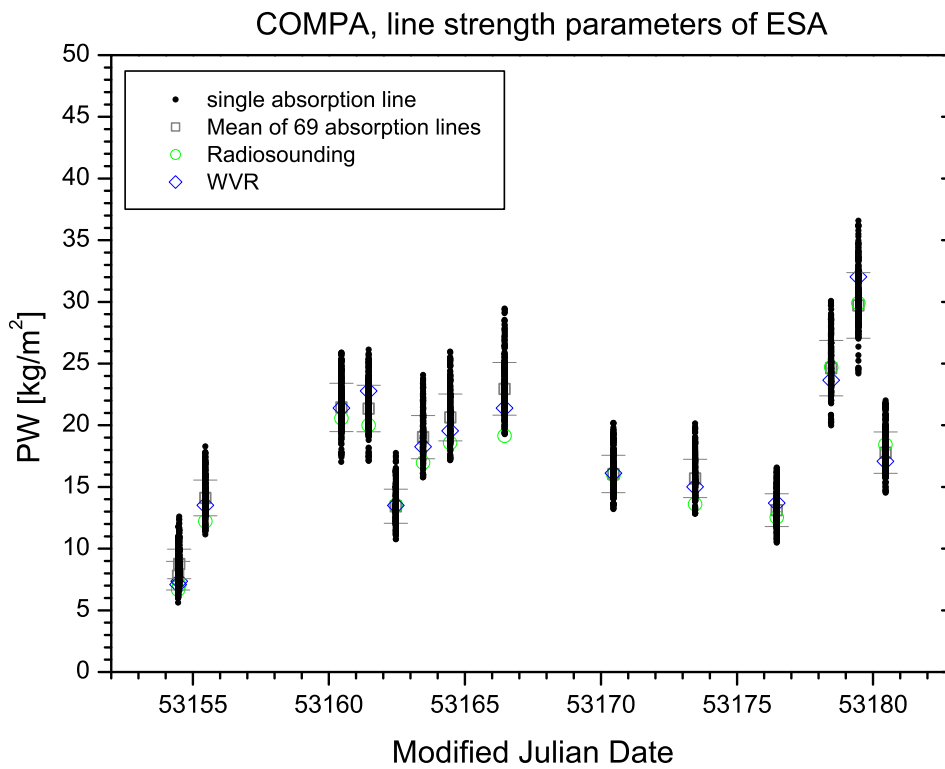


Figure 9.2: Precipitable water vapor (PW) determined by the analysis of 69 single absorption lines measured with 90 solar spectra at 15 different points of time during the “Comparison Campaign at Payerne” (COMPA) (black dots). The mean PW of all absorption lines (square with standard deviation) was validated by the measurements of the water vapor radiometer (diamond) and radiosonde soundings (circle).

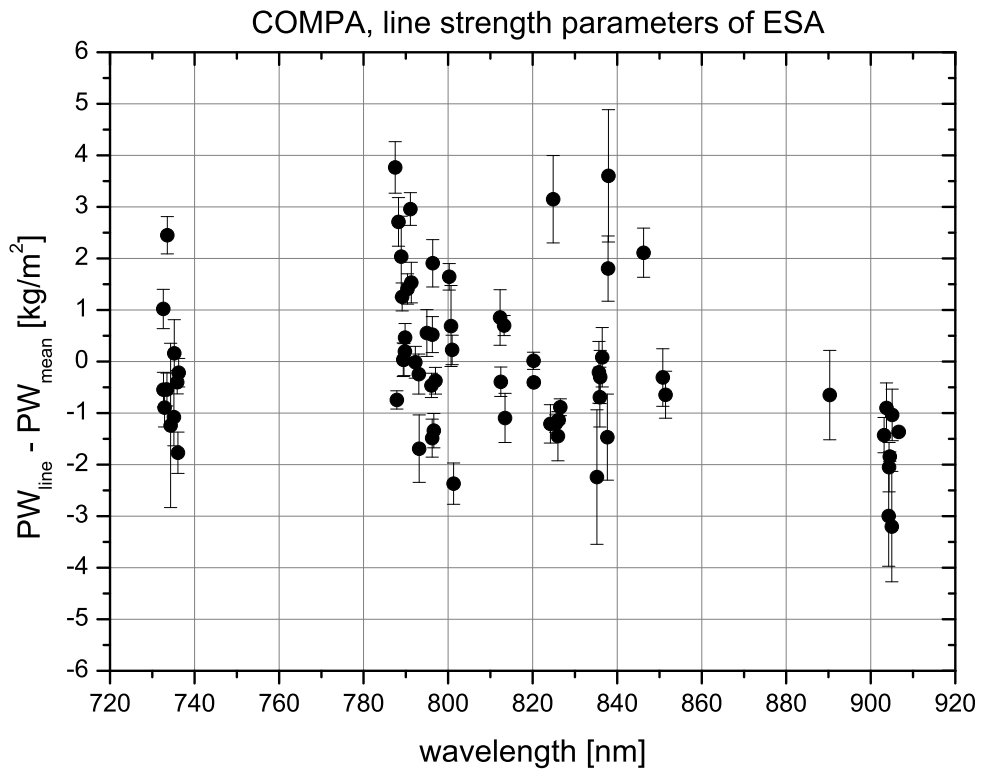


Figure 9.3: PW offset of single absorption lines with respect to the mean of all 69 lines if ESA parameters are used. The lines around 735 nm and 905 nm exhibit systematic smaller PW's. The absorption lines between 780 nm and 850 nm show a larger scattering and deviations of up to  $4 kg/m^2$ . The standard deviation of the mean PW offset is determined to  $\pm 1.52 kg/m^2$ .

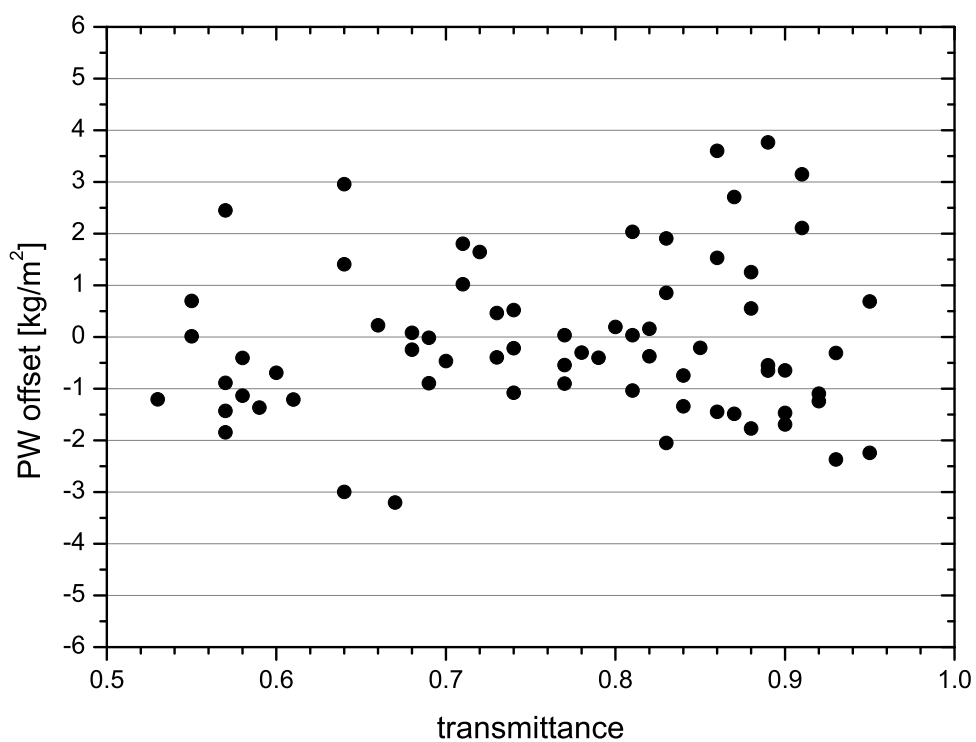


Figure 9.4: Dependence of the PW offsets determined with ESA line parameters on the individual line transmittance for the 90 selected solar spectra. The graph reveals that the PW offsets are scattered randomly and a correlation to the line transmittance does not exist.

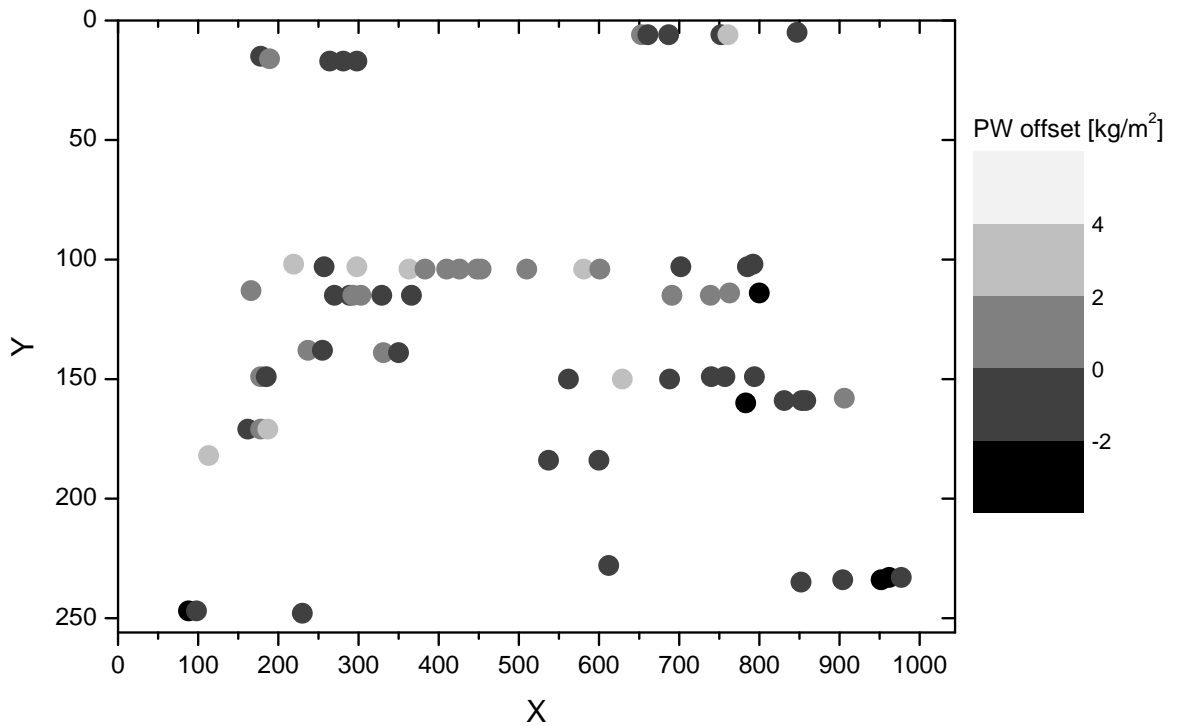


Figure 9.5: Dependence of the PW offsets determined with ESA line parameters on the positions of the absorption lines (X,Y) on the CCD sensor. A significant correlation between the PW offset and the CCD position cannot be observed. The PW offsets are distributed randomly.

Using the fitted parameters, the 90 spectra were processed again in order to verify the reduction of the PW offsets due to the improved line strength parameters. Figs. 9.6 and 9.7 show the results of the re-calculation. The mean standard deviation of PW averaged from all 69 lines decreases from  $\pm 1.7 \text{ kg/m}^2$  down to  $\pm 0.6 \text{ kg/m}^2$ . The standard error of the mean PW's is also reduced from  $\pm 0.1 \text{ kg/m}^2$  to  $\pm 0.03 \text{ kg/m}^2$ . The PW offsets are minimized and do not exceed  $0.4 \text{ kg/m}^2$ . The standard deviation of the mean PW offset is decreased from  $\pm 1.52 \text{ kg/m}^2$  to  $\pm 0.14 \text{ kg/m}^2$ . In order to validate the good results, other 90 spectra of the COMPA dataset were selected and processed with the fitted line strengths in the same way. Figs. 9.8 and 9.9 show the obtained PW's and the corresponding offsets for each of the 69 absorption lines. The mean standard deviation of PW averaged from all lines is again smaller ( $\pm 0.7 \text{ kg/m}^2$ ) compared to those calculated with the ESA line strengths. The PW offsets in Fig. 9.9 became larger ( $\sigma$  of the mean PW offset:  $\pm 0.30 \text{ kg/m}^2$ ) but show again a large improvement compared to the PW retrieved with ESA line strengths. It can be pointed out that the corrections of the line strength parameters as found by fitting simulated to measured spectra yield an significant increase of the PW accuracy.

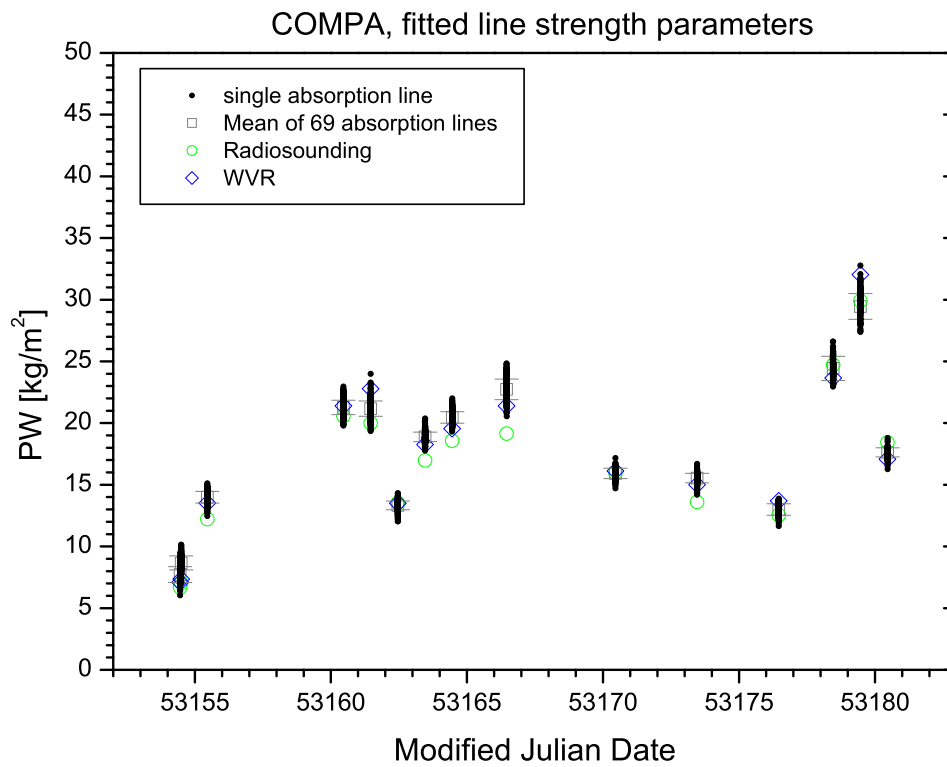


Figure 9.6: PW retrievals from 69 single absorption lines using the fitted line strength parameters (dots). The mean standard deviations of the averaged PW's is significantly reduced ( $\pm 0.6 \text{ kg/m}^2$ ).

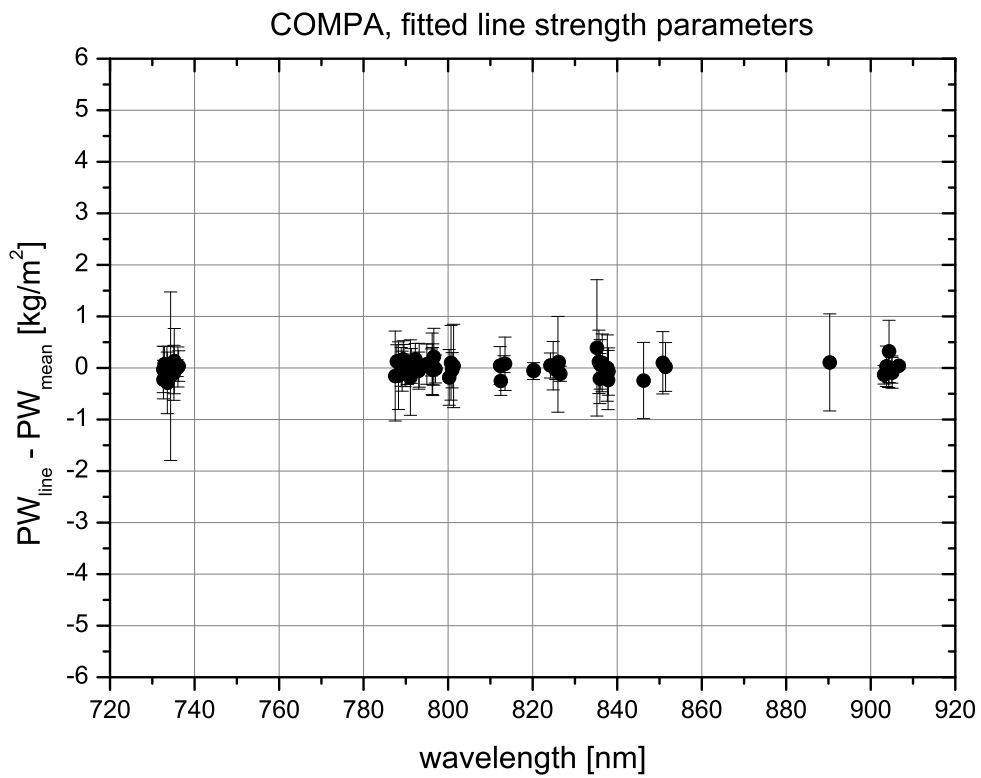


Figure 9.7: PW offsets of single absorption lines with respect to the mean of all 69 lines if the fitted line strength parameters are used for PW retrieval. The PW offsets are significantly reduced compared to those obtained with ESA parameters.

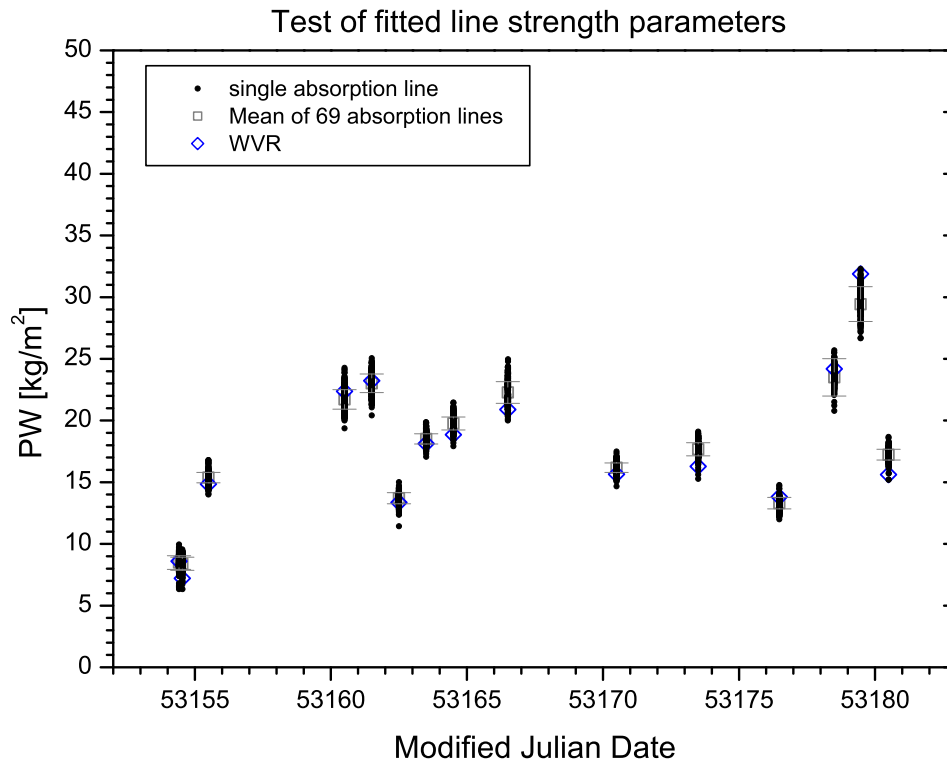


Figure 9.8: Selection of a second dataset of 90 solar spectra acquired during COMPA in order to validate the obtained line strength corrections. The mean standard deviation of the averaged PW's is again significantly reduced ( $\pm 0.7 \text{ kg/m}^2$ ) compared to the PW's retrieved with the uncorrected ESA parameters ( $\pm 1.7 \text{ kg/m}^2$ ).

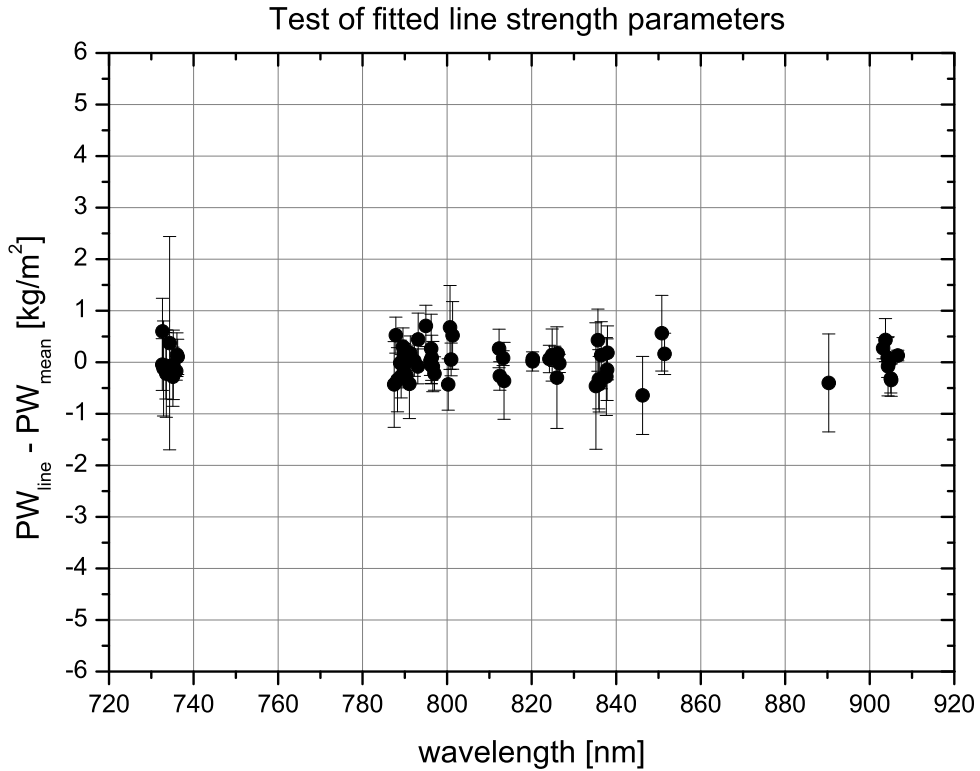


Figure 9.9: PW offsets of single absorption lines with respect to the mean of all 69 lines. The processing of the 90 spectra of the second dataset verifies the reduction of the PW offsets if the ESA parameters are corrected. The standard deviation  $\sigma$  of the mean PW offset is slightly larger ( $\pm 0.30 \text{ kg/m}^2$ ) compared to the first dataset used to fit the line strengths ( $\pm 0.14 \text{ kg/m}^2$ ) but still significantly smaller than the  $\sigma$  for uncorrected line strengths ( $\pm 1.52 \text{ kg/m}^2$ ).

$\lambda_0$ [nm]	fitted $S(T_{ref})$ [ $\frac{10^{-25}cm^{-1}}{molecule \cdot cm^{-2}}$ ]	$\sigma_{S(T_{ref})}$ [ $\frac{10^{-25}cm^{-1}}{molecule \cdot cm^{-2}}$ ]	ESA $S(T_{ref})$ [ $\frac{10^{-25}cm^{-1}}{molecule \cdot cm^{-2}}$ ]	Difference [ $\frac{10^{-25}cm^{-1}}{molecule \cdot cm^{-2}}$ ]
732.599284	32.34	1.15	30.0	-2.34
732.670108	10.55	0.22	10.6	0.05
732.938448	36.40	1.18	38.5	2.10
733.508311	21.44	0.74	22.1	0.66
733.570803	77.67	3.02	64.6	-13.07
734.337114	6.71	0.26	7.0	0.29
735.123753	10.41	1.31	12.9	2.49
735.211677	19.35	0.56	18.9	-0.45
735.912863	20.19	0.40	20.3	0.11
736.088010	9.88	0.17	10.7	0.82
736.237682	27.65	0.67	27.5	-0.15
787.496198	10.24	0.63	8.23	-2.01
787.872431	13.40	0.39	13.9	0.50
788.299119	4.77	0.67	2.51	-2.26
788.927746	16.37	0.42	14.5	-1.87
789.150008	11.01	0.35	10.1	-0.91
789.406032	17.73	0.49	17.5	-0.23
789.567632	22.19	0.61	21.9	-0.29
789.767800	19.64	0.47	19.1	-0.54
789.820153	29.19	0.74	27.8	-1.39
790.393201	36.20	1.17	32.0	-4.20
791.092945	40.05	2.16	33.5	-6.55
791.286020	13.14	0.41	11.9	-1.24
792.283920	34.88	0.75	34.6	-0.28
793.079720	33.83	1.07	33.5	-0.33
793.153408	8.26	0.22	9.05	0.79
794.992185	10.42	0.27	9.95	-0.47
796.067478	30.32	0.69	30.7	0.38
796.245676	9.85	0.28	10.6	0.75
796.292234	24.72	0.80	23.5	-1.22
796.380419	13.91	0.54	12.4	-1.51
796.653742	13.54	0.49	14.5	0.96
797.030469	15.85	0.42	15.9	0.05
800.249319	32.32	1.35	28.8	-3.52
800.717520	4.00	0.12	3.83	-0.17
800.969384	32.39	1.64	30.7	-1.69

Table 9.1: Line strength parameters  $S(T_{ref} = 296K)$  determined by applying the fit algorithm (Eq. 9.1) to the GEMOSS measurements and as published by ESA.

$\lambda_0$ [nm]	fitted $S(T_{ref})$ [ $\frac{10^{-25}cm^{-1}}{molecule \cdot cm^{-2}}$ ]	$\sigma_{S(T_{ref})}$ [ $\frac{10^{-25}cm^{-1}}{molecule \cdot cm^{-2}}$ ]	ESA $S(T_{ref})$ [ $\frac{10^{-25}cm^{-1}}{molecule \cdot cm^{-2}}$ ]	Difference [ $\frac{10^{-25}cm^{-1}}{molecule \cdot cm^{-2}}$ ]
801.310450	5.69	0.19	6.39	0.70
812.289155	19.41	0.39	18.3	-1.11
812.505698	10.12	1.41	8.83	-1.29
813.268746	61.86	1.41	57.1	-4.76
813.462591	5.64	0.19	5.91	0.27
820.224505	57.56	1.49	56.0	-1.56
820.294513	109.80	1.55	113.0	3.2
824.218493	46.3	1.21	49.2	2.9
824.888013	9.26	0.22	7.91	-1.35
825.499147	67.06	2.04	72.4	5.34
826.012877	10.00	0.52	10.8	0.8
826.195438	104.20	1.31	120.0	15.8
826.501711	3.66	0.25	3.34	-0.32
826.571291	84.53	2.55	88.8	4.27
826.722242	6.05	0.23	3.91	-2.14
834.625998	4.48	0.39	4.65	0.17
834.961717	9.21	1.20	5.93	-3.28
835.226723	2.56	0.17	2.89	0.33
835.701433	14.00	0.43	14.0	0.00
835.932243	56.98	1.88	57.7	0.72
835.972953	19.68	0.58	19.7	0.02
836.182905	9.53	0.21	9.5	-0.03
836.459804	41.81	1.28	41	-0.81
836.884303	6.57	0.43	5.29	-1.28
837.684490	7.99	0.37	8.61	0.62
837.866730	31.69	1.13	27.4	-4.29
837.945504	14.34	0.36	11.7	-2.64
838.647317	9.81	0.34	10.8	0.99
846.266472	3.01	0.67	1.3	-1.71
850.818483	5.68	0.13	5.69	0.01
851.463619	7.43	0.21	7.56	0.13
890.307128	8.41	0.40	8.61	0.20
903.186704	53.87	1.50	58.1	4.23
903.738591	23.28	0.60	24.1	0.82
904.255968	42.08	1.24	50.0	7.92
904.360225	17.43	0.78	19.6	2.17
904.529498	105.00	1.25	133.0	28.0
904.988956	37.46	0.83	44.6	7.14
905.101927	17.79	0.51	18.4	0.61
906.653141	75.07	1.34	94.0	18.93

Table 9.2: Continuation of Tab. 9.1.

# 10 Campaigns and results

## 10.1 Jason Microwave Radiometer calibration campaigns

### 10.1.1 Jason

Jason is an oceanographic altimetry satellite whose mission is to measure the level of the oceans in order to detect climate perturbations. After the first altimeter satellites Seasat (1978), Geosat (1985), ERS (1991) and Topex-Poseidon (1992) Jason was launched in 2001. It is equipped with various instruments taking 20 measurements per second and circles around the Earth at an altitude of 1330 km with a speed of 7 km per second. Fig. 10.1 shows the on-board instruments of Jason: radar altimeter Poseidon-2, Jason-1 Microwave Radiometer (JMR), Turbo Rogue Space Receiver (TRSR), Laser Retroreflector Array (LRA), Doppler Orbitography and Radio positioning Integrated by Satellite system (Doris) [Aviso (2004)].

Poseidon-2 is the main instrument on the satellite. Derived from the experimental Poseidon-1 altimeter on Topex/Poseidon, it is a compact, low-power, low-mass instrument offering a high degree of reliability. Poseidon-2 is a radar altimeter that emits pulses at two frequencies (13.6 and 5.3 GHz, the second frequency is used to determine electron content in the atmosphere) and analyses the return signal reflected by the surface. The signal round-trip time is estimated very precisely to calculate the range, after applying corrections. A correction of the propagation time of the altimeter satellite signal has to be applied due to atmospheric water vapor to avoid errors in the determined sea surface heights.

Therefore, Jason carries a Microwave Radiometer (JMR), supplied by NASA, which measures the radiation from the surface at three frequencies (18, 21 and 37 GHz). Measurements acquired at each frequency are combined to determine atmospheric water vapor and liquid water content. Once the water content is known, the correction of the radar signal due to path delay can be determined and applied.

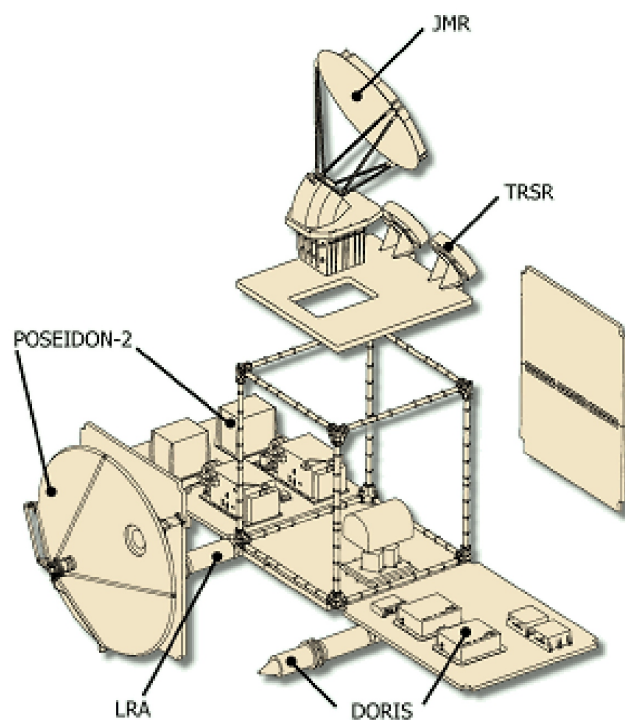


Figure 10.1: On-board instruments of Jason altimeter satellite: radar altimeter Poseidon-2, Jason-1 Microwave Radiometer (JMR), Turbo Rogue Space Receiver (TRSR), Laser Retroreflector Array (LRA), Doppler Orbitography and Radio-positioning Integrated by Satellite system (Doris) [Aviso (2004)].

### 10.1.2 Campaigns

GEMOSS has been deployed during two campaigns in Greece with the aim of calibrating and validating the on-board radiometer of the altimeter satellite Jason (JMR). In January 2003, GEMOSS was installed at Rethimnon on the island of Crete where Jason followed an ascending path from the island of Gavdos on January 11th.

The second campaign was carried out for 13 days in September 2003 at Fiskardo on the island of Kefalonia where Jason flew over on September 20th at 7:07:29 am (UTC). Next to GEMOSS a ground-based water vapor radiometer (WVR) was continuously operated, and radiosondes (Zeemet VIZ, Mark II Microsonde) were launched on two days for calibration purpose. The tracks of Jason used for the JMR calibration and both installation sites of GEMOSS and WVR are shown in Fig. 10.2.

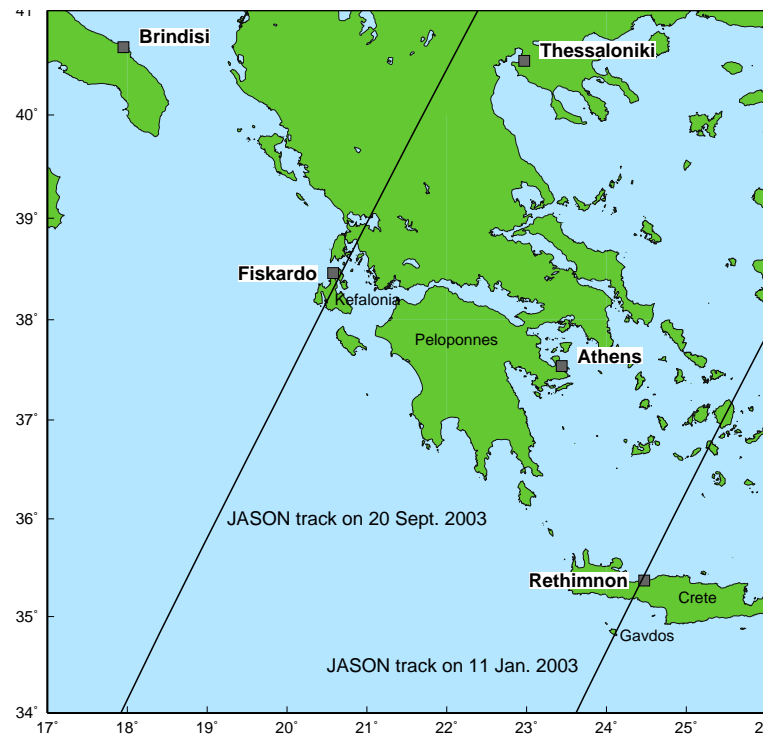


Figure 10.2: Tracks of the Jason altimeter satellite in Greece on January 11<sup>th</sup> and September 20<sup>th</sup> 2003. During the overflights GEMOSS was operated at Rethimnon on the island of Crete and at Fiskardo on the island of Kefalonia (Greece), respectively. In addition, a ground-based water vapor radiometer and radiosondes were deployed at Fiskardo.

### 10.1.3 Results

On January 11<sup>th</sup> 2003 GEMOSS was installed on the roof of the *Institute for Mediterranean Studies* in the center of Rethimnon. The acquired time series of zenithal wet path delays is shown in Fig. 10.3. The time of the Jason overflight is indicated by the vertical gray bar. The corresponding time series measured by JMR is given in Fig. 10.4. During the overflight at 10:09:22 am (UTC) JMR measured a  $\Delta L_w^z$  of  $71.6 \pm 7.4$  mm. This agrees very well with the results of GEMOSS:  $70.4 \pm 2$  mm. The GEMOSS retrievals result from averaging the zenith delays of 34 selected absorption lines between 732.40 nm and 890.10 nm which yields a high precision of 2 mm.

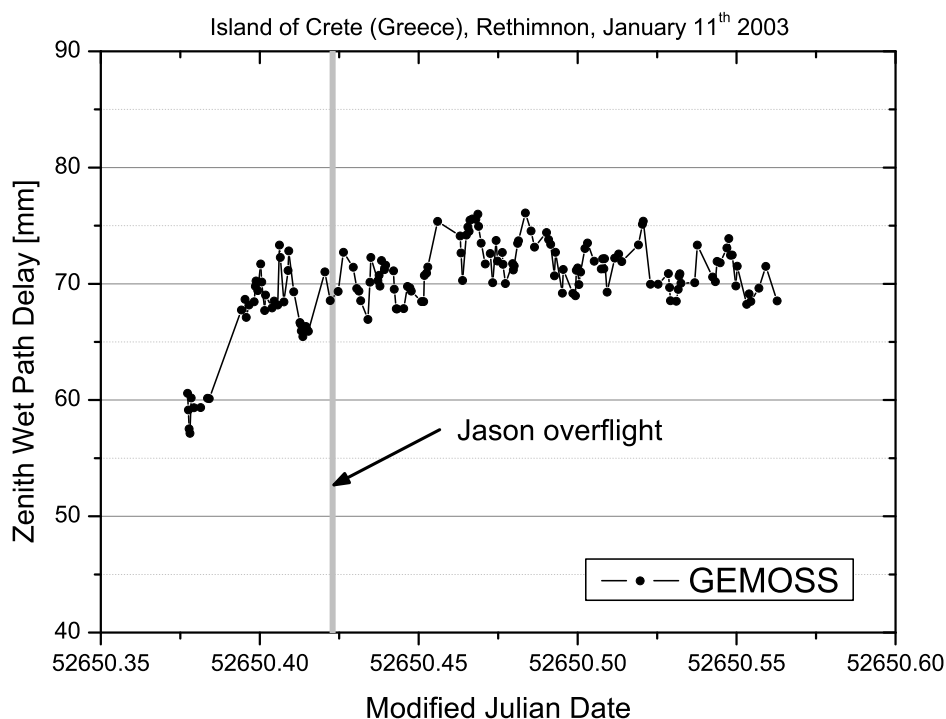


Figure 10.3: Time series of zenith wet path delay measured by GEMOSS on January 11<sup>th</sup> 2003 at Rethimnon (Crete, Greece). The time of the Jason overflight is indicated by the vertical gray bar.

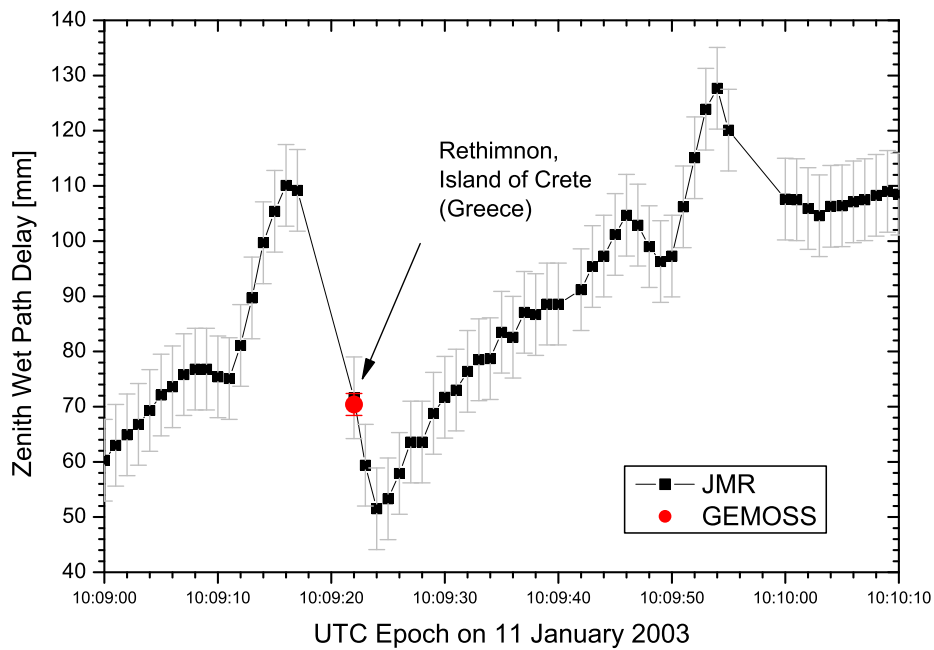


Figure 10.4: Time series of zenith wet path delay measured by the on-board microwave radiometer of Jason (JMR) along the track over Rethimnon. The retrieval of JMR at 10:09:22 am (UTC) agrees with that of GEMOSS within a few millimeters.

	$c_{eff}$ [cm/K]	$c_1$ [ $10^{-3}/hPa$ ]	$c_2$ [ $10^{-3}/K$ ]	$c_3$ [ $10^{-4}/K$ ]
Athens	$0.2866 \pm 0.0005$	$0.45 \pm 0.16$	$-1.4 \pm 0.25$	$0.28 \pm 0.34$
Brindisi	$0.2860 \pm 0.0003$	$0.13 \pm 0.062$	$-0.9 \pm 0.15$	$-0.28 \pm 0.23$
Thessaloniki	$0.2890 \pm 0.0006$	$0.25 \pm 0.13$	$-1.8 \pm 0.29$	$0.21 \pm 0.50$
Fiskardo	$0.2865 \pm 0.0016$	-	-	-
mean	$0.2870 \pm 0.0007$	$0.28 \pm 0.09$	$-1.4 \pm 0.26$	$0.07 \pm 0.18$

Table 10.1: Determination of the inversion coefficients needed to retrieve the wet path delay from microwave radiometer measurements by applying the “PTX”-algorithm (Eqs. 4.24 and 4.27). All four coefficients were computed for September 2003 from 212 radiosondes launched at Athens, Brindisi and Thessaloniki surrounding the WVR installation site at Fiskardo (Fig. 10.2). From the few radio soundings at Fiskardo only the seasonal-varying effective coefficient was computed.

During the second campaign at Fiskardo on the island of Kefalonia the water vapor radiometer and the telescope of GEMOSS were installed on the roof of the museum of the *Fiskardo’s Nautical and Environmental Club* (FNEC) (Fig. 10.5). The telescope was connected via an optical fiber to the spectrometer which was placed together with the computers inside the museum. In front of the museum radio soundings were carried out for calibration and validation purpose on two days (Fig. 10.6).

The inversion coefficients of the WVR retrieval algorithm (Eq. 4.27) were determined by analyzing data of 212 radiosondes launched at Athens, Brindisi and Thessaloniki in September 2003 [Elgered (1993), Johansson et al. (1993) and Bürki and Kahle (1995)]. In order to adjust and validate the most important effective coefficient  $c_{eff}$ , the radio soundings at Fiskardo are used to calculate  $c_{eff}$  for September 19<sup>th</sup> and 20<sup>th</sup>. The determined inversion coefficients are listed in Tab. 10.1.

Fig. 10.7 presents the entire  $\Delta L_w^z$  time series determined by GEMOSS, WVR and radiosondes during the campaign. Fig. 10.8 shows the two days September 19<sup>th</sup> and 20<sup>th</sup> when Jason flew over Fiskardo. The results of the radiosondes are well confirmed by GEMOSS measurements. The WVR measurements were smoothed by adjacent averaging with a 40 min time window. Considering the large variation of  $\Delta L_w^z$  between 50 and 220 mm the retrievals of GEMOSS and WVR exhibit a good agreement within 10 mm. During Jason overflight on September 20<sup>th</sup>  $\Delta L_w^z$  was determined to  $134.0 \pm 2$  mm (GEMOSS) and  $138.9 \pm 5$  mm (WVR), respectively. The corresponding zenith delay time series of JMR is shown in Fig. 10.9. When Jason flew over Fiskardo the on-board radiometer measured a  $\Delta L_w^z$  of  $132.4 \pm 7.4$  mm which agrees within a few millimeters with the results of GEMOSS and WVR. The results of both campaigns are listed in Tab. 10.2. The comparison between JMR, GEMOSS and WVR reveals an agreement at the few millimeters level. It can be pointed out that GEMOSS can be considered as an excellent altimeter calibration and validation system.



Figure 10.5: The telescope of GEMOSS fixed on the yellow tripod (left) and WVR (right) were installed on the museum of the *Fiskardo's Nautical and Environmental Club* (FNEC) at Fiskardo.

Zenith wet path delay [mm]		
System	Fiskardo	Rethimnon
JMR	132.4	71.6
GEMOSS	134.0	70.4
WVR	138.9	—
JMR - GEMOSS	-1.6	1.2
JMR - WVR	-6.5	—

Table 10.2: Results of the two JMR calibration campaigns. The comparison between the three different instruments reveals an agreement at the few millimeters level.



Figure 10.6: Radiosonde launch in front of the museum of FNEC in Fiskardo.

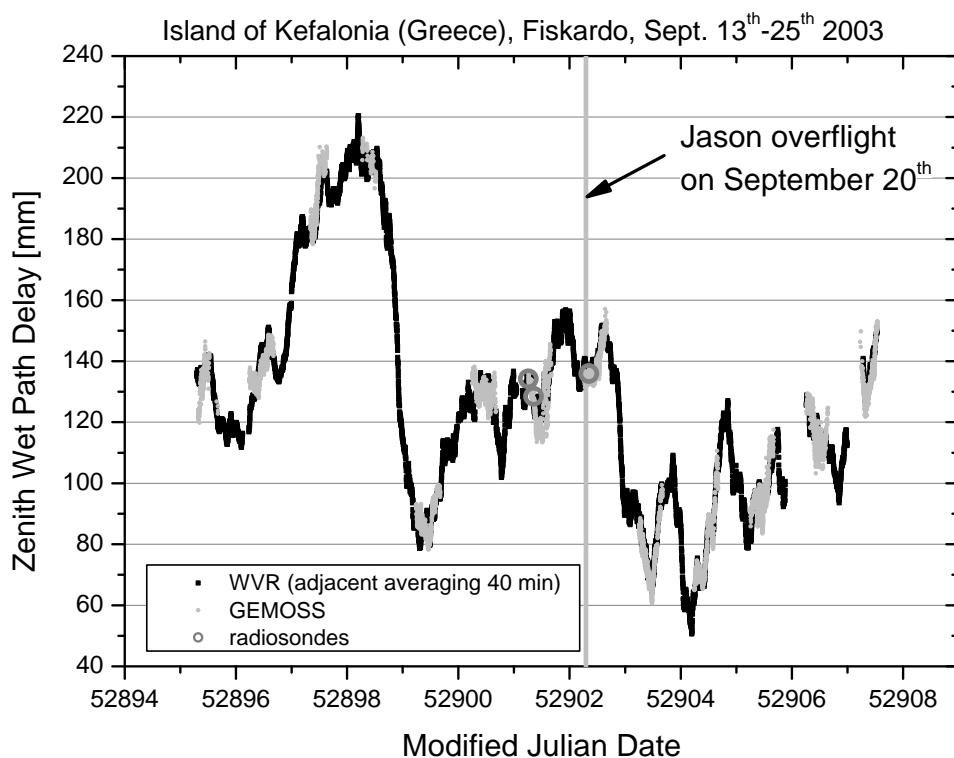


Figure 10.7: Time series of zenith wet path delay measured by GEMOSS, WVR and radiosondes during 13 day at Fiskardo in September 2003. The time of the Jason overflight is indicated by the vertical gray bar. The retrievals of the three different methods agree within 1 cm.

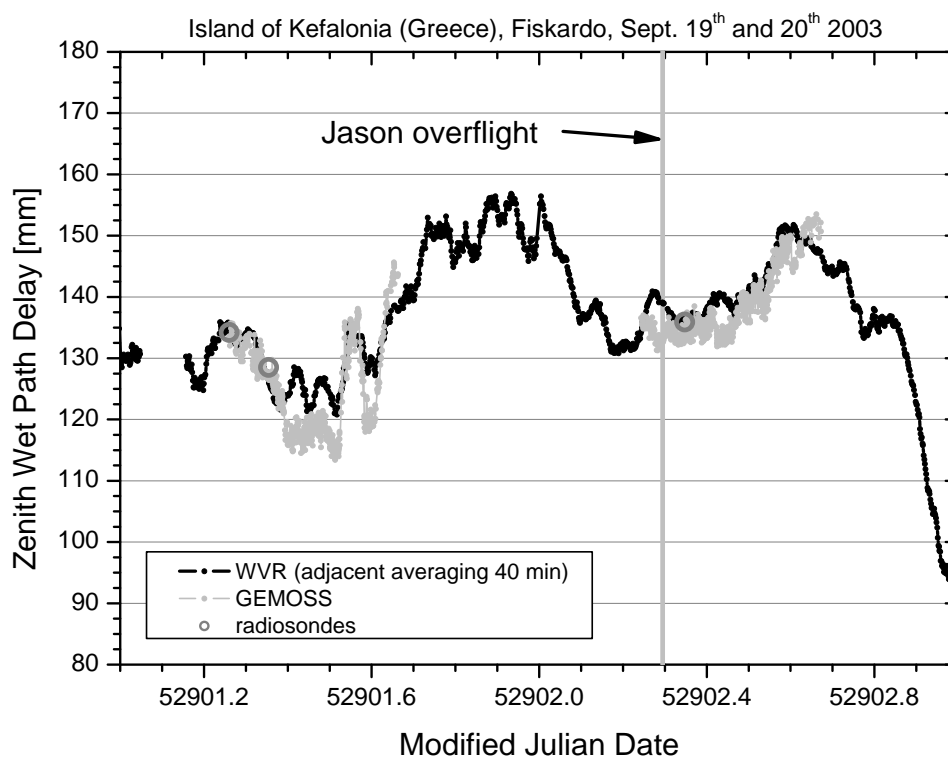


Figure 10.8: Time series of zenith wet path delay measured by GEMOSS, WVR and radiosondes on September 19<sup>th</sup> and 20<sup>th</sup> at Fiskardo. The altimeter satellite Jason flew over Fiskardo on September 20<sup>th</sup> at 07:07:29 am (UTC) (vertical gray bar).

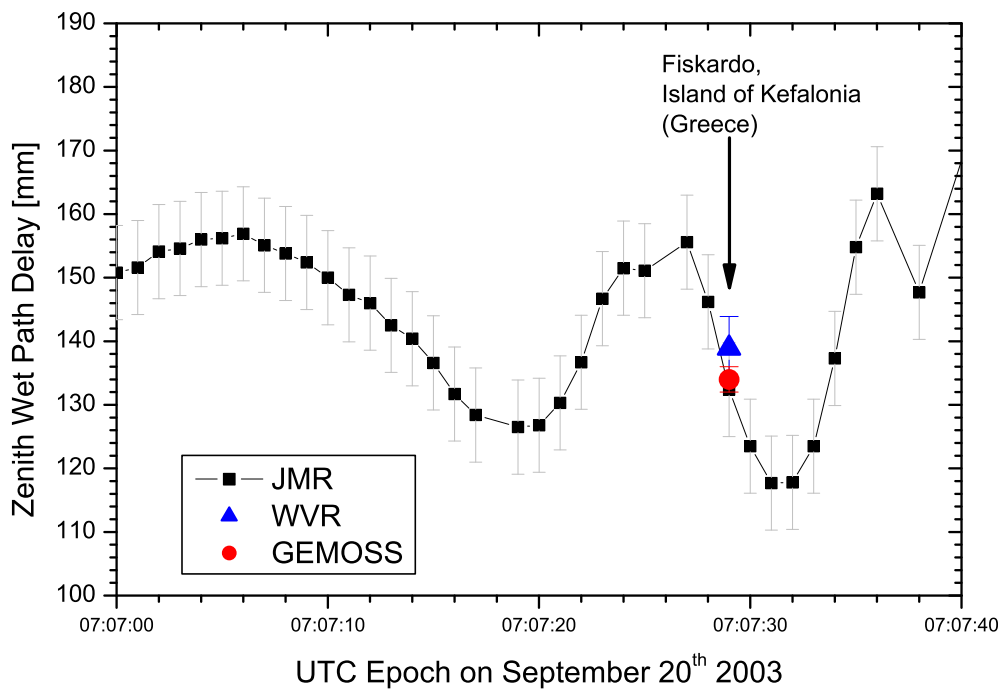


Figure 10.9: Time series of zenith wet path delay measured by JMR along the track which crossed over Fiskardo at 07:07:29 am (UTC). The measurement of JMR ( $132.4 \pm 7.4$  mm) agrees with those of GEMOSS ( $134.0 \pm 2$  mm) and WVR ( $138.9 \pm 5$  mm) within a few millimeters.



of ETH Honggerberg. The telescope of GEMOSS is installed 10 meters away from the GPS antenna on the same roof (Fig. 10.12).



Figure 10.11: GPS antenna of the AGNES station “ETHZ” on the top of the HPV building of ETH Honggerberg.



Figure 10.12: Sun-tracking telescope of GEMOSS installed next to the GPS station “ETHZ”. The glass dome protects the telescope against rain. The solar radiation is transmitted via an (blue) optical fiber into the spectrometer located inside the building.

## 10.2.2 Results

Figs. 10.13-10.16 show the zenith wet delay (ZWD) as measured by GEMOSS, estimated by GPS and calculated from ground meteorological data using the formula of Saastamoinen (Eq. 2.13). Short interpretations are given in the captions of the figures. A calculative comparison between GEMOSS and GPS is carried out in the following section.

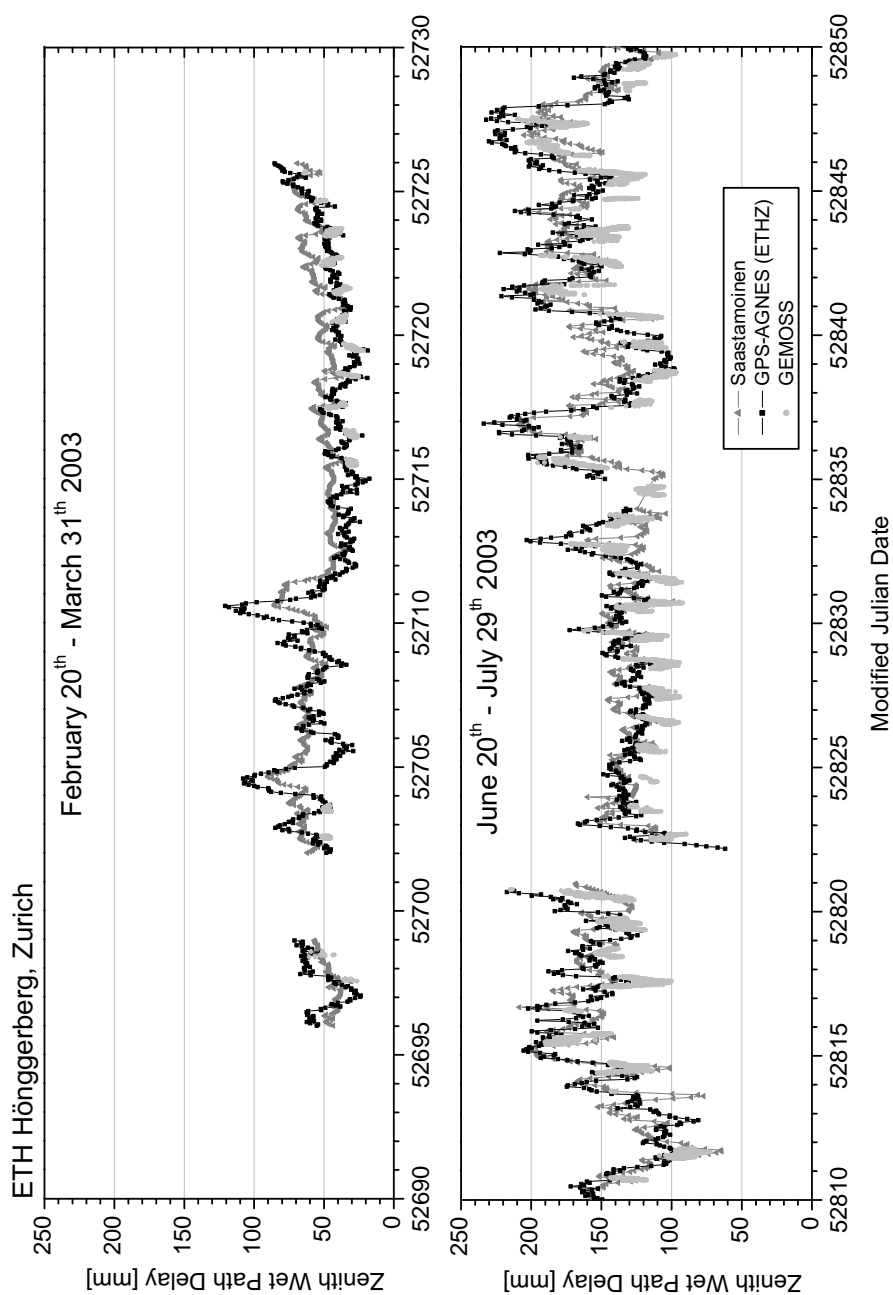


Figure 10.13: First part of the long-term series of zenith wet path delay (ZWD) measured by GEMOSS and estimated by GPS at ETH Hönggerberg (Zurich). The zenith wet delay was also calculated from ground meteorological data using the formula of Saastamoinen. In June and July GPS yields larger wet path delays than GEMOSS.

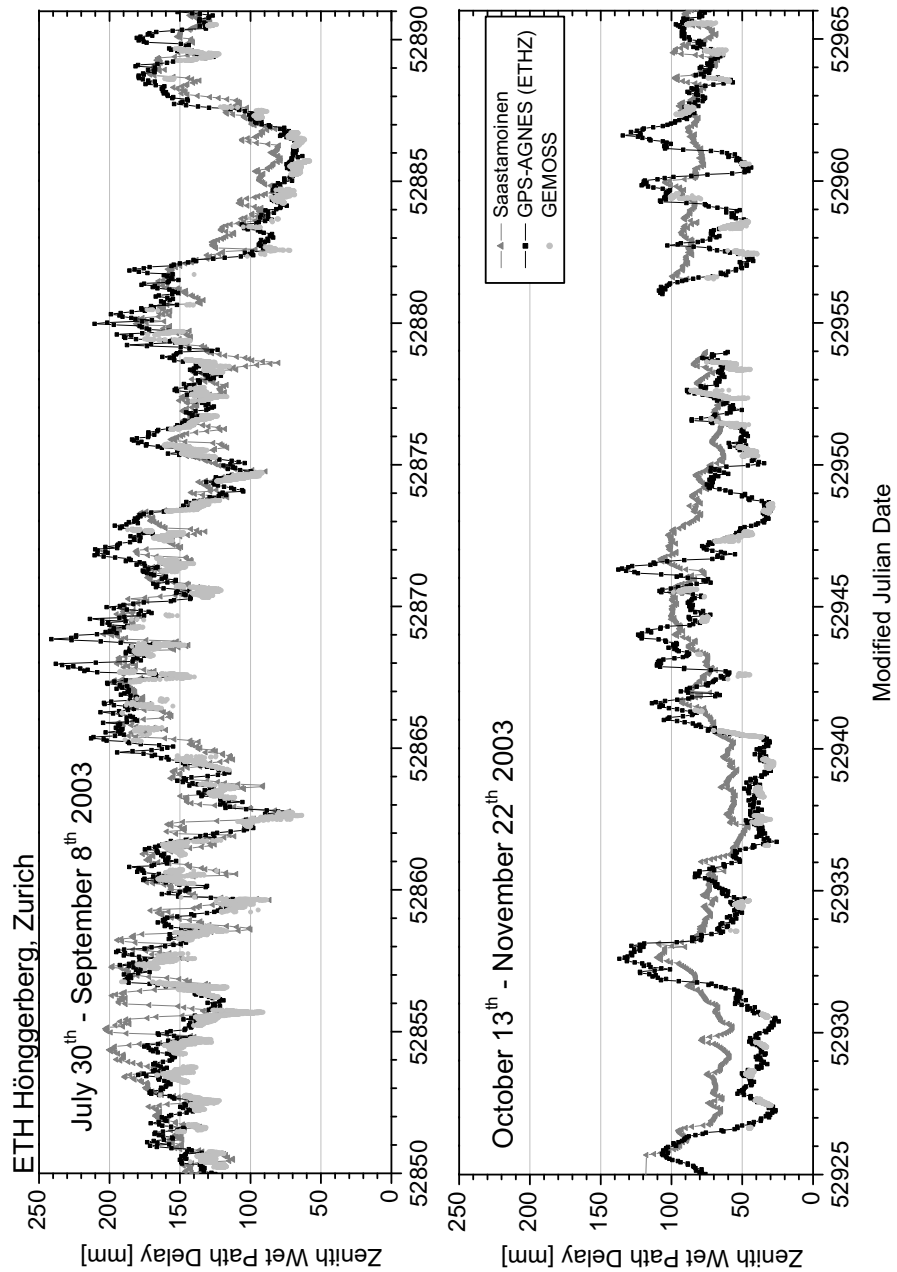


Figure 10.14: Second part of the long-term series of ZWD measured by GEMOSS and estimated by GPS at ETH Hönggerberg (Zurich). GEMOSS and GPS agree well. In the second part of October and in November Saastamoinen exhibits a smoother curve and does not follow the variations as seen by GEMOSS and GPS.

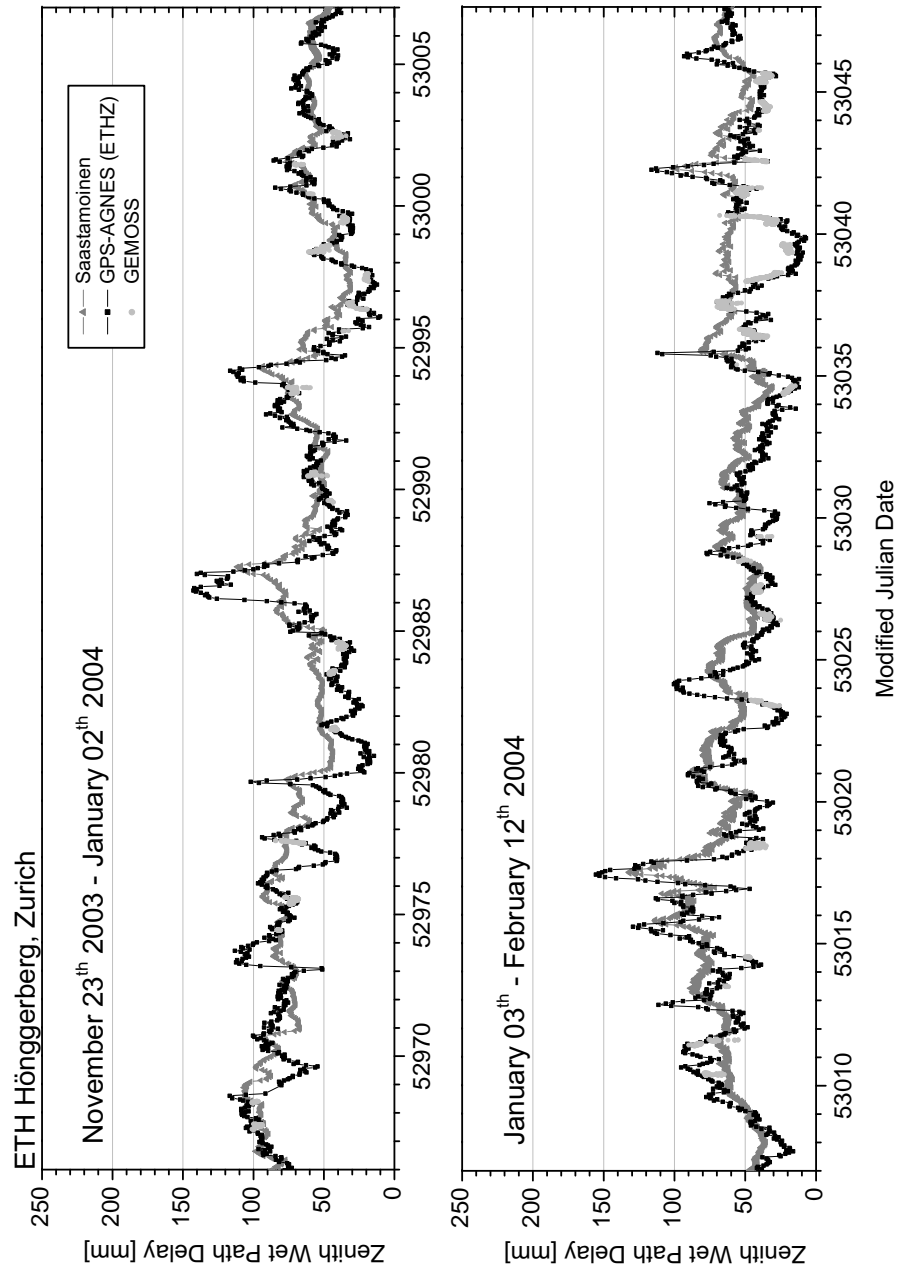


Figure 10.15: Third part of the long-term series of ZWD at ETH Hönggerberg (Zurich). During the winter 2004 GEMOSS and GPS agree very well whereas Saastamoinen often seems to be insensitive to daily water vapor fluctuation.

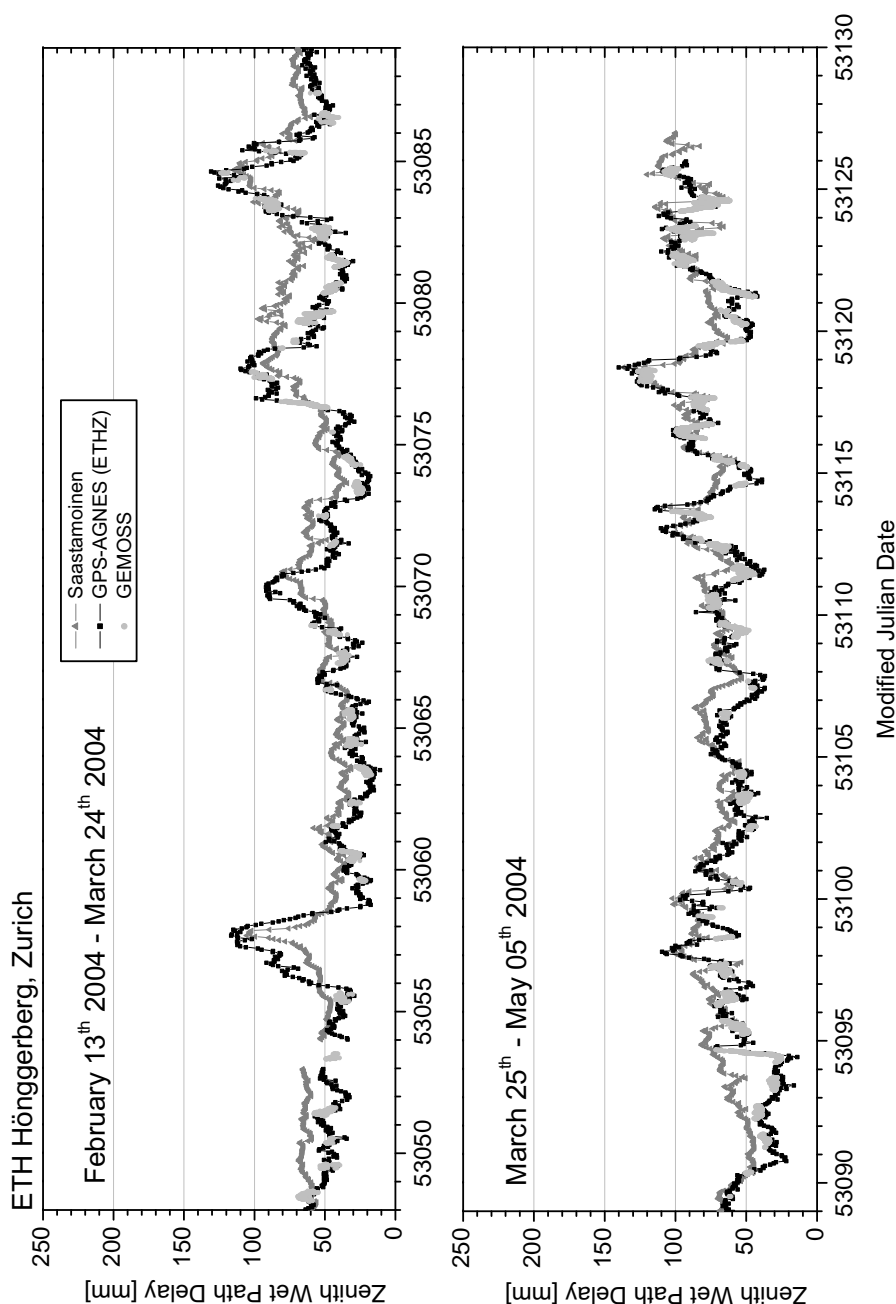


Figure 10.16: Fourth part of the long-term series of ZWD at ETH Hönggerberg (Zurich). GEMOSS again verifies the GPS estimates and the offset between both is close to zero. Especially in April, Saastamoinen agrees better than during the winter months but is not able to detect sudden changes of the zenith wet path delay as happened on the day 53094 (Modified Julian Date).

### 10.2.3 Comparison

For the time series presented in the previous section the offset between the ZPW retrieved by GPS and GEMOSS is calculated monthly. The mean offsets with their standard error are shown in Fig. 10.17 for the years 2003 and 2004. A seasonal

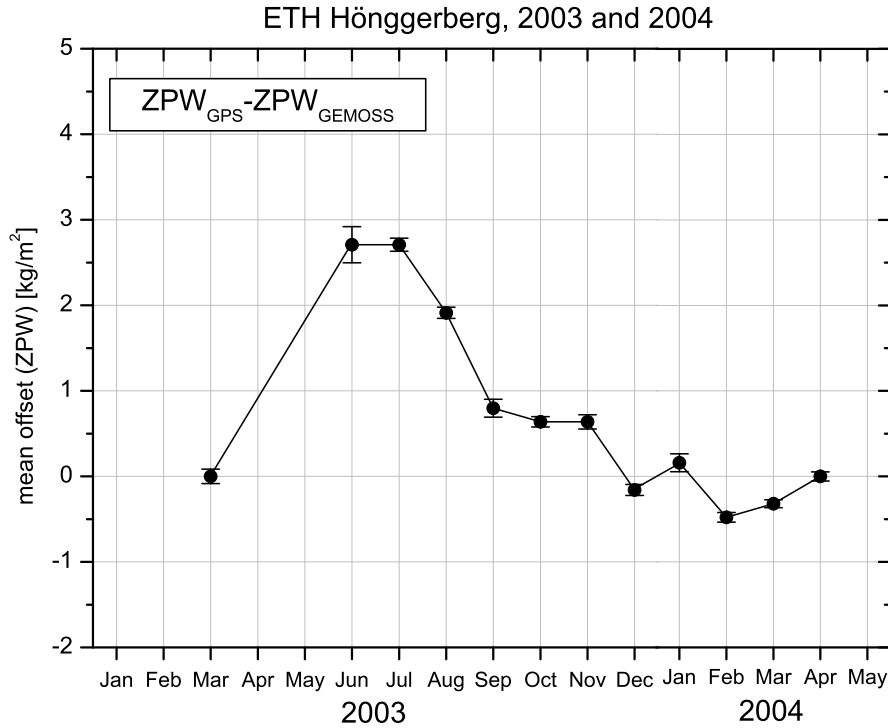


Figure 10.17: Monthly averaged offset between ZPW determined by GPS (AGNES station “ETHZ”) and GEMOSS at Höggerberg in the years 2003 and 2004. From June and July 2003 the mean offset decreased significantly from  $2.7 \text{ kg/m}^2$  down to  $-0.5 \text{ kg/m}^2$  in February 2004.

dependence of the mean offset stands out clearly with a maximum of  $2.7 \text{ kg/m}^2$  in June and July 2003 and a minimum of  $-0.5 \text{ kg/m}^2$  in February 2004. In order to investigate this seasonal behavior, the residuals are plotted versus the ZPW in Fig. 10.18. A strong linear correlation between the residuals and the amount of ZPW was found with the high correlation coefficient of 0.82. According to the determined linear equation

$$ZPW_{GPS} - ZPW_{GEMOSS} = (0.145 \pm 0.003) \cdot ZPW - (1.24 \pm 0.05) \quad (10.1)$$

GPS systematically over-estimates the integrated water vapor content if the ZPW is larger than  $9 \text{ kg/m}^2$ . In contrast, ZPW's smaller than  $9 \text{ kg/m}^2$  are under-estimated.

This linear dependence explains the increase of the offset in the summer when the ZPW reaches large values of more than  $30 \text{ kg/m}^2$ .

Since the cause of the large offsets between the results of GEMOSS and GPS can not be explained so far, an independent comparison with a microwave radiometer and radio soundings are necessary. Therefore, a comparison campaign at Payerne (COMPA) was carried out in the summer 2004 where the microwave radiometer can be operated without external disturbance and two radiosondes are launched each day. This campaign is described in the following section.

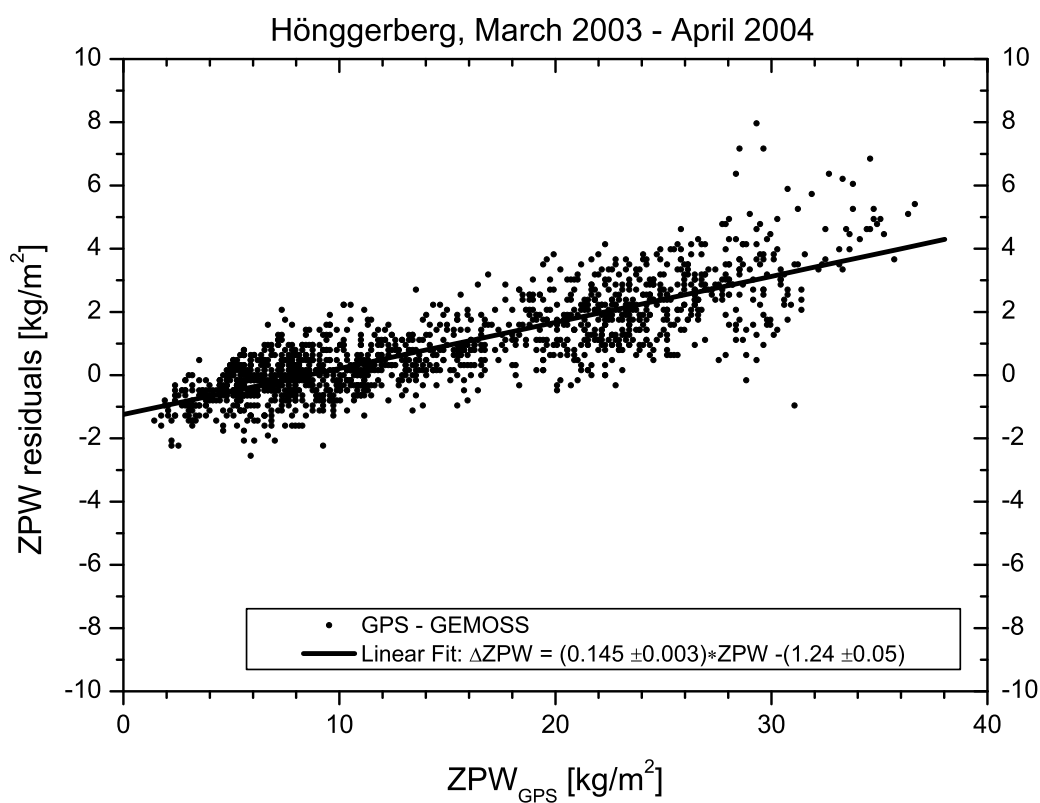


Figure 10.18: ZPW differences between GPS estimates and GEMOSS measurements at Hönggerberg in the years 2003 and 2004. A significant linear correlation between the differences and the amount of zenithal precipitable water vapor can be seen (correlation coefficient = 0.82).

## 10.3 COMPA - Comparison campaign at Payerne

### 10.3.1 Introduction

The motivation for the COMparison campaign at Payerne (COMPA) was to compare different methods determining the tropospheric water vapor content: solar spectrometry, microwave radiometry, GPS meteorology and radiosondes. Especially, the anomalous differences between GPS estimates and GEMOSS measurements observed at ETH Hnggerberg in the summer 2003 have to be investigated. The campaign was carried out at the meteorological station of *Meteoswiss*<sup>1</sup> at Payerne (Switzerland) in May and June 2004. This location was chosen because two radiosondes per day (around midday and midnight) are launched by Meteoswiss at Payerne and a co-located GPS station of the AGNES network is permanently operated by *Swisstopo*<sup>2</sup>. Figs. 10.19 and 10.20 show the telescope of GEMOSS, the GPS antenna and WVR mounted on a platform at Payerne. The spectrometer is placed inside the building below and is connected with the telescope by an optical fiber of 10 m length. Fig. 10.21 shows the launch of a radiosonde next to the installation platform.

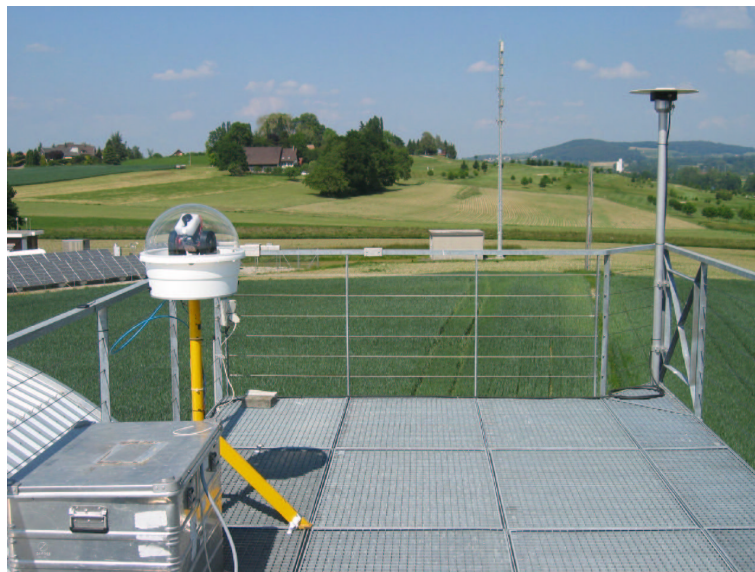


Figure 10.19: At Payerne the telescope of GEMOSS was fixed on an installation platform (left) next to the GPS antenna of the AGNES station “PAYE” (right).

---

<sup>1</sup>Swiss National Weather Service

<sup>2</sup>Swiss Federal Office of Topography



Figure 10.20: Co-located WVR (in the background) on the installation platform at Payerne.



Figure 10.21: Launch of a radiosonde by Meteoswiss at Payerne next to the platform where GEMOSS, WVR and GPS are operated.

### 10.3.2 Results

GEMOSS and WVR were deployed from May 28<sup>th</sup> to June 30<sup>th</sup> 2004 at Payerne. The corresponding time series of ZPW for GEMOSS, WVR, GPS and radiosondes is shown in Fig. 10.22. During this time period the ZPW varied between  $5 \text{ kg/m}^2$  and  $38 \text{ kg/m}^2$ . Except for June 6<sup>th</sup> and 24<sup>th</sup> GPS measurements are continuously available and one tropospheric parameter is estimated per hour. The processing of the GPS data was made by Swisstopo. The measurements of WVR are sometimes interrupted due to rainfall or dew on the cover. The radiometer was calibrated using the radiosondes launched by Meteoswiss. The device-specific offset between WVR “ZA” and the radiosondes was determined to  $5.1 \pm 0.22 \text{ kg/m}^2$ . In the following this offset was applied to the WVR retrievals in order to enable the comparison between WVR, GEMOSS and GPS. Furthermore, the inversion coefficients of the “PTX”-algorithm (Eq. 4.27) are computed for May and June 2004 using 123 radio soundings. The results are presented in Tab. 10.3.

	$c_{eff} [cm/K]$	$c_1 [10^{-3}/hPa]$	$c_2 [10^{-3}/K]$	$c_3 [10^{-4}/K]$
May 2003	$0.2960 \pm 0.0003$	$0.123 \pm 0.040$	$-1.83 \pm 0.09$	$-0.52 \pm 0.31$
June 2003	$0.2871 \pm 0.0004$	$0.041 \pm 0.092$	$-1.68 \pm 0.12$	$-1.90 \pm 0.32$

Table 10.3: Determination of the inversion coefficients of the “PTX”-algorithm for Payerne (Eqs. 4.24 and 4.27). The coefficients were computed for May and June 2004 from 123 radiosondes launched at Payerne.

The GEMOSS retrievals were determined using the absorption line parameters of ESA. Figs. 10.23-10.34 show the ZPW time series of selected days. For each figure an interpretation is given in the caption.

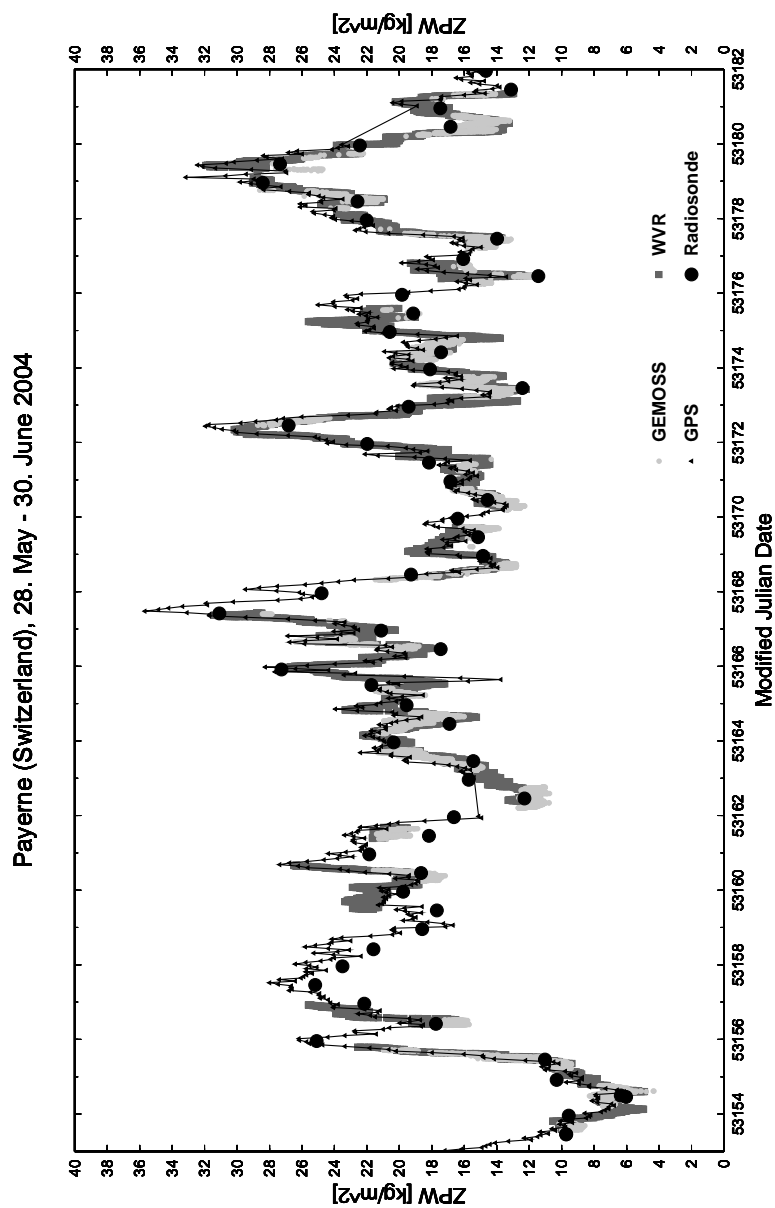


Figure 10.22: ZPW time series determined by the solar spectrometer (GEMOSS), microwave radiometer (WVR), GPS and radio soundings from May 28<sup>th</sup> to June 30<sup>th</sup> 2004 at Payerne. Except of two days the GPS provides a continuous ZPW curve. The observations of WVR are interrupted due to rainfall or dew on the cover. GEMOSS measurements are available at daylight and radiosondes were launched every mid-day and midnight. The WVR is calibrated using the radiosonde data acquired during the campaign. The GPS seems to over-estimate the ZPW compared to all other observation techniques whereas WVR, GEMOSS and radiosondes agree very well.

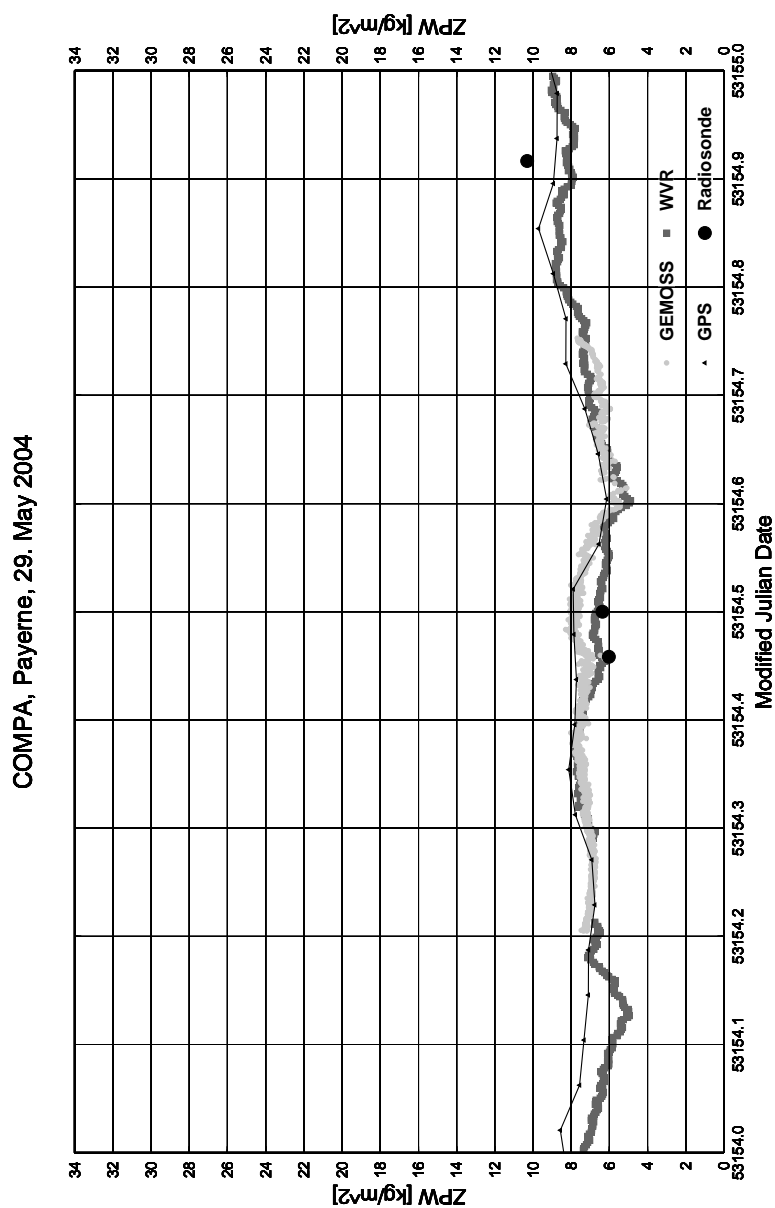


Figure 10.23: On May 29<sup>th</sup> the ZPW was very small and did not vary significantly. All four observation methods yield approximately similar values. Especially the agreement between GEMOSS and GPS is remarkable. Before sunrise around 05:00 UT (53154.2 MJD) the WVR measurements are corrupted due to dew on the cover which caused an underestimation of the ZPW. Both radiosondes at midday yielded slightly lower ZPW's as GEMOSS, WVR and GPS.

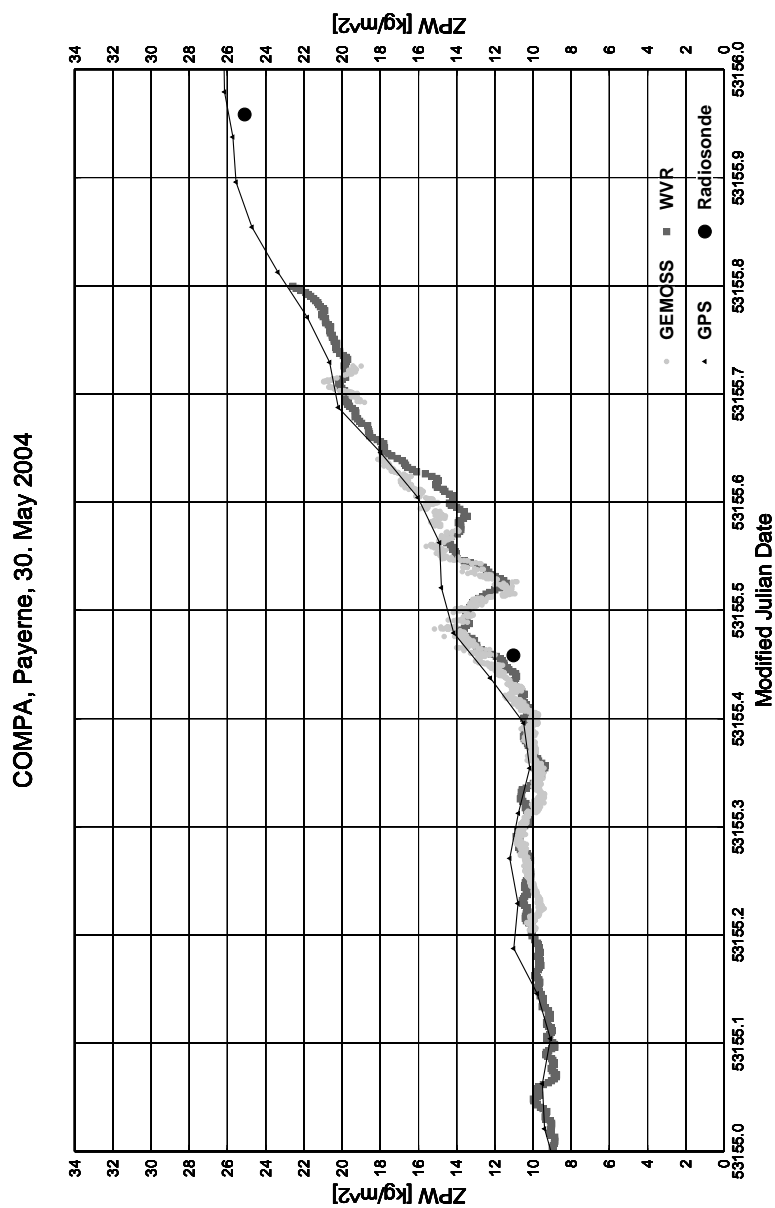


Figure 10.24: On May 30<sup>th</sup> the ZPW increased from 9  $kg/m^2$  in the morning up to 26  $kg/m^2$  at midnight. The observations of GEMOSS, WVR and GPS agree again very well. In the middle of the day the water vapor content decreased suddenly from 14  $kg/m^2$  to 11  $kg/m^2$  and increased after that in the same manner. This behavior was measured by GEMOSS and WVR as well but could not be observed by GPS. This exhibits the inability of GPS to recognize short-time variations of ZPW as happened that day from 11.30 to 13:30 UT (53155.48-56 MJD). The results of the radio soundings yield 1-2  $kg/m^2$  smaller ZPW's than those of GEMOSS, WVR and GPS.

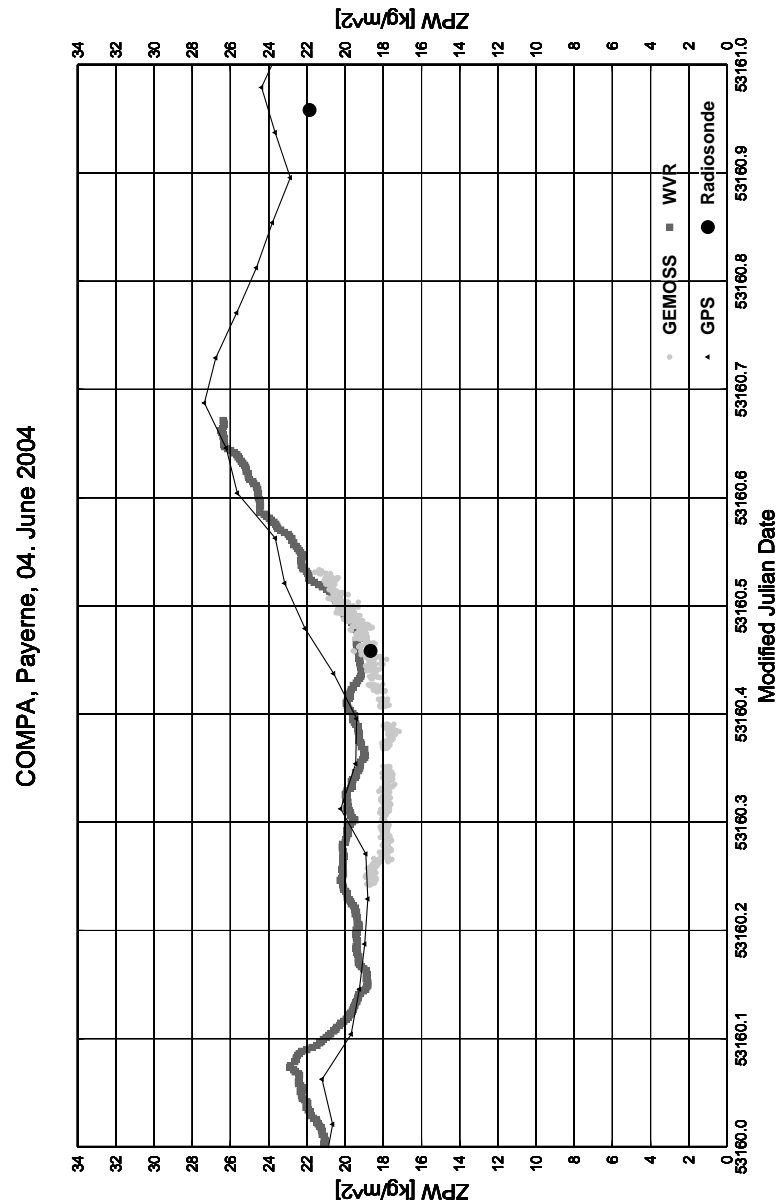


Figure 10.25: On June 4<sup>th</sup> the ZPW varied at a high level between 19 and 27  $kg/m^2$  and the differences between GEMOSS, WVR and GPS were larger than the days before. GEMOSS measured continuously a lower content of water vapor and coincided with the radiosonde at 11:00 UT (53160.46 MJD). The WVR results show strong variations compared to the GPS retrievals which indicates changeable meteorological conditions.

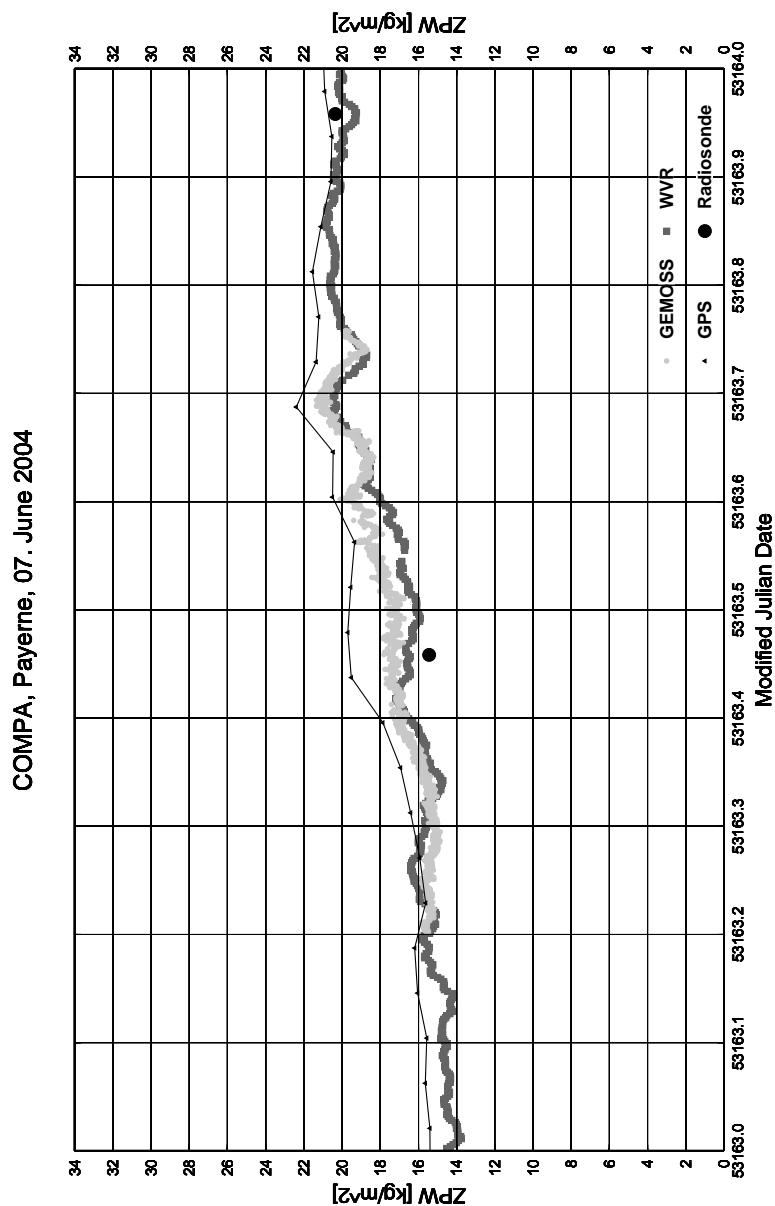


Figure 10.26: On June 7<sup>th</sup> the GEMOSS and WVR retrievals agree very well, especially at the last four hours of the GEMOSS time series. The GPS over-estimated the ZPW which can be clearly seen in the middle of the day where GEMOSS, WVR and radiosonde yielded 3-4  $kg/m^2$  lower amounts. Only after 20:00 UT (53163.85 MJD) the GPS curve matched the WVR's again and both are validated by the radiosonde launched at 23:00 UT.

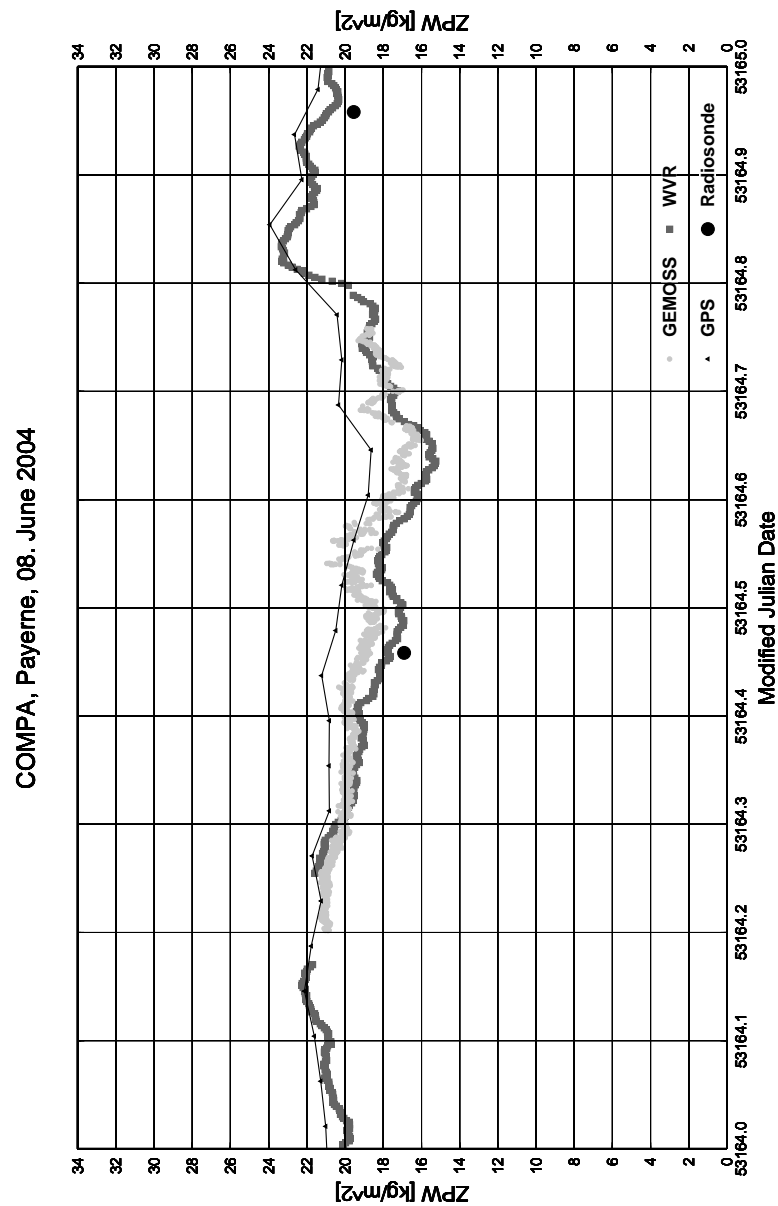


Figure 10.27: After sunrise on June 8<sup>th</sup> the WVR measurements followed the GEMOSS curve and GPS again over-estimated the ZPW. At 11:00 UT (53164.46 MJD) all four methods yielded different amounts of atmospheric water vapor. The second part of the day is characterized by strong short-time variations of ZPW which could only be observed by GEMOSS due to its high sensitivity and measurement rate. After sunset the WVR increased and matched the GPS curve.

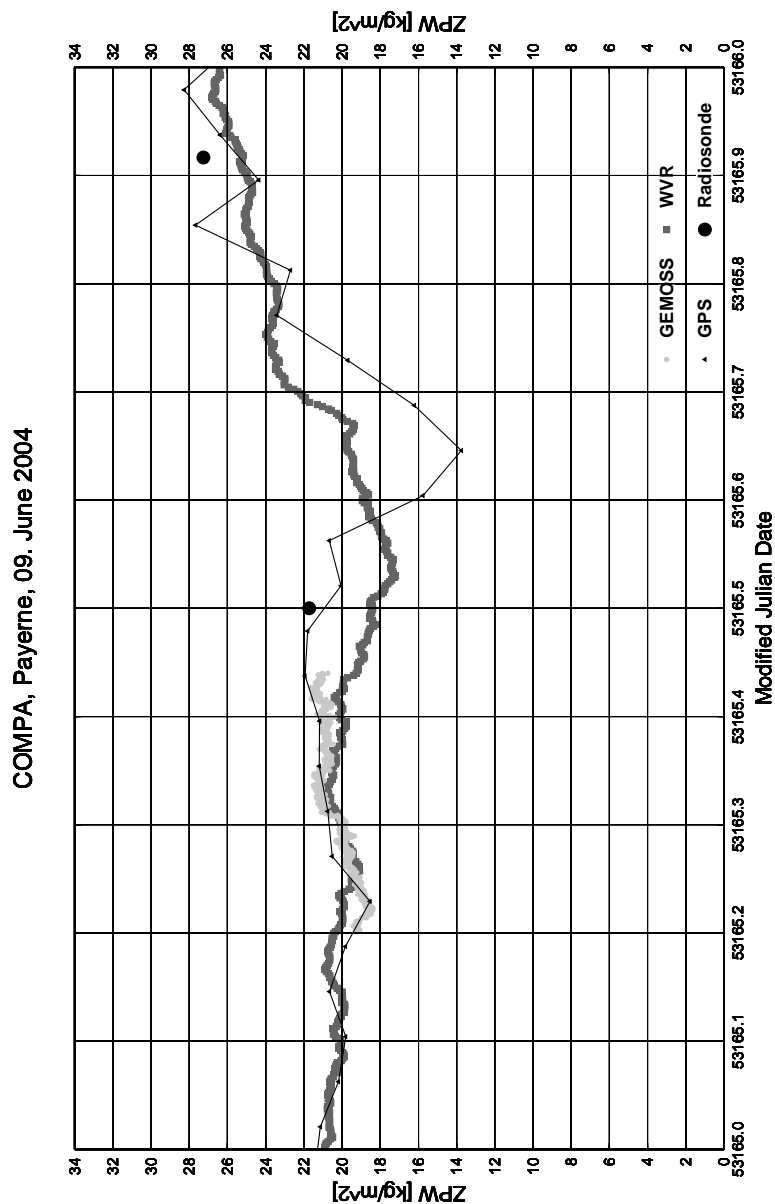


Figure 10.28: In the second part of June 9<sup>th</sup> GPS had serious difficulties estimating the ZPW. Unfortunately, GEMOSS has stopped measuring when the GPS estimates became unstable but WVR continued with reliable results. In contrast to the days before both radiosondes yielded a larger amount of water vapor than WVR and GPS.

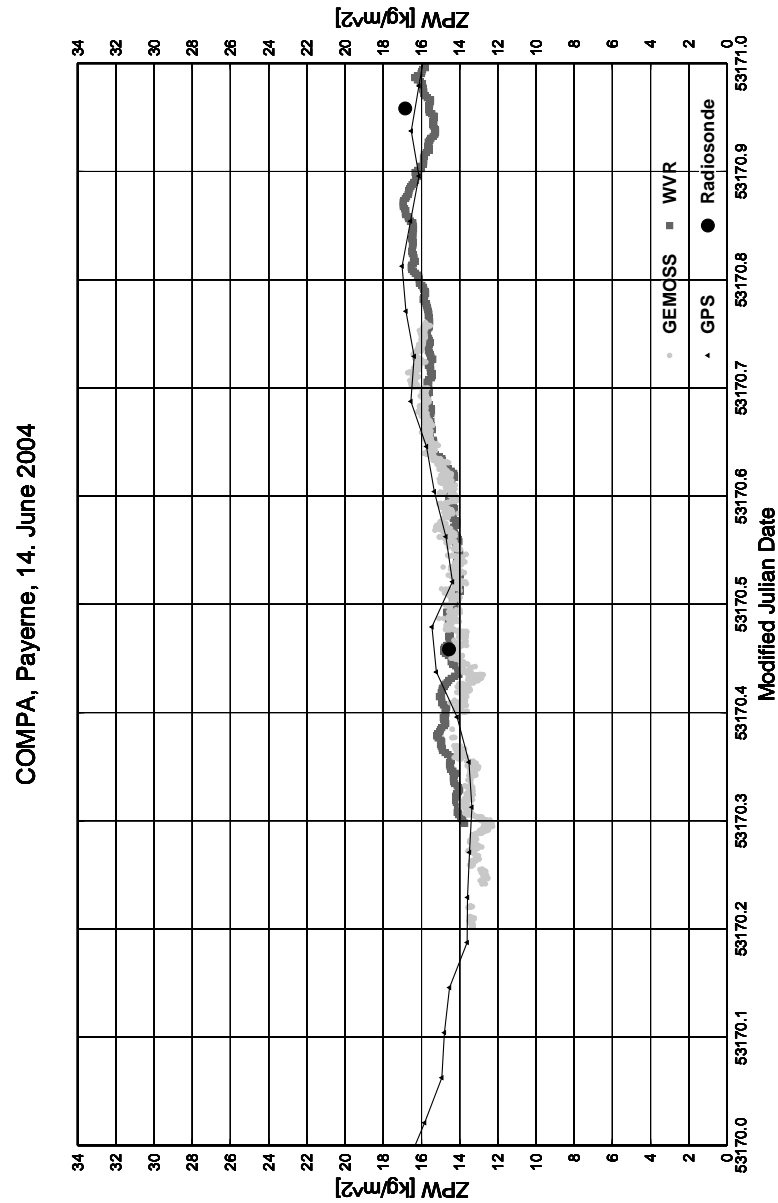


Figure 10.29: On June 14<sup>th</sup> the weather kept at stable conditions and the ZPW remained almost invariant around  $15 \text{ kg/m}^2$ . GEMOSS, WVR and GPS as well as radiosondes agreed very well within  $1 \text{ kg/m}^2$  ZPW. The stable meteorological conditions enabled GPS to estimate the water vapor content within sufficient accuracy.

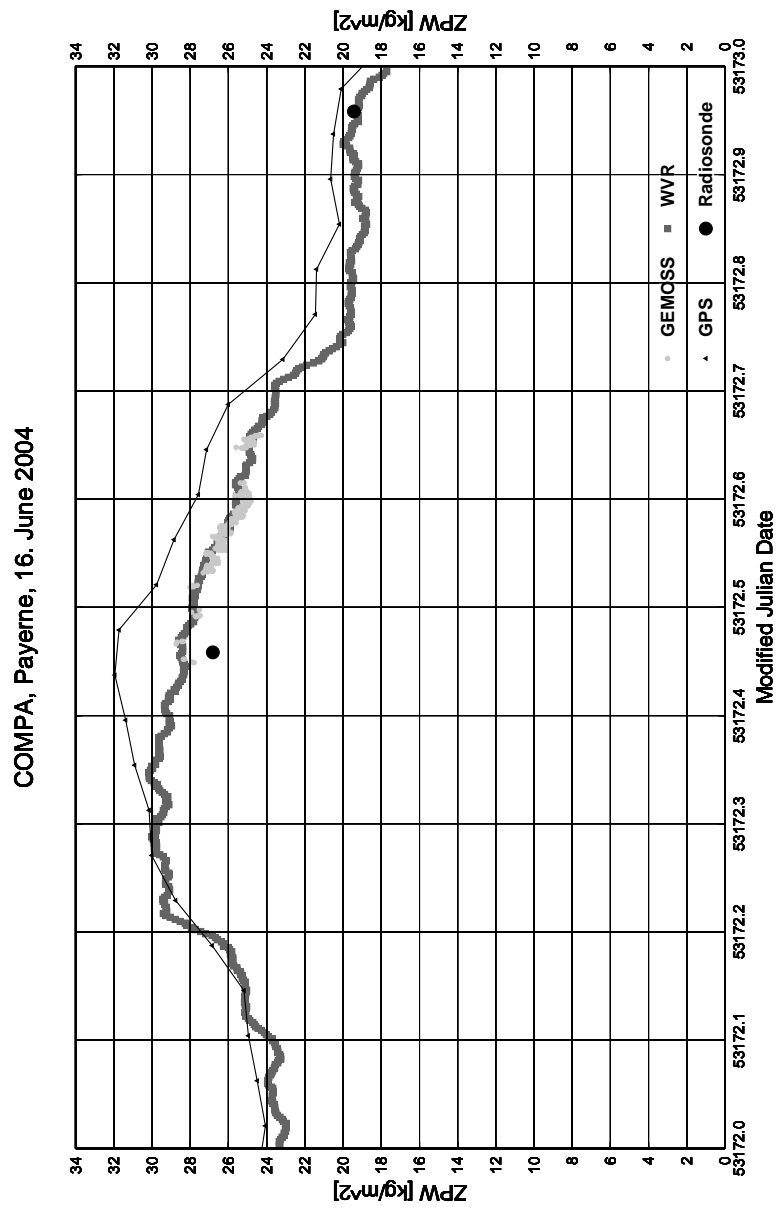


Figure 10.30: On June 16<sup>th</sup> the ZPW increased in the morning from 23  $kg/m^2$  to 30  $kg/m^2$  and decreased after 09:00 UT (53172.4 MJD) down to 18  $kg/m^2$ . Until 07:00 UT (53172.3 MJD) WVR and GPS yielded an almost similar time series of ZPW. In the following hours GPS retrieved further on an increasing amount of water vapor but WVR measured already a decrease of ZPW. In the afternoon the WVR observations are well confirmed by GEMOSS whereas the GPS retrievals are up to 4  $kg/m^2$  larger. During the night the GPS curve came closer to the WVR's which coincided with the radiosonde at 23:00 UT (53172.96 MJD).

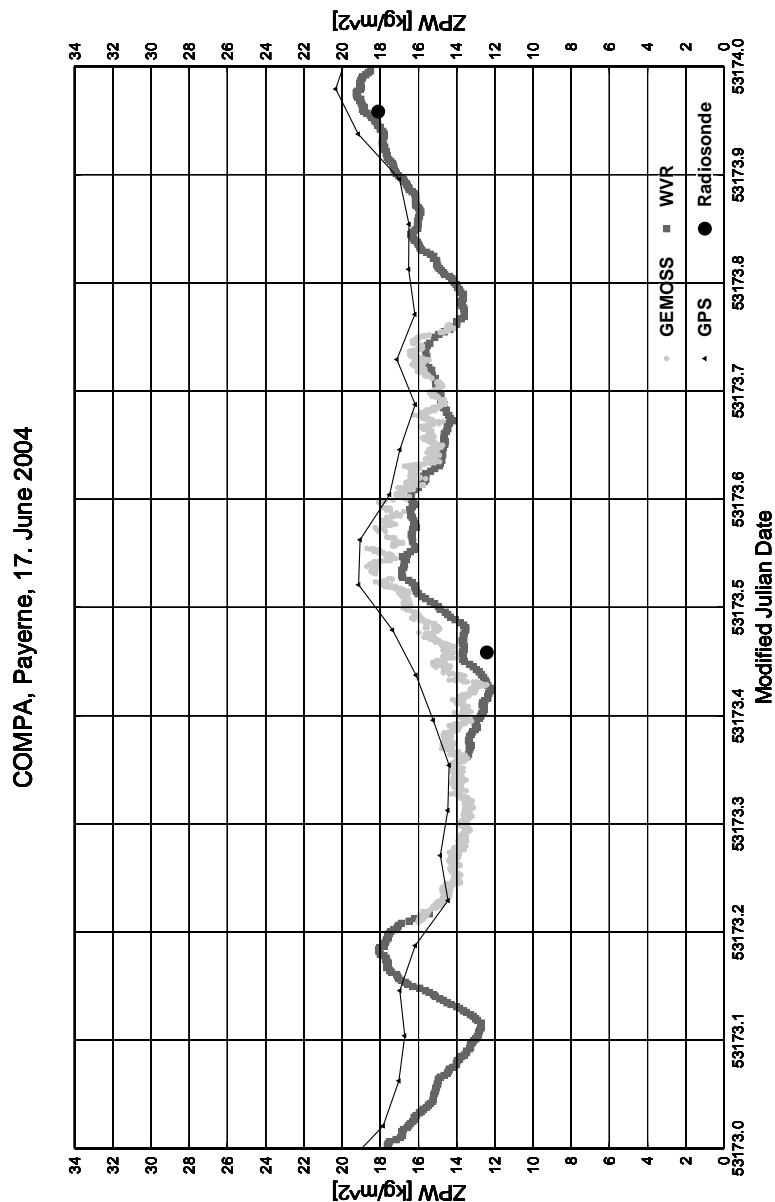


Figure 10.31: In the first hours of June 17<sup>th</sup> WVR measured a high-frequency variation of ZPW which was not recognized by GPS. The measurements of GEMOSS validate the WVR results. The GPS curve exhibits an offset in relation to GEMOSS, WVR and radiosondes with a maximum of  $3\text{-}4\text{ kg/m}^2$  at noon.

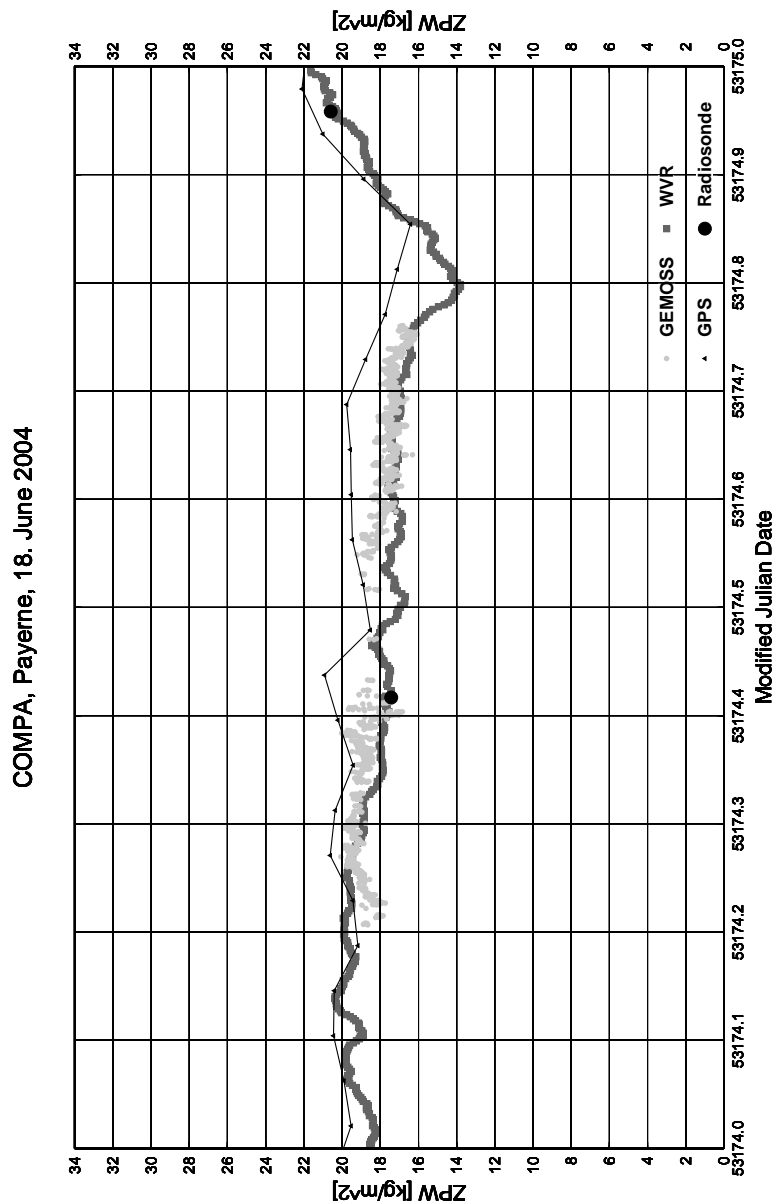


Figure 10.32: On June 18<sup>th</sup> GEMOSS, WVR and radiosondes again agreed within  $1 \text{ kg/m}^2$  whereas GPS matched the WVR time series only in the first six and the last three hours. Most of the day GPS over-estimated the ZPW about  $2\text{-}3 \text{ kg/m}^2$ . The minimum around  $14 \text{ kg/m}^2$  at 19:00 UT (53174.8 MJD) as measured by WVR was not observed by GPS.

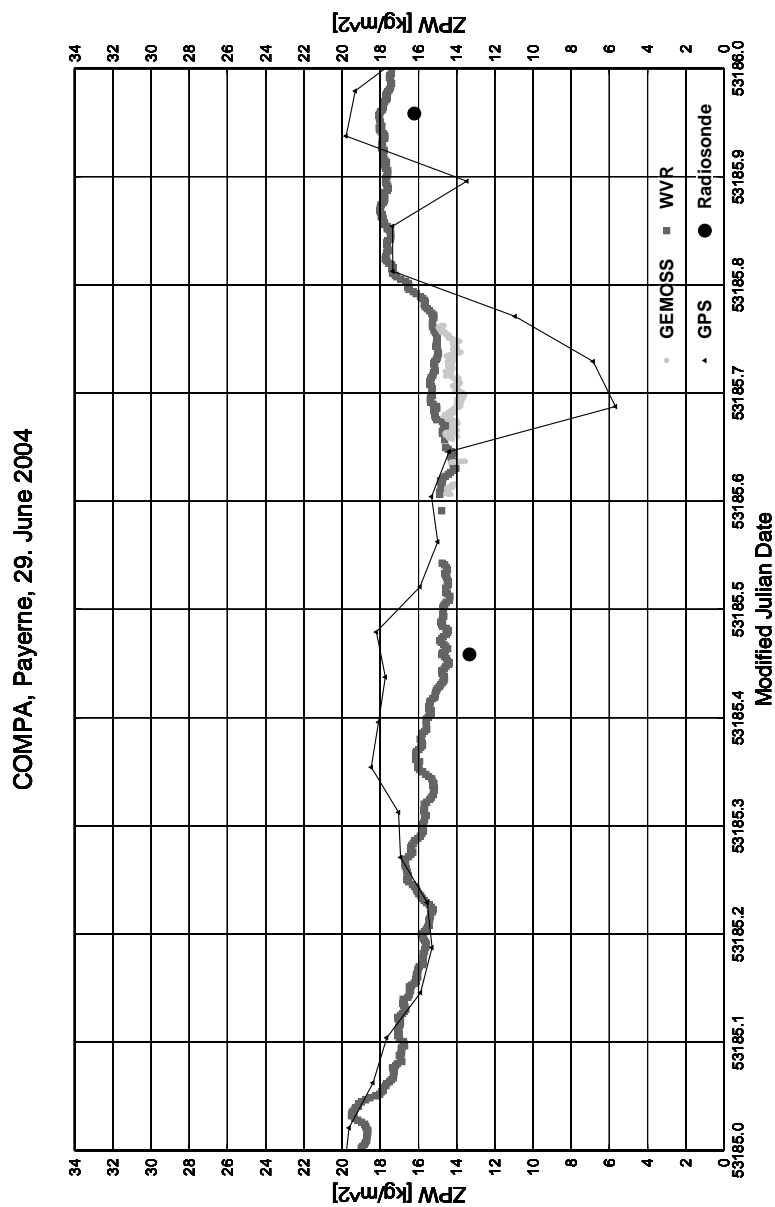


Figure 10.33: In the last third of June 29<sup>th</sup> GPS had obviously difficulties to estimate the ZPW correctly. GEMOSS, WVR as well as radiosondes indicated a smooth variation of the water vapor content over the whole day. The radiosondes show an offset of about  $-1.5 \text{ kg/m}^2$  in relation to the WVR.

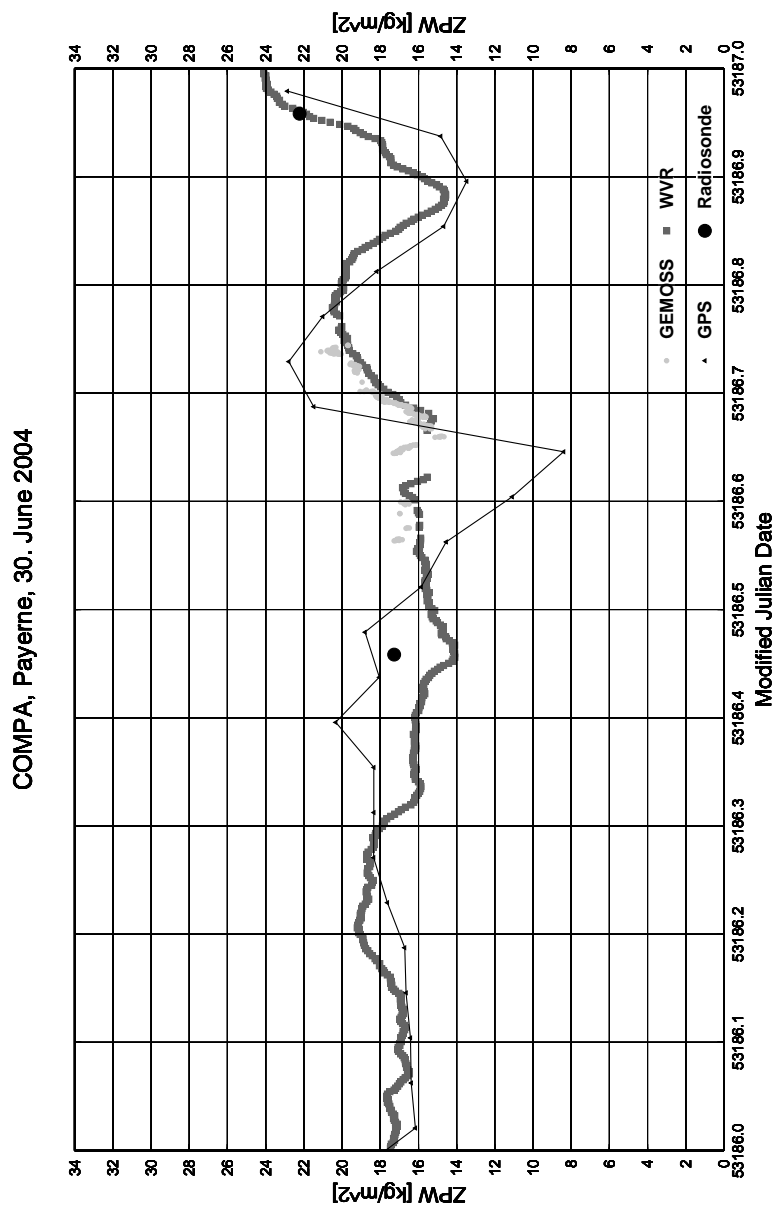


Figure 10.34: As the day before, GPS had problems retrieving the ZPW with the same accuracy and reliability as GEMOSS and WVR. Considering the bad weather on that day GEMOSS and WVR agree well during the short time period in the evening when the Sun was shining.

### 10.3.3 Comparison

In order to compare the results of GEMOSS, WVR, GPS and radiosondes the mean offsets of the ZPW time series of WVR to GEMOSS, radiosondes and GPS were calculated. Due to the calibration with radiosonde soundings and the widely continuous time series of ZPW, WVR is used as a validated reference for the comparison. The mean offset for the time period of the campaign with the corresponding standard error (sem) and standard deviation  $\sigma$  is listed in Tab. 10.4.

	WVR-GEMOSS	WVR-Radios.	GPS-Radios.
mean [ $kg/m^2$ ]	<b>-0.04</b>	<b>0.00</b>	<b>1.73</b>
sem [ $kg/m^2$ ]	0.03	0.22	0.20
$\sigma$ [ $kg/m^2$ ]	0.86	1.52	1.57

Table 10.4: Mean offset between the ZPW retrievals of WVR and GEMOSS, radiosondes and GPS for the time period May 28<sup>th</sup> - June 30<sup>th</sup> 2004 at Payerne. SEM denotes the *standard error of the mean* offset and  $\sigma$  the corresponding standard deviation. Since WVR was calibrated using the radiosonde soundings, the mean offset between both is eliminated.

Since WVR was calibrated using the radiosonde soundings, the mean offset between WVR and radiosondes is eliminated. WVR and GEMOSS agree very well with a small offset of  $-0.04 kg/m^2$ . Whereas the GPS estimates of the zenithal water vapor content are significant larger. As already observed during the long-term measurements of GEMOSS at ETH Honggerberg (section 10.2) GPS over-estimates the atmospheric water vapor content in the summer. In order to verify these seasonal discrepancies, GPS (AGNES station ‘‘PAYE’’) and radiosondes launched at Payerne were compared for the year 2003. The differences between the ZPW estimated by GPS and determined by radiosondes were averaged for every month. Fig. 10.35 shows the averaged differences. The mean offset increased significantly in June, July and August in 2003. Fig. 10.35 indicates a seasonal variation of the mean ZPW offset between GPS and radiosondes with a maximum of  $2.5 kg/m^2$  in June.

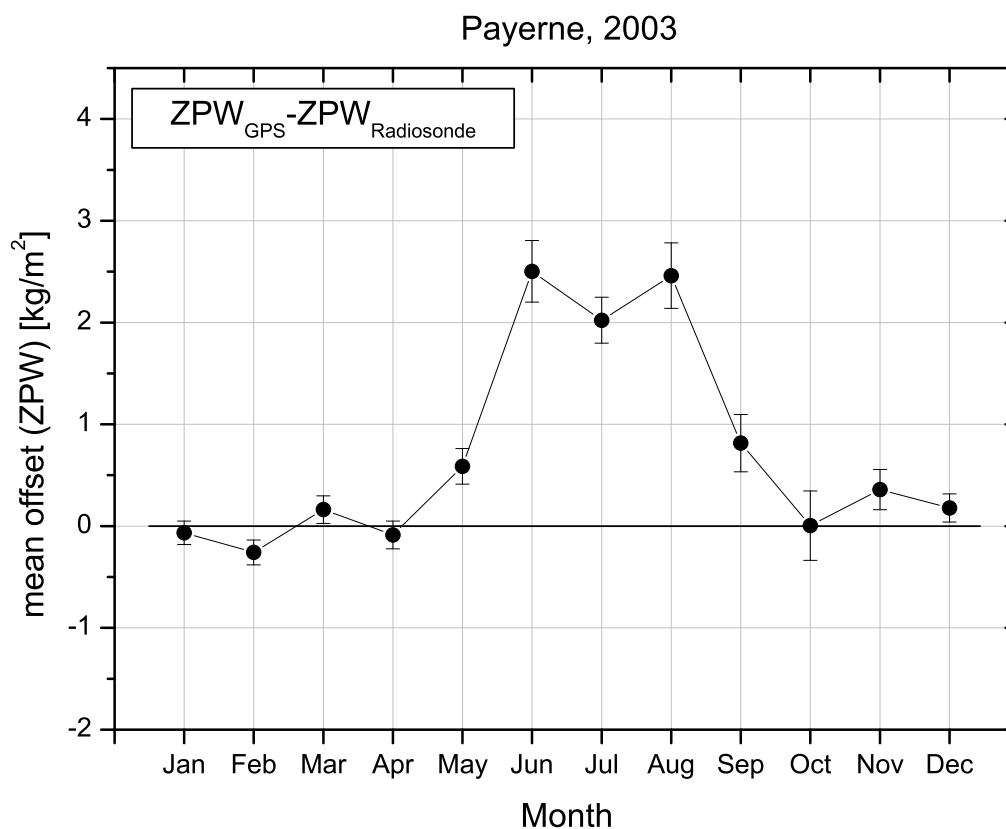


Figure 10.35: Monthly averaged offset between ZPW determined by GPS (AGNES station “PAYE”) and 746 radio soundings at Payerne in 2003. In June, July and August the mean offset increased significantly up to  $2.5 \text{ kg/m}^2$ . Before June and after August the differences were much smaller and did not exceed  $1 \text{ kg/m}^2$ .

### 10.3.4 Discussion

In order to verify the linear dependence as found in section 10.2.3, the residuals are again plotted versus the amount of ZPW. Fig. 10.36 shows the residuals between GPS and radiosondes for the year 2003.

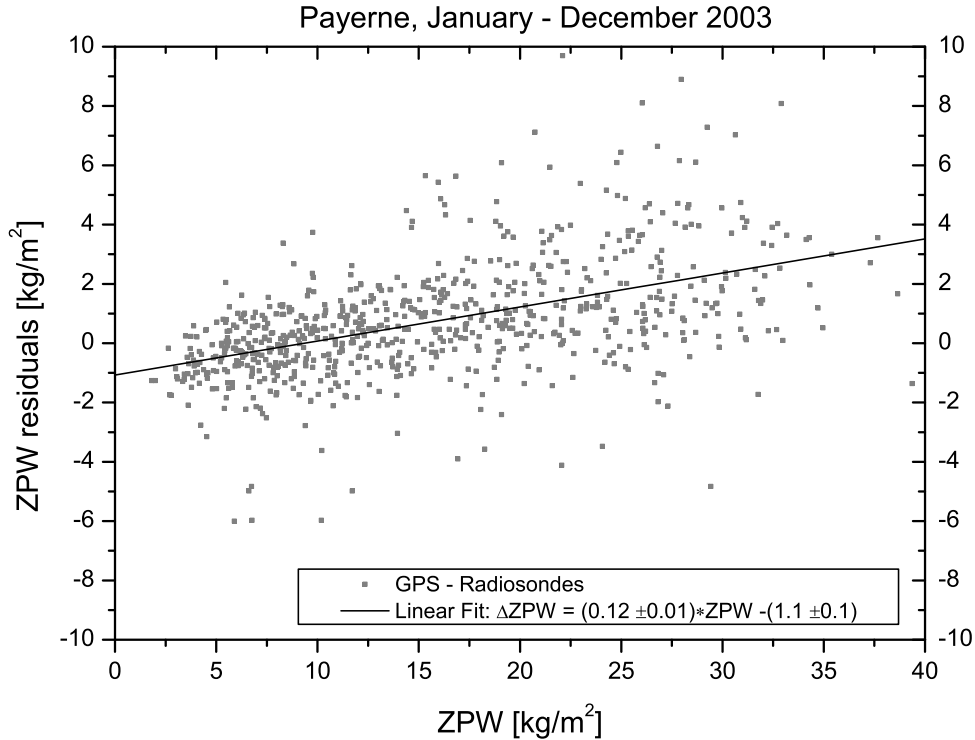


Figure 10.36: ZPW differences between GPS estimates and radiosonde soundings for the year 2003 at Payerne. The scattering is larger than observed by comparing GPS and GEMOSS (Fig. 10.18) which is supposedly caused by uncertainties in the radiosonde soundings. Nevertheless, the residuals exhibit a dependence on the amount of ZPW as already found in Fig. 10.18. The linear fit has a corresponding correlation coefficient of 0.50.

Although the scattering of the ZPW differences is larger indicating a lower measurement accuracy of the radiosondes compared to GEMOSS, almost the same trend is detected as in Fig. 10.18. The tropospheric parameters yield an over-estimated water vapor abundance for ZPW exceeding  $9 \text{ kg/m}^2$ . The corresponding linear equation was determined to

$$ZPW_{GPS} - ZPW_{Rds} = (0.12 \pm 0.01) \cdot ZPW - (1.1 \pm 0.1) \quad (10.2)$$

The analysis of the COMPA dataset yields similar results which are presented in Fig. 10.37. Furthermore, a comparison by Guerova (2003) has shown for the year 2002 that ZPW retrievals of GPS are on average  $1.45 \text{ kg/m}^2$  larger than those obtained from radiosondes launched at 12 UTC whereas the 00-UTC-radiosondes agree well with GPS. One possible reason for the observed biases in 2002 and 2003 can be the change in GPS data processing in mid September 2001. Further investigations are necessary to understand and eliminate the evident difficulties of GPS estimating accurate ZPW at noon.

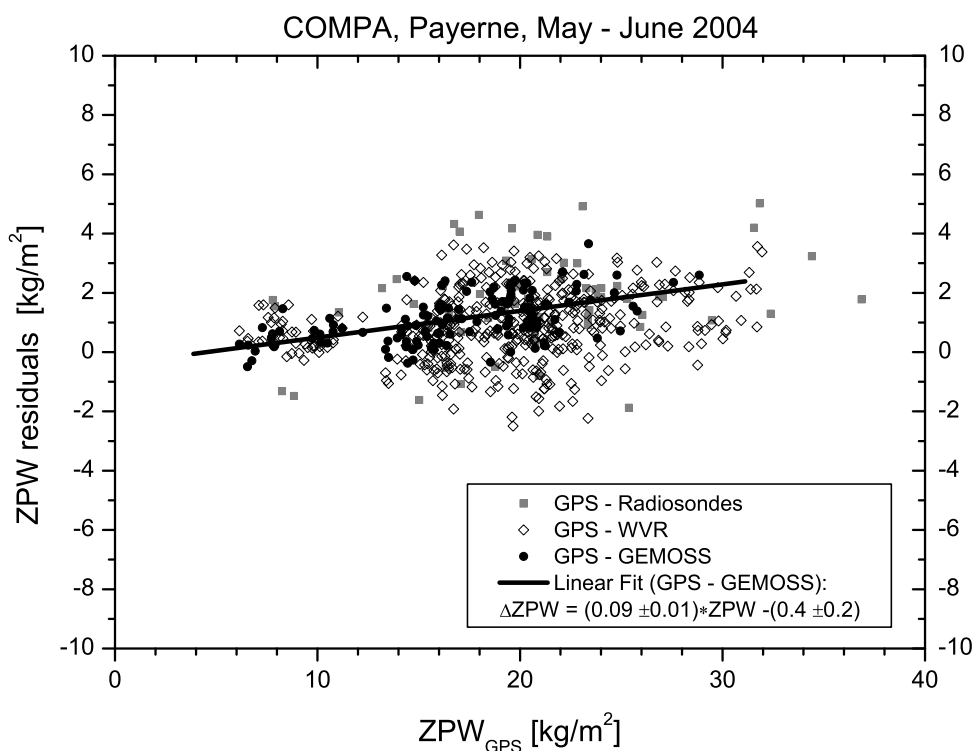


Figure 10.37: Differences between ZPW retrieved by GPS, WVR and GEMOSS during COMPA. The linear fit of the deviations ( $ZPW_{GPS} - ZPW_{GEMOSS}$ ) yields a correlation coefficient of about 0.54. The GEMOSS measurements as well as radiosonde soundings and WVR retrievals exhibit the same behavior of the GPS estimates as observed before at Höggerberg: GPS over-estimates the ZPW with increasing amount of water vapor.

The cause of the observed discrepancies cannot be explained yet. However, the linear dependence, as found and discussed above, is significant and verified by different methods at two different sites. It has to be pointed out that the ZPW is derived from

GPS observations by estimating tropospheric parameters (section 3.3). Errors in the GPS measurements, which are not caused by tropospheric refraction, can affect these parameters resulting in an inaccurate ZPW. In such a way, multipath effects and a temperature dependence of the GPS antenna can influence the retrieved ZPW. Furthermore, errors due to uncertainties in the mapping function used to relate the slant PW to the zenithal PW (Eq. 3.12) can introduce systematic deviations.

As described in section 3.3 GPS is only able to determine the *total* path delay by estimating tropospheric parameters. The wet delay  $\Delta L_w^z$  is derived from the total delay by subtracting the hydrostatic delay  $\Delta L_h^z$  calculated from the ground pressure (Eqs. 2.11 and 3.11). In order to reveal errors in  $\Delta L_w^z$  possibly introduced by the formula of Saastamoinen, the hydrostatic delay is validated by means of radiosonde data. Fig. 10.38 shows the differences of the hydrostatic delay calculated with the formula of Saastamoinen (1973) and determined by radio soundings. The good agreement within 2 mm testifies that no significant errors are introduced into the wet path delay retrievals of GPS by applying the Saastamoinen formula. This enables the accurate comparison between GPS and methods which measure the water vapor content “directly”, such as GEMOSS, radiosondes and WVR.

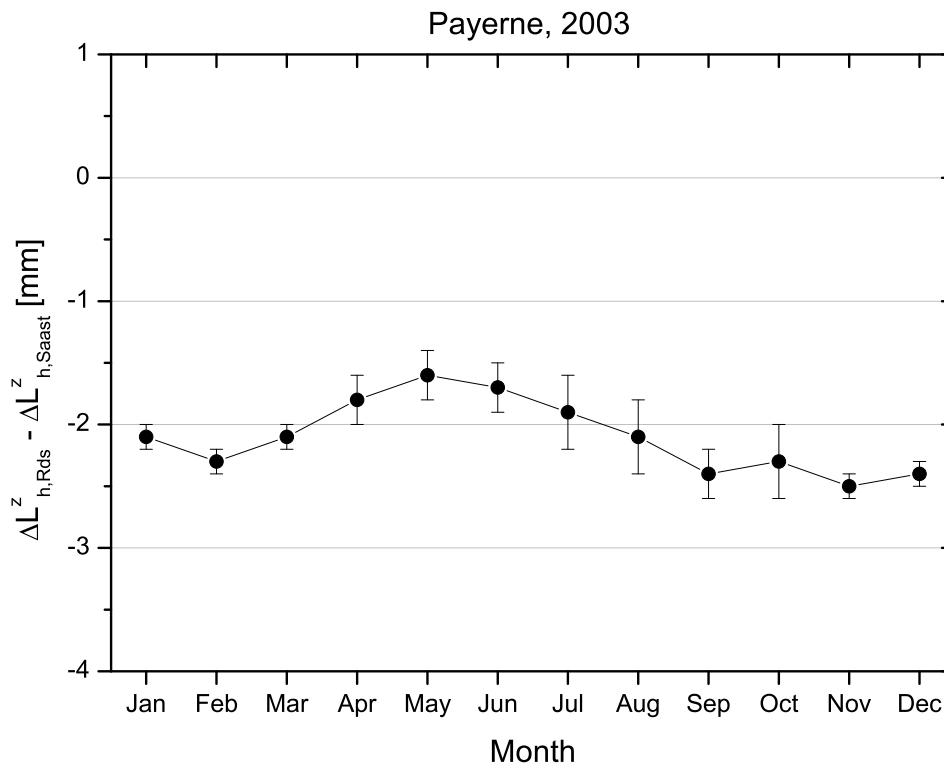


Figure 10.38: Comparison of zenithal hydrostatic delay  $\Delta L_h^z$  calculated from the ground pressure by Eq. 2.11 and measured by radiosonde soundings at Payerne in 2003. The differences of about 2 mm are small and do not explain the large deviations of up to 25 mm  $\Delta L_w^z$  between GPS and GEMOSS/radiosondes.

# 11 Conclusions and Outlook

The Global Positioning System (GPS) has become a widely used positioning technique in the field of space geodesy. In the case of highly precise positioning with GPS, extensive efforts are being made in order to determine and correct the measurement errors occurring. In this context, the influence of the troposphere on the microwave signal is one of the most important factors. Other error sources can be quantified with sufficient accuracy, like the ionospheric refraction by combining two different frequencies. The signal path excess due to the refractive properties of the troposphere, the total path delay, can be divided into a “dry” and a “wet” part. The dry part of the tropospheric delay can be determined with sufficient accuracy by measuring the air pressure at the ground. The so-called wet path delay is caused by the precipitable water vapor (PW) and cannot be mitigated as easily as the dry part.

Several techniques were developed and deployed in order to retrieve the PW, such as radiosondes, water vapor radiometers (WVR), sun photometers and solar spectrometers. Radiosondes measure vertical profiles of temperature, pressure and humidity. They provide information about the state of the atmosphere at a certain point of time, only. Due to the relatively high costs, radiosondes are usually launched two times per day, and a continuous observation cannot be carried out. Water vapor radiometers utilize the radiation emitted by the water vapor molecules from which the PW can be derived. But the retrieval algorithm has to be tuned to the local meteorological conditions of the measurement site and the season which is realized by analyzing the data of radio soundings [Somieski (2000)]. Water vapor radiometers are expensive, and especially errors of the observed brightness temperatures reduce the accuracy of the retrieved wet path delay to 1 *cm*. Sun photometers retrieve the water vapor abundance by building the ratio of the intensities of a water vapor and a reference channel where no absorption due to water molecules exist. The accuracy of the photometric technique strongly depends on the quality of the radiative transfer model taking aerosol and Rayleigh scattering into account which differ for the water vapor and the reference channel. Uncertainties concerning the water vapor continuum contribute to increasing deviations of the retrieved PW for decreasing solar elevation angles. Solar spectrometers measure the amount of absorption of the incident solar radiation which is related to the number of the absorbing water molecules in the atmosphere.

The overall goal of this work was to develop a prototype of a mobile solar spectrom-

eter dedicated for geodetic applications suffering for highly precise wet path delays. The prototype enables investigations concerning the selection of appropriate water vapor absorption lines and the validation of their line strength parameters as well as the increase of the accuracy of PW retrieved by solar spectrometry. Previous investigations revealed that the PW retrievals from single  $H_2O$  absorption lines differ from each other due to inaccurate line strength parameters [Sierk (2000)]. One of the goals of this work was the validation and correction of these parameters. Furthermore, the combination of as much water vapor absorption lines as possible was envisaged to improve the accuracy of the PW significantly. In order to achieve such high-precision retrievals, all instrumental and model errors had to be detected and eliminated or at least minimized, such as stray light, apparatus function, Fraunhofer lines, saturation effects and errors in the atmospheric absorption model. Based on these investigations carried out by means of a first prototype, the second optimized generation of mobile geodetic spectrometers can be specified.

In order to realize the issues mentioned above, a first prototype “GEodetic MOBILE Solar Spectrometer” (GEMOSS I) dedicated for high-precision geodetic applications has been developed. GEMOSS I consists of a new optical design which enables the simultaneous measurement of numerous single vibrational-rotational water absorption lines in the broad wavelength range between 728 nm and 915 nm [Becker-Ross and Florek (1997)]. Furthermore, a novel hard- and software-supported wavelength stabilization routine guarantees high wavelength accuracy under field conditions [Becker-Ross et al. (2002)]. In order to retrieve the precipitable water vapor from measured solar spectra, a processing software was written based on the line-by-line calculation of a synthetic solar spectrum and the method of the “Differential Optical Absorption Spectroscopy” (DOAS). The accurate simulation of a GEMOSS spectrum requires the determination of the apparatus function and the amount of stray light as well as investigations of the line strength parameters. Since GEMOSS I generates a pattern of 22 diffraction orders focused on the CCD array, the apparatus function and the amount of stray light are not constant for the entire spectral range. A new approach had to be found in order to measure the apparatus function and the stray light at various positions on the CCD sensor. The apparatus function was precisely determined by fitting a Voigt-function to narrow emission lines of neon gas which were shifted into two symmetrical positions (one and two pixels with maximum intensity) with respect to the pixel array of the CCD. The stray light was quantified by calculating the ratio of the maximum counts in the middle of a diffraction order and the minimum counts located between the corresponding and the neighboring diffraction order.

Since the accuracy of the line strength has a large impact on the accuracy of the amount of tropospheric  $H_2O$  molecules determined, a precise line strength is required. The spectral line parameters are usually determined in laboratories by measuring a light beam which was multiply reflected in long-path absorption cells. Since the length of the absorption path through the cells is limited to several hundred meters, the amount of absorption due to weak transitions is not strong enough to

determine the line parameters reliably. The absorption signal can be amplified by increasing the density of the absorbing gas but this will result in a stronger collision broadening and difficulties in separating the individual lines. It turned out that the line strength parameters of the **H**igh resolution **T**ransmission (HITRAN) molecular absorption database were in considerable disagreement with new measurements by the European Space Agency (ESA). For this reason, the primary aim became the re-measurement of the line intensities in order to replace the water data of HITRAN. In order to validate and correct independently the line strength parameters as published by ESA the strategy of retrieving PW from solar spectra was inverted. Instead of retrieving the PW it was introduced as known, and the line strength parameters were fitted until the simulated spectra matched the measured ones. This requires the validation of the PW by independent techniques, such as radiosondes, water vapor radiometers and GPS. Therefore, in May and June 2004 a comparison campaign (COMPA) was carried out at Payerne where GEMOSS, WVR and GPS were operated simultaneously and radiosondes were launched twice per day. For the line strength correction 69 lines were selected according to the following criteria: spectral intervals with negligible absorption in their vicinity, the absence of Fraunhofer lines and the prevention of saturation effects. With a set of 90 solar spectra acquired during COMPA the line strengths of these 69  $H_2O$  absorption lines were corrected. A test with a second set of 90 spectra revealed a significant improvement of the accuracy of the PW retrievals.

The accuracy of the PW retrieved by GEMOSS was investigated by an analysis of various error sources comprising the noise of the CCD, stray light, apparatus function, line strength parameters and the meteorological model. While the errors of the PW retrieval due to CCD noise, stray light and apparatus function were found to be small (altogether  $0.2 \text{ kg/m}^2$ ) the error caused by uncertainties in the meteorological profiles and the line strength parameters is approximately  $0.1 \text{ kg/m}^2$ . The effect of deviations of the meteorological model from the real atmospheric conditions on the PW retrieval was investigated using the profiles of temperature, pressure and humidity measured by radio soundings at Payerne. The small resulting errors indicate a relatively high insensibility of the estimated total amount of  $H_2O$  molecules concerning their vertical distribution in the atmosphere. In total, the error of the water vapor abundance retrieved from GEMOSS spectra is approximately  $0.5 \text{ kg/m}^2$  considering further error sources like the reflection of the solar radiation in clouds. It can be pointed out that the wet path delay can be determined by GEMOSS with an accuracy of  $2 - 4 \text{ mm}$  if as many appropriate  $H_2O$  absorption lines are used as possible whose line strength parameters are well known. In addition, the high measurement rate of up to eight spectra per minute contains potential to improve the accuracy by averaging the retrievals of spectra which are acquired during a certain period of time with stable atmospheric conditions.

In order to compare the solar spectrometry performance, a third generation of water vapor radiometers developed at the Geodesy and Geodynamics Laboratory (GGL) at ETH Zurich was operated during several campaigns next to GEMOSS. In con-

trast to the solar spectrometry, water vapor radiometry depends on the measurement site and season, and the inversion coefficients have to be determined regularly from radiosonde launches. During the campaign at Payerne the WVR was calibrated using more than 50 radio soundings. After eliminating an offset between radiosondes and WVR of about  $5.1 \text{ kg/m}^2$  PW in zenith direction (ZPW), GEMOSS and WVR agreed with an almost negligible offset of about  $0.04 \text{ kg/m}^2$  ZPW whereas the GPS estimates exhibit larger deviations of up to  $2.5 \text{ kg/m}^2$ . A long-term observation by GEMOSS and a co-located GPS receiver of the “Automatic GPS Network Switzerland” (AGNES) at ETH Höggerberg (Zurich) revealed similar large differences during the summer 2003. In the winter the offset almost disappeared and both systems agreed very well. But the comparison has shown, that especially in the warm months GPS over-estimates the zenithal PW by about  $3 \text{ kg/m}^2$ . A significant linear dependence between the ZPW residuals and the amount of ZPW was found which explains the large discrepancies in the summer when the water vapor abundance increases. A reason for this linearity could be the existence of errors in the GPS measurements which are included in the tropospheric parameters estimated within the GPS data processing although they are not caused by the tropospheric refraction. This can yield too large ZPW derived from over-estimated tropospheric parameters.

In the framework of the EU-project “Gavdos” GEMOSS was deployed two times in order to calibrate the on-board water vapor radiometer of the altimeter satellite Jason (JMR). First, GEMOSS was installed at Rethimnon (Crete, Greece), under the track of Jason in January 2003. Second, GEMOSS was operated at Fiskardo on the island of Kefalonia (Greece) also under a Jason track. The results of both campaigns show an agreement between GEMOSS and JMR at the few millimeters level. Moreover, the differences of GEMOSS and WVR/radiosondes do not exceed  $10 \text{ mm}$  wet path delay. Based on the promising results GEMOSS can be considered as an powerful and reliable altimeter calibration and validation system. It will be deployed again for further measurements in Greece in 2005.

The excellent performance of GEMOSS during the long-term deployment at Höggerberg and the various validation and comparison campaigns show that the instrumental errors as well as model errors are well determined. The use of more than 30 selected  $H_2O$  absorption lines, whose line strength parameters were corrected, enables the retrieval of ZPW with the aimed high accuracy of less than  $0.7 \text{ kg/m}^2$ . Since the first measurements in January 2003, GEMOSS has featured a reliability and stability without any drifts or jumps. In order to acquire also spectra using moonlight, the sensitivity of GEMOSS has to be increased. Furthermore, a lower energy consumption (supply with a 12V-battery instead of 220 V power) and a lower weight would facilitate its deployment at isolated sites.

In the future, the miniaturization of the spectrometer is envisaged and a smaller and lighter GEMOSS II will be constructed. The spectral range will be reduced to regions where  $H_2O$  absorption lines are concentrated (e.g. near 730 nm and 790 nm). Some spectral intervals do not contain valuable information about the

amount of absorption due to water molecules (e.g. between 740 and 780 nm) and can, therefore, be eliminated. The reduction of the spectral range would contribute not only to a miniaturization but also to a decrease of the cost for the hardware since the requirements of the echelle grating and the CCD sensor would be less high. The utilization of light materials for the base plate and the cage combined with a low energy consumption would improve the handling of the system in the field.

For high-precision geodetic measurements with GPS the wet path delay can be determined by GEMOSS with high accuracy. These wet path delays can be introduced into the Bernese GPS Software instead of estimating tropospheric parameters. This would improve the precision of the positioning with GPS if remaining errors are estimated which are not caused by the tropospheric water vapor. In general, the introduction of “independent” precise wet path delays offers the possibility of extended investigations concerning the separation of other errors from the tropospheric wet path delay. Moreover, GPS networks for meteorological purposes could be calibrated by a solar spectrometer which is especially important for real-time applications. Large deviations of the integral water vapor content in the summer derived from GPS observations could be corrected by means of a co-located solar spectrometer providing highly precise PW’s in real-time. Furthermore, water vapor radiometers could be calibrated using the measurements of GEMOSS. The deployment of radiosondes is relatively expensive and gives only information about the state of the atmosphere at a certain point of time. GEMOSS provides continuous measurements during daylight, and an extended and more accurate calibration of a water vapor radiometer could be realized. In general it can be pointed out that the high measurement accuracy and stability qualify GEMOSS for an excellent calibration standard. Solar spectrometry does not depend on the measurement site or the season. For example, an observed drift of the on-board water vapor radiometer of Jason could be well determined by GEMOSS.

Spectrometers with a low spectral resolution (3-4 nm) compared to GEMOSS are also used to retrieve the PW from broad-band absorption [Sierk et al. (2004)]. But these low-resolution spectrometers need to be calibrated regularly by means of an external reference since spectral intervals with negligible absorption cannot be resolved. The method of differential absorption (DOAS) cannot be applied in the same manner as for GEMOSS. Instead the ratio of the measured spectrum (foreground) and a reference spectrum (background) is being determined. The background spectrum has to be measured when the water vapor abundance is independently observed by radiosondes. For this purpose, GEMOSS can be deployed in order to calibrate the low-resolution spectrometers with high accuracy. In the future, two kinds of geodetic mobile solar spectrometers are envisaged: type I (GEMOSS I) dedicated for a permanent installation next to a continuously operated GPS receiver for high-precision purposes, and a small and lightweight type II (GEMOSS II) optimized for field deployment.

In the case of space-borne radar altimeters the wet path delay propagates into errors for the determination of sea surface heights. Therefore, modern altimeter satellites

carry microwave radiometers on board in order to measure this delay at every observation epoch. The measurements though require calibration and validation all along the lifetime of the altimeter mission to avoid the introduction of biases and drifts in the observed sea surface heights. The estimate of globally-averaged sea level change associated with climate change requires that uncertainties in the trends in such a global average be accurate to much better than the signal of 1-2 mm/year. The radiometers of ERS-1, TOPEX/Poseidon, ERS-2, JASON and ENVISAT exhibit significant drifts in at least one of the channels resulting in yet unmodeled errors in path delay of up to 1 mm/year [Scharroo et al. (2004)]. [Zlotnicki and Desai (2004)] discovered that the on-board radiometer of Jason (JMR) has shown sudden steps or spikes of up to 6 mm wet path delay since October 2002. In addition, JMR wet delay changes related to the yaw state are evident in 2003. Furthermore, an increase of uncertainties of JMR measurements are observed in coastal regions which is especially problematic over in-land seas, such as the Mediterranean sea. These instrumental problems indicate the necessity for permanent calibration and validation of Altimeter Microwave Radiometers (AMR) by highly precise independent methods in order to avoid the introduction of biases and drifts in the observed sea surface heights. The continuous operation of GEMOSS under altimeter satellite tracks can provide a reliable continuous validation and calibration of AMR.

In this way, GEMOSS does not only provide corrections for high-precision GPS positioning and calibration of meteorological GPS networks but has also the potential to contribute significantly to pending questions related to global climate change.

# Bibliography

- Aviso (2004). Aviso, Observing the Ocean from Space, <http://www.aviso.oceanobs.com>, Centre National d'Etudes Spatiales (CNES), Collecte Localisation Satellites (CLS).
- Bean, B. R. and Dutton, E. J. (1966). Radio meteorology. *Monograph*, 92.
- Becker-Ross, H. and Florek, S. (1997). Echelle spectrometers and charge-coupled devices. *Spectrochim. Acta Part B* 52, pages 1367–1375.
- Becker-Ross, H., Okruss, M., Florek, S., Heitmann, U., and Huang, M. D. (2002). Echelle-spectrograph as a tool for studies of structured background in flame atomic absorption spectrometry. *Spectrochim. Acta Part B* 57, pages 1493–1504.
- Belmiloud, D., Schermaul, R., Smith, K., Zobov, N. F., Brault, J., Learner, R. C. M., Newnham, D. A., and Tennyson, J. (2000). New studies of the visible and near infra-red absorption by water vapour and some problems with the database. *Geophysical Research Letters*, 27:3703–3706.
- Beutler, G., Bock, H., Brockmann, E., Dach, R., Fridez, P., Gurtner, W., Hugentobler, U., Ineichen, D., Johnson, J., Meindl, M., Mervart, L., Rothacher, M., Schaer, S., Springer, T., and Weber, R. (2001). *Bernese GPS software version 4.2*, edited by U. Hugentobler, S. Schaer and P. Fridez. Astronomical Institute, University of Berne.
- Bevis, M., Businger, S., Herring, T., Rocken, C., Anthes, R., and Ware, R. (1992). GPS Meteorology: Remote Sensing of Atmospheric Water Vapor Using the Global Positioning System. *Geophys. Res. Lett.*, 97:15,787–15,801.
- Bock, O., and C. Thom, J. T., Pelon, J., and Kasser, M. (2001). Study of external path delay correction techniques for high accuracy height determination with GPS. *Physics and Chemistry of the Earth, Part A*, 26(3):165–171.
- Boiffier, J.-L. (1998). *The Dynamics of Flight: The Equations*. John Wiley and Sons, Baffins Lane, Chichester, West Sussex PO19 1UD, England.
- Brown, L. R., Toth, R. A., and Dulick, M. (2002). Empirical line parameters of  $H_2^{16}O$  near  $0.94 \mu\text{m}$ : positions, intensities and air-broadening coefficients. *Journal of Molecular Spectroscopy*, 77:57–82.

- Bürki, B. and Kahle, H.-G. (1995). Mikrowellen-Wasserdampf-Radiometer für hochgenaue Messungen mit GPS. *Geodesie et Geodynamique*, 4/95:232–240.
- Callies, J., Eisinger, M., Schermaul, R., Learner, R. M., Newnham, D. A., Ballard, J., Tennyson, J., and Wickett, M. (2000). New Results of Water Vapor Spectroscopic Measurements in the Visible and Near-Infrared. *Earth Observation Quarterly*, 67.
- Camy-Peyret, C., Flaud, J. M., Mandin, J. Y., Bykov, A., Naumenko, O., Sinitsa, L., and Voronin, B. (1999). Fourier-transform absorption spectrum of the  $H_2^{17}O$  molecule in the 9711 – 11335  $cm^{-1}$  spectral region: the first decade of resonating states. *Journal of Quantitative Spectroscopy and Radiative Transfer*, 61:795–812.
- Chandrasekhar, S. (1960). *Radiative Transfer*. Dover Publications, Inc., New York.
- Chevillard, J., Mandin, J.-Y., Flaud, J.-M., , and Camy-Peyret, C. (1989).  $H_2^{16}O$ : line positions and intensities between 9500 and 11500  $cm^{-1}$ . The (041), (220), (121), (201), (102), and (003) interacting states. *Can.J.Phys.*, 67(1065-1084).
- Chevillard, J. P., Mandin, J. Y., Flaud, J. M., and Camy-Peyret, C. (1987).  $H_2^{18}O$ : line positions and intensities between 9500 and 11500  $cm^{-1}$ . *Can. J. Phys.*, 65:777–789.
- Ciddor, P. E. (1999). Refraction index of air: New equations for the visible and near infrared. *Applied Optics (Lasers, Photonics and Environmental Optics)*, 35(9):1566–1573.
- Ciddor, P. E. and Hill, R. J. (1996). Refraction index of air: 2. group indes. *Applied Optics (Lasers, Photonics and Environmental Optics)*, 38(9):1663–1667.
- Davis, J. L., Hering, T. A., Shapiro, I. I., Rogers, A. E. E., and Elgered, G. (1985). Geodesy by radio interferometry: Effects of atmospheric modeling errors on estimates of baseline length. *Radio Sci., Vol. 20 No. 6*, pages 1593–1607.
- Deuber, B., Kämpfer, N., and Feist, D. G. (2004). A new 22-GHz Radiometer for Middle Atmospheric Water Vapour Profile Measurements. *IEEE Transactions on Geoscience and Remote Sensing*, 42:974–984.
- Elgered, G. (1993). Tropospheric radio path delay from ground-based microwave radiometry. *Atmospheric Remote Sensing by Microwave Radiometry*, pages 215–258.
- Essen, L. and Froome, K. (1951). The refractive indices and dielectric constants of air and its principal Constituents at 24 GHz. *Proc Phys Soc*, B-64:862–875.
- Flores, A., Ruffini, G., and Rius, A. (2000). 4D tropospheric tomography using GPS slant wet delays. *Annales Geophysicae*, 18(2):223–234.
- Gamache (2000). Total internal partition sums for molecules in the terrestrial atmosphere. *Journal of Molecular Structure*, 517-518:407–425.

- Gamache, R. R. and Rothman, L. S. (1988). Temperature dependence of  $n_2$ -broadened halfwidths of water vapor: The pure rotation and  $\nu_2$  bands. *Journal of Molecular Spectroscopy*, 128:360–369.
- Geiger, A. (1987). Einfluss richtungsabhängiger Fehler bei Satellitenmessungen. Technical Report 130, Institute of Geodesy and Photogrammetry, ETHZ, Zürich.
- Giver, L. P., Chackerian, C., and Varanasi, P. (2000). Visible and near-infrared  $H_2^{16}O$  line intensity corrections for HIRTAN96. *Journal of Quantitative Spectroscopy and Radiative Transfer*, 66:101–105.
- Guerova, G. (2003). *Application of GPS derived water vapour for Numerical Weather Prediction in Switzerland*. PhD thesis, Universität Bern, Philosophisch-naturwissenschaftliche Fakultät.
- Herring, T. (1992). Modelling Atmospheric Delays in the Analysis of Space Geodetic Data. In *Refraction of Transatmospheric Signals in Geodesy, Proceedings of the Symposium*, volume Publ. Geod. 36, pages 157–164.
- Hollenstein, C., Kahle, H.-G., Cocard, M., Veis, G., Paradissis, D., Felekis, S., and Billiris, H. (2002). CGPS Data in Greece: Time Series of Crustal Motion and Error Analysis. WEGENER conference 2002, Eleventh General Assembly, Athens, Greece, June 12-14, 2002.
- Hollenstein, C., Kahle, H.-G., Geiger, A., Cocard, M., and Veis, G. (2003). Crustal Deformation and Strain Rates in Greece, Combined Results from GPS Reoccupation and Permanent Data. *Geophysical Research Abstract*, 5(10449).
- Humlicek, J. (1982). Optimized computation of the Voigt and complex probability functions. *J. Quant. Spectros. Radiat. Transfer*, 27(4):437–444.
- Ifadis, I. (1986). The atmospheric delay of radio waves: Modelling the elevation dependence on a global scale. Licentiate Thesis 38L, Chalmers University of Technology.
- Ingold, T., Schmid, B., Mätzler, C., Demoulin, P., and Kämpfer, N. (2000). Modeled and empirical approaches for retrieving columnar water vapor from solar transmittance measurements in the 0.72, 0.82 and 0.94  $\mu\text{m}$  absorption bands. *Journal of Geophysical Research*, 105(296):24327–24343.
- Jarlemark, P. (1997). *Analysis of Temporal and Spatial Variations in Atmospheric Water Vapor Using Microwave Radiometry*. PhD thesis, School of Electrical and Computer Engineering Chalmers University of Technology. Technical Report 308.
- Johansson, J., Elgered, G., and Davis, J. L. (1993). Wet Path Delay Algorithms for Use with Microwave Radiometer Data. *Contributions of Space Geodesy to Geodynamics Technology*, 25:81–98.

- Kruse, L. (2001). *Spatial and Temporal Distribution of Atmospheric Water Vapor using Space Geodetic Techniques*. Geodätisch-geophysikalische Arbeiten in der Schweiz, Volume 61, ETH Zurich, Schweizerische Geodätische Kommission.
- Kuntz, M. (1997). A new Implementation of the Humlicek Algorithm for the calculation of the Voigt Profile Function. *J. Quant. Spectrosc. Radiat. Transfer*, 57(6):819–824.
- Marini, J. W. (1972). Correction of satellite tracking data for an arbitrary tropospheric profile. *Radio Science*, 7(2):223–231.
- Mendes, V. B. and Langley, R. B. (2002). Revised refractive index formulae and their effect in zenith delay prediction and estimation. Position Location and Navigation Symposium 2002, Palm Springs, 15-18 April 2002.
- Mervart, L. (1995). Ambiguity Resolution Techniques in Geodetic and Geodynamic Applications of the Global Positioning System. Geodätisch-geophysikalische Arbeiten in der Schweiz, Band 53, Schweizerische Geodätische Kommission, Institut für Geodäsie und Photogrammetrie, Eidg. Technische Hochschule Zürich, Zürich.
- Niell, A. (1996). Global Mapping Functions for the Atmospheric Delay at Radio Wavelengths. *Journal of Geophysical Research*, 101(B2):3227–3246.
- Partridge, H. and Schwenke, D. W. (1997). The determination of an accurate isotope dependent potential energy surface for water from extensive ab initio calculations and experimental data. *J. Chem. Phys.*, 106:4618–4639.
- Platt, U. (1994). *Differential Optical Absorption Spectroscopy (DOAS), in Air Monitoring by Spectroscopic Techniques*. John Wiley & Sons, Inc., 605 Third Avenue, New York.
- Rodgers, C. D. (2000). *Inverse methods for atmospheric sounding: Theory and practice*, volume 2 of *Series on Atmospheric Oceanic and Planetary Physics*. World Scientific Pub Co Inc. ISBN: 981022740X.
- Rothacher, M. (1992). Orbits of Satellite Systems in Space Geodesy. Geodätisch-geophysikalische Arbeiten in der Schweiz, Band 46, Schweizerische Geodätische Kommission, Institut für Geodäsie und Photogrammetrie, Eidg. Technische Hochschule Zürich, Zürich.
- Rothman, L., Rinsland, C., Goldman, A., Massie, S., Edwards, D., Flaud, J.-M., Perrin, A., Donna, V., Mandin, J.-Y., Schroeder, J., McCann, A., Gamache, R., Wattson, R., Yoshino, K., Chance, K., Jucks, K., Brown, L., Nemtchinov, V., and Varanasi, P. (1998). The HITRAN molecular database and HAWKS (HITRAN Atmospheric Workstation). *J. Quant. Spectrosc. Radiat. Transf.*, 60:665–710.

- Rothman, L. S., Barbe, A., Benner, D. C., Brown, L. R., Camy-Peyret, C., Carleer, M. R., Chance, K., Clerbaux, C., Dana, V., Devi, V. M., A. Fayt, J.-M. F., Gamache, R. R., Goldman, A., Jacquemart, D., Jucks, K. W., Lafferty, W. J., Mandin, J.-Y., Massie, S. T., Nemtchinov, V., Newnham, D. A., Perrin, A., Rinsland, C. P., Schroeder, J., Smith, K. M., Smith, M. A. H., Tnag, K., Toth, R. A., Auwera, J. V., Varanasi, P., and Yoshino, K. (2003). The HITRAN molecular spectroscopic database: edition of 2000 including updates through 2001. *Journal of Quantitative Spectroscopy and Radiative Transfer* 82, pages 5–44.
- Saastamoinen, J. (1972). Atmospheric correction for the troposphere and stratosphere in radio ranging of satellites. In: *Henriksen, S.W.; Mancini, A.; Chovitz, B.H. (ed.): The use of artificial satellites for geodesy, Geophys. Monogr. Ser., AGU, Vol. 15:247–251.*
- Saastamoinen, J. (1973). Contributions to the Theory of Atmospheric Refraction / Introduction to Practical Computation of Astronomical Refraction. Bulletin géodésique Nrs 105, 106, 107, pp.50.
- Schaer, S. (1999). *Mapping and Predicting the Earth's Ionosphere Using the Global Positioning System*. PhD thesis, University of Berne, Astronomical Institute.
- Scharroo, R., Lillibridge, J. L., and Smith, W. H. F. (2004). Cross-Calibration and Long-Term Monitoring of the Microwave Radiometers of ERS, TOPEX, GFO, Jason, and ENVISAT. *Marine Geodesy*, 27:279–297.
- Schödlbauer, A. (1999). *Geodätische Astronomie: Grundlagen und Konzepte*. Nummer 3-11-015148-0. de Gruyter, Berlin; New York.
- Schermaul, R., Learner, R. C. M., Newnham, D. A., Williams, R. G., Ballard, J., Zobov, N. F., Belmiloud, D., and Tennyson, J. (2001). The water vapour spectrum in the region 8600 – 1500  $cm^{-1}$ : experimental and theoretical studies for a new spectral line database i: laboratory measurements. *Journal of Molecular Spectroscopy*, 208:32–42.
- Seeber, G. (2003). *Satellite Geodesy: Foundations, Methods, and Applications*. de Gruyter, 2. edition.
- Seko, H., Shimada, S., Nakamura, H., and Kato, T. (2000). Three-dimensional distribution of water vapor estimated from tropospheric delay of GPS data in a mesoscale precipitation system of the baiu front. *Earth Planets Space*, 52:927–933.
- Sierk, B. (2000). Solar spectrometry for determination of tropospheric water vapor. *Dissertation No. 13850, Swiss Federal Institute of Technology Zurich*.
- Sierk, B., Bürki, B., Becker-Ross, H., Florek, S., Neubert, R., Kruse, L., and Kahle, H.-G. (1997). Tropospheric water vapor derived from solar spectrometer, radiometer, and GPS measurements. *Journal of Geophysical Research*, Vol. 102, No. B10, p. 22411 - 22424.

- Sierk, B., Solomon, S., Daniel, J. S., Portmann, R. W., Gutman, S. I., Langford, A. O., Eubank, C. S., Dutton, E. G., and Holub, K. H. (2004). Field measurement of water vapor continuum absorption in the visible and near-infrared. *Journal of Geophysical Research*, 109(D08307).
- Sigrist, M. (1994). *Air Monitoring by Spectroscopic Techniques*. John Wiley & Sons, Inc., 605 Third Avenue, New York.
- Somieski, A. (2000). Aufbau und Inbetriebnahme von Wasserdampfadiometerstationen und Untersuchungen zur geographischen und jahreszeitlichen Variation der Inversionskoeffizienten in der Mikrowellenradiometrie im Rahmen des KFKI-Projektes NN-SAT. Diplomarbeit, TU Dresden, Geodätisches Institut.
- Somieski, A., Bürki, B., Cocard, M., Geiger, A., and Kahle, H.-G. (2002). Water Vapor Remote Sensing Techniques: Water Vapor Radiometry and Solar Spectrometry. *Geophysical Research Abstract*, (4).
- Somieski, A., Bürki, B., Geiger, A., Kahle, H.-G., Pavlis, E. C., Becker-Ross, H., Florek, S., and Okruss, M. (2004). Tropospheric Water Vapor, Solar Spectrometry, and Comparison with JASON Microwave Radiometer Measurements. *submitted to Journal of Geophysical Research - Atmosphere*, (6).
- Somieski, A., Bürki, B., Kahle, H.-G., Becker-Ross, H., Florek, S., and Okruss, M. (2003). Geodetic mobile solar spectrometer: Description of the new spectrometer gemoss and first measurements. *Geophysical Research Abstract*, (5).
- Stingl, P. (1992). *Mathematik für Fachhochschulen: Technik und Informatik*. Studienbücher der technischen Wissenschaften. Carl Hanser Verlag, München Wien, 4. edition.
- Teunissen, P. and Kleusberg, A. (1998). *GPS for Geodesy*. Springer, ISBN 3-540-63661-7.
- Thayer, G. (1974). An improved equation for the radio refractive index of air. *Radio Sci.*, 9:803–807.
- Tolchenov, R. N., Tanaka, M., Tennyson, J., Zobov, N. F., Shirin, S. V., Polyansky, O. L., and Maurellis, A. N. (2003). Water line intensities in the near-infrared and visible. *Journal of Quantitative Spectroscopy and Radiative Transfer*, 82:151–163.
- Troller, M. (2004). *GPS based Determination of the Integrated and Spatially Distributed Water Vapor in the Troposphere*. PhD thesis, Diss. ETH No. 15513, Swiss Federal Institute of Technology Zurich.
- Vleck, J. V. and Huber, D. (1974). Absorption, emission and linebreadths: A semi-historical perspective. *Reviews of Modern Physics*, 49(4):939 – 959.

- Wu, S. (1979). Optimum Frequencies of a passive Microwave Radiometer for Tropospheric Path-Length Correction. *IEEE Trans. Ant. and Prop.*, AP-27, No. 2:233 – 239.
- Zlotnicki, V. and Desai, S. D. (2004). Assessment of the Jason Microwave Radiometer's Measurements of Wet Tropospheric Path Delay Using Comparisons to SSM/I and TMI. *Marine Geodesy*, 27:241–253.
- Zuev, V. E. (1974). *Propagation of visible and infrared radiation in the atmosphere*. John Wiley & Sons, New York.



# A Statistic

The mean value  $\bar{x}$  of a data set with  $n$  measurements  $x_i$  is found by:

$$\bar{x} = \frac{\sum_{i=1}^n x_i}{n} \quad (\text{A.1})$$

The standard deviation  $\sigma$  of the data set is:

$$\sigma = \sqrt{\frac{1}{n-1} \sum_{i=1}^n (x_i - \bar{x})^2} \quad (\text{A.2})$$

The quantity  $\sigma^2$  is denoted as variance.

The standard error of the mean  $\bar{x}$  is given by:

$$sem = \frac{\sigma}{\sqrt{n}} \quad (\text{A.3})$$

The root mean square is defined by:

$$rms = \sqrt{\frac{\sum_{i=1}^n x_i^2}{n}} \quad (\text{A.4})$$

## B GEMOSS - Solar Spectrum

The following figures show two solar spectra measured with GEMOSS at ETH Höggerberg (Zurich). The spectra were acquired on January 31<sup>th</sup> 2004 at 12 and 15 UT, respectively.

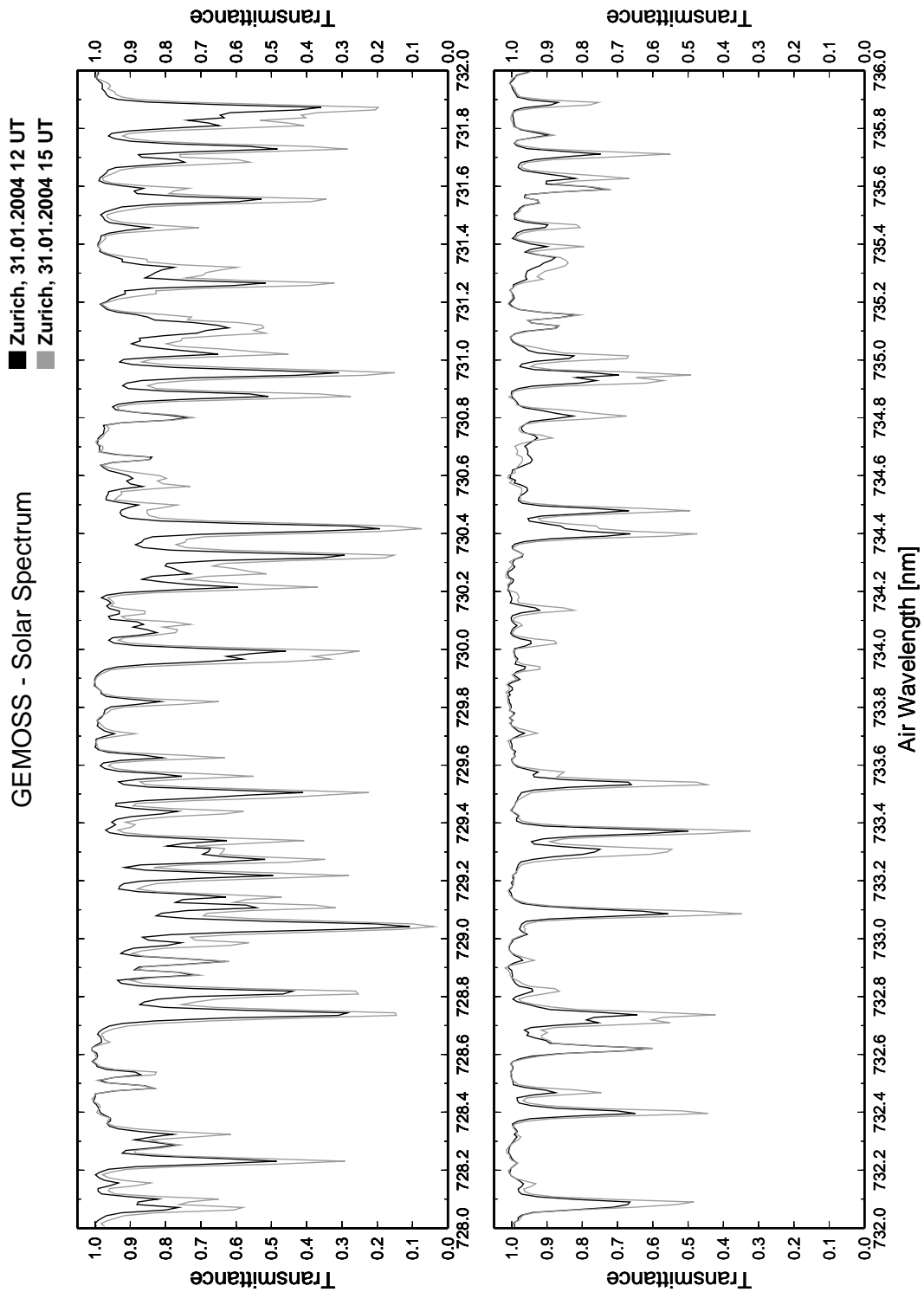


Figure B.1: Solar spectrum measured by GEMOSS between 728 and 736 nm.

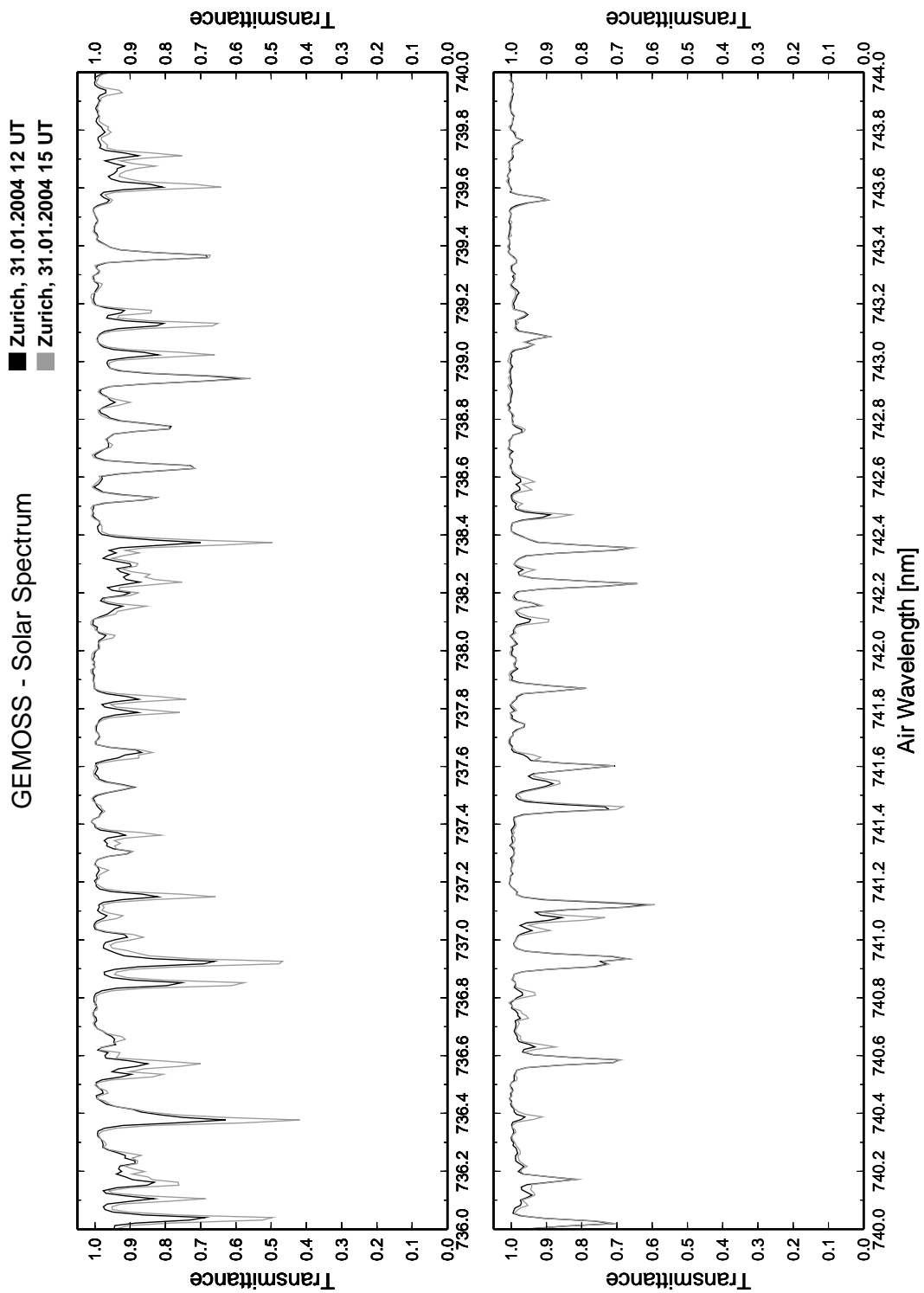


Figure B.2: Solar spectrum measured by GEMOSS between 736 and 744 nm.

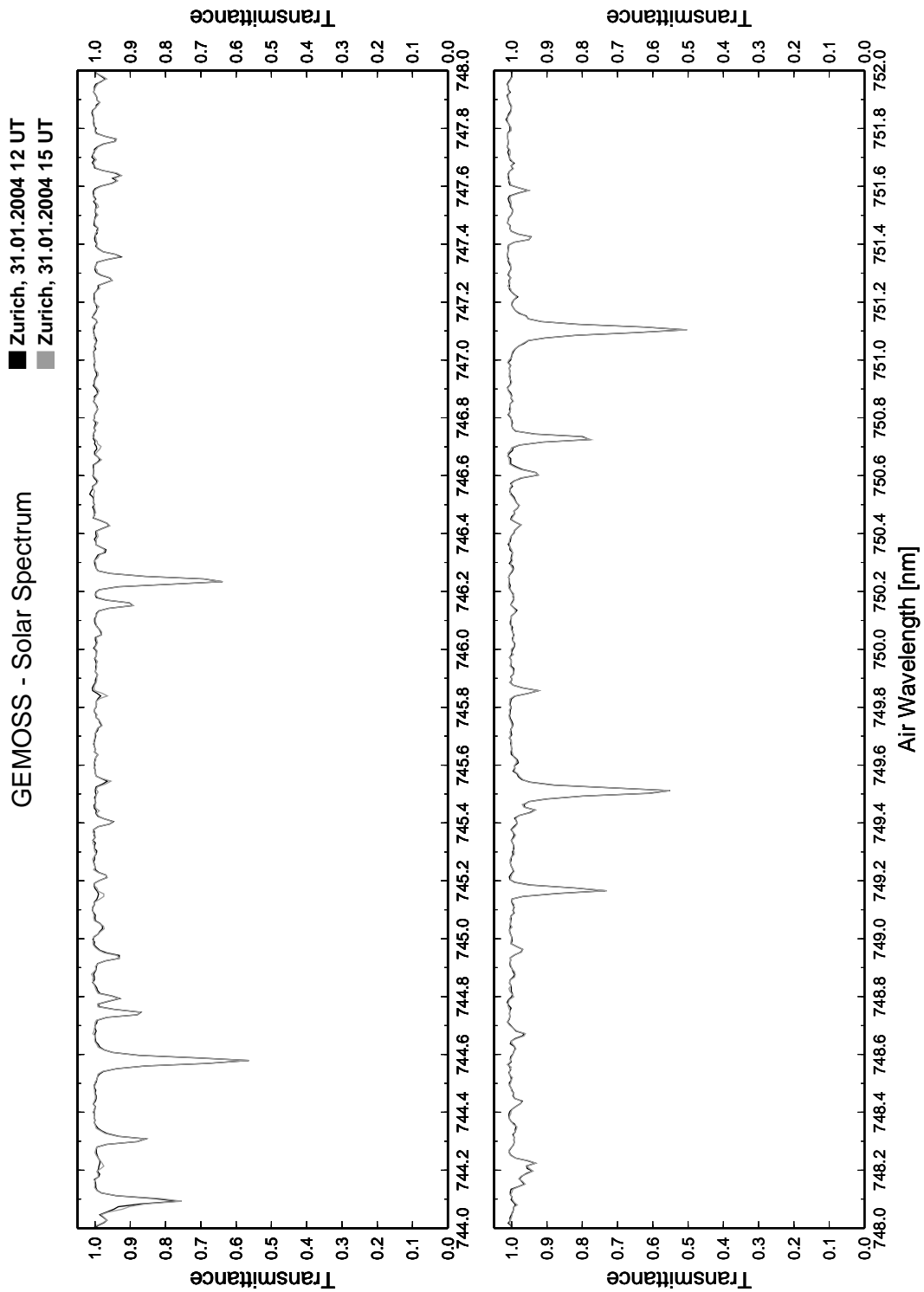


Figure B.3: Solar spectrum measured by GEMOSS between 744 and 752 nm.

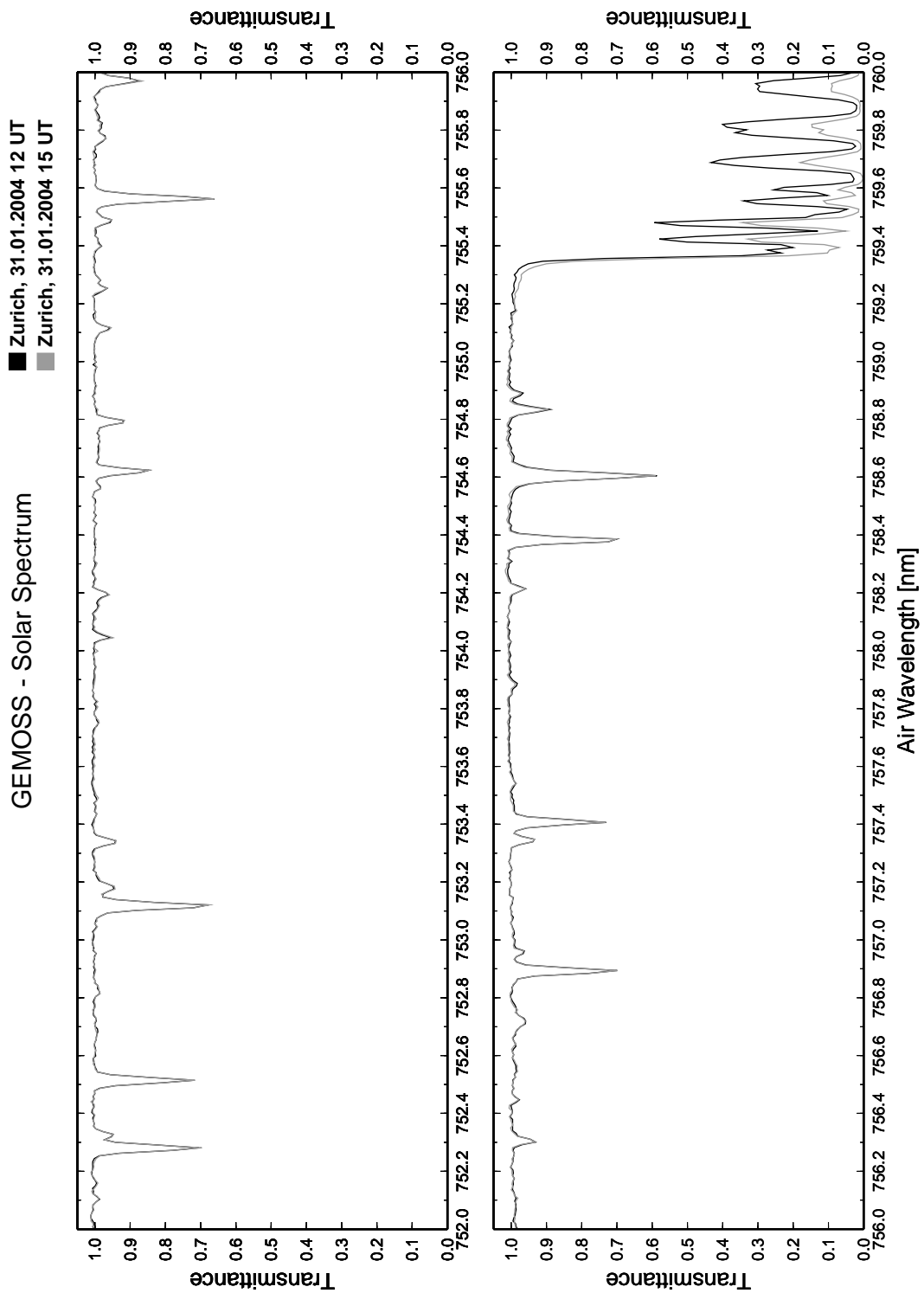


Figure B.4: Solar spectrum measured by GEMOSS between 752 and 760 nm.

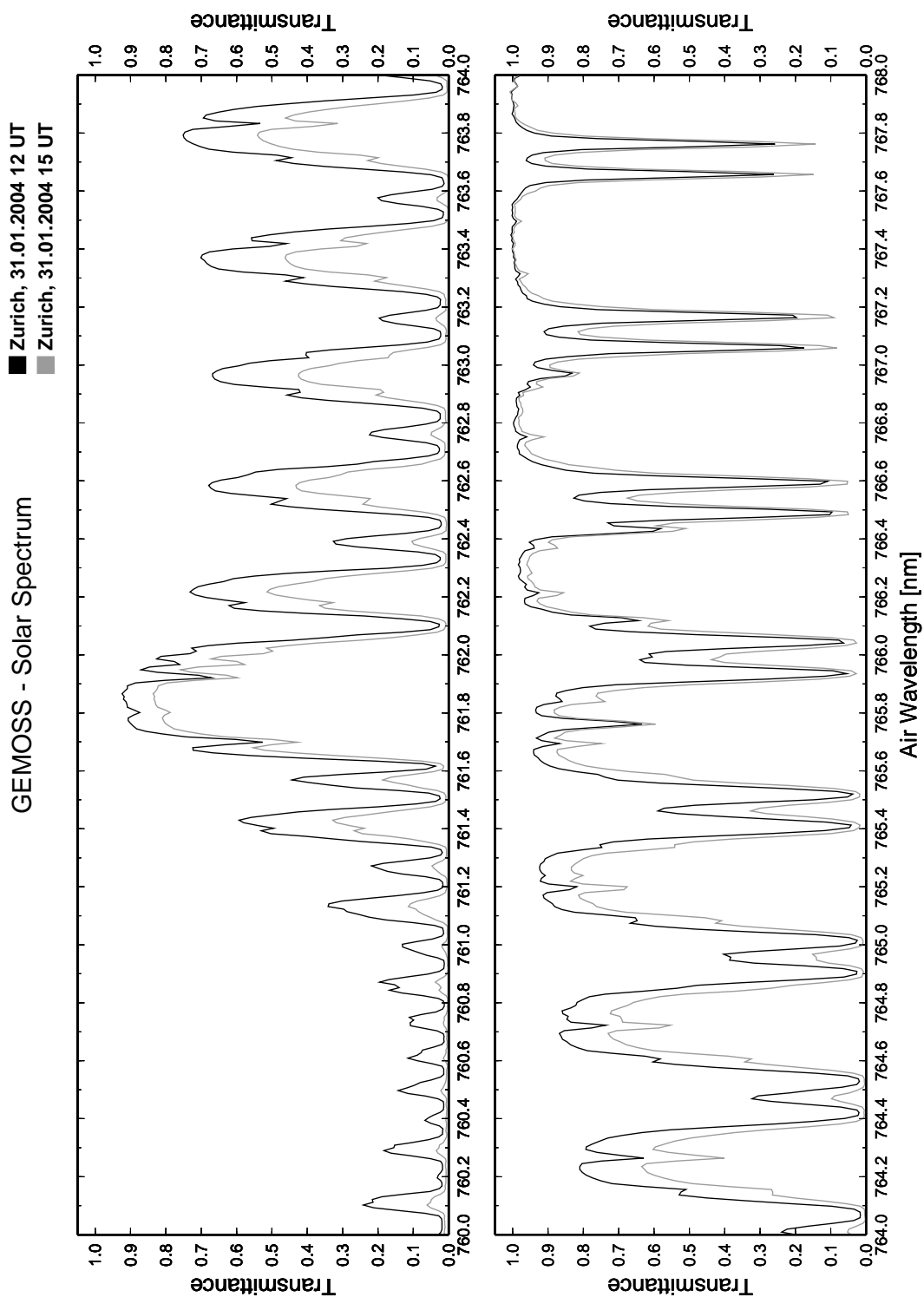


Figure B.5: Solar spectrum measured by GEMOSS between 760 and 768 nm.

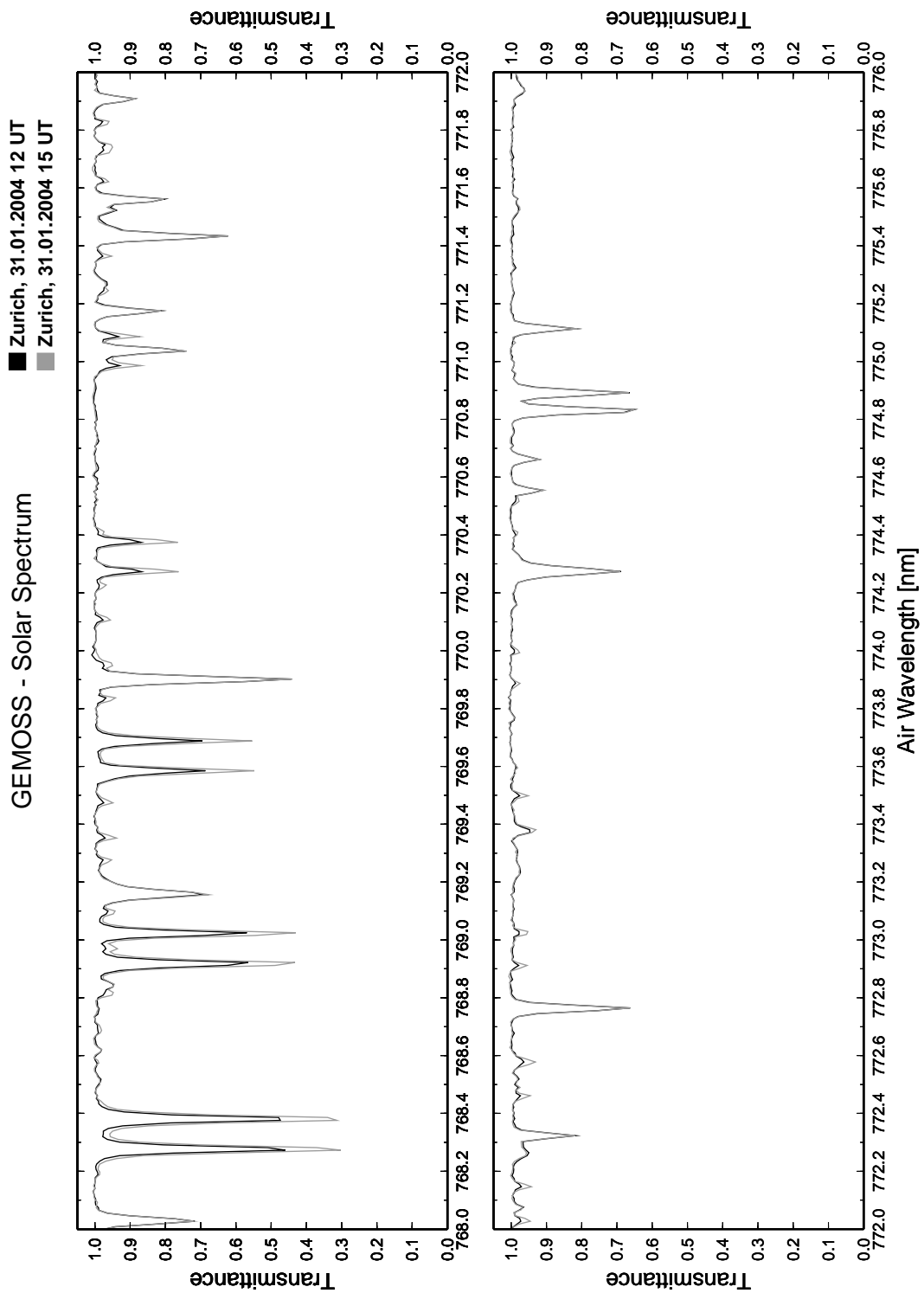


Figure B.6: Solar spectrum measured by GEMOSS between 768 and 776 nm.

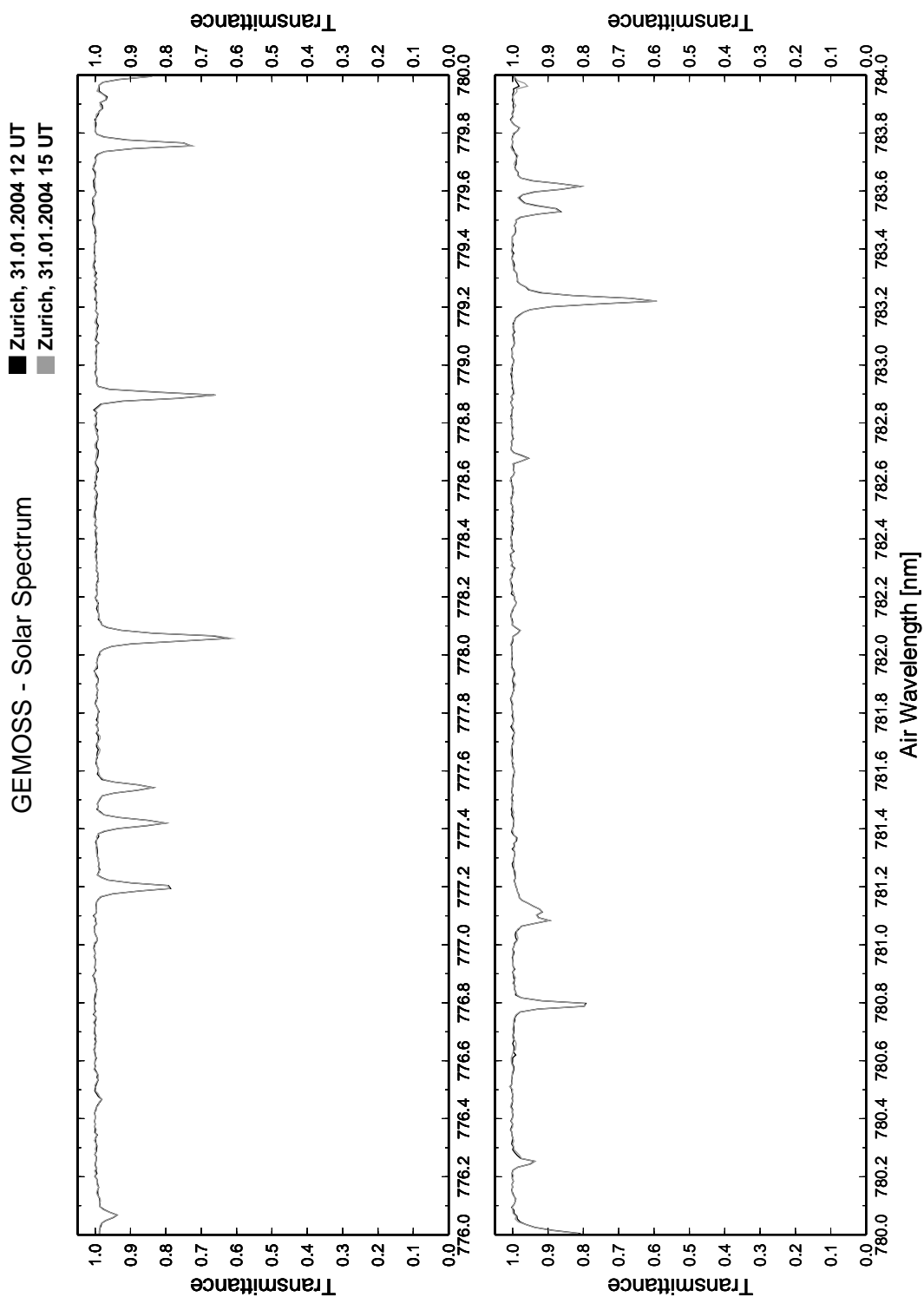


Figure B.7: Solar spectrum measured by GEMOSS between 776 and 784 nm.

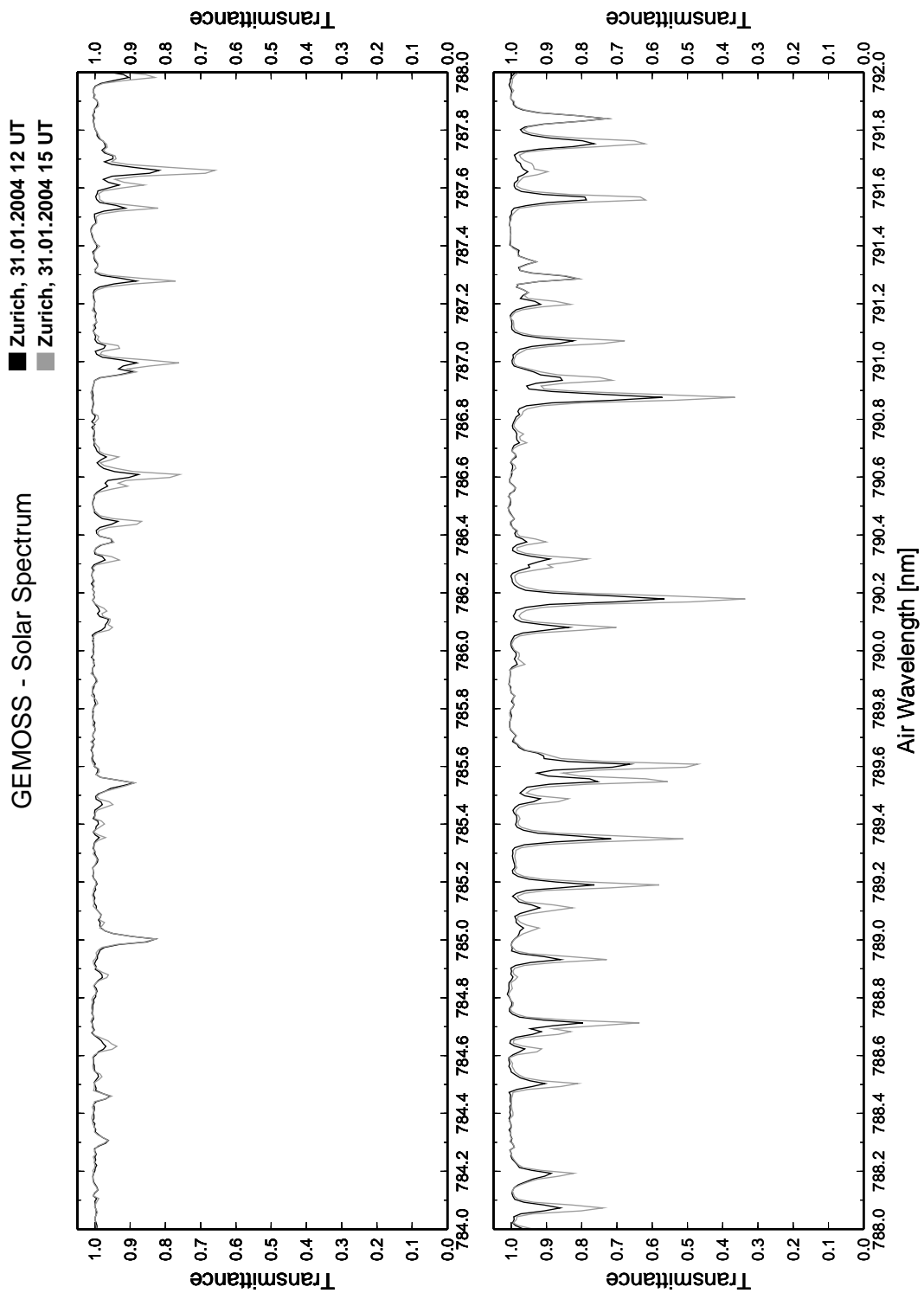


Figure B.8: Solar spectrum measured by GEMOSS between 784 and 792 nm.

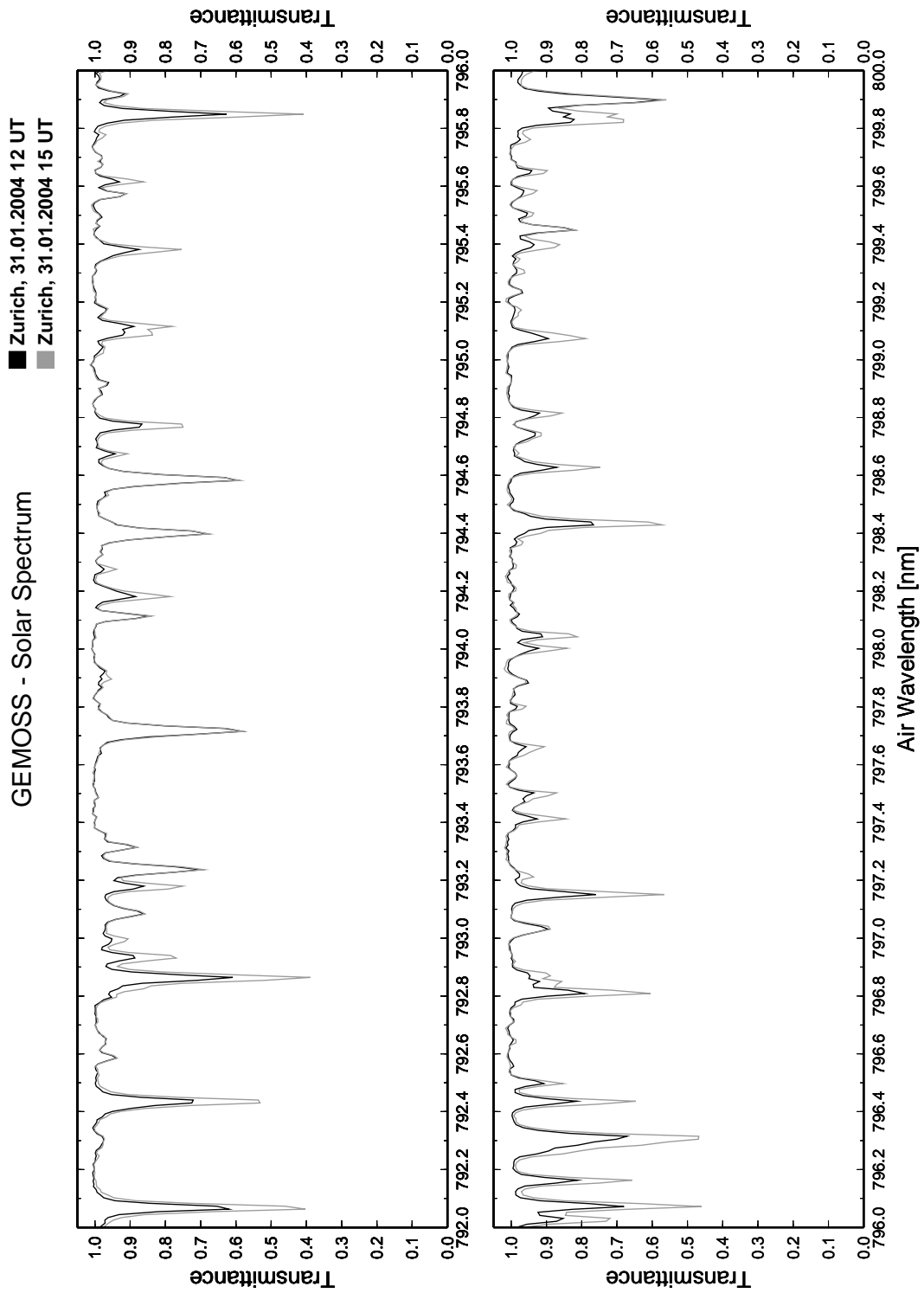


Figure B.9: Solar spectrum measured by GEMOSS between 792 and 800 nm.

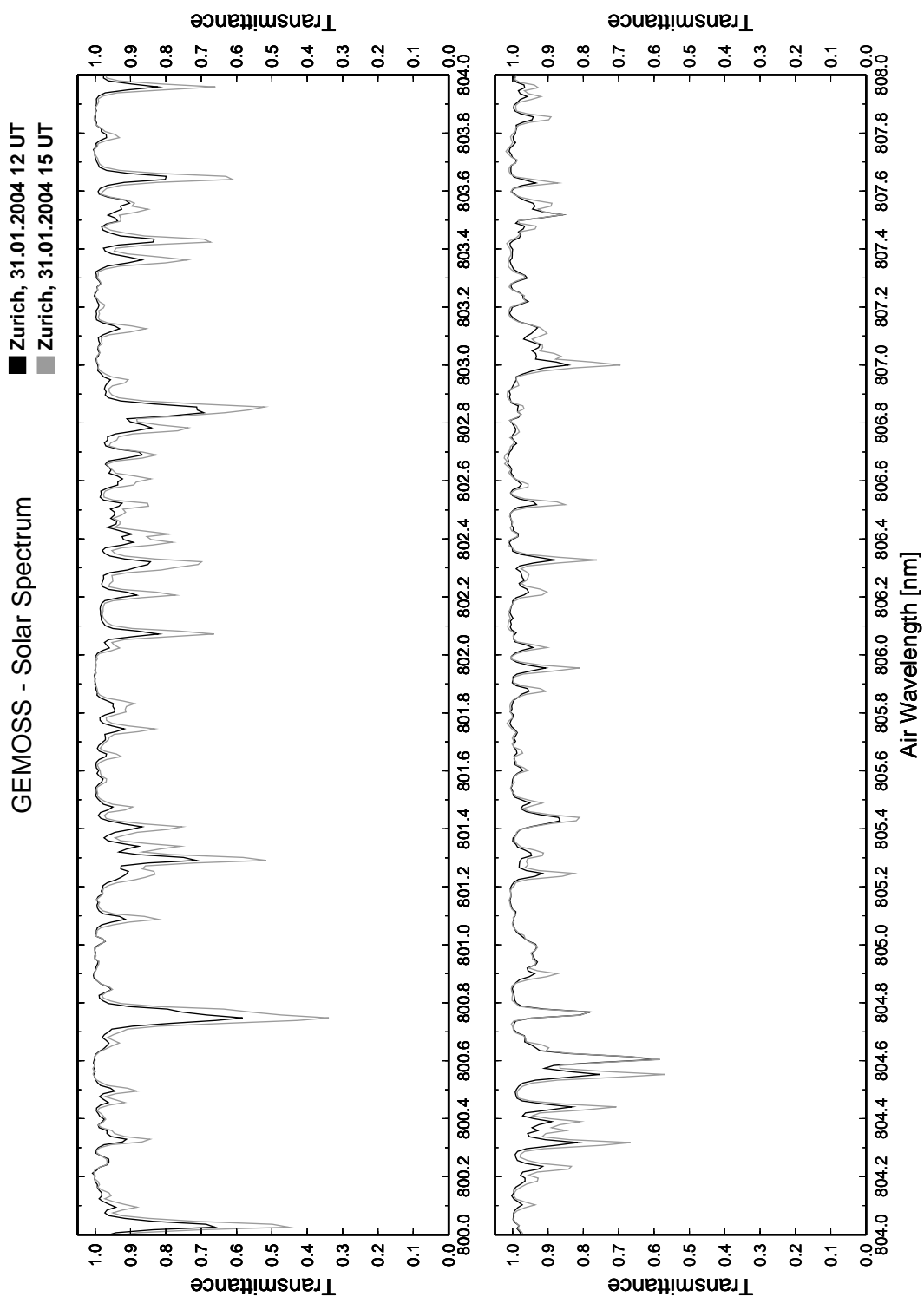


Figure B.10: Solar spectrum measured by GEMOSS between 800 and 808 nm.

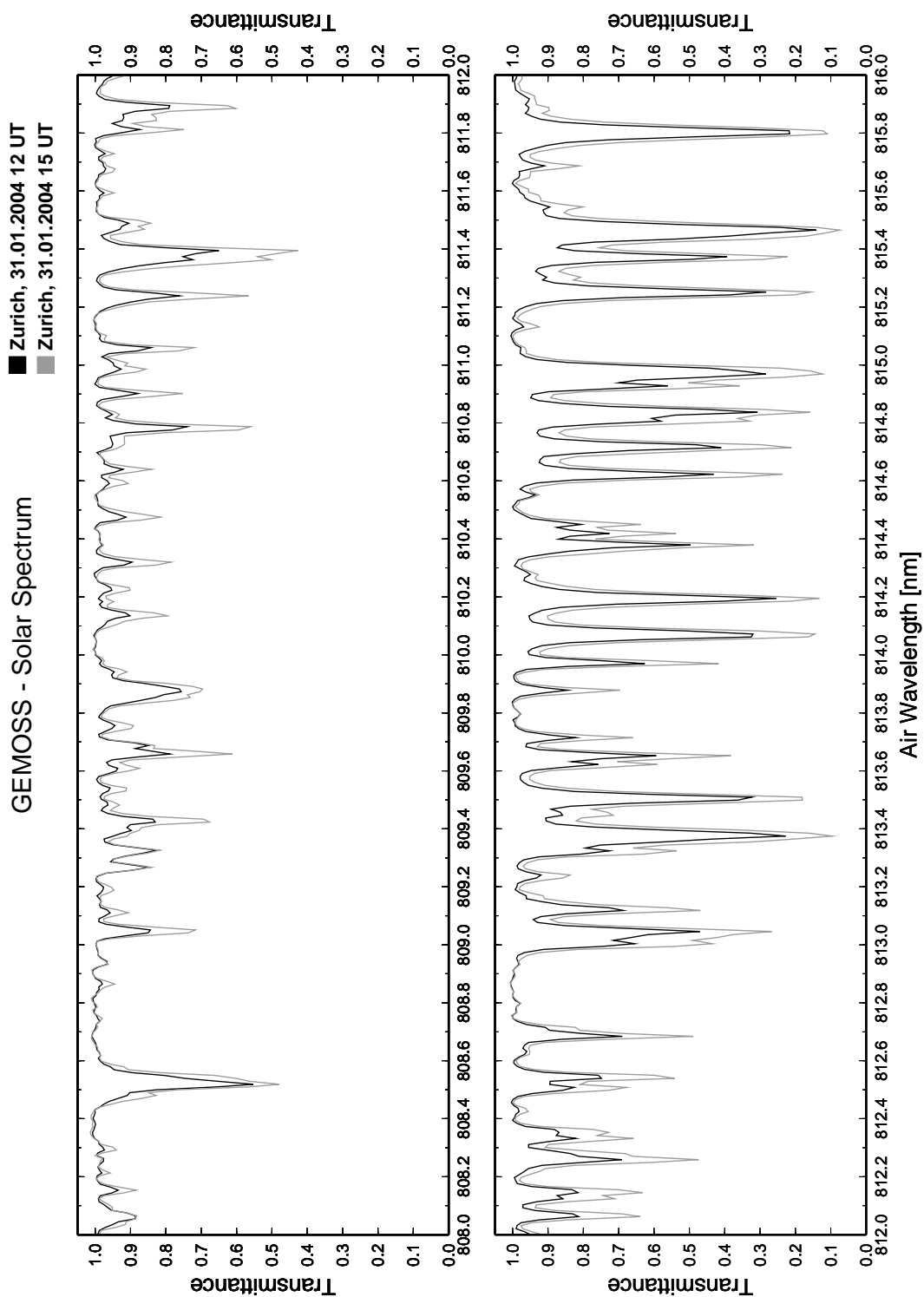


Figure B.11: Solar spectrum measured by GEMOSS between 808 and 816 nm.

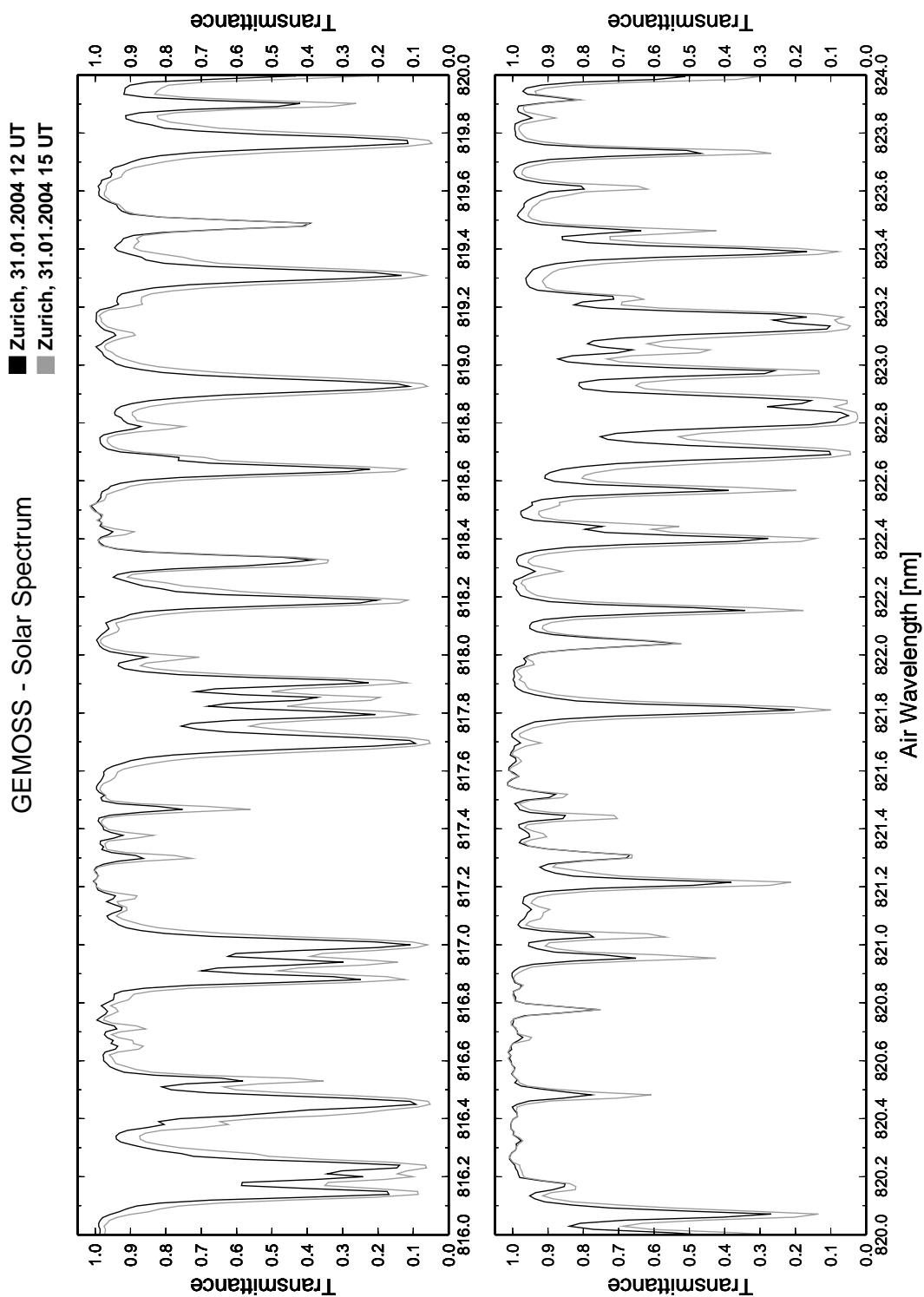


Figure B.12: Solar spectrum measured by GEMOSS between 816 and 824 nm.

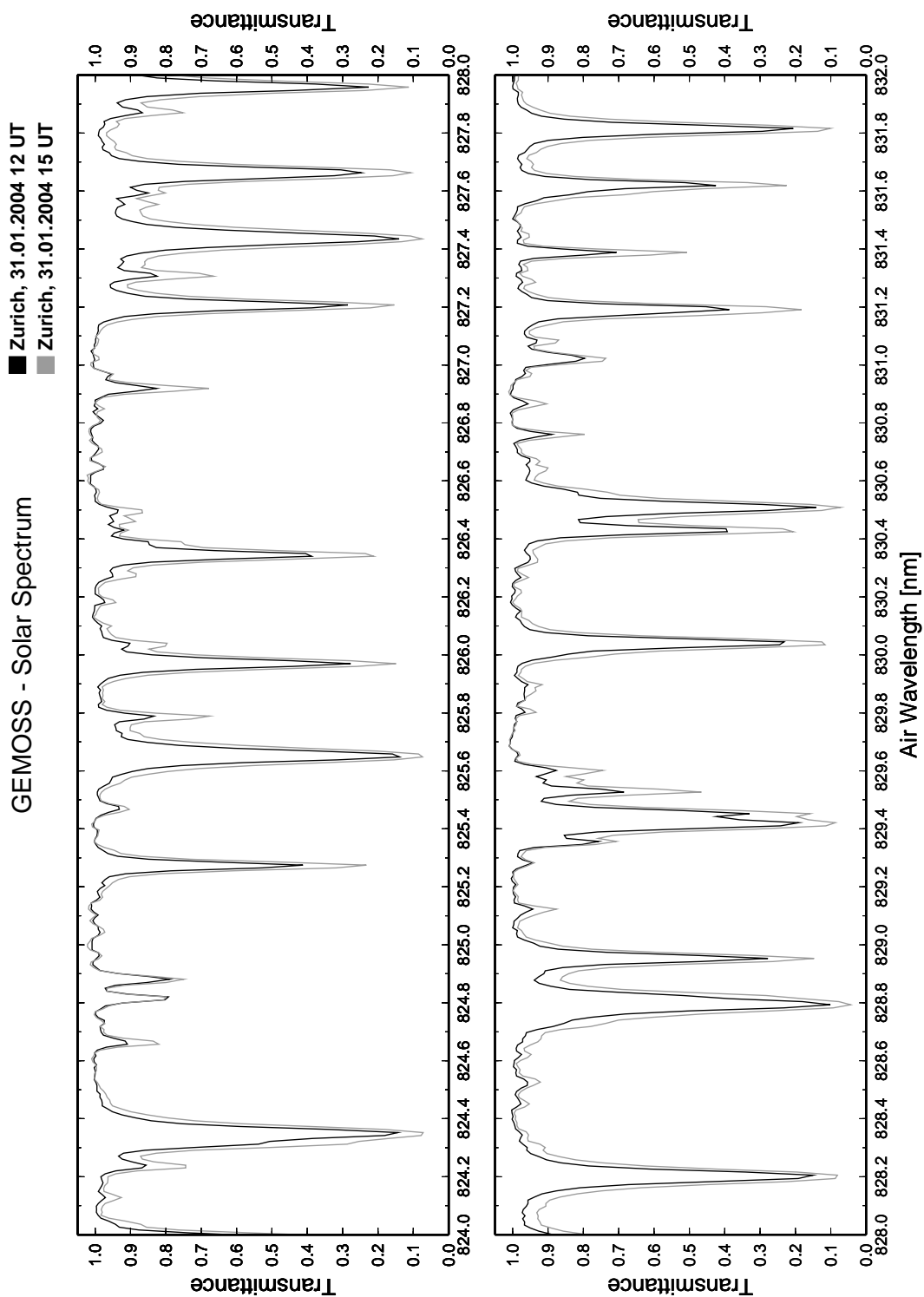


Figure B.13: Solar spectrum measured by GEMOSS between 824 and 832 nm.

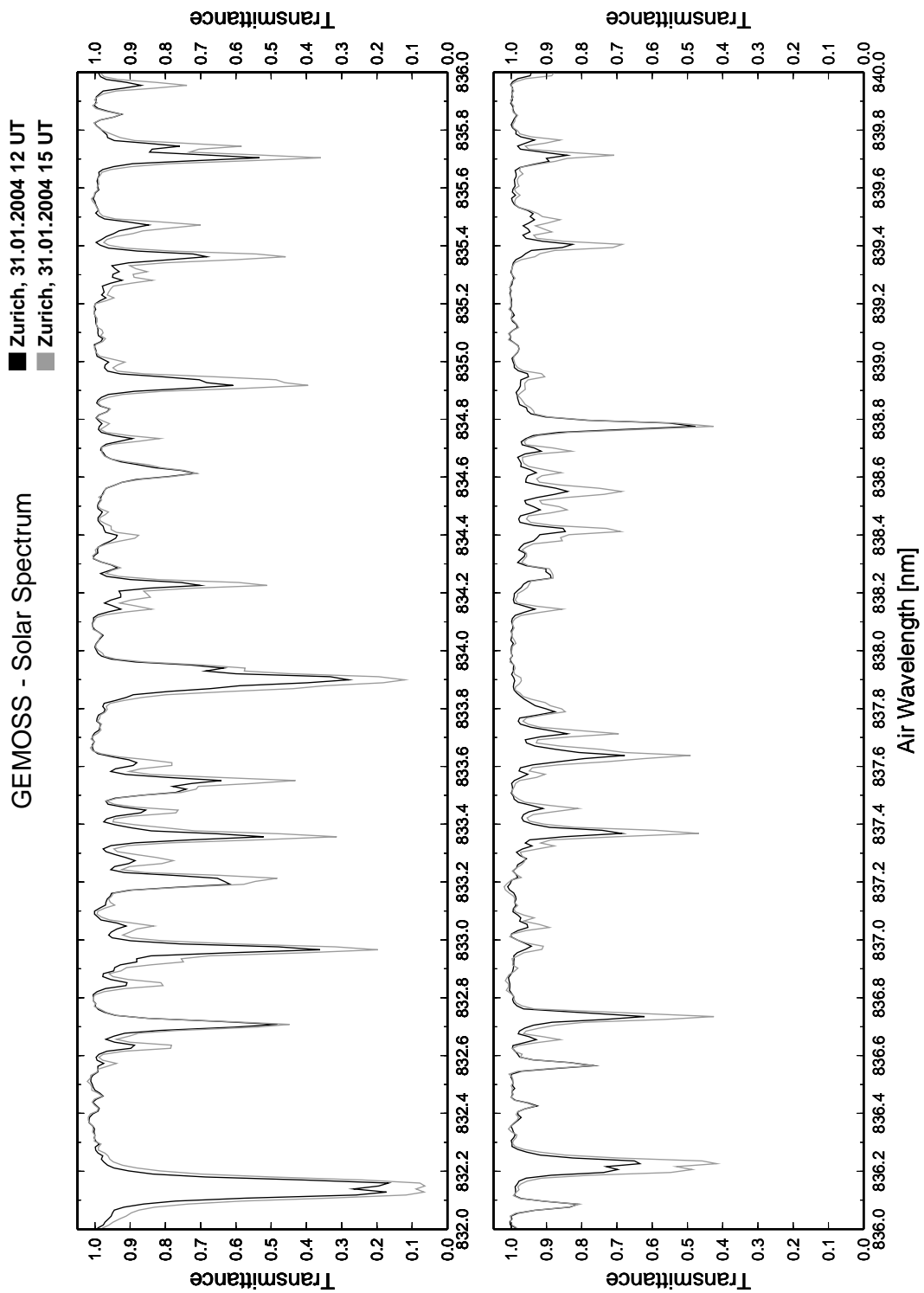


Figure B.14: Solar spectrum measured by GEMOSS between 832 and 840 nm.

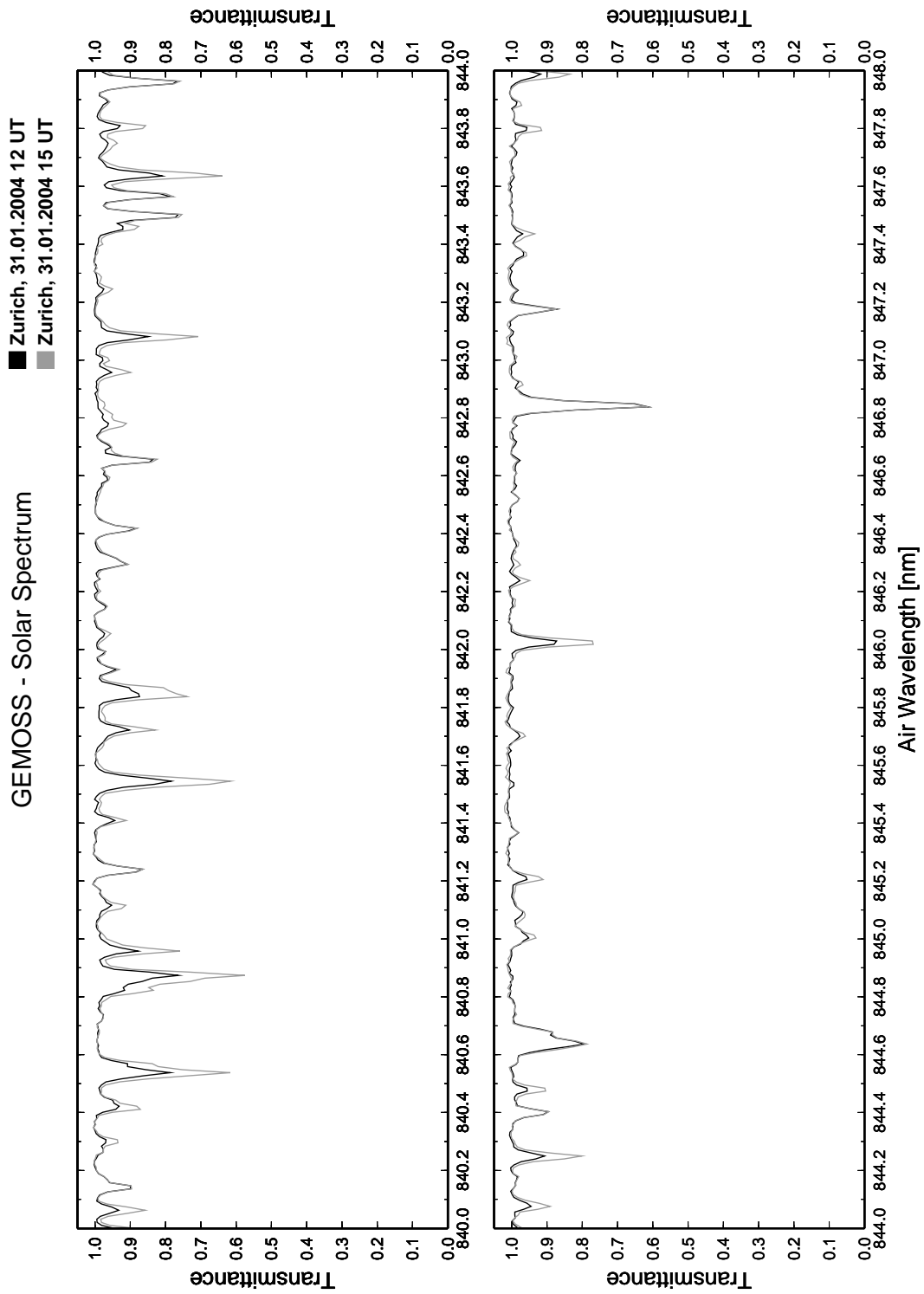


Figure B.15: Solar spectrum measured by GEMOSS between 840 and 848 nm.

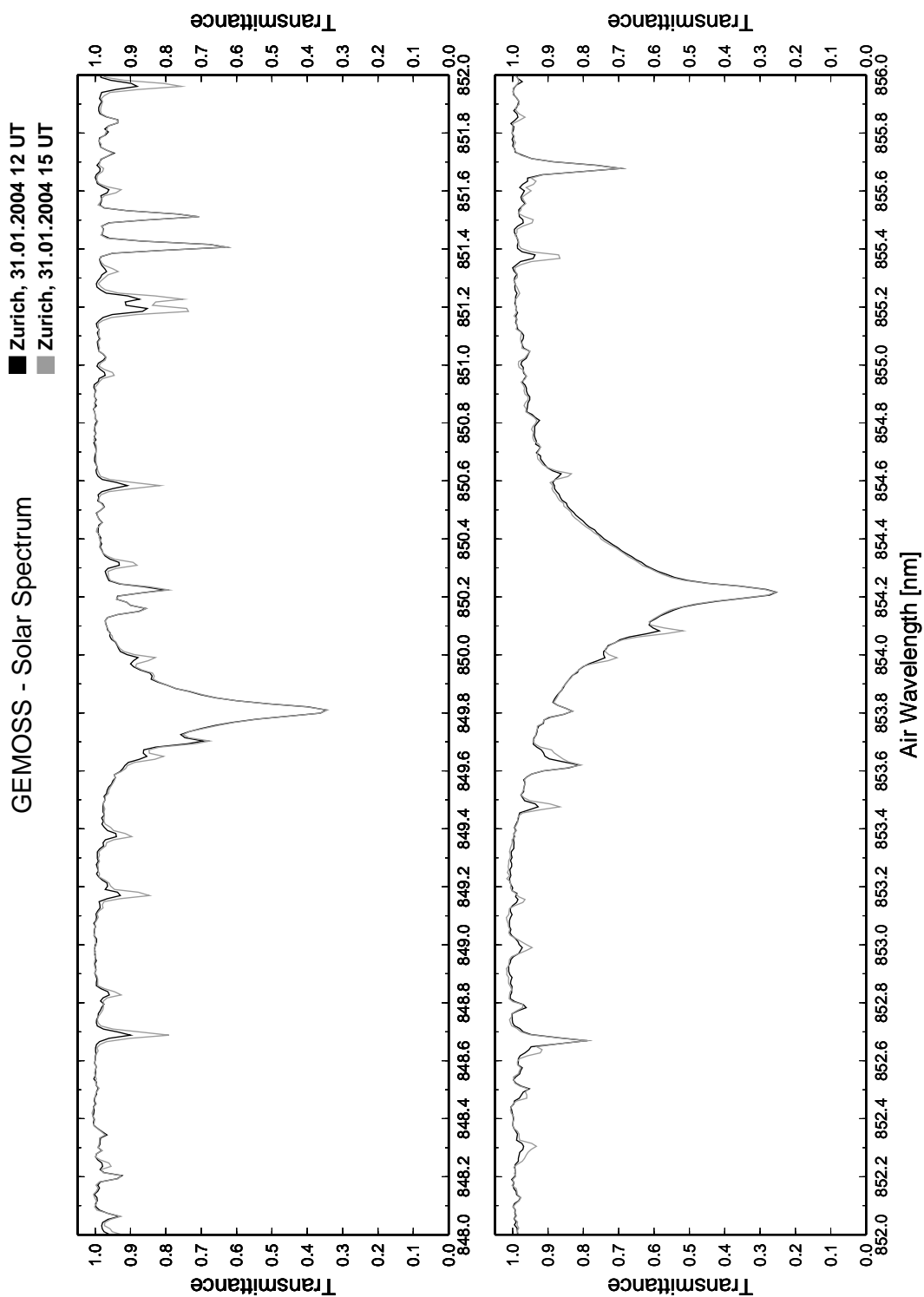


Figure B.16: Solar spectrum measured by GEMOSS between 848 and 856 nm.

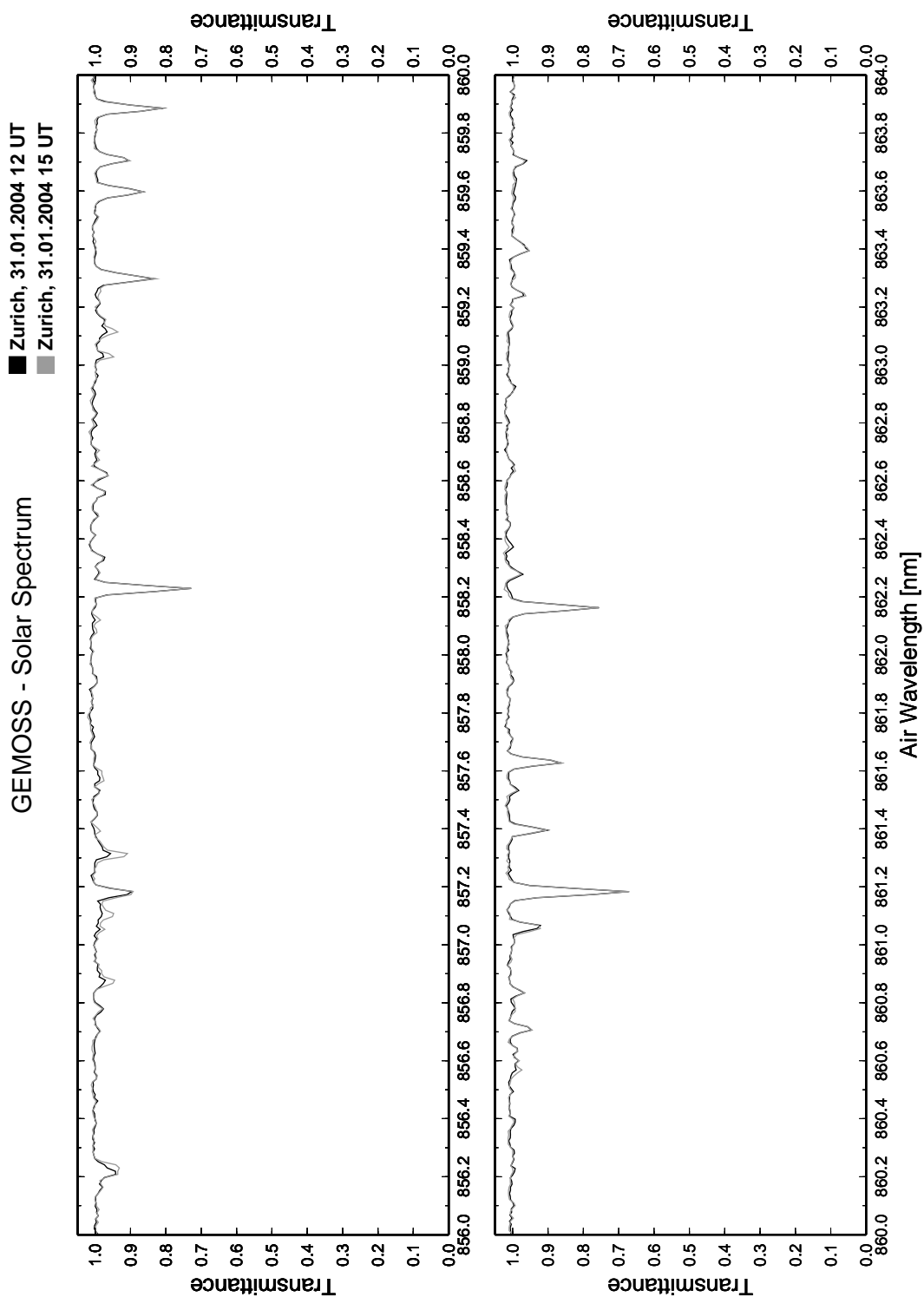


Figure B.17: Solar spectrum measured by GEMOSS between 856 and 864 nm.

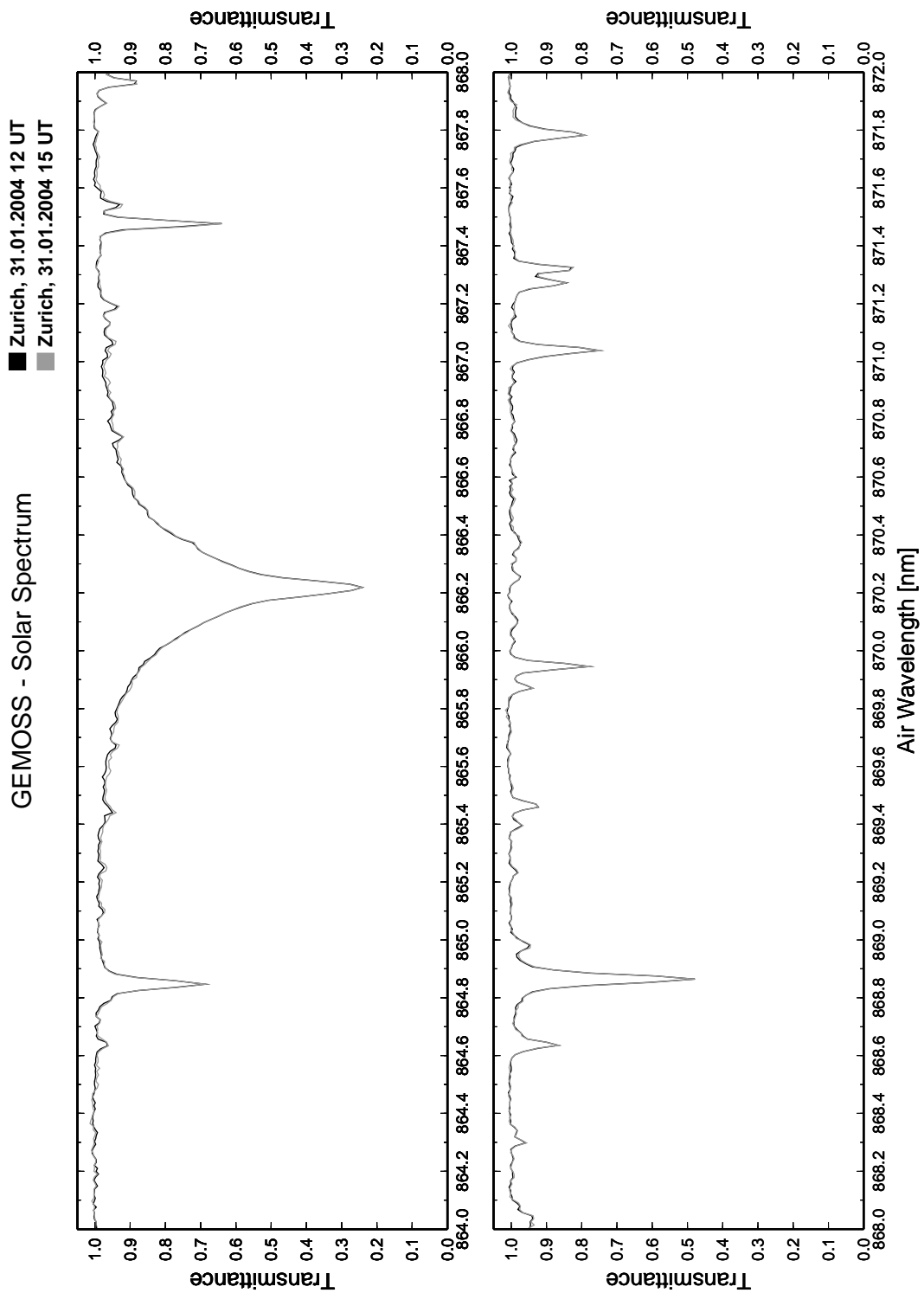


Figure B.18: Solar spectrum measured by GEMOSS between 864 and 872 nm.

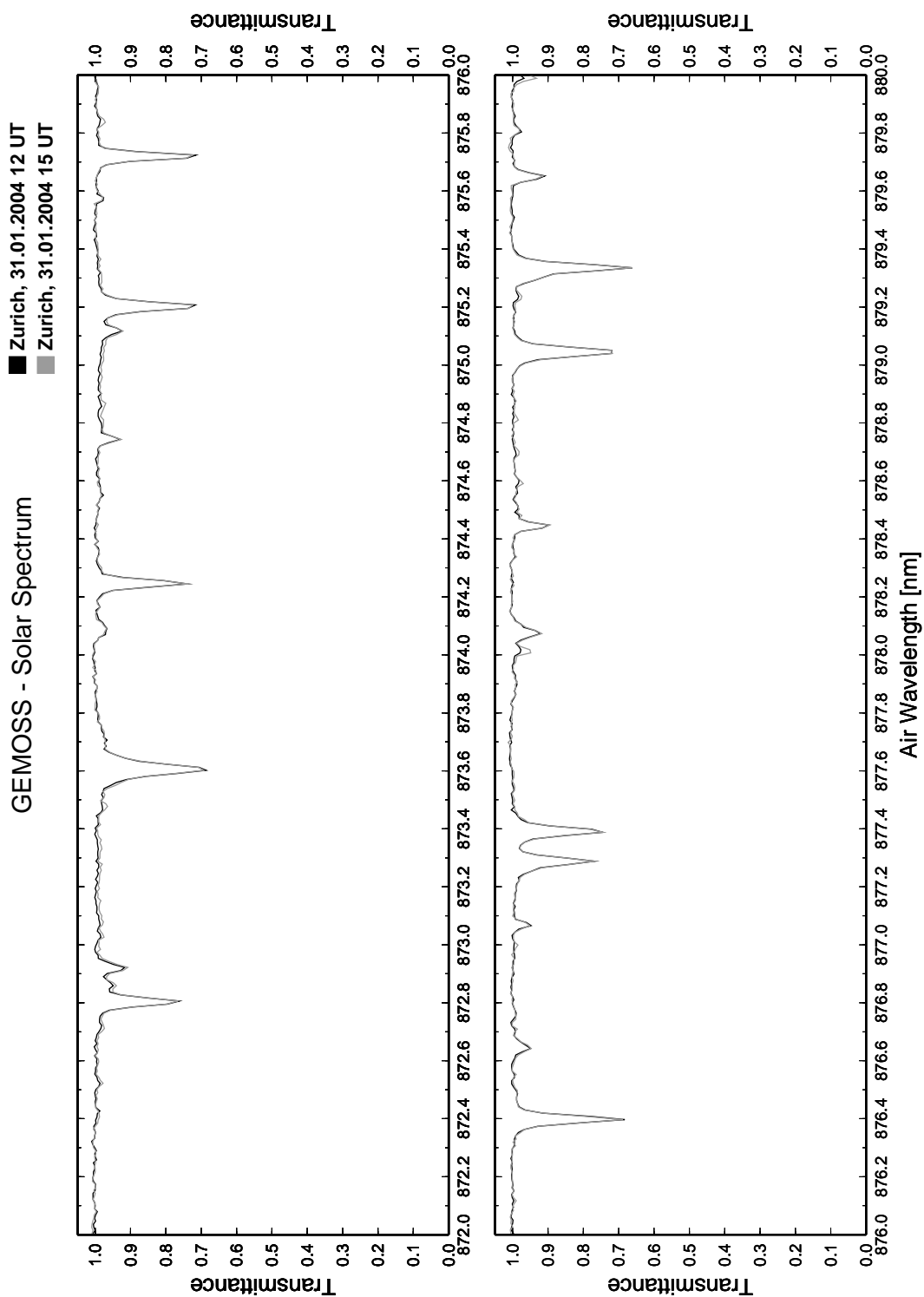


Figure B.19: Solar spectrum measured by GEMOSS between 872 and 880 nm.

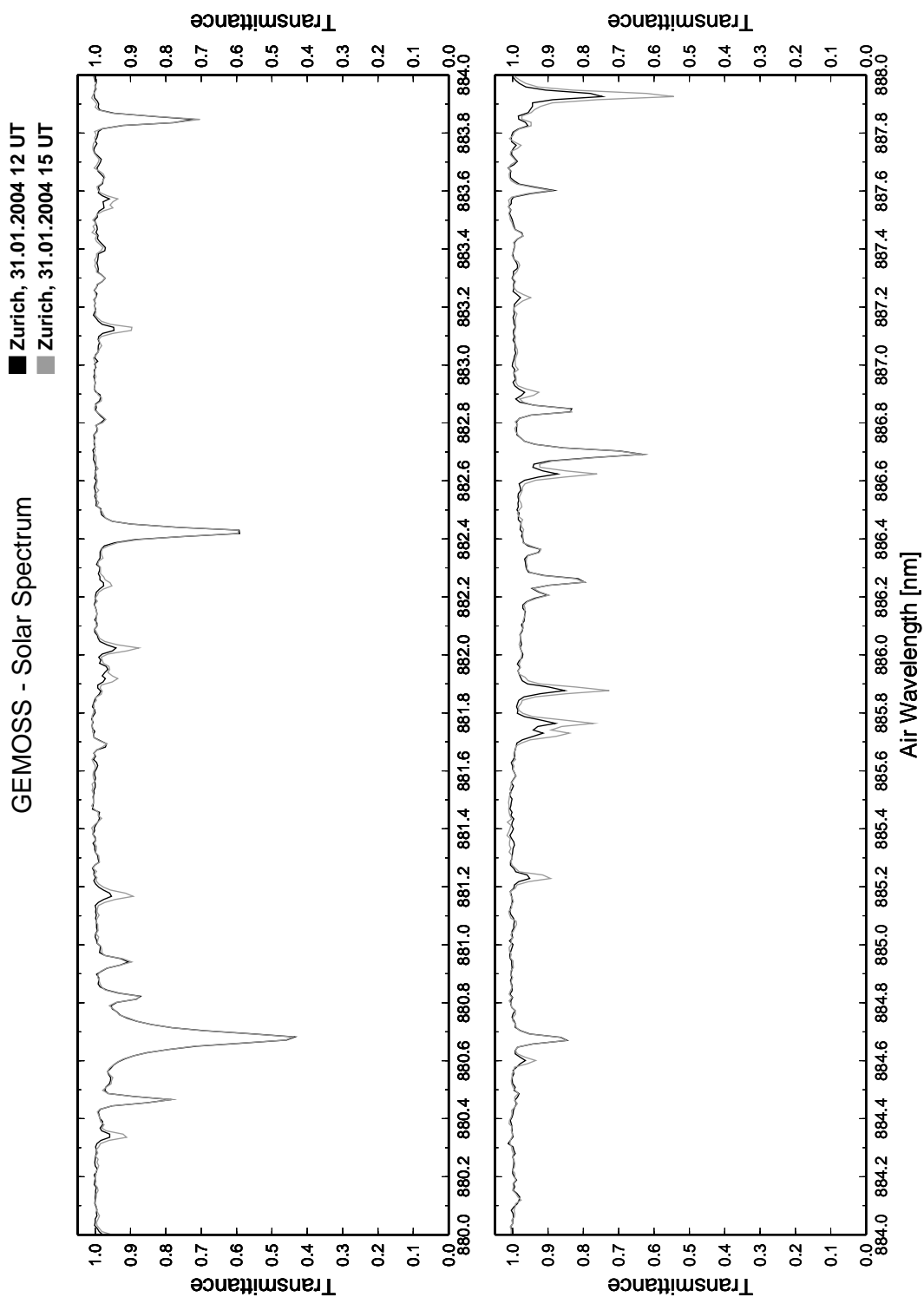


Figure B.20: Solar spectrum measured by GEMOSS between 880 and 888 nm.

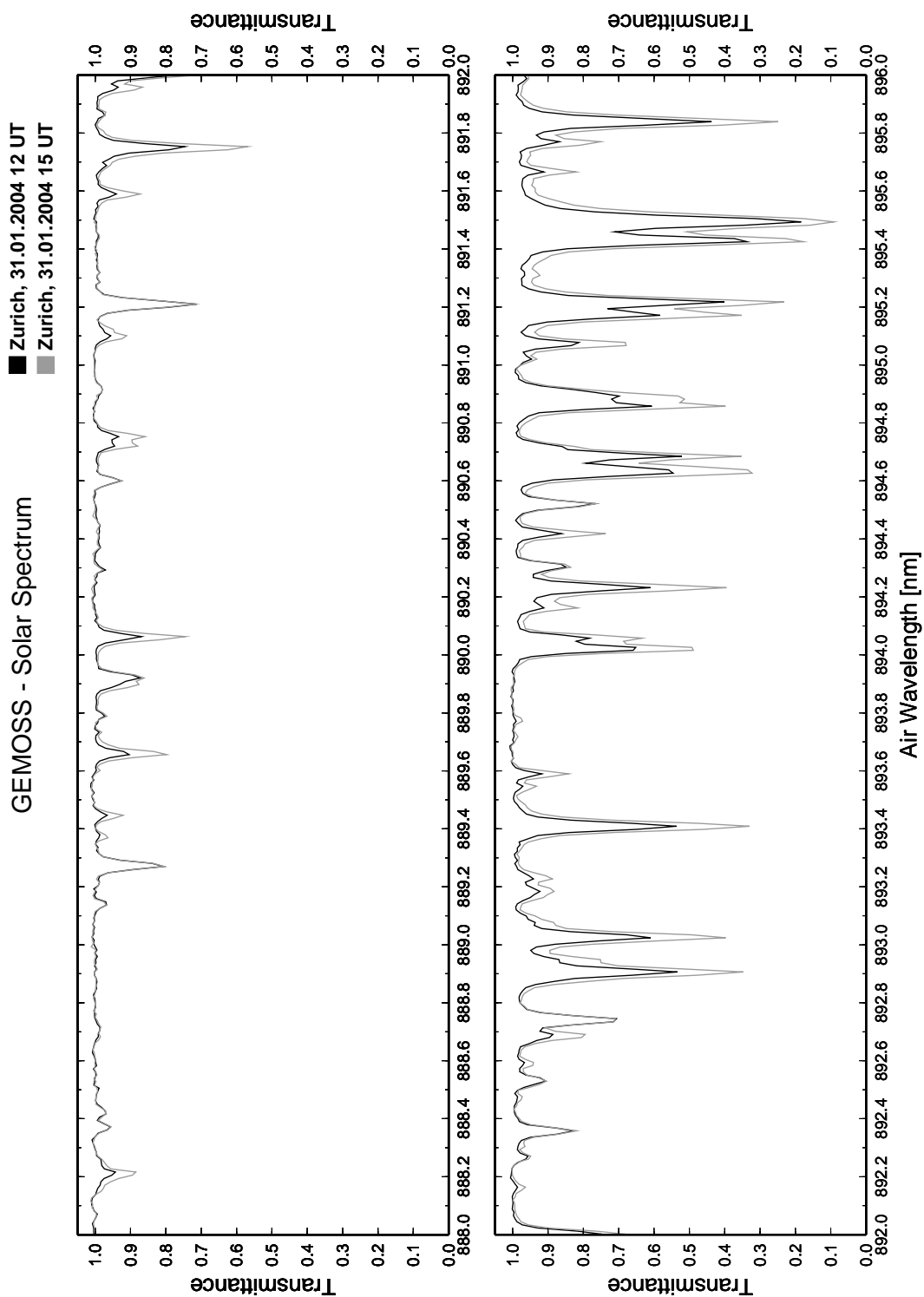


Figure B.21: Solar spectrum measured by GEMOSS between 888 and 896 nm.

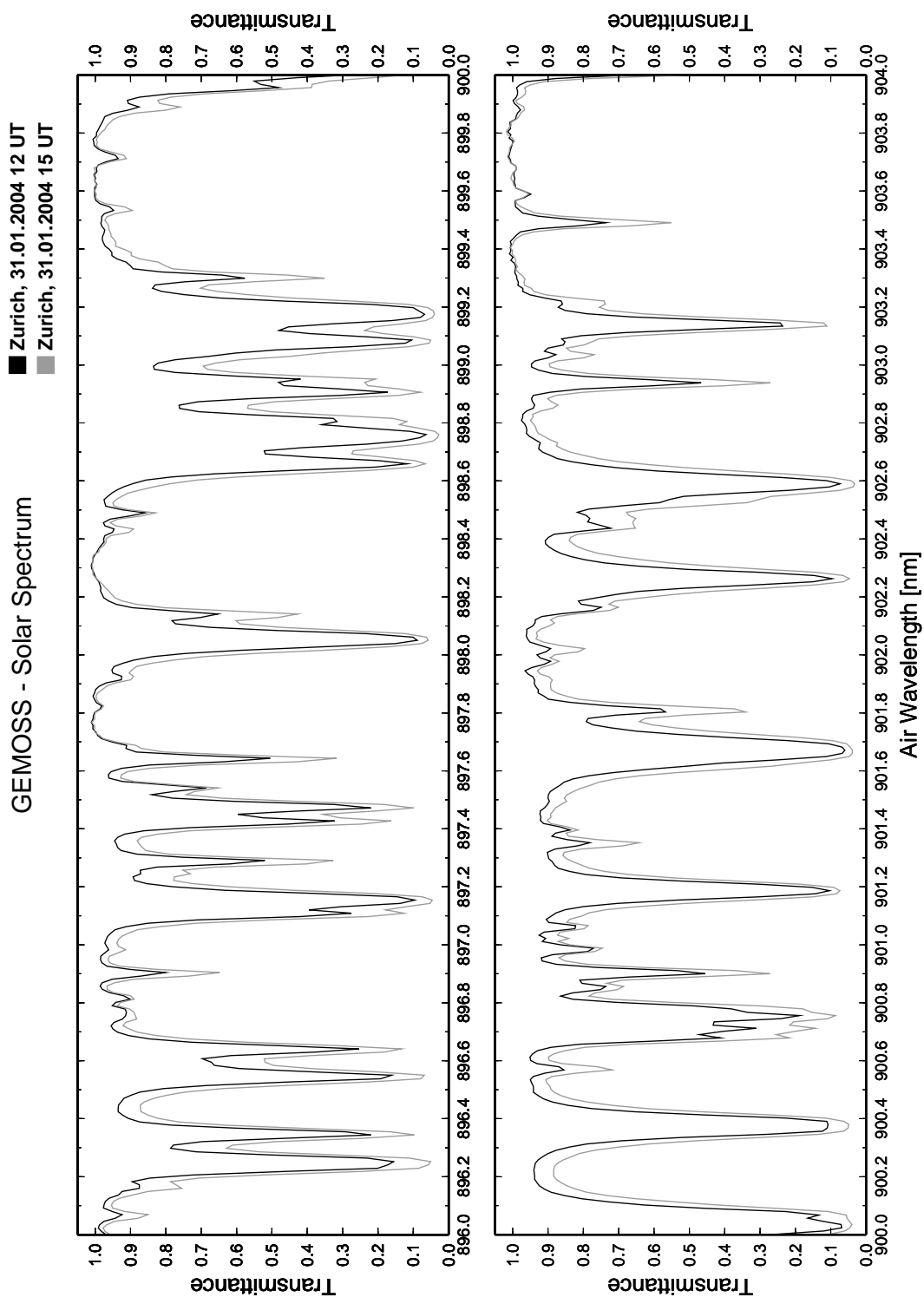


Figure B.22: Solar spectrum measured by GEMOSS between 896 and 904 nm.

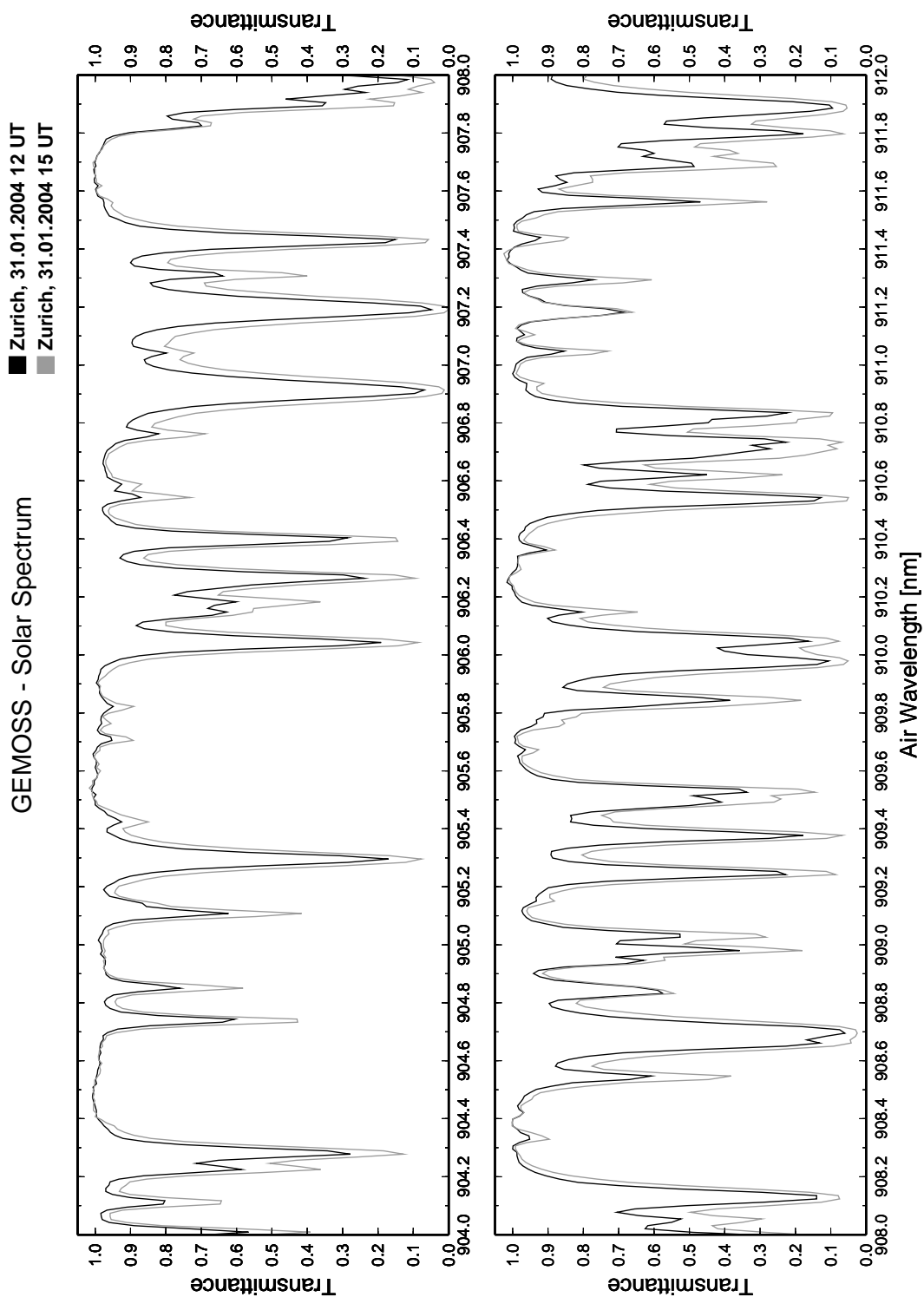


Figure B.23: Solar spectrum measured by GEMOSS between 904 and 912 nm.



## **“Geodätisch-geophysikalische Arbeiten in der Schweiz”**

**(Fortsetzung der Publikationsreihe ”Astronomisch-geodätische Arbeiten in der Schweiz”  
der Schweizerischen Geodätischen Kommission (ab Bd. 47):**

- 47** 1993 NFP 20. Beitrag der Geodäsie zur geologischen Tiefenstruktur und Alpendynamik. H.-G. Kahle (Hrsg.) Autoren: I. Bauersima, G. Beutler, B. Bürki, M. Cocard, A. Geiger, E. Gubler, W. Gurtner, H.-G. Kahle, U. Marti, B. Mattli, M. Rothacher, Th. Schildknecht, D. Schneider, A. Wiget, B. Wirth. 153 Seiten plus 90 Seiten Anhang.
- 48** 1994 Ionosphere and Geodetic Satellite Systems: Permanent GPS Tracking Data for Modelling and Monitoring: Urs Wild, 155 Seiten.
- 49** 1994 Optical Astrometry of Fast Moving Objects using CCD Detectors: Thomas Schildknecht, 200 Seiten.
- 50** 1995 Geodätische Alpen traverse Gotthard: A. Elmiger, R. Köchle, A. Ryf und F. Chaperon. 214 Seiten.
- 51** 1995 Dreidimensionales Testnetz Turtmann 1985-1993, Teil II (GPS-Netz). F. Jeanrichard (Hrsg.) Autoren: G. Beutler, A. Geiger, M. Rothacher, Stefan Schaer, D. Schneider, A. Wiget, 173 Seiten.
- 52** 1995 High Precision GPS Processing in Kinematic Mode: M. Cocard. 139 Seiten.
- 53** 1995 Ambiguity Resolution Techniques in Geodetic and Geodynamic Applications of the Global Positioning System. L. Mervart. 155 Seiten.
- 54** 1997 SG 95: Das neue Schweregrundnetz der Schweiz: F. Arnet und E. Klingelé. 37 Seiten.
- 55** 1997 Combination of Solutions for Geodetic and Geodynamic Applications of the Global Positioning System (GPS). Elmar Brockmann, 211 Seiten.
- 56** 1997 Geoid der Schweiz 1997. Urs Marti, 140 Seiten.
- 57** 1998 Astrometry and Satellite Orbits: Theoretical Considerations and Typical Applications. Urs Hugentobler, 209 Seiten.
- 58** 1998 Systematic Investigations of Error- and System-Modelling of Satellite Based Flight Approaches and Landings in Switzerland. Maurizio Scaramuzza, 165 Seiten.
- 59** 1999 Mapping and Predicting the Earth’s Ionosphere Using the Global Positioning System. Stefan Schaer, 205 Seiten.
- 60** 2000 Modeling and Validating Orbits and Clocks Using the Global Positioning System. Timon Anton Springer, 154 Seiten.
- 61** 2001 Spatial and Temporal Distribution of Atmospheric Water Vapor using Space Geodetic Techniques. Lars Peter Kruse, 128 Seiten.
- 62** 2001 Solar Spectrometry for Determination of Tropospheric Water Vapor. Bernd Sierk, 212 Seiten.
- 63** 2001 Analysis of refraction influences in geodesy using image processing and turbulence models. Philipp Flach, 175 Seiten.
- 64** 2003 INS/GPS Integration for Pedestrian Navigation. V. Gabaglio, 161 Seiten.
- 65** 2003 Efficient Methods for Determining Precise Orbits of Low Earth Orbiters Using the Global Positioning System. Heike Bock, 214 Seiten.
- 66** 2003 Capteurs et Algorithmes pour la Localisation Autonome en Mode Pédestre. Quentin Ladetto, 121 Seiten.
- 67** 2004 GPS based Determination of the Integrated and Spatially Distributed Water Vapor in the Troposphere. Marc Troller, 172 Seiten.
- 68** 2005 Geodetic Mobile Solar Spectrometer. Alexander Somieski, 205 Seiten.